DISSERTATION

SYNTHETIC AND SPECTROSCOPIC INVESTIGATIONS OF ELECTRON SPIN RELAXATION

Submitted by

Ian Moseley

Department of Chemistry

In partial fulfillment of the requirements

For the Degree of Doctor of Philosophy

Colorado State University

Fort Collins, Colorado

Spring 2025

Doctoral Committee:

Advisor: Joseph M. Zadrozny

Rick Finke
Amy Prieto
Kristen Buchanan

ABSTRACT

SYNTHETIC AND SPECTROSCOPIC INVESTIGATIONS OF ELECTRON SPIN RELAXATION

Molecular magnets (also referred to as single molecule magnets (SMMs)), are organometallic complexes which can retain their magnetization in the absence of an applied field. The loss of this magnetization due to environmental interactions is referred to as magnetic relaxation. Due to the small energy gap between electronic spin orientations, maintaining this magnetization typically requires the molecules be held at temperatures approaching absolute zero. This requirement is both costly and impractical for most of the envisioned applications, and as such considerable research efforts have been made to increase the operating temperatures of molecular magnets. This dissertation presents a series of investigations into the magnetic relaxation behavior of molecular magnets incorporating first-row transition metals coupled to adjacent spin centers through electron-electron interactions. Presented herein is a series of investigations which demonstrate a novel method for extending magnetic relaxation in spin-abundant environments, the synthesis and characterization of a low-coordinate iron species as a potential precursor to extended solids, the magnetic properties of a pair of iron-based coordination polymers, and an investigation into the design of electron paramagnetic resonance (EPR) imaging probes using spin forbidden transitions. This research serves as a starting point for future investigations into the control of magnetic relaxation phenomena through synthetic control of electron-electron interactions.

ACKNOWLEDGEMENTS

The path I have taken towards achieving my doctorate in inorganic chemistry has been shaped and guided by many people. Being who I am, I would like to preface this section by acknowledging that I will almost certainly fail to express my gratitude to each and every person who has helped me to achieve this; however, I would like to think that those who know me best will not take offense to any omissions, as they have likely experienced firsthand how my mind works (or doesn't work) more often than not.

With that out of the way, I would like to begin by acknowledging my caring, supportive parents. I was never the easiest child/ teenager/ young adult/ adult to raise. I have always been determined to learn things my own way even when presented with an easier and/or more correct way of doing things. Despite putting up with what I can only imagine was several aneurysms worth of stress and anxiety, you have been there for me along every step of this journey. Looking back, I see the countless times you silently supported me through the challenges of life while I pushed on, oblivious to the amount of effort and care you were putting into helping me. Although the list of things I am thankful for is far too long for the acknowledgements section of my thesis, I would like to thank both of you for your continuous love and support, and for always picking up the phone when I need to talk or just want to listen.

To my loving wife, best friend, and lifelong adventure buddy, Emily. I cannot imagine how I would have made it this far without your endless support and encouragement. It is hard to imagine how I would have made it through the past five years of long nights, failed experiments, and self-doubt without you by my side to help remind me that I am capable of succeeding. Thank you for the late-night snack runs, the (sometimes unintentionally long) breaks from writing my dissertation, plenty of spontaneous shenanigans, and for not leaving me when I buy new skis because they were on a really, really good sale (like really good). I love the life we are building together, and I can't wait to see what else is in store for us.

None of the work presented in this dissertation would have been possible without the guidance and instruction of my PI/Mentor Joseph Zadrozny. Joe, I did not come into this group a perfect graduate student, and I am certainly not leaving as one, but despite everything I know that I will come away having grown both as a chemist and a human being. Although the list of ways you have left a positive impact on me are innumerable, I will highlight a select few in the interest of brevity. 1) Your sharp eye for font inconsistency and elegant figure design will be ever present in the back of my mind, pushing me to produce at the highest level I can while silently critiquing those who do not. 2) I hope that whatever I find myself doing in the years to come, that I can approach it with the same level of excitement you have for spin physics and magnetochemistry. 3) I SOLEMNLY SWEAR TO NEVER REFER TO A POWDER DIFFRACTION PATTERN AS A "SPECTRUM" (unless I am nervously presenting in front of a group of my peers). Thank you for continuing to guide me even when I made you want to pull your hair out, and for never giving up on me.

Now for the part I imagine most of the readers have been waiting for, this section is for my coworkers and friends, and everyone else who has helped me along the way. The order and length of specific acknowledgements is not indicative of the level of support or guidance provided and should not be taken as such.

Anthony Campanella: We actually made it! You have been along for the ride since the first day of grad school, and what a journey it has been. Your abilities as a chemist are clear from your research and publication list, but it was your uncanny ability to navigate complicated, interpersonal issues that has undoubtedly served to keep our group intact over the last five years. While I am not sure I will ever be as levelheaded as you, I would like to think I picked up a few things along the way, and for that I am grateful. Thanks for taking “sick” days** with me to help keep us sane, and for always taking the time to offer constructive feedback and fresh perspective when I need it the most. I am fortunate to have had both a friend and a coworker close enough to fire nerf darts at whenever I needed a break from work. **[If Joe is reading this, “sick” days is an inside joke, and I would never miss an opportunity to be in the lab running my daily 3 reactions.]

Zadrozny Group Post-Docs: To Chun-Yi, Siyoung, AB, and Okten thank you all for your time and effort in helping me to grow as a researcher. Amongst the countless hours spent sitting in on practice talks or discussing science, you were always willing to lend your knowledge without expecting anything in return. I hope you each continue to spread your knowledge and love of chemistry to those around you, wherever you may find yourself next.

Zadrozny Group Elders: To Cassidy and Tyler, you didn’t ask to be stuck with me, but you did an excellent job of helping me grow as a researcher and of putting me in my place when I needed to be. Cassidy, I know we had our differences, but I am grateful to have gotten to know you. Your steadfast resolve and determination is inspiring and I hope you continue to inspire all those around you in your future endeavors. Tyler, your penchant for graphic design and meticulous lab notebook keeping is an inspiration, and contrasts well with the general state of our shared fume hood. Jokes aside, I am glad to have gotten the chance to work with and learn from you, and I hope to see you around CO in the upcoming years.

Zadrozny Group “New Guard”: To Roxanna, Josef, Andrew, Morgan, and Nick, while we have not spent as much time together, I feel confident that you will continue to take the Zadrozny group in the right direction. Grad school was not an easy journey for me, but seeing the excitement and passion you all have for chemistry has helped to keep me motivated through the ups and down of research. I hope you are all able to find balance and happiness as you continue your careers.

“The boys”: To Sabari, Bradley, Gavin, Rob, and very occasionally Luke, thank you for not giving up on me after that faithful day at Caribou, and for always being down for an impromptu adventure. I feel confident that both my mental and physical health would be in shambles without such a good group of people to spend time with, and to discuss the pros and cons of measuring tubing in square inches. I sincerely hope that we continue to find time to head out into the great outdoors and watch me yard-sale my way down the mountain.

Spencer “Uncle Hot Dog” Jonsen: To my favorite postdoc, I have spent far too much time trying to write something both poignant and humorous, without being too sappy, and as a result I am left with nothing. Although I imagine you would never admit it, you have always been and continue to be an inspiration to me. I have met very few people with the level of dedication and enthusiasm you put into everything you do, and I hope you will always be able to find something that motivates you to keep learning and teaching those around you.

Jolene Pittman Moseley Kujoh and Peter Pan: To my unofficial emotional support animals, without whom I would have never made it through late night study sessions, late night editing sessions, or late night dissertation writing sessions. I am thankful for your mostly unconditional love, so long as I continue to feed you on time, twice a day, every day.

To everyone who I have failed to mention, you each played your own, special, albeit less memorable role in my journey through graduate school. Thank you, and goodnight.

Acknowledgements by Dissertation Chapter

Chapter 1 contains work reproduced in part from the published manuscript "A Reaction-Coordinate Perspective on Magnetic Relaxation by Cassidy E. Jackson, Ian P. Moseley, Roxanna Martinez, Siyoung Sung, and Joseph M. Zadrozny (*Chemical Society Reviews*, **2021**, 50, 6684-6699). All authors contributed to the writing and editing of the manuscript. Cassidy E. Jackson made the figures.

This research was performed with the support of Colorado State University (CSU), the NSF-GRFP (006784-0002), the NSF (CHE-1836537), and the NIH (R21EB027293).

Chapter 2 contains work reproduced from the journal article "Slowing Magnetic Relaxation with Open Shell Diluents" by Ian P. Moseley, Christopher P. Ard, Joseph A. DiVerdi, Andrew Ozarowski, Hua Chen, and Joseph M. Zadrozny (*Cell Rep. Phys. Sci.,* **2022**, 3, 3, 100802). Christopher P. Ard, and Hua Chen performed dipolar field calculations and analyses. Joseph A DiVerdi assisted with solid state NMR experiments and analysis. Andrew Ozarowski collected HFHF-EPR spectra and assisted with analysis.

This research was performed with the support of Colorado State University (CSU) and the NSF-GRFP (006784-0002). Part of the work described in this publication was performed at the National High Magnetic Field Laboratory, which is supported by National Science Foundation Cooperative Agreement No. DMR-1644779 and the State of Florida. Magnetometry, EPR, and standard molecular characterization were performed at the CSU Analytical Resources Core, which is supported by an NIH-SIG award (1S10OD021814-01) and the CSU-CORES Program.

Chapter 3 contains work reproduced from the journal article “Synthesis and Magnetic Characterization of a Dinuclear Complex of Low-Coordinate Iron(II)” by Ian P. Moseley, Chun-Yi Lin, David. Z. Zee, and Joseph M. Zadrozny (*Polyhedron,* **2021**, 175, 114171). David Z. Zee performed Mössbauer spectroscopy and analysis.

This research was performed with the support of Colorado State University (CSU) and the NSF-GRFP (006784-0002). Magnetometry, EPR, and standard molecular characterization were performed at the CSU Analytical Resources Core, which is supported by an NIH-SIG award (1S10OD021814-01) and the CSU-CORES Program.

Chapter 4 contains work reproduced from the journal article “Geometry-Dependent Valence Tautomerism, Magnetism, and Electrical Conductivity in 1D Iron-Tetraoxolene Chains” by Ashlyn A. Kamin, Ian P. Moseley, Jeewhan Oh, E.J. Brannan, Paige M. Gannon, Werner Kaminsky, Joseph M. Zadrozny, and Dianne J. Xiao (*Chemical Science*, **2023**, Advance Article). Ashlyn A. Kamin performed all synthetic chemistry and wrote the manuscript, Ian P. Moseley performed magnetic spectroscopy and analysis.

This research was performed with the support of Colorado State University (CSU) and the NSF-GRFP (006784-0002). Magnetometry was performed at the CSU Analytical Resources Core, which is supported by an NIH-SIG award (1S10OD021814-01) and the CSU-CORES Program. This research is also supported by the U.S. Department of Energy Grant (DE-SC0021966).

Chapter 5 contains unpublished work from a manuscript in preparation titled “Weakly Exchange Coupled, Dinuclear Complexes of Cu(II) as Low-Frequency EPRI Probes” by Ian P. Moseley, and Joseph M. Zadrozny. Ian P. Moseley has performed the synthetic and experimental work.

This research was performed with the support of Colorado State University (CSU) and the NSF-GRFP (006784-0002). Magnetometry, EPR, and material characterization was performed at the CSU Analytical Resources Core, which is supported by an NIH-SIG award (1S10OD021814-01) and the CSU-CORES Program.

DEDICATION

For my parents, who have always encouraged me to follow my dreams.

TABLE OF CONTENTS

CHAPTER 1 – Introduction

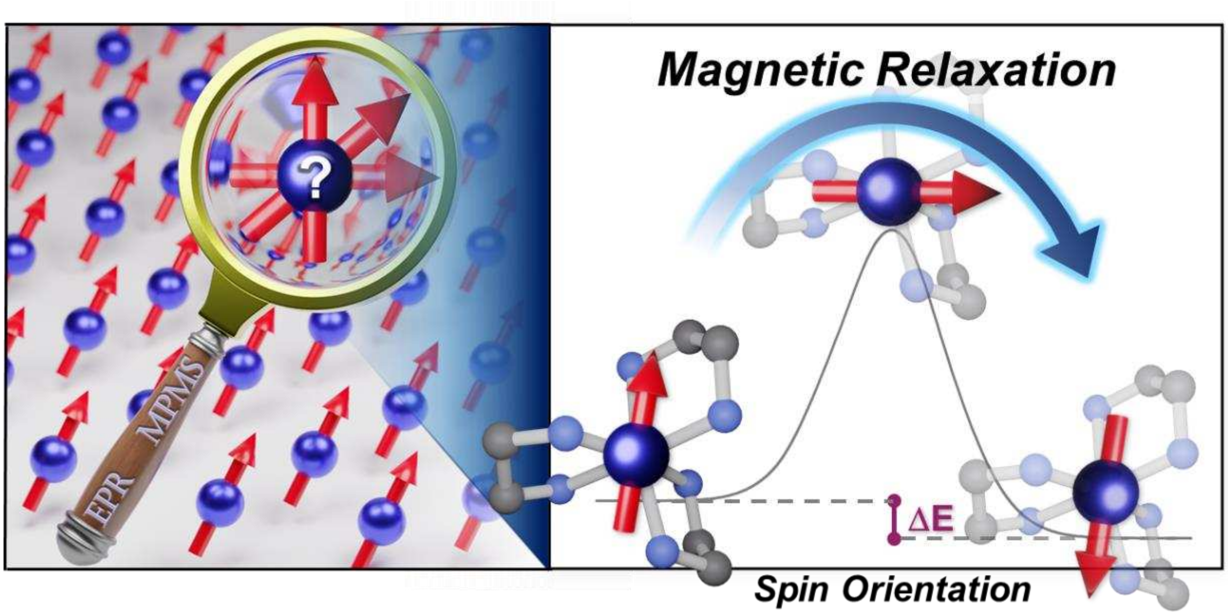

Fig. 1.1 Graphical overview of the introduction chapter.

Motivations

Magnetic molecules are centerpiece components of numerous areas of research, ranging from quantum information processing[1–3] and classical data storage[1,4] to magnetic resonance imaging [5–7] and spin-controlled reactions.[8] Of these, open-shell transition metal complexes are particularly popular, with proposed applications as molecular qubits[2,3,9], spin-crossover sensors[10,11], single molecule magnets[12,13], and molecular spintronic materials.[14] Molecular compounds are notably advantageous for these applications because they offer a blank slate to design magnetic properties by harnessing synthetic chemistry.

Magnetic relaxation (sometimes called spin relaxation), which is the response of the magnetic moment after misalignment from an applied magnetic field is a key property of magnetic materials. A slow relaxation rate permits many important and exciting possibilities, for example, the storage of information (quantum or classical) in the orientation of the magnetic molecule (here a spin-up orientation could be “0” versus spin-down orientation of “1” in analogy to a simple bit). Slow relaxation rates will also enable certain magnetic resonance spectroscopic experiments (e.g., to noninvasively detect local chemistry) while fast relaxation can make these measurements more challenging. As a result, there is considerable interest in understanding how synthetic chemistry can be used to extend relaxation rates of these complexes.

Magnetic relaxation is primarily driven by interaction of the relaxing species with local electronic and magnetic fields. These fields are influenced by intrinsic properties of the molecule. For example, metal-ion identity, spin state, oxidation state, ligand field, and geometry can all affect the relaxation rate of an open-shell metal ion. Extrinsic properties, such as counterion, concentration, temperature, and matrix (e.g., solvent or local chemical surroundings), are also important. Thus, there is considerable overlap between the molecular factors that control magnetic relaxation and those that dictate commonly approached properties by chemists, like reactivity.

The subsequent chapter offers a broad overview of magnetic relaxation as well as the specific relaxation processes discussed throughout this dissertation. In addition, we provide a summary and outlook to offer some insight into the motivations behind the research. Interested readers will find useful references throughout which discuss each topic in more depth.

A Reaction-Coordinate Picture of Relaxation

Magnetic relaxation is the process of a magnetic moment (or a spin) coming to alignment with an applied magnetic field from some other orientation. This misaligned orientation is an excited state while the ground state is when the spin is aligned with the field. For this reason, magnetic relaxation can be thought of analogous to an exergonic reaction that proceeds from

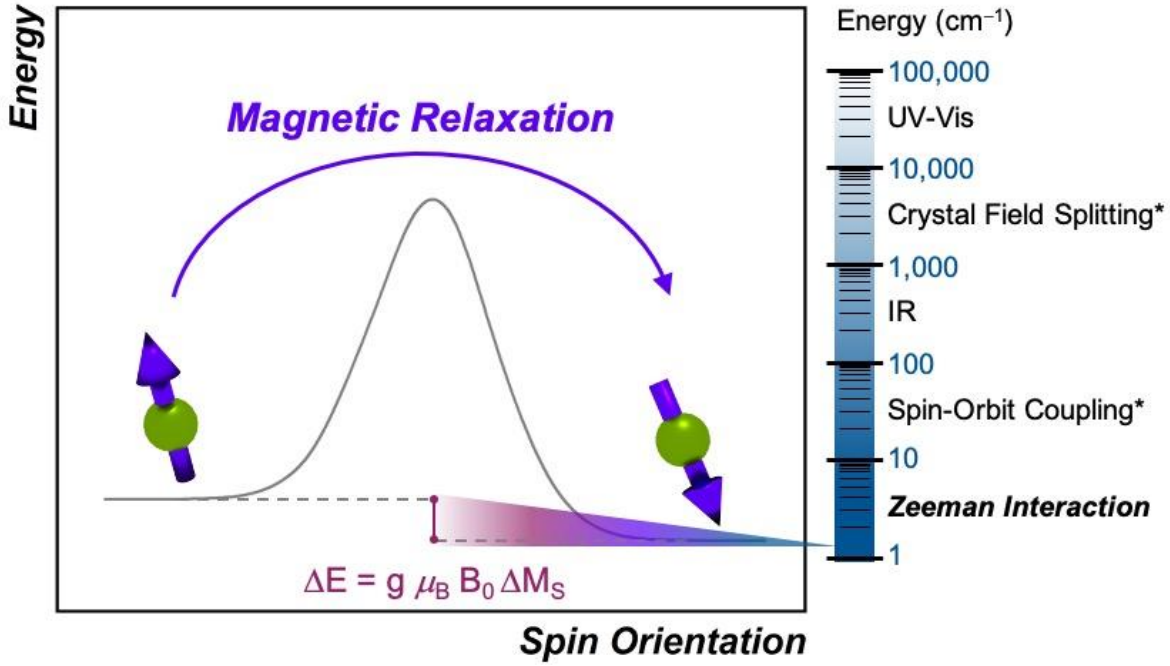

Fig. 1.2. Magnetic relaxation in analogy to a standard reaction-coordinate diagram. Here, the reaction coordinate corresponds to spin orientation, with the products aligned parallel to the applied field and the starting materials aligned against it. The energy difference (DE) between the starting materials and products is the Zeeman energy, as defined in the plot. The energy scaling on the right compares the Zeeman interaction to other important energies. Scaling in the reaction coordinate diagram is arbitrary. Asterisks denote energy scaling for 3d transition metals.

relatively high energy reactants (the misaligned orientation) to lower-energy products (the aligned orientation). In the case of a single unpaired electron in an external magnetic field undergoing relaxation (**Fig. 1.2**), the starting materials could be "spin up", corresponding to the spin quantum number $m_S = +^1/_2$. Likewise, the products could be "spin down", bearing the $m_S = -^1/_2$ spin quantum number. The relaxation process is then the "reaction" that enables the spin to convert orientation.

There are some important similarities between the relaxation process and a chemical reaction. Just like many reactions, the process of magnetic relaxation is thermodynamically favored.[15] There are also often many possible mechanisms by which the system can proceed with relaxation, similar to how many different reaction pathways can exist in a catalytic system. Though there are many of these pathways available to a molecule, again just like with a reaction system, it is the fastest relaxation process that typically proceeds under a given set of conditions. Several relaxation processes have an activation energy, directly analogous to a chemical reaction. However, other relaxation mechanisms can proceed by tunneling through the activation barrier, just like proton-tunneling reactions that can be interrogated through kinetic isotope studies.[20] Owing to all the foregoing similarities, it should be no surprise that elucidating the operative magnetic relaxation processes is just as rich and intellectually rewarding as mechanistic investigations of reactions.

There are also some critical differences between magnetic relaxation and a typical chemical reaction. First, the energy difference separating the starting materials and products is extremely small, typically on the order of a few wavenumbers or less so the relaxation process is nearly thermoneutral. This small energy difference is because the energy separating the spin orientations in a typical applied magnetic field (from the "Zeeman" interaction, Fig. 1.2) is weak. This situation is in stark contrast to the multiple-kcal-energy magnitudes (1 kcal/mol = 350 cm^{-1}) separating starting materials and products in a general chemical reaction. Second, the transition states of molecules in the "relaxation reaction" can correspond to high-energy spin orientations, which are discrete and quantized energy levels with m_S (or M_S if $S > {}^1/_2$) values, or other quantum phenomena entirely. This point highlights a key contrast to a chemical reaction, where a transition state is a transient, high-energy, and distorted molecular geometry. Third, because these transition states are quantized, a given relaxation process does not proceed along a continuous potential-energy curve like molecular transformations, but instead by discrete jumps with emission/absorptions of energy.

We also note that, just like a chemical reaction, the rate of relaxation reflects the slowest step in the operative pathway. Indeed, there are often competing mechanisms, yet the slowest step in the fastest pathway is most important for the observed rate. In this light, the “rate-determining step” for magnetic relaxation is whether the environment can provide the energy to drive the process or accommodate the energy emitted during relaxation.[21] This process is in contrast to reactions where rate determining steps involve structural transformations or proton/electron transfers, and possibly isolable chemical intermediates.

The figure of merit for magnetic relaxation is the time constant of the process, the magnetic relaxation time, which is the inverse of the relaxation rate. The timescale of a magnetic relaxation time is highly variable, typically ranging from picosecond to minute timescales. There are two basic types of magnetic relaxation, spin-lattice relaxation, T_1, and spin-spin relaxation, T_2. Both parameters are vital for the applications mentioned above. Considering this importance, it is essential that we understand how to control the processes that govern these relaxation times and

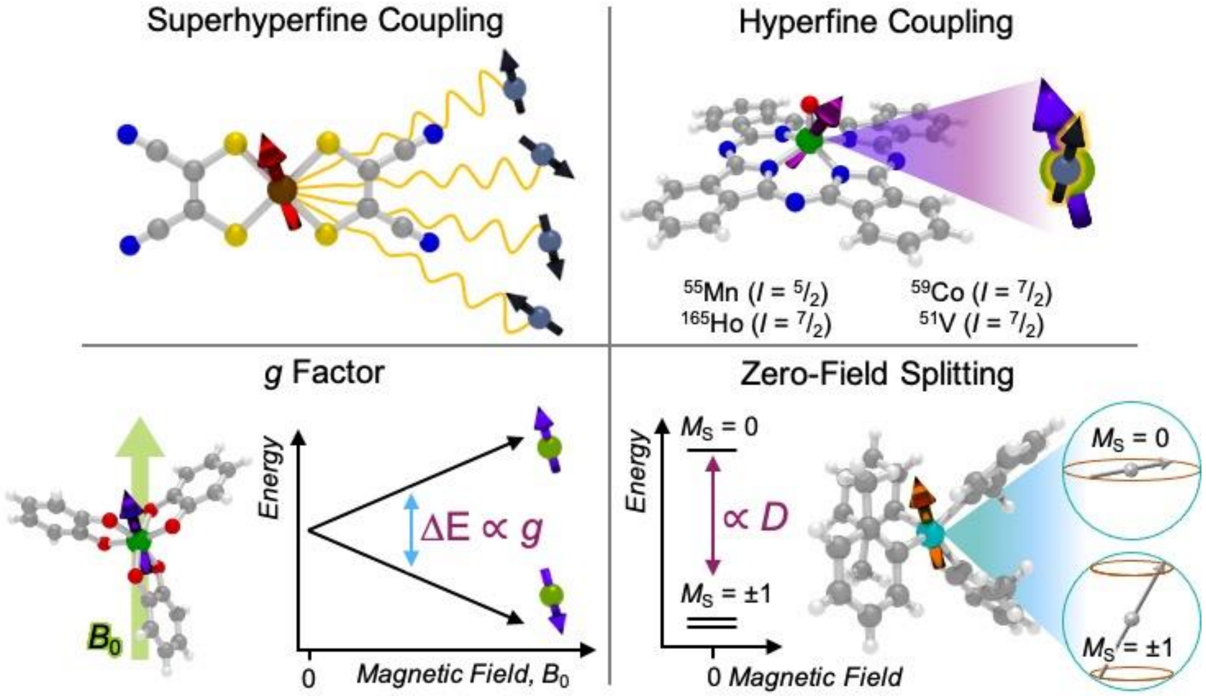

Fig. 1.3. Graphical overview of chemical features that impact relaxation processes.

how they correlate to molecular structure. Below we describe the different relaxation mechanisms that govern these two relaxation times, again in analogy to the basic chemical reaction-coordinate paradigm described above.

Basic Molecular Spin Properties Relevant to Relaxation.

In evaluating the reactivity of a metal complex used in a reaction or as a catalyst, common considerations might be steric congestion or electron abundance/deficiency in the ligand scaffold. Similarly, for coarse-grain prediction of a magnetic relaxation property, there are several key magnetic parameters that are important to consider as a starting point. These parameters are the *g* factor, hyperfine coupling interactions, and zero-field splitting (Fig. 1.3). Comprehensive treatments of *all* the magnetic properties in metal complexes, which are diverse, can be found elsewhere.[15]

The first magnetic factor is the electron gyromagnetic ratio, or *g* factor. Electrons possess an intrinsic angular momentum that possesses a magnetic moment which interacts with an applied magnetic field. The strength (or energy) of this interaction is proportional to the applied magnetic field (B_0), the Bohr magneton (m_B, a fundamental constant), the m_S value of the given spin orientation, and the *g* factor: $E = gm_bB_0m_S$. The part relevant to relaxation is the *g* factor, a proportionality constant that describes the sensitivity of the magnetic moment to an external magnetic field. Simply stated – a larger *g* factor indicates a larger change in energy between different spin orientations in an applied magnetic field (Fig. 1.3).

The *g* factor often gives different values based on the orientation of a molecule in a magnetic field. The *g* value is often referred to as the *g* tensor for this point. For an organic radical, *g* will be close to 2.0023, which is the *g* factor for a free electron, and relatively independent of orientation. In contrast, metal complexes often have highly orientation dependent *g* values that can range from 0 to nearly 20 and are often anisotropic (i.e. g_x, g_y, and g_z are all different, x, y, and z here defined with respect to molecular axes). The largest and most anisotropic *g* factors tend to be found in rare-earth ions and low-coordinate transition metals.[22] Generally speaking, anisotropic *g* values tend to produce faster relaxation rates, though there are many exceptions.

The second important factor is the magnetic interaction between an unpaired electronic spin and a nuclear spin on the same atom. This interaction is known as the hyperfine coupling interaction and has a strength denoted by the hyperfine coupling constant (*A*) (Fig. 1.3). An example of this interaction occurs in Co(II) complexes, from the coupling of the magnetic nucleus of ^{59}Co ($I = {}^{7}/_{2}$) and the unpaired electrons. Hyperfine interactions are very similar to *J*-coupling in proton nuclear magnetic resonance (NMR) spectroscopy. Hyperfine couplings can also be anisotropic, just like the *g* factor.

Magnetic nuclei are abundant in complexes beyond the spin-bearing ion and are often located in the ligand shell, counterions, and the surrounding matrix (e.g., proton-rich organic solvents, $I = {}^{1}/_{2}$ ^{1}H). Magnetic interactions with these latter three classes of nuclei is commonly referred to as “superhyperfine” coupling. Typically, stronger superhyperfine interactions with environmental magnetic species engender faster relaxation rates, though there is nuance to this statement that will be described later.

The final interaction that is noteworthy to highlight, known as the zero-field splitting, is a specific manifestation of spin-orbit coupling in metal ions with spin states *greater* than ${}^{1}/_{2}$ (as a result of bearing two or more unpaired electrons) (Fig. 1.3). For an electronic spin with $S > {}^{1}/_{2}$, there are $|2S + 1|$ accessible M_S levels. Each M_S level corresponds to a different alignment of the electronic spin relative to a molecular axis. A high $|M_S|$ value represents a spin precessing tightly around a molecular z axis, or closely aligned with that axis. A low $|M_S|$ value, in contrast, is a spin precessing far away from that same axis, commonly represented with perpendicular alignment to z. In the absence of zero-field splitting, or for a light atom (like an $S > {}^1/_2$ organic radical), the M_S levels are degenerate, or nearly so, at zero applied magnetic field. In the presence of zero-field splitting, which is common for heavy metal atoms (3d, 4d, 5d, 4f, and 5f elements) however, they are not, as shown in Fig. 1.3.

There are two parameters that describe the zero-field splitting. The first, the *axial* zero field splitting, or D, splits the energies of $|M_S|$ levels away from one another (e.g., it will separate a pair of $M_S = \pm1$ levels from $M_S = 0$ levels as in Fig. 1.3). For first-row transition metal complexes, values of D can range from less than 1 cm^{-1} to hundreds of cm^{-1}.[22] The sign of D causes two limiting cases of M_S-level orderings. A positive D indicates a spin where the lowest energy level is $M_S = 0$ or $M_S = \pm\, {}^1/_2$, depending on whether S is integer (even number of electrons) or half-integer (odd number of electrons). A negative D indicates a spin where the M_S levels with largest $|M_S|$ are lowest in energy (e.g., $M_S = \pm1$ for an $S = 1$ Cr^{4+} ion, as shown in Fig. 1.3). The second parameter, E, the *transverse* zero-field splitting or rhombic zero field splitting parameter, will cause an energy splitting of M_S levels in a pair (e.g., it will split $M_S = \pm1$ levels from each other at zero field). The ratio $|E/D|$ is often referred to as the *rhombicity* parameter.[23]

The zero-field splitting is important for relaxation because individual M_S levels are the starting points, end points, and transition states of the magnetic relaxation process. Thus, the zero-field splitting parameters directly modify the relaxation rates by dictating the relative energies of all involved steps in a relaxation pathway. The parameters D and E are also a direct result of the electronic structure of the metal complex, meaning that many intuitive molecular features, primarily symmetry and ligand field, can be modified to direct the sign and magnitude of D and

E. This fact also means that general correlations between *D*, *E*, and relaxation times are challenging to make, and are best discussed on a case-by-case basis.

Spin-Lattice Relaxation (T_1)

Spin-lattice relaxation (also called longitudinal relaxation) refers to relaxation driven by interactions between the molecule and the environment, or "lattice," that exchange energy. Spin-lattice relaxation specifically describes the process for a spin to relax from a starting spin-up (destabilized) orientation to the spin-down (stabilized) product orientation (Fig. 1.2). There is an enormous mechanistic diversity in how this process occurs depending on how a magnetic molecule exchanges energy with the lattice.

The energy exchanged with the environment during spin-lattice relaxation is in discrete amounts. Here, energy is exchanged through phonons, which are collective, long-range vibrations in a solid, often spanning multiple molecules.[24] The availability of phonons in a system is dependent on the temperature of the system and the nature of the surrounding matrix (e.g., a crystalline v. frozen solvent glass environment).[27]

The rates of the different mechanisms of relaxation that we discuss below generally follow different temperature, magnetic field, or environmental dependencies. Furthermore, the rates of these processes may be impacted by the lattice just as much as the molecule itself. Thus, in any real system, unraveling the operative mechanisms requires measuring the dependence of the relaxation process on all of these parameters. This process, though applied to dynamic magnetic processes, is therefore comparable to how one might determine the full picture of potential reaction pathways in a catalytic system. Below we give an overview of each of the known mechanisms of spin-lattice relaxation, their relation to the reaction analogy established earlier, and the dependence of the processes on the molecule and environment.

Measurement of T_1.

Spin-lattice relaxation is measured primarily by two different instruments: a magnetometer such as a magnetic properties measurement system (MPMS), or a pulsed electron paramagnetic resonance (EPR) spectrometer. Magnetometers allow for the study of magnetic relaxation processes across a range of temperatures, time scales and magnetic field strengths with the technique of alternating current (ac) susceptibility. However, the limited frequency range for ac susceptibility measurements (typically 0.01 Hz - 1500 Hz) means that quickly relaxing systems ($T_1 <$ *ca.* 0.1 ms) are not able to be observed directly with this instrument. An alternative analysis is by pulsed EPR spectroscopy, which can measure T_1 through inversion or saturation recovery experiments. This technique can measure much faster relaxation times ($T_1 \sim 1$ ms lengths), but pulsed spectrometers are far less common than magnetometers. There are some slight differences in the time constant measured by the techniques, because ac susceptibility extracts T_1 from bulk magnetization while the EPR experiment is probing a specific transition.[25] However, at the microscopic level, the same process is occurring – a spin is flipping during the process of relaxation. We direct the interested reader to several key resources to learn about these techniques in deeper detail.[4,26]

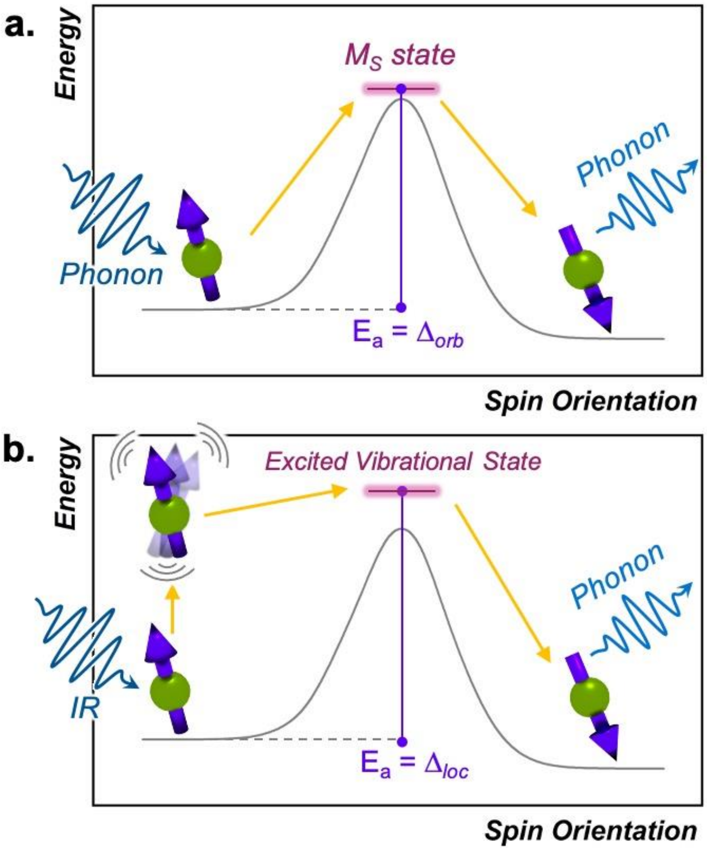

Fig. 1.4. (**a**) Depiction of the Orbach process in analogy to a reaction-coordinate diagram. The transition state is an actual high-energy M_S level for the relaxing spin. **(b)** Energy profile of the local mode process. Here, discrete vibrations in a molecular species promote the spin to overcome the barrier and enable relaxation.

Mechanisms of Spin-Lattice Relaxation

Below we discuss the collection of mechanisms that drive T_1 relaxation, starting from those that most closely resemble the reaction-coordinate analogy, then move on to processes that deviate from the analogy and demonstrate the complexity of relaxation phenomena in magnetic molecules.

Orbach Process.

The Orbach process proceeds by excitation from the starting spin orientation to a higher energy spin orientation with energy provided by a phonon. This higher-energy M_S level is the effective transition state for the Orbach process. Relaxation then proceeds from this transition state to the lower energy spin orientation by releasing energy (in the form of a phonon) to the lattice (Fig. 1.4).[26,27] For this process to occur, there must be available phonons of the appropriate energy to excite to the transition state. The Orbach process is not limited to a single "transition state" and can involve multiple steps to a higher energy M_S level before relaxation via phonon emission.

High-spin metal ions frequently relax via the Orbach process, as other M_S levels within the $|2S + 1|$ manifold often serve as transition states. In contrast, $S = {}^1/_2$ molecules do not show the Orbach process, as there are only two m_S levels for an $S = {}^1/_2$ system ($m_s = \pm{}^1/_2$) (and thus no transition state). The relaxation rate of the Orbach process is described by:

$$\frac{1}{T_1} = A_{orb} e^{(\Delta_{orb}/k_B T)} \qquad (1)$$

This equation mirrors the form of the Arrhenius law, where $1/T_1$ is the rate constant. A_{orb} is the attempt frequency for the Arrhenius description and a larger A_{orb} means there is higher probability the mechanism will contribute to relaxation. A_{orb} is determined by several factors: it decreases in magnitude with increasing phonon availability (or energy availability) and generally increases as the activation energy increases.[15] Hence, it is challenging to determine A_{orb} *a priori* on the basis of intuitive molecular considerations. Indeed, the basic theories for understanding relaxation (and the origins of A_{orb}) are developed for solid state defects, not molecular systems. As such, A_{orb} is frequently just extracted from experimental data, and is typically found with values of 10^{-2} to 10^{-10} s^{-1}.[4,15] The term Δ_{orb} is the activation energy (E_a) to the M_S-level transition state. Finally, note that A_{orb} is denoted as t_0 and Δ_{orb} as "U_{eff}" or "effective energy barrier" in the single-molecule magnet literature, which tends to focus on this parameter as the key figure of merit.[4] An example molecule that exhibits the Orbach process is presented in the state-of-the-art section.

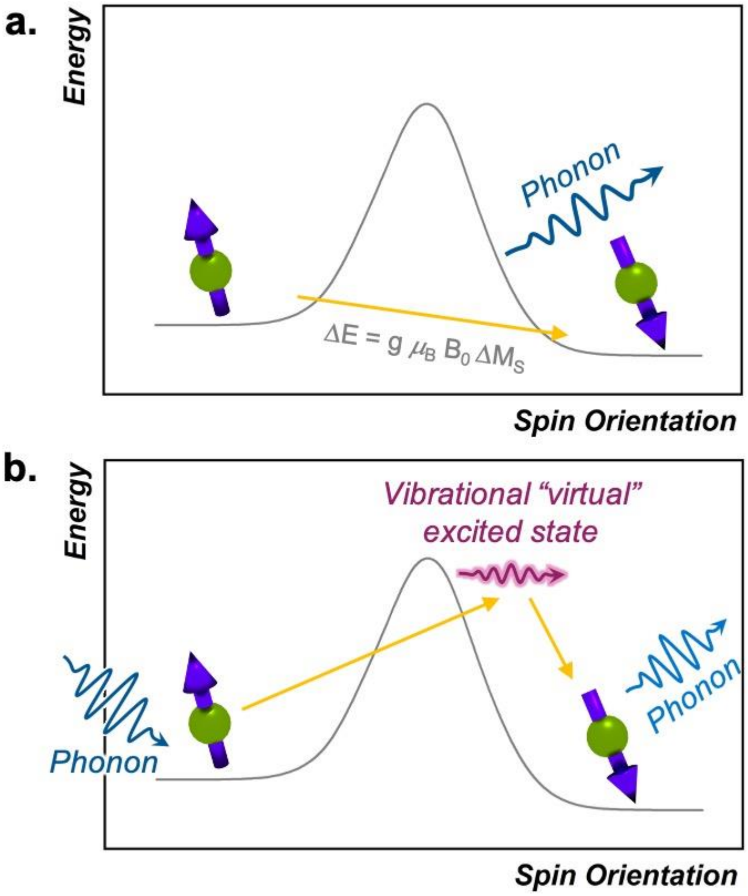

Fig. 1.5. **(a)** Depiction of the direct process in analogy to a reaction coordinate diagram. The spin flip energy is the Zeeman energy and relaxation emits a single phonon of that energy to the lattice. **(b)** Depiction of the Raman process in analogy to a reaction coordinate diagram. The "virtual" transition state is a superposition of vibrational states in the solid and is not an actual defined energy level. Relaxation involves two phonons in a simultaneous excitation and deexcitation of the spins, ultimately transferring energy to the environment of an amount equal to the DE between the starting and product spin orientations.

Direct Process.

The direct process is the first one we discuss that does not have an activation energy. In this process, a spin directly proceeds from the starting orientation to the final orientation because of an energy match between the energy separation of the two levels and a lattice phonon.[33,34] Importantly, the process effectively circumvents any possible transition states (Fig. 1.5). The direct process is analogous to the emission step of phosphorescence in photochemistry, where relaxation from an excited triplet to a ground singlet occurs without an activation energy, with a release of energy in the form of a phonon (a visible photon in the phosphorescence picture). However, unlike for phosphorescence emission, which involves a change in the number of unpaired electrons, the direct process is simply a change in spin orientation for the relaxing species.

The direct process has a distinctive magnetic field and temperature dependence that can enable diagnosis with relaxation studies. Indeed, the rate of relaxation for the direct process is described by the follow equation:

$$\frac{1}{T_1} = A_{dir} B^4 T \qquad (3)$$

A_{dir} is related to many features of a relaxing molecule's environment, specifically the number of phonons available that match the ΔE separation of the starting/end orientations and speed of sound of the matrix.[35,36] Like A_{loc} and A_{orb}, A_{dir} is generally treated as the weight of the contribution of this process to relaxation at a given field and temperature. B is the applied magnetic field, and T is the temperature. The linear dependence of relaxation rate on temperature and B^4 field dependence are characteristic of the direct process. Furthermore, the involved phonons must be a direct energy match to the splitting of the starting materials and products of the spin system, which is small (usually 1-2 cm^{-1} or less) because the Zeeman energy is very small. As a result, this process is typically dominant only at low temperatures (< 10 K), when the only available phonons from the lattice are small in energy. Examples of the direct process are abundant in copper(II) square planar complexes which tend to exhibit relaxation through the direct process below 20 K.[37]

Raman Process.

The Raman relaxation process is more common at higher temperatures than the direct process. The Raman relaxation process proceeds when a spin system simultaneously absorbs and emits phonons of differing energies. This action is fundamentally different than the direct process, which emits only one phonon, or the Orbach process, which involves successive absorption then emission. The difference in energies between the two phonons of the Raman process must match the difference in energy between the starting and final orientations. The fact that these phonons have defined energies suggests that there is absorption to and from a well-defined transition state. However, for the Raman process, that "state" is a superposition of lattice vibrations and does not actually exist, and is commonly referred to as a "virtual state"[15,33] (Fig. 1.5, b). This relaxation mechanism therefore does not have a clear connection to the classical reaction-coordinate picture developed earlier in this tutorial.[12] Nevertheless, the observation of the Raman process is incredibly common in relaxation studies. One example of a molecule exhibiting this process is the cobalt complex [Co(acac)$_2$(H$_2$O)$_2$], which demonstrates the Raman process above 3 K when measured by ac susceptibility under *ca.* 1000 G magnetic fields.[38]

The rate of relaxation via the Raman process is described by the following equation:

$$\frac{1}{T_1} = A_{Ram}\left(\frac{T}{\theta_D}\right)^n J_8\left(\frac{\theta_D}{T}\right) \quad (2)$$

Where A_{Ram} is an experimentally determined factor like A_{loc}, A_{dir}, and A_{orb} (and controlled by many similar parameters).[35] Like those coefficients, it also describes the contribution from the Raman process to the overall relaxation rate. B is the applied magnetic field, T is the temperature, θ_{D} is the Debye temperature (which corresponds to the energy above which phonons do not exist in a solid, converted to an energy by 1 K ≈ 0.7 cm^{-1}), n is an exponent dependent on the relaxing system, and J_8 is the transport integral.[‡] The transport integral describes the energy distribution of phonons in the matrix. This integral and the characteristic temperature of the solid, or the Debye temperature (θ_D), depend on the physical composition of the solid.[39] Qualitatively, these two parameters signify that an environment with a larger distribution of accessible lattice vibrations will better facilitate the simultaneous absorption/emission process that drives the Raman process.

The Raman process produces a characteristic temperature dependence because of the exponent n. In theory, the rate of relaxation should scale with T^9 ($n = 9$) for species with a half-integer spin state and T^7 ($n = 7$) for integer spin state. In practice, however, multiple processes are often active and thus the apparent exponent extracted from fitting variable-temperature T_1 data is a non-integer value or ranges down to $n = 2$ to 3.[40] The Raman process commonly occurs at temperatures where the lattice does not have available phonons of sufficient energy to excite the spin system to an actual transition state for the relaxation process. For this reason, this process "undercuts" the barrier, just like the direct process.

Quantum Tunneling Processes.

All previous mechanisms require energy input/release via interacting with the phonon system of the environment. However, there are two processes that circumvent this requirement by tunneling straight through the activation barrier for relaxation. It is for this reason that these processes are referred to as quantum tunneling of the magnetization (QTM) processes (Fig. 1.6).[23]

There are two QTM-based processes. One occurs directly between the starting and final spin orientations, without any input energy, and is referred to as "ground-state" QTM (Fig. 1.6). This type of tunneling mechanism is operative if there is a magnetic interaction between the wavefunctions of the starting and final spin orientations, which opens a tunnel-splitting energy gap in the barrier (Δ_T, Fig 1.6). In the same way an electron tunnels because its spatial wavefunction can exist on both sides of an impenetrable barrier, the spin wavefunction of a system can exist on both sides of the activation barrier for reorientation. A stronger interaction between the starting and final orientations will generate a larger Δ_T and enable more efficient tunneling. Ground-state QTM is most facile near (or at) zero applied magnetic field, because interactions that drive QTM are strongest when the energy difference between the start and endpoint is smallest. Furthermore,

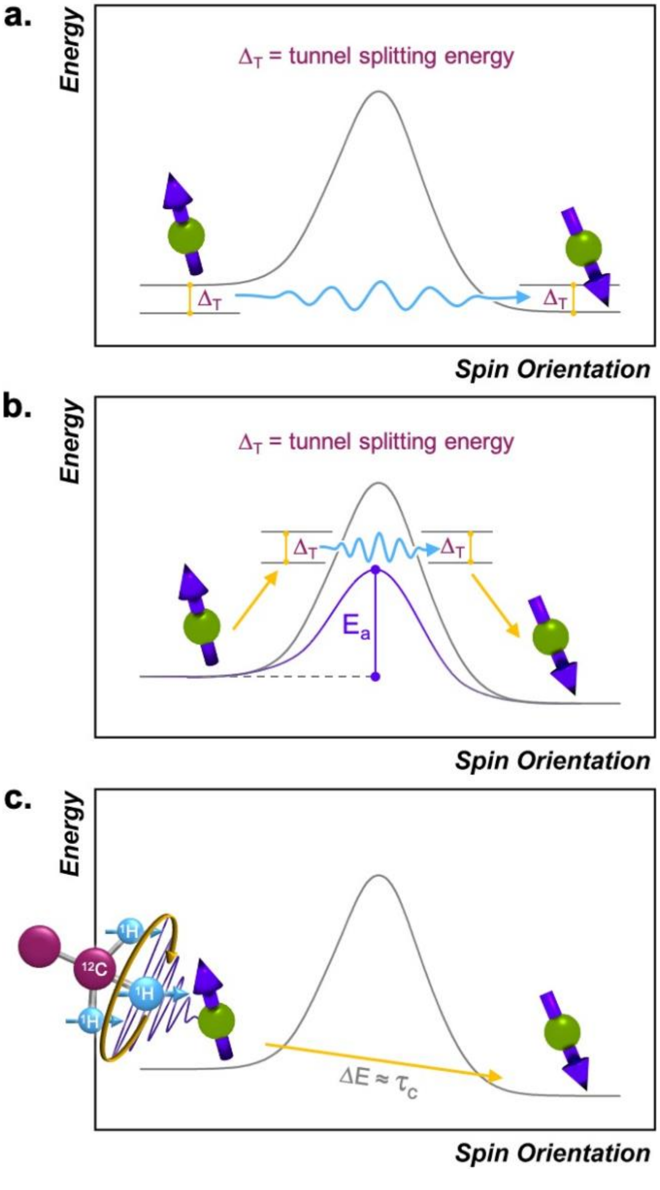

Fig. 1.6. Reaction-coordinate depictions for (**a**) ground-state and (**b**) thermally assisted quantum tunneling of the magnetization processes and (**c**) thermally activated processes.

the relaxation rate is generally temperature-independent because the tunneling mechanism does not require energy from phonons to ascend over a barrier. Tunneling is typically dominant only at the lowest temperatures, when the available phonons lack sufficient energy to enable any of the other processes. For example, the molecule $[Ph_4P]_2[Co(SPh)_4]$ displays tunneling below 2.5 K when measured by ac susceptibility under zero applied field.[41]

The second tunneling mechanism, thermally assisted QTM, requires exchange of energy with the lattice (Fig. 1.6). This mechanism involves an initial promotion (via phonon) of the starting spin orientation to a higher-energy M_S level. For the thermally assisted process, this level is below the highest-energy M_s level within a given manifold of an $S > {}^1/_2$ species (Fig. 1.6). Once promoted, the system then tunnels through the barrier to another M_s level, from which it can finally relax to the product. The thermally activated QTM mechanism behaves analogously to the Orbach process because of the promotion and phonon emission. However, this mechanism proceeds with an activation energy that is lower than the theoretical maximum defined by the zero-field splitting. An example of this phenomenon is illustrated with the $S = 2$ species $[(TPA^{tBu})Fe]^-$, which exhibits a Δ_{Orb} of 65 cm^{-1}, which is lower than the theoretical maximum of 192 cm^{-1} for this molecule.[42]

Thermally Activated Processes.

Thermally activated processes are relaxation processes that are driven by thermal motion in the environment, for example methyl or amino group rotations, wherein magnetic nuclei are located on the moving structure (Fig. 1.6). This process is common at higher temperatures, when the surrounding matrix of a magnetic molecule softens to allow physical motion to occur, when they would otherwise be frozen at low temperature.[28,33,43] A given local motion will affect relaxation if the correlation time of that motion (t_c, or the inverse of the rate of the local motion) approaches the energy difference of the starting/ending orientation (w, in frequency).[43] The rates of thermally activated processes follow this equation:

$$\frac{1}{T_1} = A_{therm}\left(\frac{2\tau_c}{1+\omega^2{\tau_c}^2}\right) \qquad (4)$$

Here, A_{therm} correlates to the amplitude of the local magnetic field fluctuations from the thermally activated motion (but is generally treated as a weight for this process' contribution to T_1, like A_{orb}, A_{loc}, A_{Ram}, and A_{dir}), τ_c[§] is the correlation time of the thermally activated process, and w is the frequency of the energy gap between the starting/ending spin configurations.[43] t_c is temperature-dependent but depends on the activated motion and molecule, as t_c needs to approach 1/w. As such, there is no diagnostic temperature dependence for this process in the absence of other information about the molecular structure. One example of a molecule that displays this type of thermally activated process is in RbC_{60} fulleride, where a metal-to-insulator phase transition triggers fast relaxation (measured by pulsed EPR) at ca. 25 K and 3400 G.[43]

Intrinsic and Extrinsic Factors That Impact T_1.

There are many chemical and physical factors that impact T_1 relaxation in 3d transition metal ions. First, we describe the important (and synthetically tunable) factors for T_1 that are intrinsic to molecules then move on to extrinsic parameters that impact T_1.

Strength and Symmetry of the Ligand Field.

The effects of the ligand field on relaxation most commonly manifest through zero-field splitting in high-spin ions. This tendency is for two main reasons. First, the magnitudes of D and E, which are governed by the ligand field, can shift the energies of the M_S levels involved in relaxation. Thus, D and E will dictate the activation energies for both the Orbach and thermally assisted QTM mechanisms. Second, a nonzero value of E will induce ground-state QTM as an efficient relaxation pathway. Generally, the magnitudes of D and E are greater when the ligand field for a high-spin metal ion is weaker. However, the dependence of D (both in sign and magnitude) on the ligand field is extremely intricate, and so many exceptions to this rule exist. Furthermore, the magnitude of E is heavily dependent on symmetry. Coordination geometries that have one principal axis of rotation and adhere to nearly idealized uniaxial symmetry tend to have lower-magnitude E parameters and thus, suppressed ground-state tunneling. We refer the reader to excellent reviews of these parameters, which demonstrate the power of molecular design for tuning relaxation processes.[12,13,44,45]

Spin State.

The effects of integer ("non-Kramers") versus half-integer spin ("Kramers") systems of unpaired electrons are evident most clearly in the QTM relaxation pathways. Here, a species with an integer spin is far more likely to exhibit relaxation by ground-state QTM than a half-integer-spin complex, because the term E is more effective at opening a tunneling gap for integer spin than half-integer-spin species.[4] A second place the spin state impacts relaxation is the difference in temperature dependence of the Raman process, as described earlier.

Isotopic Identity.

Many metal ions possess isotopes that have non-zero nuclear spin, for example ^{59}Co (I = $^{7}/_{2}$, 100% natural abundance) or ^{165}Ho (I = $^{7}/_{2}$, also 100% natural abundance). The impact of a non-zero nuclear spin is primarily observed at zero field, low temperatures, and primarily affects quantum tunneling mechanisms.[46] The origin of this effect is the hyperfine coupling to the metal-ion nuclear spin, which can open a tunneling gap and increase the rate of QTM.

Spin-Orbit Coupling.

Spin-orbit coupling (SOC) is an intrinsic property of a molecule. This fundamental electronic structure feature is broadly important in dictating relaxation, but has two different effects, generally depending on whether relaxation occurs at high temperature or low temperature. The high temperature impact is because the SOC interaction ties the energies of the M_S levels (e.g., potential activation energies for the Orbach process) directly to the spin-bearing orbital energies of the metal ion. Consequently, small changes in the structure of a molecule (e.g., from a vibration that modulates metal-ligand bond distances) impact the spin-bearing orbitals, when then modulate the M_S-level energies via the SOC to facilitate relaxation. The stronger the SOC for a given system, the more efficient this effect, and the shorter T_1 tends to become. For this reason, light-element species, for example, organic radicals tend to have T_1 values (often ms) that are longer at higher temperature than metal-ion systems. At lower temperature, the effect of a large SOC is different, particularly if the Orbach mechanism is active. In this case, a large SOC can push transition states to higher energies, enhancing the activation energy and ultimately slowing relaxation. The Dy-containing molecule in the state-of-the-art section later in the manuscript is a prime example of this point.

The importance of the SOC also means that the relaxation time can be dependent on precisely what orbital an electron resides in. Indeed, this effect is seen for the $[V(C_6H_4O_2)_3]^{2-}$ versus $[VO(C_6H_4O_2)_2]^{2-}$ molecules, which possess a single d electron in the d_{z2} versus d_{x2-y2} orbital, respectively. T_1 is different by approximately an order of magnitude between these two molecules owing to this difference.[47–49]

Temperature.

Temperature is one of the main extrinsic mechanisms of controlling relaxation. A given spin system will relax via the most efficient mechanism available. Thus, over a given temperature regime, one process is typically dominant, and cooling/heating the system can transition the system to relaxation via a different mechanism. The exact ordering of these domains with temperature is highly dependent on the studied system. Nevertheless, a general ordering scheme is still possible. Ground-state QTM and the direct process are often observed at the lowest temperatures, where high-energy phonons are unavailable. A system will then usually transition to a regime where the Raman process is active upon warming. With further increasing temperature, where high-energy phonons become available in the solid, the Orbach process (or the analogous thermally assisted QTM) will typically take over. At even higher temperatures, local-mode and thermally activated mechanisms become active. A complete picture of magnetic relaxation for a molecule requires scanning an abundance of temperatures, just like understanding the kinetics of a chemical reaction.

Magnetic Field.

The applied magnetic field is the second most-commonly varied extrinsic factor for studying relaxation. Most relaxation processes exhibit a field dependence because the magnetic field will vary the energies of the starting and final spin orientations. The only relaxation process with a rate that has a field dependence explicitly written into the equation is the direct process, which displays a B^4 field dependence. However, in the case of processes that involve an M_S-level transition state, the applied field can also vary the energy of the transition state, thereby modifying the activation energies and rates, though this impact is relatively small. A changing applied field can also affect the efficiency of the thermally activated process, by modulating the difference between the ΔE for the starting/ending spin configurations and the correlation times of environmental motions. Applied fields are also enormously impactful in the quantum tunneling, as they split the M_S levels nominally involved in tunneling, effectively killing the process and inducing slower magnetic relaxation. The effect of a magnetic field is much stronger on the ground-state tunneling process than the thermally assisted one, as larger M_S levels have energies that are more sensitive to changes in the magnetic field. The foregoing discussion justifies the widespread nature of using variable fields for studying relaxation: it can enhance T_1 by orders of magnitude and is thus a powerful handle for optimization.

In summary, there are many dials available to the experimentalist to turn when controlling the operative T_1 processes. However, the foregoing points are not the only factors that affect T_1. Indeed, there are many other effects stemming from specifics of measurement. We direct those interested to read further for more in depth information.[15]

Local Magnetic Species.

The local magnetic species surrounding a molecule (the "spin bath") also exert important effects on relaxation. This factor is readily altered by the chemist, who can choose, for example, to co-crystallize a molecule of interest with other molecules or dilute by dissolution in different

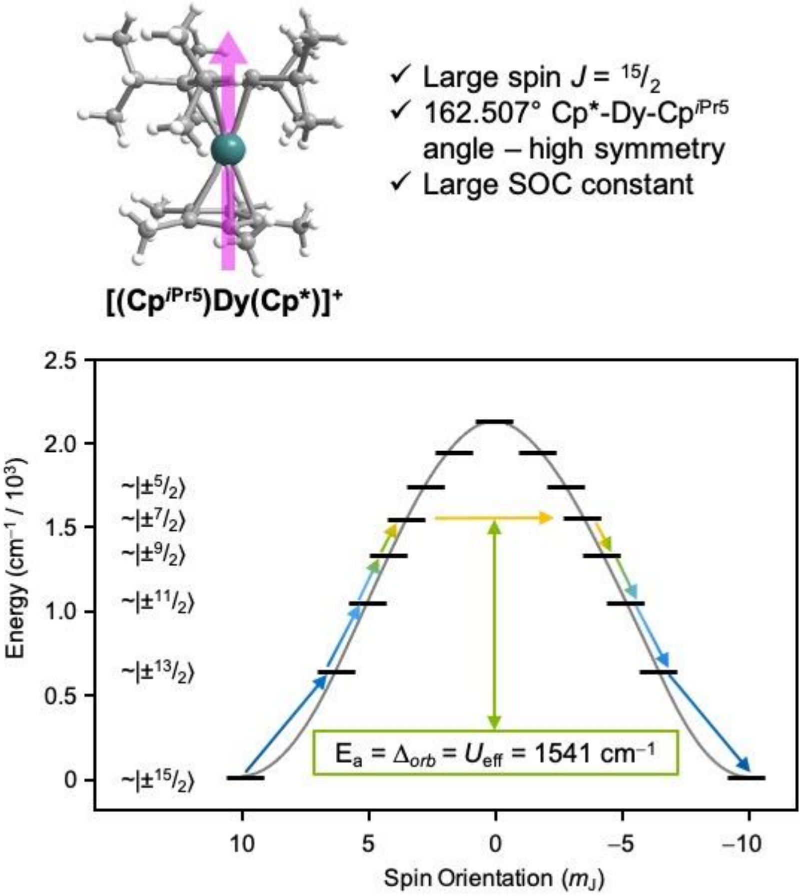

Fig. 1.7. Recent ground-breaking system for targeting a long T_1. The highly axial geometry of the metal complex suppresses tunneling, which combines with the high spin state and large spin-orbit coupling to enable an exceptionally high activation energy to relaxation. Cp* = pentamethylcyclopentadiene ; $\mathrm{Cp}^{i\mathrm{Pr5}}$ = pentaisopropylcyclopentadiene. The levels in the bottom plot are labeled in "ket" notation, which here simply give the M_J values of the $^6H_{15/2}$ Dy^{3+} ion, which reach up to $M_J = \pm^{15}/_2$.

organic solvents.[4] These studies show that relaxation times generally increase when local magnetic content decreases, specifically the concentration of open-shell molecules. This general observation is because the presence of nearby magnetic units can hasten several of the above relaxation processes. For example, magnetic coupling to nearby electron spin systems will produce discrete spin levels that are relatively low-lying above the energies of the starting/ending spin orientations. Thus, the activation energy is lowered, and the relaxation rate accelerates via an Orbach process. Another common observed impact is through quantum tunneling, wherein proximate magnetic species enable the ground state QTM via a tunneling gap created by dipolar interactions. The work detailed in chapter two presents a unique investigation into these precise dynamics, and the possibility of synthetic control of dipolar mediated relaxation processes.

Complexes with Slow Spin-Lattice Relaxation.

One prominent class of molecular species with long spin-lattice relaxation times, single molecule magnets, features a single metal ion (transition-metal or lanthanide) with carefully crafted ligand shells to facilitate a long T_1. Many of these design strategies rely on controlling the activation energies of spin-lattice relaxation through the Orbach or thermally assisted QTM process and suppressing the non-thermally activated processes. With a suitably high activation energy and the absence of these other processes, one may expect sufficiently long relaxation to enable information storage in a molecular magnetic moment. In pursuit of this goal, in 2017, Layfield, Chilton, Mills, and coworkers reported new Ln-based metallocene complexes that show a slow relaxation process up to and above liquid nitrogen temperatures (Fig. 1.7).[20,64] Analyses of the temperature dependence of T_1 in these species revealed that one molecule, $[(\mathrm{Cp}^{i\mathrm{Pr}5})\mathrm{Dy}(\mathrm{Cp}^*)]^+$, exhibited an activation energy for relaxation of 1541(11) cm^{-1} for a thermally assisted QTM process, the highest reported value for any molecule. There are two key aspects of the molecule that enable this remarkable observation. First, the molecule possesses a Dy^{3+} ion, which leverages a large spin state and spin-orbit coupling to produce a large potential activation energy. The spin orbit coupling in particular leads to a $^6H_{15/2}$ term ground state and magnetic orientations that are described with M_J values up to $\pm{}^{15}/_2$ (stemming from $J = L + S$, where J is the total angular momentum, L the orbital angular momentum, and S the spin).[44] Second, the species also possesses a highly pseudo-axial molecular symmetry. These two properties suppress tunneling in the ground state and lower lying levels. The result is a thermally assisted tunneling mechanism that is nearly the maximum possible activation energy for the molecule.

Outlook

Magnetic molecules are an essential component of next-generation applications in quantum information processing to magnetic resonance imaging. But to reach that vision, we need a comprehensive understanding of how molecular structure and the environment control magnetic relaxation.

The subsequent chapters detail several experimental investigations studying relaxation in highly magnetic and dynamic environments. Indeed, many of the proposed applications for magnetic metal complexes require long relaxation times in proton-rich biological environments, room-temperature solutions, or the stray-magnetic-field-rich interiors of electronic devices. Yet, as touched on herein, current studies of magnetic molecules focus almost exclusively on electron- and nuclear-spin-free conditions to suppress magnetic noise and very low temperatures to freeze out structural dynamics. These studies revealed that extraordinarily long relaxation times are achievable. One pressing goal, then is the discovery of how to translate those proof-of-concept observations into spin abundant environments.

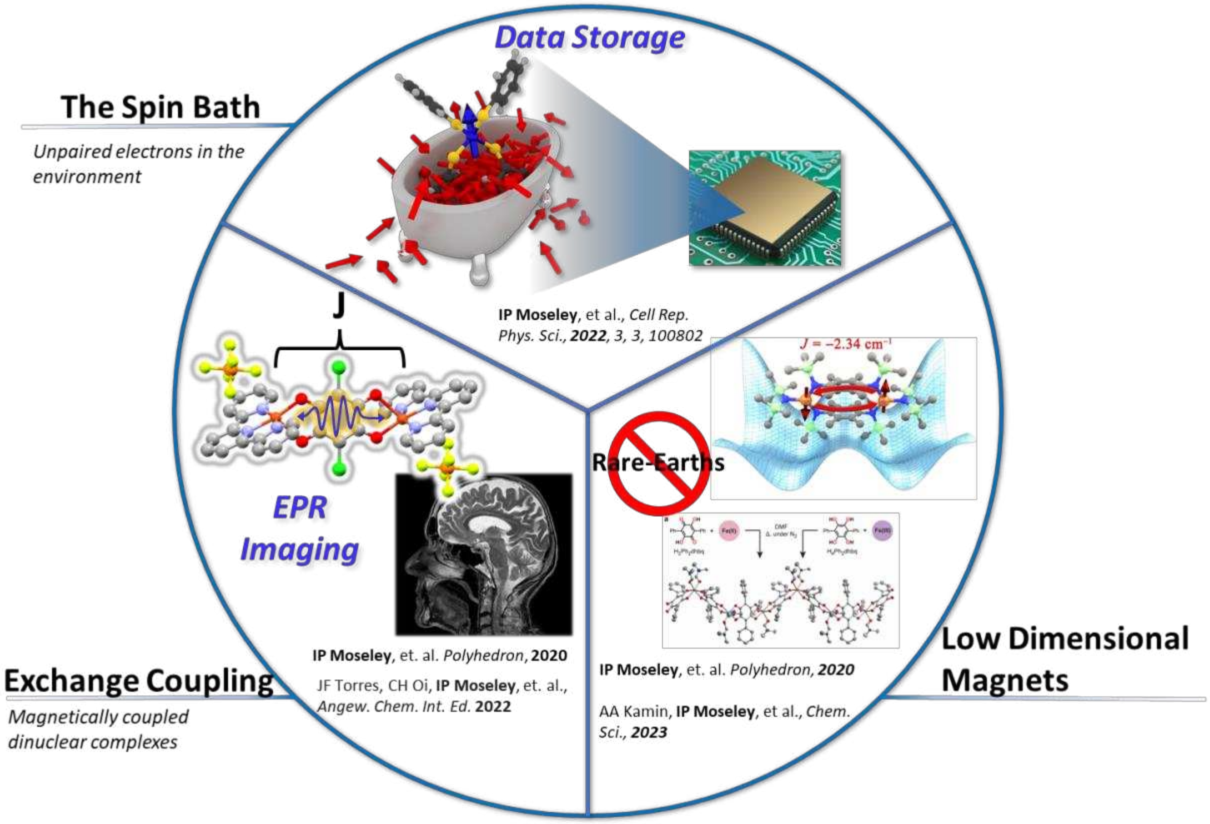

Fig. 1.8. *Graphical overview of the research presented in this dissertation.*

Dissertation Organization

The work presented in this dissertation investigates the magnetic behavior of several unique, transition metal based systems (Fig. 1.8). Although the magnetic properties of interest differ from system to system, in each case, the correlations between magnetism and chemical structure are investigated. Chapter two details a series of experiments investigating the relaxation dynamics of the canonical single molecule magnet $[Co(SPh)_4][PPh_4]_2$ in spin abundant environments. The third chapter focuses on an exchange-coupled, low coordinate iron(II) dinuclear complex featuring a pair of bulky, diamino bridging ligands. Chapter four examines the relaxation dynamics of three Fe(II/III) single chain magnets, highlighting the magneto-structural impacts of subtle changes in synthetic chemistry. Chapter five discusses preliminary investigations into a family of weakly exchange coupled, Cu(II) dinuclear complexes which display unusual EPR forbidden transitions. Finally, chapter six presents a summary of the work as well as future outlooks for the research discussed.

References

1 G. Aromí, D. Aguilà, P. Gamez, F. Luis and O. Roubeau, *Chem. Soc. Rev.*, 2012, **41**, 537–546.

2 M. J. Graham, J. M. Zadrozny, M. S. Fataftah and D. E. Freedman, *Chem. Mater.*, 2017, **29**, 1885–1897.

3 A. Gaita-Ariño, F. Luis, S. Hill and E. Coronado, *Nat. Chem.*, 2019, **11**, 301–309.

4 D. Gatteschi, R. Sessoli, J. Villain, *Molecular Nanomagnets*, Oxford University Press, Oxford, New York, 2006.

5 J. Wahsner, E. M. Gale, A. Rodríguez-Rodríguez and P. Caravan, *Chem. Rev.*, 2019, **119**, 957–1057.

6 G. Tircs and Z. Baranyai , *The Chemistry of Contrast Agents in Medical Magnetic Resonance Imaging Stability and Toxicity of Contrast Agents*, John Wiley & Sons, 2013.

7 M. C. Heffern, L. M. Matosziuk and T. J. Meade, *Chem. Rev.*, 2014, **114**, 4496–4539.

8 A. L. Buchachenko and V. L. Berdinsky, *Chem. Rev.* 2002, **102**, 603-612.

9 D. Aravena and E. Ruiz, *Dalton Trans.*, 2020, **49**, 9916–9928.

10 S. Brooker, *Chem. Soc. Rev.*, 2015, **44**, 2880–2892.

11 E. Coronado, *Nat. Rev. Mater.*, 2020, **5**, 87–104.

12 S. T. Liddle and J. van Slageren, *Chem. Soc. Rev.*, 2015, **44**, 6655–6669.

13 G. A. Craig and M. Murrie, *Chem. Soc. Rev.*, 2015, **44**, 2135–2147.

14 L. Bogani and W. Wernsdorfer, *Nat. Mater.*, 2008, **7**, 179–186.

15 L. J. Berliner, S. S. Eaton and G. R. Eaton, *Distance Measurements in Biological Systems by EPR*, Springer US, 2000.

16 L. J. Berliner, Ed., *In Vivo EPR (ESR): Theory and Application*, Springer US, 2003.

17 B. A. Reisner, S. R. Smith, J. L. Stewart, J. R. Raker, J. L. Crane, S. G. Sobel and L. L. Pesterfield, *Inorg. Chem.*, 2015, **54**, 8859–8868.

18 J. R. Raker, B. A. Reisner, S. R. Smith, J. L. Stewart, J. L. Crane, L. Pesterfield and S. G. Sobel, *J. Chem. Educ.*, 2015, **92**, 980–985.

19 L. J. Fox and G. H. Roehrig, *J. Chem. Educ.*, 2015, **92**, 1456–1465.

20 F.-S. Guo, B. M. Day, Y.-C. Chen, M.-L. Tong, A. Mansikkamäki and R. A. Layfield, *Science*, 2018, **362**, 1400–1403.

21 L. Tesi, A. Lunghi, M. Atzori, E. Lucaccini, L. Sorace, F. Totti and R. Sessoli, *Dalton Trans.*, 2016, **45**, 16635–16643.

22 J. M. Frost, K. L. M. Harriman and M. Murugesu, *Chem. Sci.*, 2016, **7**, 2470–2491.

23 D. Gatteschi and R. Sessoli, *Angew. Chem. Int. Ed.*, 2003, **42**, 268–297.

24 M. Vallone, *Phys. Status Solidi B*, 2020, **257**, 1900443.

25 M. S. Fataftah, M. D. Krzyaniak, B. Vlaisavljevich, M. R. Wasielewski, J. M. Zadrozny and D. E. Freedman, *Chem. Sci.*, 2019, **10**, 6707–6714.

26 A. Schweiger and G. Jeschke, *Principles of Pulse Electron Paramagnetic Resonance*, Oxford University Press, 2001.

27 A. Lunghi, F. Totti, R. Sessoli and S. Sanvito, *Nat. Commun.,* 2017, **8**, 14620.

28 Y. Zhou, B. E. Bowler, G. R. Eaton and S. S. Eaton, *J. Magn. Reson.*, 1999, **139**, 165–174.

29 D. W. Feldman, J. G. Castle and J. Murphy, *Phys. Rev.*, 1965, **138**, A1208–A1216.

30 P. G. Klemens, *Phys. Rev.*, 1962, **125**, 1795–1798.

31 C. B. Harris, R. M. Shelby and P. A. Cornelius, *Phys. Rev. Lett.*, 1977, **38**, 1415–1419.

32 N. V. Vugman and M. R. Amaral, *Phys. Rev. B*, 1990, **42**, 9837–9842.

33 D. Goldfarb and S. Stoll, *EPR Spectroscopy: Fundamentals and Methods*, John Wiley & Sons, 2018.

34 J. Murphy, *Phys. Rev.*, 1966, **145**, 241–247.

35 A. Abragam, B. Bleaney, *Electron Paramagnetic Resonance of Transition Ions*, Oxford University Press, Oxford, New York, 2012.

36 K. J. Standley, *Electron Spin Relaxation Phenomena in Solids*, Springer US, 1969.

37 A. J. Fielding, S. Fox, G. L. Millhauser, M. Chattopadhyay, P. M. H. Kroneck, G. Fritz, G. R. Eaton and S. S. Eaton, *J. Magn. Reson.*, 2006, **179**, 92–104.

38 S. Gómez-Coca, A. Urtizberea, E. Cremades, P. J. Alonso, A. Camón, E. Ruiz and F. Luis, *Nat. Commun.*, 2014, **5**, 4300.

39 W. M. Rogers and R. L. Powell, *Tables of Transport Integrals*, U.S. Government Printing Office, 1958.

40 L. Gu and R. Wu, *Phys. Rev. B*, 2021, **103**, 014401.

41 J. M. Zadrozny and J. R. Long, *J. Am. Chem. Soc.*, 2011, **133**, 20732–20734.

42 W. H. Harman, T. D. Harris, D. E. Freedman, H. Fong, A. Chang, J. D. Rinehart, A. Ozarowski, M. T. Sougrati, F. Grandjean, G. J. Long, J. R. Long and C. J. Chang, *J. Am. Chem. Soc.*, 2010, **132**, 18115–18126.

43 V. A. Atsarkin, V. V. Demidov and G. A. Vasneva, *Phys. Rev. B*, 1997, **56**, 9448–9453.

44 J.-L. Liu, Y.-C. Chen and M.-L. Tong, *Chem. Soc. Rev.*, 2018, **47**, 2431–2453.

45 B. N. Figgis and M. A. Hitchman, *Ligand field theory and its applications*, Wiley-VCH, 2000.

46 E. Moreno-Pineda, M. Damjanović, O. Fuhr, W. Wernsdorfer and M. Ruben, *Angew. Chem. Int. Ed.*, 2017, **56**, 9915–9919.

47 M. Atzori, E. Morra, L. Tesi, A. Albino, M. Chiesa, L. Sorace and R. Sessoli, *J. Am. Chem. Soc.*, 2016, **138**, 11234–11244.

48 C.-J. Yu, M. J. Graham, J. M. Zadrozny, J. Niklas, M. D. Krzyaniak, M. R. Wasielewski, O. G. Poluektov, D. E. Freedman, *J. Am. Chem. Soc.*, 2016, **138**, 14678-14685.

49 S. R. Cooper , Y. B. Koh and K. N. Raymond , *J. Am. Chem. Soc.*, 1982, **104** , 5092 —5102

50 M. Atzori and R. Sessoli, *J. Am. Chem. Soc.*, 2019, **141**, 11339–11352.

51 M. A. Schlosshauer, *Decoherence: and the Quantum-To-Classical Transition*, Springer-Verlag, Berlin Heidelberg, 2007.

52 K. Bader, D. Dengler, S. Lenz, B. Endeward, S.-D. Jiang, P. Neugebauer and J. van Slageren, *Nat. Commun.*, 2014, **5**, 5304.

53 C. E. Jackson, C.-Y. Lin, S. H. Johnson, J. van Tol and J. Zadrozny, *Chem. Sci.*, 2019, **10**, 8447-8454.

54 M. Atzori, L. Tesi, E. Morra, M. Chiesa, L. Sorace and R. Sessoli, *J. Am. Chem. Soc.*, 2016, **138**, 2154–2157.

55 J. M. Zadrozny, J. Niklas, O. G. Poluektov and D. E. Freedman, *ACS Cent. Sci.*, 2015, **1**, 488–492.

56 K. Bader, M. Winkler and J. van Slageren, *Chem. Commun.*, 2016, **52**, 3623–3626.

57 E. R. Canarie, S. M. Jahn and S. Stoll, *J. Phys. Chem. Lett.*, 2020, **11**, 3396–3400.

58 W. E. Blumberg, *Phys. Rev.*, 1960, **119**, 79–84.

59 J. Chen, C. Hu, J. F. Stanton, S. Hill, H.-P. Cheng and X.-G. Zhang, *J. Phys. Chem. Lett.*, 2020, **11**, 2074–2078.

60 J. P. Wolfe, *Phys. Rev. Lett.*, 1973, **31**, 907–910.

61 R. Hussain, G. Allodi, A. Chiesa, E. Garlatti, D. Mitcov, A. Konstantatos, K. S. Pedersen, R. De Renzi, S. Piligkos and S. Carretta, *J. Am. Chem. Soc.*, 2018, **140**, 9814–9818.

62 J. P. Klare, *Biomed. Spectrosc. Imaging*, 2012, **1**, 101–124.

63 R. Rahimi, H. J. Halpern and T. Takui, in *Oxygen Transport to Tissue XXXIX*, eds. H. J. Halpern, J. C. LaManna, D. K. Harrison and B. Epel, Springer International Publishing, Cham, 2017, pp. 335–339.

CHAPTER 2 – Slowing Magnetic Relaxation with Open Shell Diluents

Introduction

Single-molecule magnets are potential next-generation components in information storage/processing,[1–3] spintronics,[4] and magnetic resonance imaging.[5] These complexes display an activation energy barrier (*U*) to reorientation of the magnetic moment that can induce extremely long magnetic relaxation times (> s) at low temperature. [6–12] Environmental spins (which constitute the "spin bath") frequently induce rapid relaxation through dipolar interactions, and nearly all envisioned applications of single-ion magnets (the mononuclear family of single-molecule magnets) involve the existence of a spin bath in some form (e.g. high-density arrays of open-shell molecules on surfaces or ^{1}H nuclear-spin-rich aqueous environments).[13] Hence, developing new ways to study understand, and chemically control the impact of the spin bath is vital to eventual application.

At low temperatures, the spin bath of a metal ion hastens relaxation by enhancing quantum tunneling of the magnetization.[14] In this process, a single-ion magnet's spin will flip and undercut the barrier.[15] Tunneling in these systems is typically driven by dipolar interactions with adjacent molecules and can be disrupted by diamagnetic dilution.[1,16] Diamagnetic dilution is achieved by taking a magnetic molecule and either (1) dissolving it into an organic solvent or matrix (as was done for $Mn_{12}O_{12}$),[17,18] or (2) cocrystallization with a structurally analogous, closed-shell species. For example, mononuclear M^{2+} complexes can be diluted with Zn^{2+}[19] or low-spin Ni^{2+} analogues,[20] M^{3+} species can be diluted with low-spin Co^{3+},[21] Y^{3+},[22,23] or Ga^{3+},[24] and M^{4+} species can be diluted with Ti^{4+}.[25] In these dilute systems, wherein the potential size advantage of molecular information storage is lost, magnetic relaxation is often slowed by several orders of magnitude. It is vital to deviate away from these magnetically quiet confines to discover how to slow relaxation rates when the environment is noisy. Thus, it is essential to develop new, chemical means of modifying the local magnetic environment to study mechanisms of magnetic relaxation.

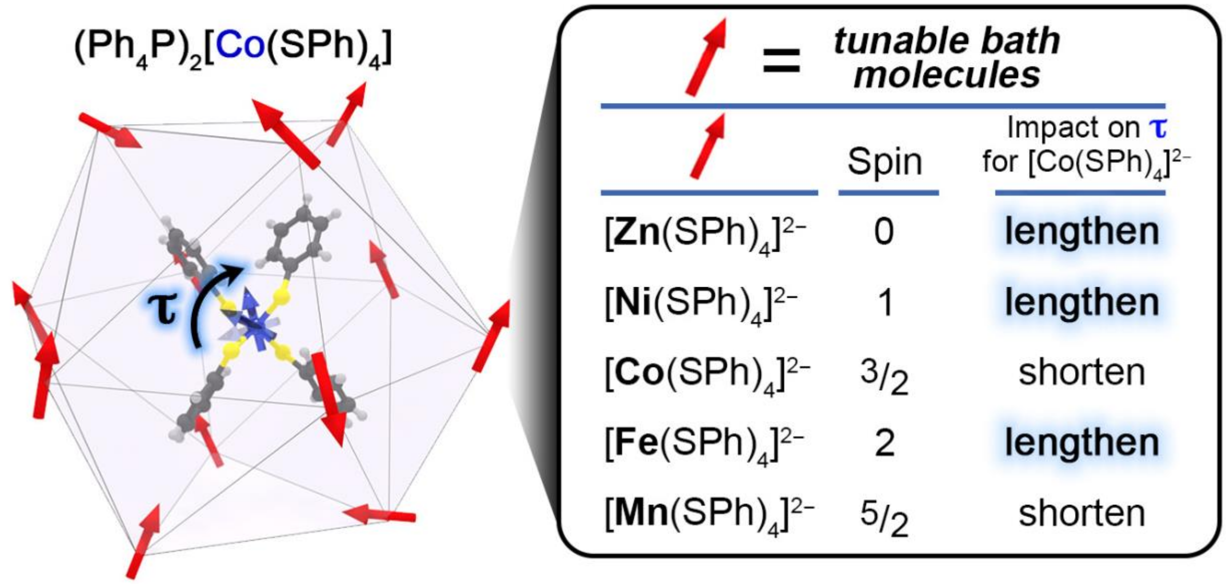

Fig. 2.1. (left) The local environment of $[Co(SPh)_4]^{2-}$ in crystals of pure $(Ph_4P)_2[Co(SPh)_4]$ (**Co**) is rich in high-spin Co(II) ions. (right) We show via chemical control of the spin bath that certain paramagnetic diluents can lengthen magnetic relaxation times (τ) analogous to diamagnetic diluents, like Zn^{2+}.

Herein, we illustrate a way of chemically manipulating relaxation via cocrystallization within a synthetically tunable *paramagnetic* matrix. Importantly, we use this method to show that select $S = 1$ and $S = 2$ ions can produce a spin bath that suppresses tunneling similar to a bath of closed-shell Zn^{2+}, yet still possessing unpaired electrons. This work focuses on the single-ion magnet $[Co(SPh)_4]^{2-}$ (Fig. 2.1), which demonstrates facile quantum tunneling at low temperature in the pure phase.[19] We measured the magnetization dynamics of dilutions of $(Ph_4P)_2[Co(SPh)_4]$ (**Co**, $S = {}^3/_2$) in the paramagnetic diluents $(Ph_4P)_2[Ni(SPh)_4]$ (**Ni**, $S = 1$), $(Ph_4P)_2[Fe(SPh)_4]$ (**Fe**, S

= 2), $(Ph_4P)_2[Mn(SPh)_4]$ (**Mn**, $S = {}^5/_2$), and the diamagnetic diluent $(Ph_4P)_2[Zn(SPh)_4]$ (**Zn**, S = 0). These data reveal an exciting disruption of tunneling for baths of S = 1 **Ni** and S = 2 **Fe**, like the effects observed for the traditional diamagnetic diluent S = 0 **Zn**. Through EPR, susceptibility, and theoretical modeling data, we correlate the viability of the S = 1 **Ni** and S = 2 **Fe** diluents with the positive zero field splitting (D) of these species. This feature, we propose, makes them effective-spin zero ($S_{\mathrm{eff}} = 0$) at low temperature despite possessing multiple unpaired electrons (unlike Zn^{2+}) and effectively quiets the local dipolar fields that hasten relaxation.[26,27] Whereas most dilutions of single-molecule magnets exploit strictly diamagnetic environments, this study is, to the best of our knowledge, the first to explicitly target magnetically concentrated diluting conditions.

Results and Discussion

The $(Ph_4P)_2[M(SPh)_4]$ species (M = Mn, Fe, Co, Ni, and Zn), denoted **Mn**, **Fe**, **Co**, **Ni**, and **Zn**, respective, are isostructural mononuclear complexes.[28,29] A tetragonal elongation in the tetrahedral MS_4 unit of these complexes makes the local symmetry D_{2d} and engenders an extreme magnetic anisotropy and slow magnetic relaxation for **Co**.[30] A slight change is observed in the average M–S distances as a function of M (2.328(4) for **Co**,[29] 2.288(4) for **Ni**,[28] 2.356(6) for **Fe**,[29] 2.442(3) for **Mn**, and 2.352(3) Å for **Zn**,[31] but all crystallize in the $Pbc2_1$ space group. Furthermore, the same tetragonal distortion toward D_{2d} symmetry is seen in all $[M(SPh)_4]^{2-}$ units, with two S–M–S angles exhibiting a "pinch" as a function of the elongation. These angles are 96.7(2)° (**Zn**), 92.0(2)° (**Ni**), 95.6(2)° (**Co**), 97.58(10)° (**Fe**) and 98.4(1)° (**Mn**). We note that these specific bond angles are bisected by the magnetic easy-axis of the $[Co(SPh)_4]^{2-}$ unit in **Co**.

Finally, each metal ion has 12 nearest neighbors, with closest M•••M distances of around 10.456(7) Å (Fig. 2.1).[25,28]

Multiple sets of solid solutions of **Co** in **Ni**, **Fe**, **Mn**, and **Zn** were made to test the impact of paramagnetic spin baths on magnetic relaxation of **Co**. First, we prepared variable-concentrations of **Co** in **Ni** (73%, 58%, 25%, 9%, and 3% **Co** relative to **Ni**). Second, we prepared dilutions of **Co** in **Fe** (83%, 57%, 24%, 16%, and 6% **Co** to **Fe**). Third, dilutions of **Co** in **Mn** (81% and 43% **Co** to **Mn**) and finally, dilutions of **Co** in **Zn** (30% and 3% **Co** to **Zn**). PXRD demonstrates that these dilutions assume the same crystalline phases of their pure components, and preliminary energy dispersive X-ray spectroscopy (EDS) data suggests homogeneous distribution over µm-length scales (see Appendix A and Figs. A1, A2).[33]

DC Susceptibility

Magnetic analyses via direct-current (dc) magnetic susceptibility ($\chi_M T$) measurements indicate that Co, Ni, Fe, and Mn are isolated spin systems with varying magnetic anisotropies. Room-temperature (300 K) $\chi_M T$ values of 2.45, 1.34, 2.90, and 4.56 cm^{3}K/mol for Co, Ni, Fe, and Mn (Fig. A3), indicate $S = {}^3/_2$, 1, 2, and ${}^5/_2$ metal ions, respectively, matching previous results.[33] With decreasing temperature, $\chi_M T$ decreases, most dramatically for Ni, somewhat less for Co and Fe, and almost negligibly for Mn, decreases likely attributable to zero-field splitting. The $\chi_M T$ data were fit with a spin Hamiltonian accounting for zero-field splitting (using the program PHI[34] – see SI for fitting details). The final extracted D values are $D \approx -61$ cm^{-1} for Co, $D = +68$ cm^{-1} for Ni, $D = +5.85$ cm^{-1} for Fe, and $D = -0.12$ cm^{-1} for Mn, all values are in keeping with previous reports for other similar, 4-coordinate MS_4 complexes.[35–38]

High-Field, High-Frequency Electron Paramagnetic Resonance Imaging (HF-HF EPR)

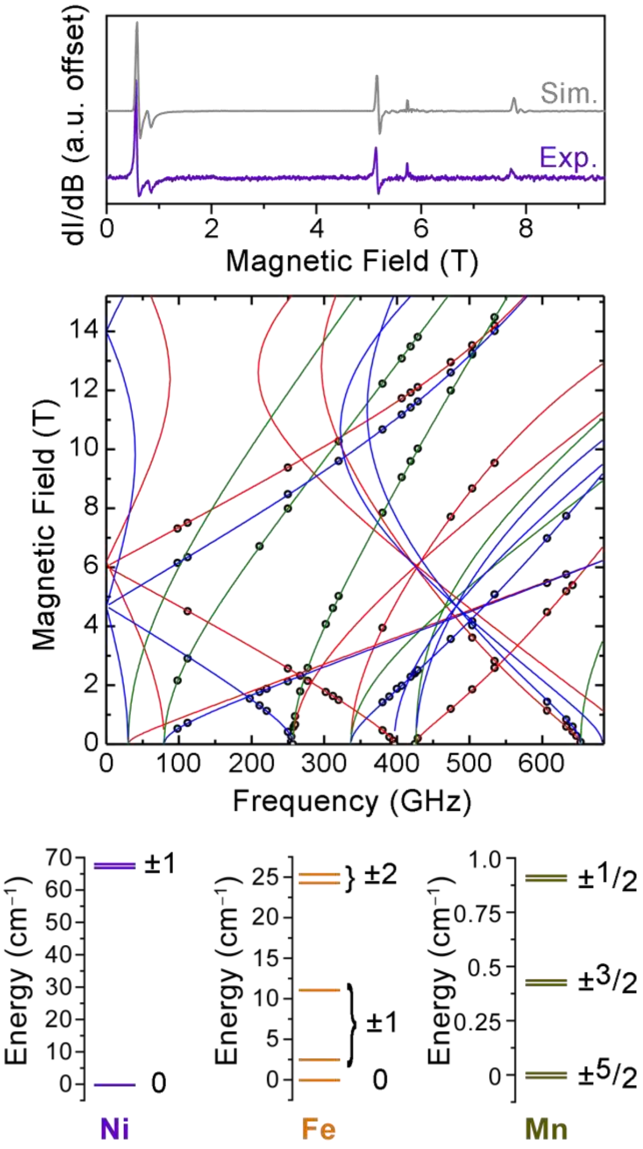

Fig. 2.2. **Top:** 633 GHz EPR spectra for a powder of **Fe** collected at 20 K. See SI for experimental and simulation details. **Middle:** Field versus frequency dependence of the EPR transitions for **Fe**. Each circle represents a transition observed at that field and frequency. Green, blue, and red lines were calculated with the **Fe** x, y, and z axes, respectively, aligned with the magnetic field. **Bottom:** Zero-field energies of the M_S levels for **Ni**, **Fe,** and **Mn** on the basis of spin Hamiltonian parameters derived from EPR and dc susceptibility analyses. Note that M_S labels for **Fe** correspond to high-field values (near zero-field the M_S = ±1 levels are highly mixed by E, and for **Mn**, the energies of the Kramers doublets (e.g. the $\pm{}^5/_2$ M_S levels) are actually degenerate but depicted as separate for clarity.

Electron paramagnetic resonance (EPR) measurements were pursued to better quantitate the zero-field splitting for **Mn**, **Fe**, and **Ni** (Figs. 2.2, A4-A7), as dc susceptibility can sometimes incorrectly assign the signs/magnitudes of these parameters.[39] High-field and high-frequency EPR (HF-EPR) analyses of **Co** were previously reported and generally agree with the large, negative D obtained from dc susceptibility fits.[29] For **Mn**, **Ni,** and **Fe**, which also appeared by $\chi_M T$ to have large D values, we used high-field (up to 17 T) and high-frequency analyses (up to 650 GHz). For **Fe**, a highly frequency- and temperature-dependent EPR spectrum was observed, with multiple sharp peaks detected at all frequencies (see Figs. 2.2, A4-A6). In contrast, no EPR signal was observed for **Ni** from 0 to 17 T and frequencies up to 650 GHz.

The EPR spectra generally agree with the susceptibility analyses and were simulated with Easyspin[40] and the program *SPIN* (see Appendix A for full details). First, for $S = 1$ **Ni** with a D of ca. $+67\ \mathrm{cm}^{-1}$, we observed, as expected, no EPR signal under the experimental fields and frequencies. Second, for **Fe** ($S = 2$), relatively sharp, well resolved peaks were observed, and the frequency/field dependence of these peaks can be convincingly modeled with $D = +5.848(1)\ \mathrm{cm}^{-1}$, and $E = +1.428(1)\ \mathrm{cm}^{-1}$, in general agreement with other lower-frequency EPR analyses (Fig 2.2).[41–43] Finally, for **Mn**, simulations of the 381 GHz spectra produce average D and E values of $-0.12\ \mathrm{cm}^{-1}$, and $-0.04\ \mathrm{cm}^{-1}$, respectively, close to the small values from $\chi_M T$ simulations (Fig. S7) and the general expectations for an Mn^{2+} ion.[44–46]

Modeling the HF-EPR spectra of **Fe** and **Mn** was attempted for both positive and negative values of the anisotropy parameters (D and E). The models for **Fe** obtained when $D > 0$ resulted in significant improvements over the model with $D < 0$ (Fig. A6). In the case of **Mn**, which possesses a much smaller ZFS, the simulations of the HF-EPR spectra were of generally equal quality with negative or positive D, which is expected as E approaches the $E \leq \left|\frac{1}{3}D\right|$ limit.

Together, the susceptibility and EPR data highlight an important varying aspect of the different bath spins, beyond just *S*: the ground-state M_S values (Fig. 2.2). The large positive *D* for Ni suggests that the $M_S = 0$ level of Ni bath spins is the lowest energy and separated from the $M_S = \pm1$ levels by a ~67 cm^{-1} gap. The data for Fe likewise indicate that the Fe^{2+} ions possess a ground $M_S = 0$ level. But, the $M_S = 0$ level is only separated by ~3 cm^{-1} from the $M_S = \pm1$ levels and ~24 cm^{-1} from the $M_S = \pm2$ levels for Fe relative to the 67 cm^{-1} gap for Ni. Note that the $M_S = \pm1$ levels are split for Fe by a transverse anisotropy $|E| = 1.43$ cm^{-1}, and this anisotropy also mixes these levels. For Mn, the separation in all M_S levels is even smaller, with the ground-state $M_S = \pm{}^5/_2$ levels only 0.439 cm^{-1} below the $M_S = \pm{}^3/_2$ levels and 0.876 cm^{-1} below the $M_S = \pm{}^1/_2$ levels (Fig. 2.2). As is shown below, these specific arrangements of M_S levels are likely critical to the roles of Mn, Ni, and Fe as diluents for Co.

AC Susceptibility

Out-of-phase, alternating-current (ac) magnetic susceptibility (χ_M'') measurements of pure **Co**, **Ni**, **Fe** and **Mn** reveal slow magnetic relaxation at zero applied dc field for only **Co** at ac frequencies from 0.1 to 1500 Hz. For **Co**, we observe a nonzero, frequency-dependent χ_M'' with a peak at 27.7 Hz at 2.0 K (Fig. A8). From 2 to 2.6 K, the frequency of this peak is temperature-independent, indicative of quantum tunneling. In contrast, above 3.0 K the peak position is highly temperature dependent. This behavior is typical of magnetic relaxation that transitions to thermally activated processes.[18,47] In contrast **Ni**, **Fe**, and **Mn** display a featureless χ_M'' at zero applied dc field (Fig. A9). The only indication of slow magnetic relaxation in these latter compounds is in

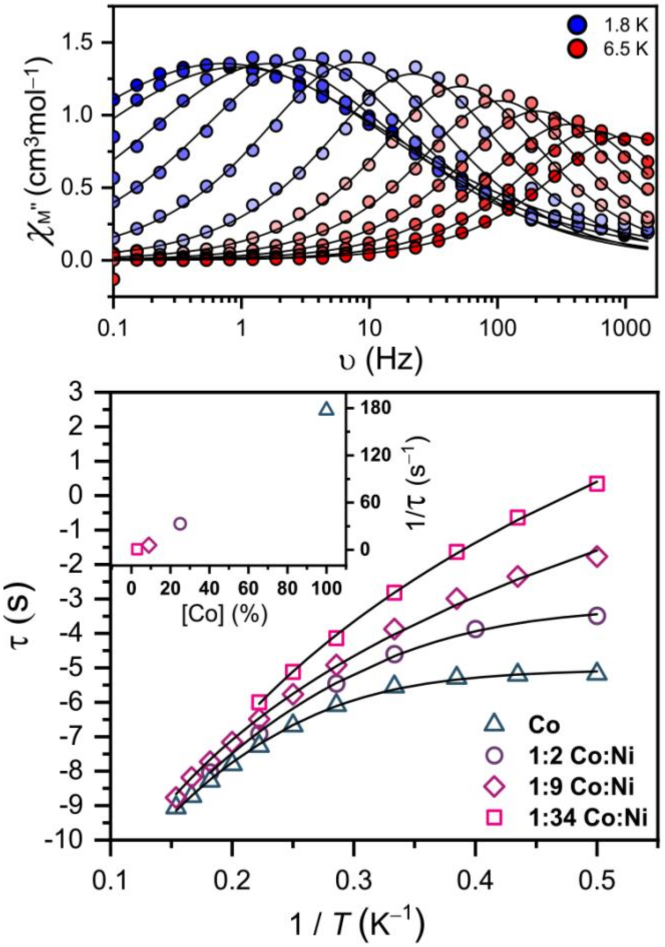

Fig. 2.3. **Top:** Out-of-phase ac susceptibility data (χ_M'') for a 1:10 dilution of **Co** in **Ni** as a function of temperature in zero applied magnetic field. Data were collected at temperature intervals of 0.3 K from 1.8 K to 2.7 K and intervals of 0.5 K from 3.0 to 6.5 K. Lines were generated via fits to the Cole-Cole equation (see SI). **Bottom:** Temperature dependence of the zero-field relaxation times (t) for **Co** dilutions in **Ni**. Solid black lines are fits of the temperature dependence following the Raman and tunneling model proposed in the main text. Inset: 1/t as a function of dilution level.

Mn, which shows a high- frequency rise in χ_M'' (200-1000 Hz) under 500-1500 G applied fields, but a peak maximum is never fully resolved (Fig. A10). These data establish the zero-field ac susceptibility measurement as an effective probe of the dynamics of **Co** alone in the three probed spin baths (composed of **Ni**, **Fe**, and **Mn**), owing to the absence of a zero-field χ_M'' signal in these diluents.

Zero-field ac magnetic susceptibility studies of **Co** diluted to different extents in **Ni** (Figs. 2.3, and A11-A13) reveal a slowing of magnetic relaxation at 2 K upon dilution in the $S = 1$ bath. For pure **Co**, there is a region of temperature independence in χ_M'' below 2.5 K when no external field is applied, an indication of magnetic dipole-mediated tunneling relaxation processes. In contrast, for the dilutions, magnetic relaxation is increasingly temperature dependent below 2.5 K with increasing dilution level, indicating that the tunneling process is disfavored in the diluted samples. Furthermore, the χ_M'' peaks for **Co** broaden at low temperature when diluted, an additional indicator that the dilution process is effectively modulating the tunneling-based magnetic relaxation in the < 3 K temperature regime.

Quantitation of the relaxation times (t) from a Cole-Cole analysis[48] of the ac data enabled the construction of Arrhenius plots (Fig. 2.3) for the relaxation dynamics of **Co** in **Ni**. For pure **Co**, τ is temperature-independent from 2.0 to 2.6 K at a value of 27.6 Hz (Fig. A8). The values of τ become longer over this temperature window and generally more temperature-dependent with increasing dilution level in **Ni**. The parameter a, which is also obtained from the Cole-Cole fitting (and characterizes the broadness of the χ_M'' peak), increases from 0.276 at 2.0 K for pure **Co** to 0.579 at 2.0 K for the 1:34 **Co:Ni** dilution. A larger value of α in the Cole-Cole analysis suggests a larger distribution of relaxation times for the **Co** unit upon dilution in **Ni**, which is likely because of some inhomogeneity in the disruption of the tunneling process.

The variable-temperature t data for pure **Co** can be easily modeled with two common magnetic relaxation processes, Raman and quantum tunneling,[15,49] via the following equation: $1/\tau = AT^n + 1/\tau_{QTM}$ (see Fig. A14 and Appendix A for full details). Here, $1/\tau$ is the relaxation rate, A is the Raman coefficient related to physical properties of the crystal, n is the Raman exponent, T is temperature, and t_{QTM} is the timescale of the quantum tunneling of the magnetization. As a function of dilution, the best fits change, most notably for the tunneling process, which slows considerably, with τ_{QTM} = 6.6(4) ms for pure **Co** lengthening to t_{QTM} = 41(3) ms for 1:2 **Co**:**Ni** (Figs. 2.3, A15). These data indicate a slowing of magnetic relaxation via reduction of tunneling with increasing **Ni** concentration, just like dilution with **Zn**.[18] At higher dilutions, tunneling is no longer required to simulate the data, which can be modeled solely with a Raman process. The parameters for the Raman process change upon dilution, with A ranging from 0.03(1) to 0.8(2) $K^{-n}s^{-1}$ and n = 5.6(1) to 7.96(9) for **Co**:**Ni** dilutions. The Raman process is predicted to be dependent on dipolar interaction.[49] These data may provide the first quantitative evidence of the spin-bath impact on Raman relaxation; however, caution should be exercised in analyzing this change too deeply as the present analysis only spans a 5 K window of relaxation dynamics.

Additional variable-concentration ac susceptibility analyses of the dilutions of **Co** in $S = 2$ **Fe**, $S = {}^5\!/_2$ **Mn**, and $S = 0$ **Zn** were performed to test the effect of the different paramagnetic baths (Figs. 2.4, A11-A19). Zero-field, 2 K analyses of dilutions with **Fe** demonstrate a similar effect as **Ni** and **Zn**, in that increasing concentration of the diluent slows the relaxation rate of **Co** and the χ_M'' peaks broaden considerably. Importantly, however, **Fe** appears slightly less effective as a diluent than **Ni**, as the relaxation rates for **Co** appear faster in the **Fe** diluent at all studied concentrations. Just like with **Fe** and **Ni**, the peak in χ_M'' for **Co** when diluted in **Mn** becomes broadened in frequency space, indicating a distribution in relaxation times. However, in contrast to **Fe** and **Ni**, the χ_M'' peak maximum for **Co** in **Mn** rapidly moves to higher frequencies with increasing Mn concentration, indicating relaxation times that rapidly hasten beyond the detectable range of our magnetometer.

The presented relaxation time data suggest that the functional feature of the Fe and Ni spin baths is related to the magnetic anisotropy of the spin-bath ions. For an integer spin ion with a positive D (e.g. Ni and Fe), the ground M_S levels are $M_S = 0$ and bear no spin angular momentum. Note that this scenario is distinct from being completely diamagnetic, as both Fe and Ni still possess unpaired electrons (i.e., they are not undergoing a low-temperature spin crossover),[50] and there is no zero-field splitting for an $S = 0$ spin state. At 2 K, the 67 cm^{-1} energy gap between the $M_S = 0$ and ±1 levels in Ni is significant, and the $M_S = 0$ level is populated by nearly 100 % of the spins in the Ni bath (following a simple Boltzmann distribution). Hence, to the magnetization dynamics of **Co** ions embedded in the Ni bath, this "effective $S = 0$" state for Ni appears to wield the same impact as the $S = 0$ **Zn** bath, despite **Ni** still bearing two unpaired electrons. **Fe** is also an integer spin with positive D, and hence it shows a similar effect on the quantum tunneling process for **Co**, owing to a high population of the $M_S = 0$ level (73 %). However, the data in Fig. 2.4 demonstrate that Fe does not disrupt the tunneling process as effectively as Ni, as the relaxation rates for **Co** diluted in Fe are faster than when diluted in Ni at all measured concentrations. To explain this discrepancy, we note that the D of Fe is smaller than that of Ni by a factor of 11.7. This relatively smaller D (and the appreciable E) for **Fe** means that one of the $M_S = \pm 1$ levels is populated by 26 % at 2 K. Hence, **Fe** is less effective as a diluent because there is sufficient population of the magnetic $M_S \neq 0$ levels at 2 K, and the spin bath can hence induce quantum tunneling for **Co**. This explanation mirrors previous work by Cornia and coworkers on chain compounds, which showed that integer-spin ions with strong easy-plane anisotropy incorporated into chains of open-shell species will block intrachain exchange interactions.[51]

In contrast to **Fe** and **Ni**, dilutions of with **Mn** hastened the relaxation time for embedded **Co**. For half-integer, high-spin ions (e.g. **Mn**), no matter the sign of D, the ground M_S levels are either $M_S = \pm {}^1/_2$ or $M_S = \pm S$ for the ion – both configurations are magnetic, and the small D suggests that even in the low-T regime, all M_S levels will be populated. As a result, **Mn** provides a strongly magnetic local environment to drive tunneling beyond what is possible for pure **Co**.

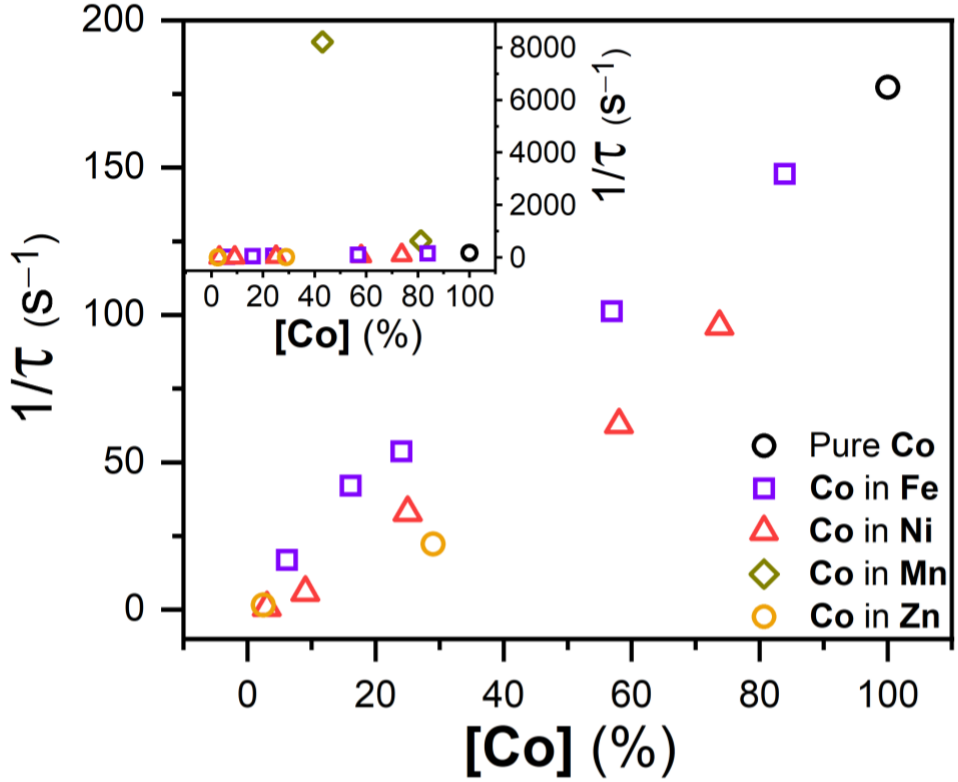

Fig. 2.4. Variable-concentration relaxation rates (1/τ) for **Co** diluted in **Ni**, **Fe**, **Mn,** and **Zn**. All relaxation rates were extracted from variable frequency ac susceptibility measurements at 2 K and zero applied magnetic field. *Inset*: Scale altered to show **Mn** dilution data.

Dipolar Field Calculations

Intermolecular dipole-dipole forces strongly influence the rate of QTM for mononuclear SMMs, and it is known that both axial ($H^{dip}{}_{\parallel}$) and transverse ($H^{dip}{}_{\perp}$) dipolar fields increase the rate of tunnelling.[52,53] We hypothesized that the positive D of Ni and Fe would subdue the magnitudes of dipolar fields, which would suppress tunneling to enable slow relaxation rates. To test this hypothesis and characterize the local dipolar field created by the paramagnetic diluents, we estimated the local magnetic dipolar field of a **Co** embedded in matrices of **Mn, Co, Ni,** and **Zn**, using g, D, and S values from EPR and $\chi_M T$ analyses for the diluting molecules (Fig. 2.5). **Fe** baths were not directly computed, as the **Ni** bath is computationally equivalent. We assumed that the dipolar field $\boldsymbol{h}$ can be approximated by a zero-mean Gauss-Markov stochastic process fully characterized by its autocorrelation function with variance $c_h^n \equiv \langle h_n h_n \rangle$, with $n = x, y, z$, and decay rate Γ_h, in the spirit of the Kubo-Toyabe theory of zero-field spin relaxation. [54] c_h^n serves as a measure of the fluctuating $\boldsymbol{h}$ and is related to the Co spin relaxation time t as detailed in the SI. c_h^n can then be calculated from the static spin-spin correlation function of the bath spins, which are assumed to be independent as a first approximation. We selected x, y, and z to be coincident with the zero-field splitting axes of the embedded **Co** species, taken from the crystal structure. Detailed computational methods and results can be found in Appendix A (Figs. A22, A23).

The dipolar fields imparted on an embedded **Co** are generally anisotropic, evidenced by the different magnitudes of c_h^x, c_h^y, and c_h^z. For example, at 2.2 K, pure **Ni** produces c_h^x, c_h^y, and c_h^z magnitudes of 0.61, 0.11, and 0.18 mT^2 respectively. This anisotropy stems from the relative orientations of the surrounding spins since the molecular axes of each of the four $[\mathrm{M(SPh)_4}]^{2-}$ species in the unit cell are not aligned with one another. We also determined that the field strength is not dependent on which molecular site we choose as the origin, provided that the x, y, and z axes are defined according to the molecular axes of that site.

More importantly, the calculated c_h^n have very different magnitudes for different bath spins, especially at low temperatures. In contrast to the values for pure **Ni** mentioned above, we found that at 2.2 K the c_h^x, c_h^y, and c_h^z in pure **Co** ($S = 3/2$) are much larger, 59.8, 10.6, and 17.7 mT^2, respectively, and those in **Mn** ($S = 5/2$) are even larger: 107, 79, and 114 mT^2, respectively (Figs. 2.5c; A22). The fluctuating dipolar fields for the half-integer-spin baths are therefore one order of magnitude larger than that for the integer-spin bath (**Ni**) at low temperatures, in agreement with our qualitative picture above. That the c_h^n for **Mn** is larger than that for **Co** is mainly due to the larger spin of the former. A more complete description of the observed trends can be found in Appendix A.

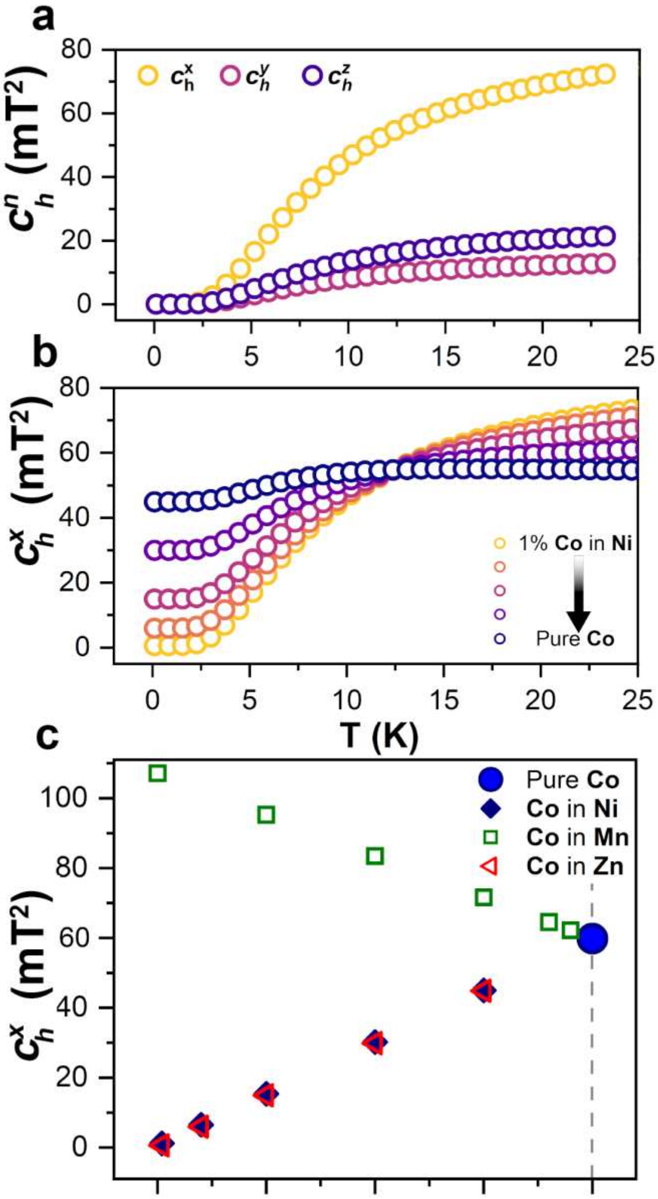

Fig. 2.5. a. Computed variable-temperature local dipolar field variance for the *x*, *y*, and *z* components ($c_h^{x,y,z}$) of pure **Ni**. ***b.*** Computed variable-temperature c_h^x for a [Co(SPh)$_4$]$^{2-}$ embedded in **Ni**. ***c.*** Computed variable-concentration c_h^x for [Co(SPh)$_4$]$^{2-}$ diluted in **Mn**, **Ni**, and **Zn** at 2.6 K.

Since the very small c_h^n for pure **Ni** is a result of the dominant occupancy of the $M_S = 0$ singlet at low temperatures, we expect that c_h^n will undergo a nontrivial transition upon increasing temperature. Indeed, Fig. 5a shows that c_h^n changes significantly around $T = 10$ K, comparable to the zero-field splitting of **Ni**. Specifically, c_h^x dramatically drops from 84 mT^2 at 50 K to 0.61 mT^2 at 2.5 K, a 99% decrease, with c_h^y and c_h^z behaving similarly. In contrast, the c_h^n for **Co** and **Mn** have much milder temperature dependence in the same temperature range (Fig. A22). For **Co**, two of the components, c_h^y and c_h^z, also drop with decreasing temperature from 50 to 2.2 K, but not dramatically and level off at 10.6 and 17.7 mT^2 at 2.2 K, respectively. In contrast, c_h^x increases for **Co** with decreasing temperature, eventually reaching 59.8 mT^2 at 2.2 K. That c_h^x, c_h^y, and c_h^z have different trends vs. temperature is partly because they must approach the same value at temperatures higher than the zero-field splitting. **Mn** is similar to **Co**, except there is only a pronounced temperature dependence below *ca.* 0.5 K.

With increasing dilution, both the local field magnitude and its temperature dependence gradually change from that of pure **Co** to that of the diluent, as shown in Fig. 5b for the case of **Co** in **Ni**. At a fixed temperature, we found that c_h^n depends linearly on the dilution for all baths (Fig 2.5c; A23), a consequence of our independent bath spin assumption. The nice agreement between the linear dependences of c_h^n and the experimental 1/t data on dilution confirms the applicability of this assumption.

The observed orientation, temperature, and diluent dependence of the local dipolar fields are all in agreement with our interpretation of the effect of the different $[M(SPh)_4]^{2-}$ environments. Thus, we see the operative mechanism of the **Ni** and **Fe** diluents. The $M_S = 0$ level is almost entirely populated at low temperature, causing all dipolar fields to fall to 0. This reduction of the dipolar field then suppresses the tunnelling relaxation, as observed for diamagnetic **Zn** dilution. Furthermore, we see why **Co** and **Mn** both enable tunnelling of embedded **Co** species: the half-integer spins of these bath complexes (in contrast to the integer-spin, positive-*D* Ni) ensure that a substantial, nonzero dipolar field (**Mn** larger than **Co**) exists at low temperature. Consequently, we see tunnelling proceed in pure **Co** and the relaxation rate increase in **Mn**.

Conclusion

The foregoing demonstration is the first slowing of the magnetization dynamics of a single-molecule magnet by deliberate chemical dilution in a magnetically concentrated environment. Furthermore, the results reveal that S = 1 and S = 2 complexes can be used to reduce quantum tunneling of the magnetization, like S = 0 analogues, if D is positive and of sufficient magnitude.

There are two broader implications of these results. First, from a practical standpoint, the ability to realize magnetic dilution with open-shell complexes opens the door to effective dilutions when closed-shell analogues are chemically unstable or impossible to synthesize, as for example, radical-bridged bimetallic species.[55] Second, we show that the paramagnetic dilution technique is a valid means of manipulating relaxation via chemical engineering of the dipolar field. The work thus provides a new experimental technique for studying the relaxation dynamics of molecular magnets, one that, critically, approaches the proposed conditions where many magnetic molecules may be applied. Finally, we note that this work describes the impact on a single-molecule magnet with easy-axis magnetic anisotropy, for which quantum tunneling is the dominant relaxation mechanism. There are many other relaxation mechanisms, several of which are predicted to be affected by dipolar fields, but these predictions have yet to be quantitatively tested.[56–58] Additionally, although cocrystallization of magnetic/ diamagnetic species has been demonstrated countless times, the structural impacts of dilution have not been well characterized. Considering the impacts of subtle structural changes on molecular magnetism are well documented, it stands to reason that even the subtle size differences between the SMM and diluent molecules could result in measurable changes to the spin Hamiltonian parameters and subsequently to the relaxation dynamics of the system. Future work will test these theories harnessing the new paramagnetic dilution approach presented here, and those results will be presented in due course.

References

1. D. Gatteschi, R. Sessoli and J. Villain, Molecular Nanomagnets, Oxford University Press, New York, NY, 2006.

2. J. Lehmann, A. Gaita-Ariño, E. Coronado and D. Loss, J. Mater. Chem., 2009, 19, 1672–1677.

3. G. Aromí, D. Aguilà, P. Gamez, F. Luis and O. Roubeau, Chem. Soc. Rev., 2012, 41, 537–546.

4. S. Thiele, F. Balestro, R. Ballou, S. Klyatskaya, M. Ruben and W. Wernsdorfer, Science (80-.)., 2014, 344, 1135–1138.

5. J. Wahsner, E. M. Gale, A. Rodríguez-Rodríguez and P. Caravan, Chem. Rev., 2019, 119, 957–1057.

6. Y. Rechkemmer, F. D. Breitgoff, M. Van Der Meer, M. Atanasov, M. Hakl, M. Orlita, P. Neugebauer, F. Neese, B. Sarkar and J. Van Slageren, Nat. Commun., 2016, 7, 1–8.

7. T. P. Latendresse, N. S. Bhuvanesh and M. Nippe, J. Am. Chem. Soc., 2017, 139, 8058–8061.

8. S. Cardona-Serra, J. M. Clemente-Juan, E. Coronado, A. Gaita-Ariño, A. Camón, M. Evangelisti, F. Luis, M. J. Martínez-Pérez and J. Sesé, J. Am. Chem. Soc., 2012, 134, 14982–14990.

9. Y. C. Chen, J. L. Liu, L. Ungur, J. Liu, Q. W. Li, L. F. Wang, Z. P. Ni, L. F. Chibotaru, X. M. Chen and M. L. Tong, J. Am. Chem. Soc., 2016, 138, 2829–2837.

10. N. Ishikawa, M. Sugita, T. Ishikawa, S. Y. Koshihara and Y. Kaizu, J. Am. Chem. Soc., 2003, 125, 8694–8695.

11. F.-S. Guo, B. M. Day, Y.-C. Chen, M.-L. Tong, A. Mansikkamäki and R. A. Layfield, Science (80-.)., 2018, 362, 1400–1403.

12. C. A. P. Goodwin, F. Ortu, D. Reta, N. F. Chilton and D. P. Mills, Nature, 2017, 548, 439–442.

13. L. J. Berliner, G. R. Eaton and S. S. Eaton, Distance Measurements in Biological Systems by EPR, Springer US, Boston, MA, 2002, vol. 19.

14. D. A. Garanin, Eur. Phys. J. B, 2012, 85, 1–10.

15. D. Gatteschi and R. Sessoli, Angew. Chemie Int. Ed., 2003, 42, 268–297.

16. R. Sessoli, D. Gatteschi, A. Caneschi and M. A. Novak, Nature, 1993, 365, 141–143.

17. R. Sessoli, H.-L. Tsai, A. R. Schake, S. Wang, J. B. Vincent, K. Folting, D. Gatteschi, G. Christou and D. N. Hendrickson, J. Am. Chem. Soc., 1993, 115, 1804–1816.

18. J. M. Zadrozny and J. R. Long, J. Am. Chem. Soc., 2011, 133, 20732–20734.

19. D. Attanasio, I. Collamati and C. Daul, Inorg. Chem., 2005, 24, 2746–2750.

20. I. Bhowmick, A. J. Roehl, J. R. Neilson, A. K. Rappé and M. P. Shores, Chem. Sci., 2018, 9, 6564–6571.

21. F. Habib, P. H. Lin, J. Long, I. Korobkov, W. Wernsdorfer and M. Murugesu, J. Am. Chem. Soc., 2011, 133, 8830–8833.

22. F. Luis, M. J. Martínez-Pérez, O. Montero, E. Coronado, S. Cardona-Serra, C. Martí-Gastaldo, J. M. Clemente-Juan, J. Sesé, D. Drung and T. Schurig, Phys. Rev. B - Condens. Matter Mater. Phys., 2010, 82, 3–6.

23. J. M. Zadrozny and D. E. Freedman, Inorg. Chem., 2015, 54, 12027–12031.

24. D. Stinghen, M. Atzori, C. M. Fernandes, R. R. Ribeiro, E. L. De Sá, D. F. Back, S. O. K. Giese, D. L. Hughes, G. G. Nunes, E. Morra, M. Chiesa, R. Sessoli and J. F. Soares, Inorg. Chem., 2018, 57, 11393–11403.

25. M. Atanasov, D. Aravena, E. Suturina, E. Bill, D. Maganas and F. Neese, Coord. Chem. Rev., 2015, 289–290, 177–214.

26. C. Campochiaro, E. G. Pavel and E. I. Solomon, Inorg. Chem., 1995, 34, 4669–4675.

27. D. Swenson, N. C. Baenziger and D. Coucouvanis, J. Am. Chem. Soc., 1978, 100, 1932–1934.

28. D. Coucouvanis, D. Swenson, N. C. Baenziger, D. G. Holah, A. Kostikas, A. Simopoulos and V. Petrouleas, J. Am. Chem. Soc., 1976, 98, 5721–5723.

29. E. A. Suturina, J. Nehrkorn, J. M. Zadrozny, J. Liu, M. Atanasov, T. Weyhermüller, D. Maganas, S. Hill, A. Schnegg, B. Eckhard, J. R. Long and F. Neese, Inorg. Chem., 2017, 56, 3102–3118.

30. D. E. Fenton, R. R. Schroeder and R. L. Lintvedt, J. Am. Chem. Soc., 1978, 100, 1932–1934.

31. D. Coucouvanis, D. Swenson, N. C. Baenziger, C. Murphy, D. G. Holah, N. Sfarnas, A. Simopoulos and A. Kostikas, J. Am. Chem. Soc., 2005, 103, 3350–3362.

32. D. Shindo and T. Oikawa, in Analytical Electron Microscopy for Materials Science, Springer Japan, Tokyo, 2002, pp. 81–102.

33. D. G. Holah and D. Coucouvanis, J. Am. Chem. Soc., 1975, 97, 6917–6919.

34. N. F. Chilton, R. P. Anderson, L. D. Turner, A. Soncini and K. S. Murray, J. Comput. Chem., 2013, 34, 1164–1175.

35. S. Sottini, G. Poneti, S. Ciattini, N. Levesanos, E. Ferentinos, J. Krzystek, L. Sorace and P. Kyritsis, Inorg. Chem., 2016, 55, 9537–9548.

36. E. J. Hawrelak, W. H. Bernskoetter, E. Lobkovsky, G. T. Yee, B. Eckhard and P. J. Chirik, Inorg. Chem., 2005, 44, 3103–3111.

37. J. Cirera, E. Ruiz, S. Alvarez, F. Neese and J. Kortus, Chem. - A Eur. J., 2009, 15, 4078–4087.

38. A. T. Kowal, J. LeGall, M. K. Johnson, I. C. Zambrano, I. Moura and J. J. G. Moura, Inorg. Chem., 1988, 27, 1162–1166.

39. O. Kahn, Molecular Magnetism, VCH, 1993.

40. S. Stoll and A. Schweiger, J. Magn. Reson., 2006, 178, 42–55.

41. R. Boča, Coord. Chem. Rev., 2004, 248, 757–815.

42. J. Bendix, M. Brorson and C. E. Schäffer, Inorg. Chem., 1993, 32, 2838–2849.

43. M. J. Knapp, J. Krzystek, L. C. Brunel and D. N. Hendrickson, Inorg. Chem., 2000, 39, 281–288.

44. C. Duboc, M. N. Collomb, J. Pécaut, A. Deronzier and F. Neese, Chem. - A Eur. J., 2008, 14, 6498–6509.

45. M. Azarkh, L. V. Penkova, S. V. Kats, O. A. Varzatskii, Y. Z. Voloshin and E. J. J. Groenen, J. Phys. Chem. Lett., 2014, 5, 886–889.

46. R. M. Wood, D. M. Stucker, L. M. Jones, W. B. Lynch, S. K. Misra and J. H. Freed, Inorg. Chem., 1999, 38, 5384–5388.

47. Y. S. Ding, K. X. Yu, D. Reta, F. Ortu, R. E. P. Winpenny, Y. Z. Zheng and N. F. Chilton, Nat. Commun., 2018, 9, 1–10.

48. K. S. Cole and R. H. Cole, J. Chem. Phys., 1941, 9, 341–351.

49. R. Orbach, Proc. R. Soc. London. Ser. A. Math. Phys. Sci., 1961, 264, 458–484.

50. G. Molnár, M. Mikolasek, K. Ridier, A. Fahs, W. Nicolazzi and A. Bousseksou, Ann. Phys., 2019, 531, 1–21.

51. A. Nava, L. Rigamonti, E. Zangrando, R. Sessoli, W. Wernsdorfer and A. Cornia, Angew. Chemie - Int. Ed., 2015, 54, 8777–8782.

52. D. S. Krylov, F. Liu, A. Brandenburg, L. Spree, V. Bon, S. Kaskel, A. U. B. Wolter, B. Büchner, S. M. Avdoshenko and A. A. Popov, Phys. Chem. Chem. Phys., 2018, 20, 11656–11672.

53. J. J. Henderson, C. Koo, P. L. Feng, E. Barco, S. Hill, I. S. Tupitsyn, P. C. E. Stamp and D. N. Hendrickson, 2009, 017202, 3–6.

54. R. Kubo and T. Toyabe, in Magnetic resonance and relaxation: Proceedings of the XIVth Colloque Ampere Ljubljana, eds. R. Blinc, D. Hadzi and M. Osredkar, Amsterdam, 1968, p. 810.

55. S. Demir, I.-R. Jeon, J. R. Long and T. D. Harris, Coord. Chem. Rev., 2015, 289–290, 149–176.

56. C. E. Jackson, I. P. Moseley, R. Martinez, S. Sung and J. M. Zadrozny, Chem. Soc. Rev., 2021, 50, 6684–6699.

57. J. Murphy, Phys. Rev., 1966, 145, 241–247.

58. D. Goldfarb and S. Stoll, Eds., EPR Spectroscopy: Fundamentals and Methods, Wiley-VCH, 2018.

CHAPTER 3 – Synthesis and Magnetic Characterization of a Dinuclear Complex of Low-Coordinate Iron(II)

Introduction

Low-coordinate, high-spin ions (those with three or fewer bound atoms) are an exotic inorganic unit that demonstrate exciting chemical and physical properties.[1] For example, low-coordinate, high-spin ions of the earth-abundant elements exhibit extremely strong magnetic anisotropy,[2–4] a property common to rare-earth elements. Separately, low-coordinate, high-spin ions exhibit novel reactivities and catalytic transformations common for precious metals.[5] For example, low-coordinate, high-spin iron complexes will catalyze alkyne trimerization,[6] a reaction that is typical for Rh catalysts.[7]

Incorporation of low-coordinate high-spin metal ions into solids is an enticing strategy toward incorporating the aforementioned magnetic and reactive properties into new functional materials. Indeed, preliminary studies show the success of this design principle in isolating extreme magnetic anisotropies in inorganic solids.[8–10] However, there are considerable challenges to designing generalizable synthetic pathways to new solids with low-coordinate ions stemming from the reactivity of these species. Low-coordinate, high-spin ions tend to possess 2+ and 3+ oxidation states and the low number of directly bound atoms only weakly compensates this charge. Hence, low-coordinate metal ions are extremely Lewis acidic and will readily bind nucleophiles. This propensity means that many traditional materials synthesis techniques are incompatible with low-coordinate ions. For example, traditional solvothermal techniques use bases and nucleophilic solvents (like H_2O and dimethylformamide) that will bind to or react with low-coordinate metal ions to produce high-coordinate ions and quench many of the exciting properties.[11–14] Some success has been realized by the groups of Figueroa, Hey-Hawkins, and Peris, who have isolated extended solids with closed-shell (d^{10}) metal ions.[15–18] However, analogous frameworks with high-spin, open-shell ions are still lacking; hence, novel, low-coordinate-tolerant material synthesis strategies are still a pressing need.

Strategies based on transamination are potentially promising routes toward new solids with low-coordinate ions. In this synthetic strategy, a homoleptic complex of $M\{N(SiMe_3)_2\}_n$ (n = 2 or 3) could be used as a metal source, and reaction with a bridging, bulky, multitopic amine could afford an extended solid whilst releasing $HN(SiMe_3)_2$ as a byproduct.[19–22] Transamination reactions readily produce low-coordinate, high-spin mononuclear species.[23,24] Yet, this reaction strategy has never been shown to result in extended solids. In the process of our efforts in this line of work, we discovered a dinuclear iron complex, $[\{(Me_3Si)_2N\}Fe\{\mu\text{-}p\text{-}\{HN(SiMe_3)\}(C_6Me_4)\{N(SiMe_3)\}\}_2Fe\{N(SiMe_3)_2\}]$ (**1**) (Fig. 3.1) that results from a successful transamination reaction between $[Fe\{N(SiMe_3)_2\}_2]_2$ and the ditopic, bulky bridging ligand $p\text{-}\{HN(SiMe_3)\}_2(C_6Me_4)$ (L). In this manuscript, we detail the characterization of this unit, which can be thought of as a fragment for a potential future extended solid.

Experimental Details

All manipulations and syntheses were performed under a N_2 atmosphere using either a Vigor glovebox or Schlenk techniques. Glassware was either oven-dried at 150 °C for at least four hours and/or flame-dried before bringing into the glovebox. Toluene, tetrahydrofuran (THF), diethyl ether (Et_2O), and hexanes were dried using a commercial solvent purification system from LC Technology Solutions and were stored over 3 or 4 Å molecular sieves prior to use. 3 or 4 Å molecular sieves were stored in a 150 °C oven and were activated at 250 °C under reduced pressure for at least 12 h prior to use. n-BuLi (1.6 M in hexanes) was purchased from Sigma-Millipore and used as is. C_6D_6 was distilled from CaH_2 and stored over molecular sieves inside of an N_2-glovebox. C_6D_6, THF, Et_2O, and hexanes were subjected to a test with a standard purple solution of sodium benzophenone ketyl in THF to confirm low O_2 and H_2O content. 2,3,5,6-Tetramethyl-p-phenylenediamine was purchased from Sigma-Aldrich (electronic grade, 99% trace metal basis) or TCI Chemicals and used as received. $[Fe(N(SiMe_3)_2)_2]_2$ and p-$\{HN(SiMe_3)\}_2(C_6Me_4)$ (L) were prepared following literature procedures.[25,26]

$[\{(Me_3Si_2)_2N\}Fe\{\mu\text{-p-}\{HN(SiMe_3)\}(C_6Me_4)\{N(SiMe_3)\}\}_2Fe\{N(SiMe_3)_2\}]$ (**1**)

In a N_2-filled glovebox, a 20-mL scintillation vial was charged with 0.156 g (0.207 mmol) $[Fe(N(SiMe_3)_2)_2]_2$, 0.131 g (0.424 mmol) p-$\{HN(SiMe_3)\}_2(C_6Me_4)$, and a Teflon-coated magnetic stir bar. 5 mL toluene was added to the vial with gentle shaking and the color of the solution turned from pale yellow to dark red in ca. 2 min. The reaction mixture was left to stir overnight and all volatiles (toluene and hexamethyldisilazane, $(HN(SiMe_3)))$ were then removed under reduced pressure. 5 mL toluene was then added to the resulting pale-yellow residue, resulting dissolution of the solid and a dark red solution. The dark red solution was filtered through a Celite pipet filter and ca. 5 mL hexanes was layered on top of the toluene solution. The vial was stored in a −35 °C freezer in the glovebox for 1-2 days to afford 0.119 g (0.114 mmol, 55.2 % yield based on iron) of large off-white crystals of **1** suitable for single-crystal X-ray diffraction. The powder diffraction pattern for bulk solid product matches that predicted from the single-crystal unit cell (Fig. B1). ^1H-NMR: (400 MHz, 25 °C, C_6D_6) δ -30.24 (br), δ -8.58 (br), δ 24.92 (br), δ 39.42 (br), δ 65.89 (br) . Transmission IR (ν, cm^{-1}): 3367 (w), 3263 (vs), 2949 (vs), 2897 (s), 1458 (br), 1302(s), 1091 (s), 1050 (s), 962 (s), and 831 (br). Combustion analyses calculated for $C_{44}H_{98}Fe_2N_6Si_8$ (found): 50.44 (50.36) % C; 9.43 (9.27) % H; 8.02 (8.07) % N.

p-{DN(SiMe$_3$)}$_2$(C$_6$Me$_4$) (L-D)

In a N$_2$-filled glovebox, 0.606 mL (0.970 mmol) of n-BuLi (1.6 M in hexanes) was added to 150 mg (0.485 mmol) of L in 10 mL of diethyl ether at room temperature. This solution moved outside the glovebox, attached to a Schlenk line, and allowed to stir, slowly producing a white precipitate over the course of the day. To this mixture was added 17.5 µL of degassed D$_2$O (0.970 mmol) with stirring, producing a clear solution and colorless solid (presumably LiOD). The volatiles were removed under reduced pressure and the ligand was extracted from the residue with hexanes (3 × 10 mL). Removal of the hexanes under reduced pressure yielded a white, semi-crystalline solid (130 mg; 86% yield). Product was confirmed through ^{1}H-NMR: (400 MHz, 25 °C, C$_6$D$_6$) δ 2.16 (s, 12H, phMe), 0.00 (s, 18H, SiMe$_3$) and Transmission IR (λ, cm^{-1}): 2959 (w), 2493 (w), 1460 (br), 1261 (s), 1006 (br), 1018 (br), and 801 (br).

[{(Me$_3$Si$_2$)$_2$N}Fe{µ-p-{DN(SiMe$_3$)}(C$_6$Me$_4$){N(SiMe$_3$)}}$_2$Fe{N(SiMe$_3$)$_2$}] (1-D)

Compound **1-D** was prepared following the procedure outlined for compound **1**. In an N$_2$-filled glovebox, a 20 mL scintillation vial was charged with 0.121 g (0.161 mmol) [Fe(N(SiMe$_3$)$_2$)$_2$]$_2$, and 0.100 g (0.322 mmol) p-{DN(SiMe$_3$)}$_2$(C$_6$Me$_4$). The solids were dissolved in ca. 5 mL of toluene, rapidly changing from green to dark red over the course of a minute. The reaction was then allowed to stir over night. The volatiles were removed under reduced pressure to yield a light tan solid (166 mg; 98% yield). ^{1}H-NMR: (400 MHz, 25 °C, C$_6$D$_6$) δ -9.34 (br), δ 24.70 (br), δ 38.24 (br), δ 64.79 (br). Transmission IR (λ, cm^{-1}): 2949 (vs), 2902 (w), 2417 (s), 1461 (br), 1252 (vs), 1089 (s), 1055 (s), 962 (s), and 839 (br).

Magnetic Measurements

Magnetic measurements were performed with a Quantum Design MPMS-XL5. Samples of polycrystalline **1** were pulverized using a glass rod to yield a fine microcrystalline powder for analysis. This powder was loaded into a polyethylene bag and vacuum sealed to prevent torquing during the measurement cycle. Samples were contained in an inert atmosphere and only briefly brought out of N_2 prior to insertion into the instrument. Dc susceptibility measurements were fit using PHI [27]. All measurements were corrected for the diamagnetic contributions of the compound itself (estimated using Pascal's constants)[28] as well as the polyethylene bag.

X-Ray Diffraction Measurements

Single-crystal X-ray diffraction data were collected at the X-Ray Diffraction facility of the Central Instrument Facility at Colorado State University. Data for **1** were collected on a Bruker D8 Quest ECO single-crystal X-ray diffractometer equipped with Mo Kα (λ = 0.71073 Å) radiation. Data were collected and integrated using Bruker Apex 3 software.[29] Absorption correction was applied using SADABS.[30] Space group assignments were determined by examination of systematic absences, E-statistics, and successive refinement of the structures. Crystal structures were solved using SHELXT and refined with the aid of successive difference Fourier maps by SHELXL operated in conjunction with OLEX2 software.[31–33] None of the crystals demonstrated decay by X-ray radiation over the course of the experiment. Hydrogen atoms were placed in ideal positions and refined using a riding model for all structures. Disorder in the location of the iron ions was modeled with free variables. The crystal structure can be accessed via CSD 1946979.

Powder X-Ray diffraction data were obtained using a Bruker D8 Discover Series II diffractometer utilizing the LYNXEYE detector and a CuKα radiation source at 1600W (40 kV, 40mA). Samples were prepared in an inert atmosphere glovebox by loading 0.6mm diameter quartz capillaries with uniformly powdered sample and sealed using capillary wax before being centered on the goniometer. All patterns were collected from $2\theta = 5\text{-}50^\circ$, with a 0.02° increment, and a 1 sec exposure time.

Mössbauer Spectroscopy

The zero-field ^{57}Fe Mössbauer spectrum of **1** was obtained at 80 K with a constant acceleration spectrometer with a rhodium matrix cobalt-57 source. Prior to the measurement, the spectrometer was calibrated at 295 K with a 30 µm-thick α-iron foil. The absorber was prepared under a dinitrogen atmosphere by placing 82 mg of compound **1** into a polyethylene holder (7.7 mg of natural Fe/cm^2) and restrained with a small drop of Paratone-N oil. The absorber was sealed and frozen in liquid N_2 immediately upon removal from the glovebox. The collected spectrum was fit to a single Lorentzian doublet using the WMOSS software package.[34] Isomer shifts are reported relative to the centroid of the iron metal spectrum recorded at 295 K.

Other Physical Measurements

Transmission Infrared (IR) spectra of the ligands and dinuclear species were collected on a Bruker Tensor II spectrometer. Labels for IR peaks in sections 2.4 – 2.5 are as defined as: vs = very sharp, s = sharp, m = medium, w = weak, br = broad. Samples were prepared inside an N_2 glovebox by taking a small amount of each complex (< 1 mg) and mixing it with potassium bromide (ca. 5 mg) using an agate mortar and pestle. This powder was then pressed into a thin pellet and quickly transported to the IR spectrometer for measurement to prevent oxidative degradation. Minimal degradation occurred on the timescale of the experiment; however, KBr pellets left in air were observed to degrade over the course of 24 hours. Combustion analyses were performed by Midwest Microlab.

Results and Discussion

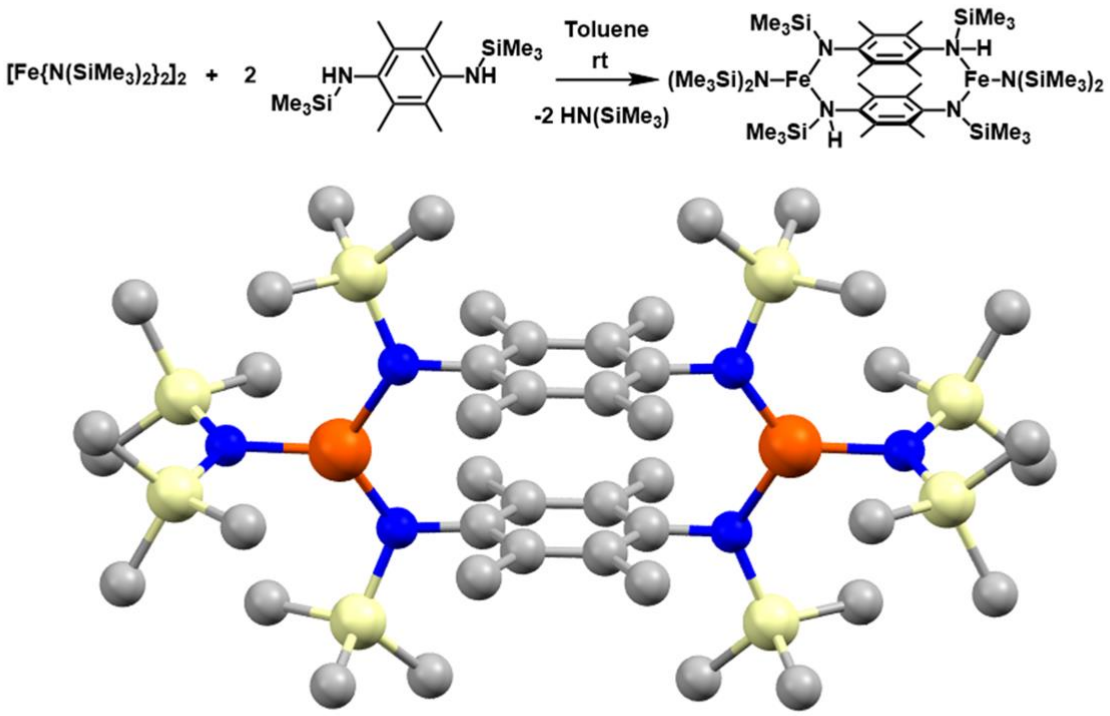

Fig. 3.1. **Top:** Synthetic transamination scheme for **1. Bottom:** Structure of the molecular species determined from a single crystal of **1**. Orange, blue, yellow, and grey spheres represent Fe, N, Si, and C respectively. Hydrogen atoms are omitted for clarity. Selected interatomic distances (Å): Fe–N_{Bridge} (1.905(3)), Fe–N_{Bridge} (2.183(3)), Fe–N_{HMDS} (1.938(3)), and Fe•••Fe (7.674(3)). Fe atoms are displayed as the average position of the solved two-position disorder.

Synthesis and Structures

Complex **1** was prepared following the addition of one equivalent of $[Fe\{N(SiMe_3)_2\}_2]_2$ to two equivalents of the diamine ligand L in toluene, which resulted in a rapid color change from the green of $[Fe(N(SiMe_3)_2)_2]_2$ to deep red, a common color for two coordinate complexes.[23] Upon removal of the volatiles (toluene and $HN(SiMe_3)$) a tan solid is left, which upon dissolution returns the deep red color seen initially. Layering of this deep red solution with hexanes at –35 ˚C yielded tan crystals suitable for single-crystal x-ray diffraction.

X-ray diffraction experiments on single crystals of **1** reveal a dinuclear structure consisting of two trigonal-planar, three-coordinate iron atoms bridged by two diamine ligands (Fig. 3.1). The molecule bears an inversion center, and the second half of the structure was symmetry generated. The iron centers were solved by modeling disorder over two positions, separated by 0.367(3) Å. Each iron atom is coordinated by three nitrogen atoms, two coming from the bringing diamine ligands (N_{Bridge}) and one from a $N(SiMe_3)_2^-$ ligand ($N_{(N(SiMe3)2)}$). The aromatic rings of the bridging rings are p-stacked in a slightly offset face-to-face arrangement, with ≈ 3.5 Å distance between the centroids of the two rings. The Fe–$N(SiMe_3)_2$ bond lengths of **1**, 1.938(3) Å, are within the range of those observed in Fe(II) complexes of the type $[Fe(N(SiMe_3)_2)_3]^-$ (1.905(2)-1.988(5) Å).[35,36] The other Fe–N bonds, the Fe–N_{Bridge} bonds, are different from one another, at 1.905(3) and 2.183(3) Å respectively. These values are also within range of reported iron(II)–amine and –amide bond lengths.[37,38] All of these observations are in line with reported analogues featuring similar aminocyclophane structures of non-transition metal ions, which display pseudo-trigonal planar nitrogen geometries on the bridging amines.[39,40]

At first glance, the structural data preclude definitive oxidation state assignment for the iron atoms. For one, an obvious N–H hydrogen cannot be located (important for charge balance), likely attributable to disorder of the iron center over two positions, and, hence disorder of the amine proton. Further, the trigonal planar geometries of the two N-atoms from the bridging ligands are highly similar, also making proton location challenging. However, the difference (nearly 0.3 Å) between the two Fe–N_{Bridge} bonds at each Fe suggests different electron donation characteristics. Second, Fe–N bond lengths found in similar three-coordinate iron(II) species vary widely with changes to the second coordination sphere (~ 0.08 Å). Indeed, the Fe–N distances of the Fe(II) complex [$Fe_2(N(SiMe_3)_2)_4$] (1.925(3) and 2.086(2) Å)[41] and the Fe(III) complex $Fe(N(SiMe_3)_2)_3$ (1.918(4) Å)[42] span the range of observed Fe–N bond lengths in **1**. Hence, making oxidation state assignment in **1** on the basis of bond distances is difficult. Determining the oxidation state of these complexes is integral to a deeper understanding of the magnetism and properties of **1**. Furthermore, identifying possible redox reactions would be important knowledge in any future synthetic scheme featuring these bridging ligands and metals. Hence, the below studies were pursued to conclusively assign the metal oxidation states.

Mössbauer Spectroscopy

The zero-field Mössbauer spectrum of **1** (Fig. 3.2) shows a well resolved doublet of peaks at 0.07 and 1.15 mm/s, denoting an isomeric shift of $\delta = 0.641(2)$ mm/s and quadrupolar splitting of $\Delta E_Q = 1.134(8)$ mm/s. These values are in the range of high-spin iron(II),[43] and indeed, the spectrum can be readily fit assuming a single, high-spin iron(II) ion for **1**. The fit parameters closely resemble those of $Fe(N(SiMe_3)_2)_2$•xTHF, which also features a three coordinate, planar Fe(II) high-spin ground state with anionic amine donors.[25] Given the air-sensitivity of **1**, we also fit the spectrum with a single high-spin iron(II) impurity (6.8 %), which slightly improves the overall fit. However, the line-width of the impurity is unrealistically narrow.

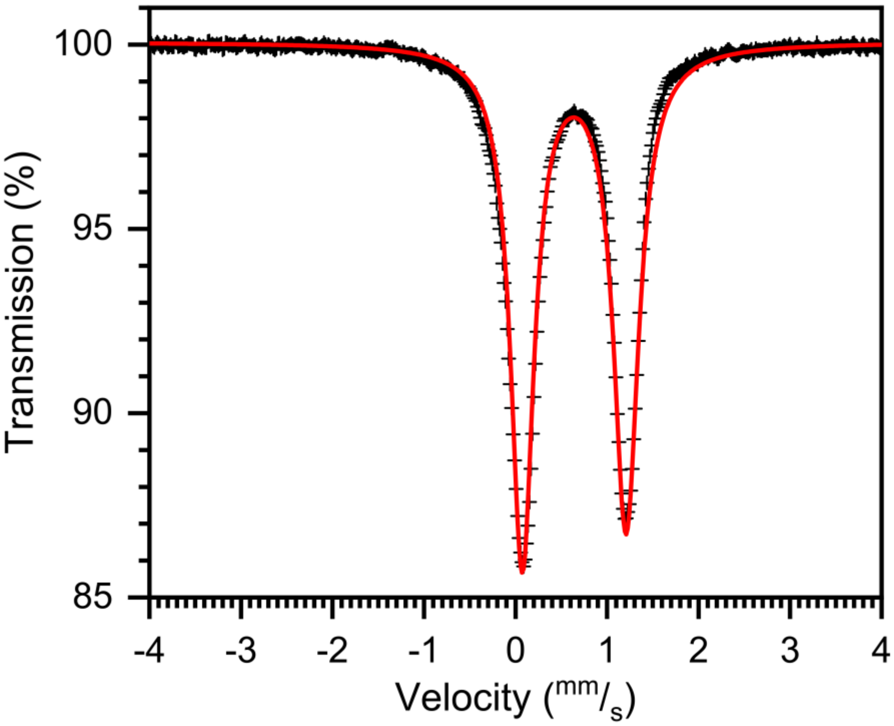

Fig. 3.2. Zero-field Mössbauer spectrum of **1** at 80 K**.** Experimental data is shown in black crosses and the fit is shown in red. Single-site fitting parameters: $\delta = 0.641(2)$ mm/s, $\Delta E_Q = 1.134(8)$ mm/s, $\Gamma_L = 0.311(1)$ mm/s, and $\Gamma_R = 0.336(1)$ mm/s.

IR Spectroscopic Analysis

For iron atoms to be iron(II) as suggested by the Mössbauer data, one of the nitrogen atoms from the bridging ligands needs to be protonated for charge balance. Hence, IR spectroscopy should confirm the presence of the N–H bond. To test that hypothesis, we performed IR spectroscopy on **1** and **1** prepared with a N–D deuterated analogue (L-D) of the bridging ligand, **1-D**. The IR spectrum of the lone ligand (Fig. 3.3) displays a weak peak at 3366 cm^{-1}, slightly above the C–H region. Upon complexation, this stretch moves to lower energy, 3263 cm^{-1}. In contrast, the IR spectrum of the deuterated ligand, L-D, no longer features the 3366 cm^{-1} peak, but instead a new, weak one at 2493 cm^{-1} (in the expected range of an N–D stretch) [44]. Upon complexation, this peak is also red-shifted down to 2418 cm^{-1}. The fingerprint regions for both ligands resemble those regions for their respective dimeric complexes yet shifted slightly.

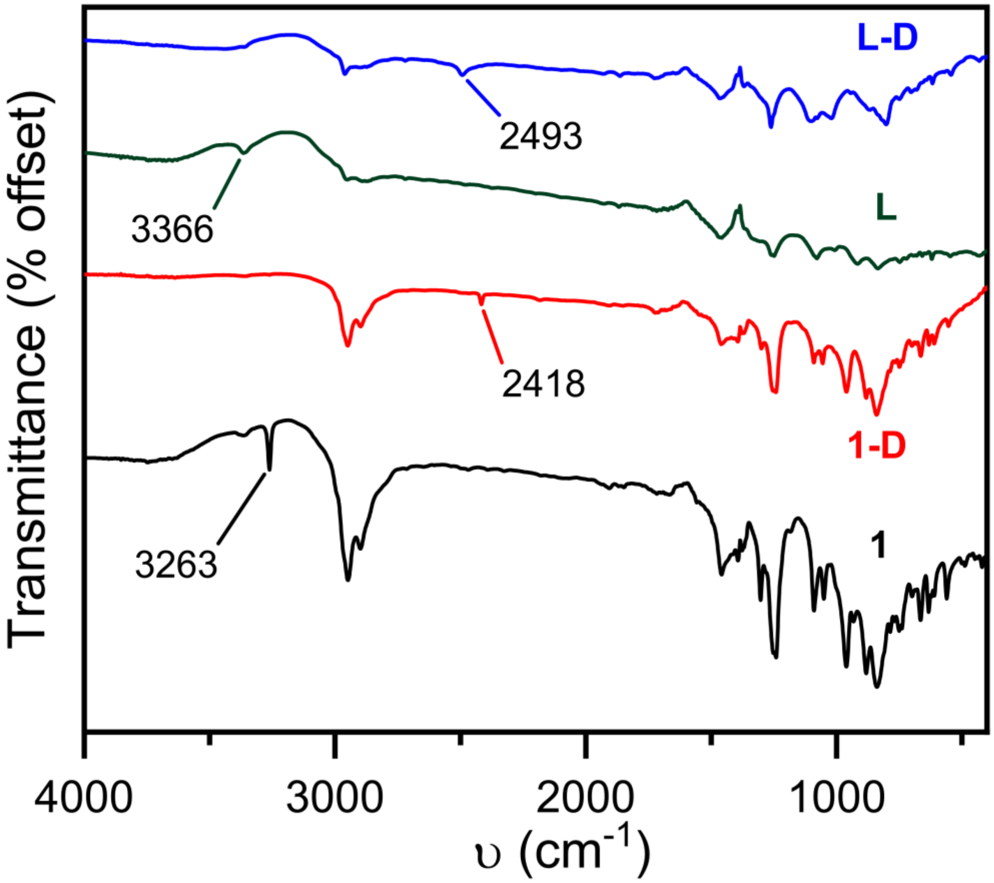

Fig. 3.3. Solid-state IR spectra for **1** and **1-D** stacked with IR spectra for pure ligand (**L**) and deuterated ligand (**L-D**). Selected peaks corresponding to respective amine protons (N–H for **L** and **1**) and deuterons (N–D for **L-D** and **1-D**) are labeled for emphasis.

Inspection of the spectra let us make two important conclusions. First, the disappearance of the 3366 (and 3263) cm^{-1} peaks as a function of deuteration suggests that these peaks are the N–H stretches. Second, the fact that the IR spectra of the lone ligands L and L-D and those of the complexes **1** and **1-D**, respectively, retain the N–H (and N–D) stretches also suggests that the ligand is still protonated (at least once) in the final complex. In conjunction with the Mossbauer data, we conclude that these results conclusively point to a redox assignment of 2 × Fe(II) for **1**.

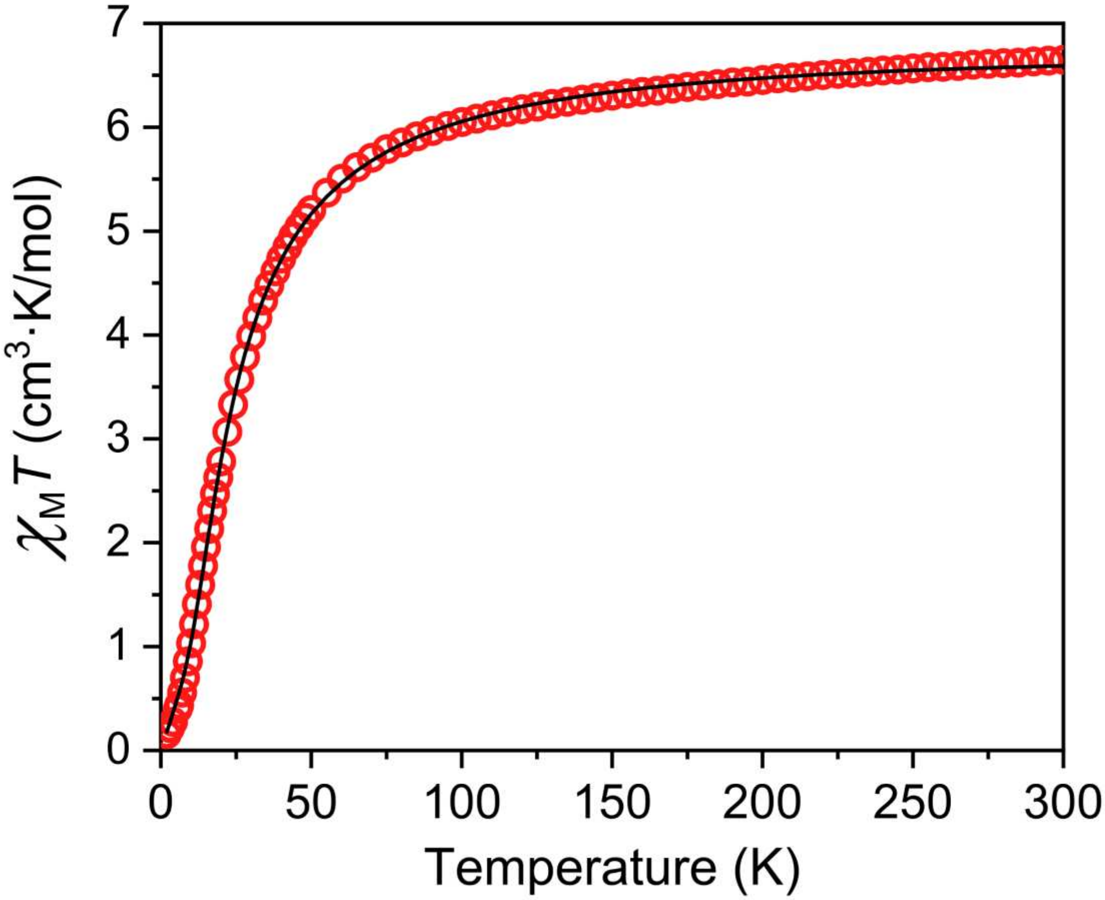

Fig. 3.4. Variable temperature dc susceptibility ($\chi_M T$) data under an applied dc magnetic field of 1000 G for pure, polycrystalline sample of **1**. Fit line was generated using PHI [49] and the spin Hamiltonian parameters $g_{iso} = 2.18$, $D = 7.51$ cm^{-1}, and $J = -2.33$ cm^{-1}.

Magnetic Properties

The magnetic properties of **1** were investigated by variable-temperature dc susceptibility (χ_M) from 2 – 300 K under a magnetic field of 1000 G (Fig. 3.4). At 300 K, $\chi_M T$ for **1** is 6.65 cm^{3}K/mol, which is slightly larger than the expected $\chi_M T = 6$ cm^{3}K/mol for two non-interacting S = 2 iron(II) centers. With decreasing temperature, $\chi_M T$ slowly decreases until 50 K, when $\chi_M T$ sharply decreases, ultimately reaching a minimum at 0.15 cm^{3}K/mol at 2 K. This decrease in $\chi_M T$ could be attributed to superexchange coupling between the Fe atoms or zero-field splitting (a common property for three-coordinate Fe(II)) [45]. Accordingly, the magnetic susceptibility data were fit using the following spin Hamiltonian:

$$\hat{H} = g_{iso}\mu_{\beta}B\hat{S} - 2J(\hat{S}_{Fe1} \cdot \hat{S}_{Fe2}) + D\hat{S}_{z}^{2}$$

Here, g_{iso} is an isotropic g value (assumed equal for both iron atoms), μ_B is the Bohr magneton, *B* is the applied magnetic field, *J* is the superexchange coupling constant, and *D* is the axial anisotropy (zero-field splitting). $\hat{S}_i$ are the spin operators. Fits for the dc susceptibility experiment were attempted for both dinuclear 2 × Fe(II) S = 2 and 2 x Fe(III) $S = {}^5/_2$ models, yet the best agreement was observed for the $S = 2$ model. The values obtained from the fitting are $g_{iso} = 2.18$, $J = -2.33$ cm^{-1}, and $D = 7.51$ cm^{-1}. We also tried additional fits using a spin Hamiltonian that incorporated an additional transverse anisotropy term, $E(\hat{S}_x^2 - \hat{S}_y^2)$, which yielded the parameters $g_{iso} = 2.14$, $D = 8.07$ cm^{-1}, $E = 2.61$ cm^{-1}, and $J = -1.94$ cm^{-1}. The *g*, *D*, and *J* values here are close to the magnitudes obtained from the fit without *E*, and the improvement in fit quality by inclusion of *E* is borderline negligible. Incorporating a small TIP value (~8×10^{-4} cm^3/mol), typical for first-row metal ions[46] slightly improved the fit quality. Finally, the extracted small negative *J* value is to be expected given the large size of the bridge, which imposes a six-atom pathway for superexchange.

Importantly, the magnetic data (and the fits) corroborate the 2 × Fe(II) oxidation state assignments. The data also rule out other potential redox configurations for **1**. For example, if the ligand had been reduced by the iron(II) in situ to give the formulation of 2 × Fe(III) and 2 × radical bridge, we would anticipate strong Fe•••Fe interactions (as a result of extremely strong Fe-radical bridge exchange interactions). Such interactions would dramatically impact the $\chi_M T$ data and the fit quality with the above model would be exceptionally poor.[47,48] Additionally, while we are cautious about the sign of *D* determined here owing to the difficulty in extracting this property from powders, the observed magnitudes are in the expected range for low coordinate iron(II) complexes with amine donors,[45] not high-spin iron(III) ions. As one final point, out-of-phase ac susceptibility measurements reveal no slow magnetic relaxation for **1** under zero field, meaning that **1** is not a single molecule magnet (Fig. B3). Together, these data conclusively describe **1** as a weakly coupled, antiferromagnetic dinuclear Fe(II) complex with moderate magnetic anisotropy.

Conclusions and Outlook

In our pursuit of novel extended structures featuring high-spin, low-coordinate ions, a new, exchange coupled dinuclear iron complex was synthesized, **1**, which behaves as a weakly coupled antiferromagnetic system. The reactivity of low-coordinate ions is often complex, unpredictable, and can readily involve oxidation state changes[1]. Accordingly, a battery of crystallographic, spectroscopic, and magnetometric techniques were applied to confirm the identity of the iron ions as iron(II). Importantly, these results demonstrate that the transamination reaction is a plausible route to linking together high-spin ions while retaining their low-coordinate environment, when the selected bridging unit is sufficiently bulky. Hence, this transamination reaction offers a promising pathway forward. Future work by us will explore ways of increasing nuclearity in analogous molecules on the path toward new extended solids.

References

1. Power, P.P. (2012). Stable Two-Coordinate , Open-Shell (d1 − d9) Transition Metal Complexes. Chem. Rev. *112*, 3482–3507.
2. Zadrozny, J.M., Xiao, D.J., Atanasov, M., Long, G.J., Grandjean, F., Neese, F., and Long, J.R. (2013). Magnetic blocking in a linear iron(I) complex. Nat. Chem. *5*, 577–81.
3. Guo, F.S., Bar, A.K., and Layfield, R.A. (2019). Main Group Chemistry at the Interface with Molecular Magnetism. Chem. Rev.
4. Bunting, P.C., Atanasov, M., Damgaard-Møller, E., Perfetti, M., Crassee, I., Orlita, M., Overgaard, J., van Slageren, J., Neese, F., and Long, J.R. (2018). A linear cobalt(II) complex with maximal orbital angular momentum from a non-Aufbau ground state. Science (80-.). *362*, eaat7319.
5. Taylor, L.J., and Kays, D.L. (2019). Low-coordinate first-row transition metal complexes in catalysis and small molecule activation. Dalt. Trans.
6. Lipschutz, M.I., Chantarojsiri, T., Dong, Y., and Tilley, T.D. (2015). Synthesis, characterization, and alkyne trimerization catalysis of a heteroleptic two-coordinate Fe^{I} complex. J. Am. Chem. Soc. *137*, 6366–6372.
7. Kirchner, K., Calhorda, M.J., Schmid, R., and Veiros, L.F. (2003). Mechanism for the cyclotrimerization of alkynes and related reactions catalyzed by CpRuCl. J. Am. Chem. Soc. *125*, 11721–11729.
8. Xu, L., Zangeneh, Z., Yadav, R., Avdoshenko, S., Van Den Brink, J., Jesche, A., and Hozoi, L. (2017). Spin-reversal energy barriers of 305 K for Fe2+ d6 ions with linear ligand coordination. Nanoscale *9*, 10596–10600.

9. Ballé, T.J., Zangeneh, Z., Hozoi, L., Jesche, A., and Höhn, P. (2019). Ferromagnetic ordering of linearly coordinated Co ions in LiSr2[CoN2]. Phys. Rev. B *99*, 1–9.

10. Jesche, A., McCallum, R.W., Thimmaiah, S., Jacobs, J.L., Taufour, V., Kreyssig, A., Houk, R.S., Bud'Ko, S.L., and Canfield, P.C. (2014). Giant magnetic anisotropy and tunnelling of the magnetization in Li2(Li1-xFex)N. Nat. Commun. *5*, 1–9.

11. Stein, A., Keller, S.W., and Mallouk, T.E. (1993). Turning Down the Heat : Design and Mechanism in Solid-State Synthesis Published by : American Association for the Advancement of Science Turning Down the Heat : Design and Mechanism in Solid State Synthesis. Science (80-.). *259*, 1558–1564.

12. McMillen, C.D., and Kolis, J.W. (2016). Hydrothermal synthesis as a route to mineralogically-inspired structures. Dalt. Trans. *45*, 2772–2784.

13. Li, J., Chen, Z., Wang, R.-J., and Proserpio, D.M. (1999). Low temperature route towards new materials: solvothermal synthesis of metal chalcogenides in ethylenediamine. Coord. Chem. Rev. *190–192*, 707–735.

14. Stock, N., and Biswas, S. (2012). Synthesis of metal-organic frameworks (MOFs): Routes to various MOF topologies, morphologies, and composites. Chem. Rev. *112*, 933–969.

15. Agnew, D.W., Gembicky, M., Moore, C.E., Rheingold, A.L., and Figueroa, J.S. (2016). Robust, Transformable, and Crystalline Single-Node Organometallic Networks Constructed from Ditopic m-Terphenyl Isocyanides. J. Am. Chem. Soc. *138*, 15138–15141.

16. Agnew, D.W., Dimucci, I.M., Arroyave, A., Gembicky, M., Moore, C.E., MacMillan, S.N., Rheingold, A.L., Lancaster, K.M., and Figueroa, J.S. (2017). Crystalline Coordination Networks of Zero-Valent Metal Centers: Formation of a 3-Dimensional Ni(0) Framework with m-Terphenyl Diisocyanides. J. Am. Chem. Soc. *139*, 17257–17260.

17. Hoy, R., Lönnecke, P., and Hey-Hawkins, E. (2018). Selective formation of a two-dimensional coordination polymer based on a tridentate phospholane ligand and gold(i). Dalt. Trans. *47*, 14515–14520.

18. Gonell, S., Poyatos, M., and Peris, E. (2014). Main-Chain Organometallic Microporous Polymers Bearing Triphenylene-Tris(N-Heterocyclic Carbene)-Gold Species: Catalytic Properties. Chem. - A Eur. J. *20*, 5746–5751.

19. Burger, H., and Wannagat, U. (1964). Silylamido-Verbindungen von Chrom, Mangan, Nickel, and Kupfer. Mh. Chem., Bd. *292*, 4–5.

20. Ellison, J.J., Power, P.P., and Shoner, S.C. (1989). First Examples of Three-Coordinate Manganese(III) and Cobalt(III): Synthesis and Characterization of the Complexes M[N(SiMe3)2]3 (M = Mn or Co). J. Am. Chem. Soc. *111*, 8044–8046.

21. Alyea, E.C., Bradley, D.C., and Copperthwaite, R.G. (1972). Three-co-ordinated transition metal compounds. Part I. the preparation and characterization of tris(bistrimethylsilylamido)-derivatives of scandium, titanium, vanadium, chromium, and iron. J. Chem. Soc. Dalt. Trans., 1580–1584.

22. Derivate, S., and Wannagat, H.B.U. (1963). Silylamido-Derivate von Eisen und Kobalt. Mh. Chem., Bd. *1540*.

23. Zadrozny, J.M., Atanasov, M., Bryan, A.M., Lin, C.Y., Rekken, B.D., Power, P.P., Neese, F., and Long, J.R. (2013). Slow magnetization dynamics in a series of two-coordinate iron(ii) complexes. Chem. Sci. *4*, 125–138.

24. Merrill, W.A., Stich, T.A., Brynda, M., Yeagle, G.J., Fettinger, J.C., De Hont, R., Reiff, W.M., Schulz, C.E., Britt, R.D., and Power, P.P. (2009). Direct spectroscopic observation of large quenching of first-order orbital angular momentum with bending in monomeric,

two-coordinate Fe(II) primary amido complexes and the profound magnetic effects of the absence of Jahnand- and Renner-Teller distortions. J. Am. Chem. Soc. *131*, 12693–12702.

25. Broere, D.L.J., Čorić, I., Brosnahan, A., and Holland, P.L. (2017). Quantitation of the THF Content in Fe[N(SiMe3)2]2·xTHF. Inorg. Chem. *56*, 3140–3143.
26. Antiñolo, A., Dorado, I., Fajardo, M., Garcés, A., Kubicki, M.M., López-Mardomingo, C., Otero, A., and Prashar, S. (2006). Synthesis and reactivity of new mono- and dinuclear niobium and tantalum imido complexes: X-ray crystal structure of [Ta(η5-C5H4SiMe3)Cl2{=NC6Me 4-4-(N(SiMe3)2)}]. J. Organomet. Chem. *691*, 1361–1368.
27. Chilton, N.F., Anderson, R.P., Turner, L.D., Soncini, A., and Murray, K.S. (2013). PHI: A powerful new program for the analysis of anisotropic monomeric and exchange-coupled polynuclear d- and f- block complexes. J. Comput. Chem. *34*, 1164–1175.
28. Bain, G.A., and Berry, J.F. (2009). Diamagnetic Corrections and Pascal's Constants. J. Chem. Educ. *85*, 532.
29. Bruker (2012). APEX3.
30. Sheldrick, G.M. (2000). SADABS.
31. Sheldrick, G.M. (2015). SHELLX. Acta Crystallogr. Sect. A Found. Crystallogr. *71*, 3–8.
32. Sheldrick, G.M. (2015). OLEX2. Acta Crystallog. Sect. C Struct. Chem. *71*, 3–8.
33. Dolomanov, O. V., Bourhis, L.J., Gildea, R.J., Howard, J.A.K., and Puschmann, H. (2009). OLEX2: A complete structure solution, refinement and analysis program. J. Appl. Crystallogr. *42*, 339–341.
34. Prisecaru, I. WMOSS4 Mössbauer Spectral Analysis Software.
35. Eichhöfer, A., Lan, Y., Mereacre, V., Bodenstein, T., and Weigend, F. (2014). Slow magnetic relaxation in trigonal-planar mononuclear Fe(II) and Co(II)

bis(trimethylsilyl)amido complexes - A comparative study. Inorg. Chem. *53*, 1962–1974.

36. Putzer, M.A., Neumüller, B., Dehnicke, K., and Magull, J. (1996). Synthese und kristallstrukturen der amino-komplexe [Na(12-Krone-4)2][M{N(SiMe3)2}3] mit = Mn, Fe und Co M = Mn, Fe und czo. Chem. Ber. *129*, 715–719.

37. Layfield, R.A., McDouall, J.J.W., Scheer, M., Schwarzmaier, C., and Tuna, F. (2011). Structure and bonding in three-coordinate N-heterocyclic carbene adducts of iron(ii) bis(trimethylsilyl)amide. Chem. Commun. *47*, 10623–10625.

38. Dimitrova, N., Zamudio, J.R., Jong, R.M., Soukup, D., Resnick, R., Sarma, K., Ward, A.J., Raj, A., Lee, J., Sharp, P.A., et al. (2017). Ligand Dependence of Binding to Three-Coordinate Fe(II) Complexes. PLoS One *32*, 736–740.

39. Braunschweig, H., Drost, C., Hitchcock, P.B., Lappert, M.F., and Pierssens, L.J.-M. (1997). A Dinuclear Tin(II) Amide, a meta-Stannylaminocyclophane and Its Orthostannylated Derivative, a Dimeric Trinuclear Tin(II) Cluster. Angew. Chemie Int. Ed. English *36*, 261–263.

40. Paetzold, P., Welling-Osterloh, U., and Englert, U. (2004). Tetraazadibora[3,3]paracyclophane. Zeitschrift fur Anorg. und Allg. Chemie *630*, 2569–2570.

41. Olmstead, M.M., Power, P.P., and Shoner, S.C. (1991). Three-Coordinate Iron Complexes: X-ray Structural Characterization of the Amide-Bridged Dimers [Fe(NR2)2]2 (R = SiMe3, C6H5) and the Adduct Fe[N(SiMe3)2]2(THF) and Determination of the Association Energy of the Monomer Fe{N(SiMe3)2}2 in Solution. Inorg. Chem. *30*, 2547–2551.

42. Bradley, B.D.C., and Hursthouse, M.B. (1969). The Structure of a Three-Co-ordinate Iron (III) Compound. 94–95.

43. Drago, R.S. (1992). Physical Methods for Chemists 2nd Ed. 2nd ed. (Surfside Scientific Publishers).

44. Farquhar, E.L. (1962). The infrared spectra of primary aromatic amides.

45. Broere, D.L.J., Mercado, B.Q., Lukens, J.T., Vilbert, A.C., Banerjee, G., Lant, H.M.C., Lee, S.H., Bill, E., Sproules, S., Lancaster, K.M., et al. (2018). Reversible Ligand-Centered Reduction in Low-Coordinate Iron Formazanate Complexes. Chem. - A Eur. J. *24*, 9417–9425.

46. Kahn, O. (1993). Molecular Magnetism (VCH).

47. Hua, C., Degayner, J.A., and Harris, T.D. (2019). Thiosemiquinoid Radical-Bridged Cr III2 Complexes with Strong Magnetic Exchange Coupling. Inorg. Chem. *58*, 7044–7053.

48. Degayner, J.A., Jeon, I.R., and Harris, T.D. (2015). A series of tetraazalene radical-bridged M2 (M = CrIII, MnII, FeII, CoII) complexes with strong magnetic exchange coupling. Chem. Sci. *6*, 6639–6648.

49. Chilton, N.F., Anderson, R.P., Turner, L.D., Soncini, A., and Murray, K.S. (2013). PHI: A powerful new program for the analysis of anisotropic monomeric and exchange-coupled polynuclear d- and f- block complexes. J. Comput. Chem. *34*, 1164–1175.

CHAPTER FOUR – Geometry Dependent Valence Tautomerism, and Magnetism in 1D Iron-Tetraoxolene Chains

Introduction

As described in chapter three, the development of extended solids incorporating first-row transition metals is crucial to their eventual incorporation into device architecture. In this work, the magnetic properties of a family of three, iron-based coordination polymers are investigated. It is shown that despite possessing near identical chemical composition, the three complexes display vastly different magnetic properties. Structural and spectroscopic characterization performed by our collaborators confirms that the origin of these magnetic properties lies in the structural conformation of each chain (Fig 4.1, 4.2). *Cis*-Fe(Ph_2dhbq)(DMF)$_2$, displays valence tautomerization upon cooling, which results in oxidation of the Fe(II) by the bridging quinoid ligands. The resulting Fe(III) radical coupled chain displays considerable long range coupling of spins due to strong exchange coupling between the metal and radical spins.

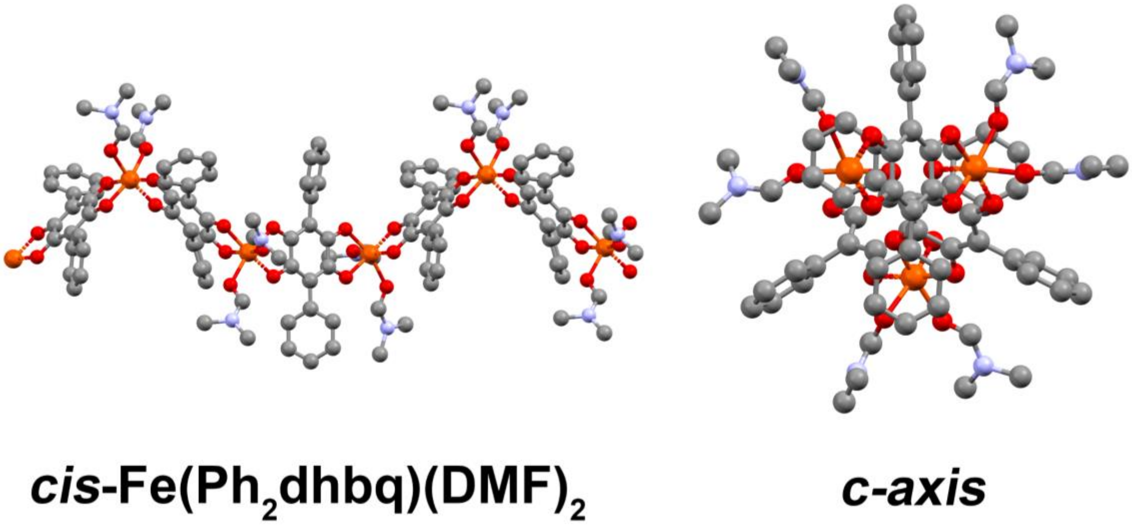

cis-Fe(Ph_2dhbq)(DMF)$_2$

c-axis

Figure 4.1. (*left*) SCXRD Structure of *cis*-Fe(Ph_2dhbq)(DMF)$_2$ collected at 100 K. (*right*) View of the helical chain structure of *cis*-Fe(Ph_2dhbq)(DMF)$_2$ viewed along the crystallographic c-axis. Hydrogens have been omitted for clarity.

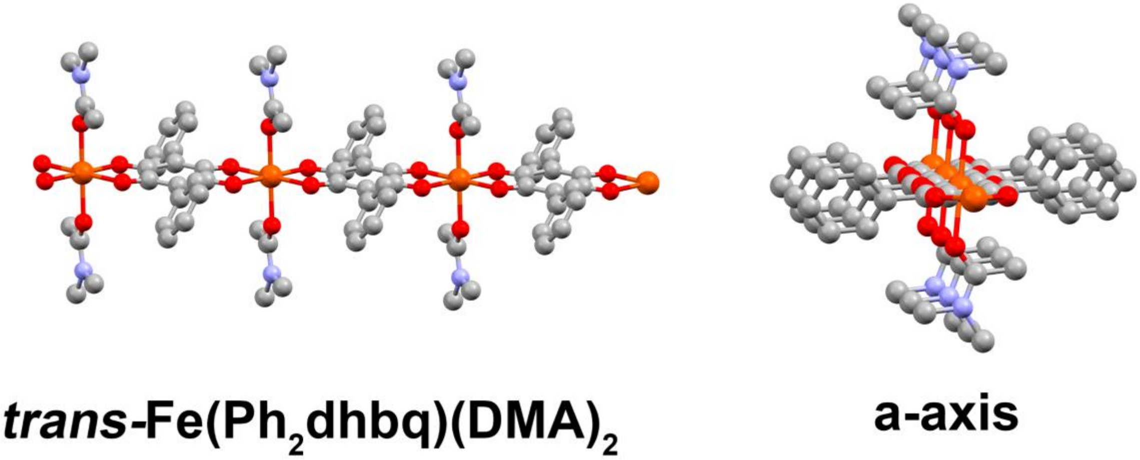

Figure 4.2. (*left*) SCXRD Structure of *trans*-Fe(Ph$_2$dhbq)(DMF)$_2$ collected at 250 K. (*right*) View of the linear chain structure of *trans*-Fe(Ph$_2$dhbq)(DMF)$_2$ viewed along the crystallographic a-axis. Hydrogens have been omitted for clarity.

Results and Discussion

DC Magnetic Susceptibility

The magnetic behavior of each chain system was probed using direct-current (dc) magnetic susceptibility measurements to test how these distributions affect the magnetic properties. We discuss *cis*-Fe(Ph$_2$dhbq)(DMF)$_2$ first. Consistent with the valence tautomerism observed by both X-ray crystallography and Mössbauer spectroscopy, dc magnetic susceptibility measurements of *cis*-Fe(Ph$_2$dhbq)(DMF)$_2$ show strong temperature-dependent magnetic behavior (**Fig. 4.3**). At 300 K, $\chi_M T$ = 3.59 cm^{3}K/mol which is consistent with the expected value for uncoupled high-spin

Fe(II) ions ($S = 2$). As the temperature is decreased, a sigmoidal feature centered at 202.5 K is observed and $\chi_M T$ increases rapidly to 10.4 cm^{3}K/mol at 194 K. This feature is consistent with valence tautomerization between high-spin Fe^{II} with Ph$_2$dhbq^{2-} and high-spin Fe^{III} with Ph$_2$dhbq$^{3\bullet-}$

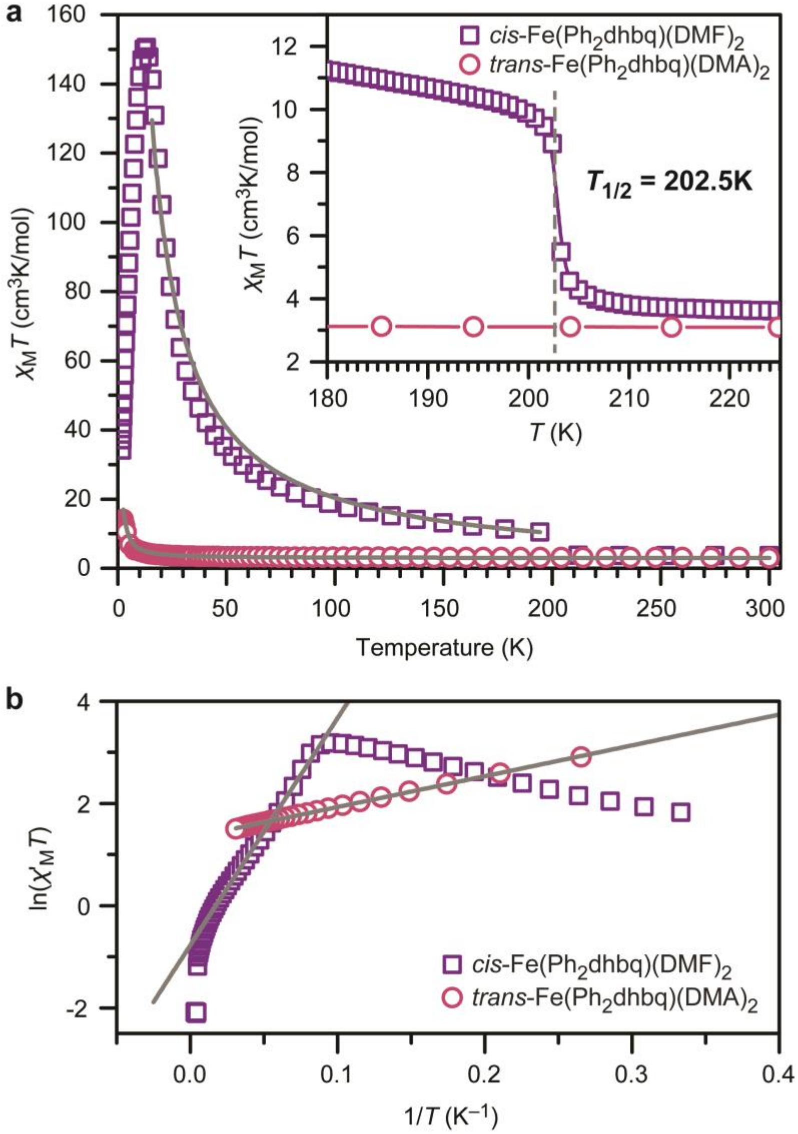

Figure 4.3. (a) Dc magnetic susceptibility ($\chi_M T$) measurements for *cis*-Fe(Ph$_2$dhbq)(DMF)$_2$ (purple) and *trans*-Fe(Ph$_2$dhbq)(DMA)$_2$ (pink) under an applied field of 1000 G. The solid black lines are best fits with $J_{cis} = -230$ cm^{-1} and $J_{trans} = +0.30$ cm^{-1}. Inset: zoom in of the valence tautomerization temperature ($T_{1/2}$) of the *cis* chain. **(b)** Variable-temperature zero-field dc magnetic susceptibility (χ_M') of *cis*-Fe(Ph$_2$dhbq)(DMF)$_2$ and *trans*-Fe(Ph$_2$dhbq)(DMA)$_2$. The gray lines are linear fits that yield correlation lengths of 14 for the *cis* chain and 6 for the *trans* chain. Data were collected at zero dc field with an applied ac field frequency of 1 Hz. See main text and Appendix C for fitting details.

. A similar feature was observed by Harris *et al.* at the valence tautomerization transition temperature ($T_{1/2}$) of the related chain, $(Me_4N)_2[Fe(Cl_2dhbq)Cl_2]$.

The presence of the ligand radical, $Ph_2dhbq^{3\bullet-}$, at lower temperatures should give rise to strong metal–ligand magnetic coupling. Indeed, below the valence tautomerization transition of *cis*-$Fe(Ph_2dhbq)(DMF)_2$, the value of χ_MT exceeds the value expected for uncoupled high-spin Fe^{III} ($S = {}^5/_2$) with $Ph_2dhbq^{3\bullet-}$ radicals ($S = {}^1/_2$). This indicates that magnetic coupling between the metal ions and ligand radicals is enabled as soon as valence tautomerization takes place. The best simulations of this data suggest a strong, antiferromagnetic metal–radical exchange coupling constant of $J = –230$ cm^{-1}. Due to the differing numbers of unpaired electrons on the metal versus the ligand, the χ_MT increases with decreasing temperature, reaching a maximum at 13 K (χ_MT_{Max} = 150 cm^{3}K/mol). In the case of single-chain magnets, this increase in susceptibility is indicative of an increasing intrachain spin correlation length (2ξ) between domain walls.[39] Below 13 K, the magnetic behavior becomes governed by defect sites that limit the chain growth.[40] As this chain growth becomes limited, χ_MT decreases precipitously, reaching 34 cm^{3}K/mol at 1.8 K.

To the best of our knowledge, the magnitude of the exchange coupling constant observed in *cis*-$Fe(Ph_2dhbq)(DMF)_2$ ($J = –230$ cm^{-1}) is the largest reported for a single-chain magnet and is almost three times that observed for $(Me_4N)_2[Fe(Cl_2dhbq)Cl_2]$ ($J = –81$ cm^{-1}).[6,41,42] The relative increase in the magnitude of the exchange coupling constant observed in chains constructed from Ph_2dhbq verses Cl_2dhbq may be attributable to improved orbital overlap between the metal ion and ligand radicals.[43] While the average Fe–O bond lengths can be assigned to Fe^{III} in both cases, the Fe–O bond length in *cis*-$Fe(Ph_2dhbq)(DMF)_2$ is 1.991(13) Å, which is shorter than the value of 2.027(2) Å observed in the Cl_2dhbq chain, which should promote stronger magnetic coupling.[6]

In contrast to the *cis* chain, dc magnetic susceptibility measurements of *tran*s-Fe(Ph_2dhbq)(DMA)$_2$ exhibit no valence tautomerism. Instead, the susceptibility data reflect the expected behavior for a chain of ferromagnetically-coupled Fe^{II} centers (**Fig. 4.3**). Best fits to the data suggest a modest ferromagnetic exchange coupling, with $J = +0.30$ cm^{-1}. *Trans*-Fe(Ph_2dhbq)(DMA)$_2$Br$_{0.55}$ exhibits similar magnetic behavior to *trans*-Fe(Ph_2dhbq)(DMA)$_2$, neither of which display the valence tautomerization behavior of the cis chain (**Fig. C9**). Based on the Mössbauer analysis, the DC susceptibility of *trans*-Fe(Ph_2dhbq)(DMA)$_2$Br$_{0.55}$ was fit assuming an intermediate spin ($S = 2.25$). Best fits yielded an exchange coupling value ($J = +0.64$ cm^{-1}) similar in magnitude to *trans*-Fe(Ph_2dhbq)(DMA)$_2$, yet still small relative to *cis*-Fe(Ph_2dhbq)(DMF)$_2$.

Magnetic hysteresis was not observed for any of the chains (See Fig. C9-C11), and charging curves reveal negligible interchain interaction to be present (See Fig. C12-C14).

AC Magnetic Susceptibility

Alternating current (ac) magnetic susceptibility measurements of all chains were performed at zero applied magnetic field to test for slow magnetic relaxation of the coupled chains and to provide a second quantification of the magnetic coupling. The out-of-phase ac susceptibility (χ_M”) data show slow magnetic relaxation for both *cis*-Fe(Ph_2dhbq)(DMF)$_2$ and *trans*-Fe(Ph_2dhbq)(DMA)$_2$, as evidenced by a peak appearing between frequencies of 1 and 1500 Hz which shifts to higher frequencies with increasing temperature (Figs. C1–C3). However, the relative intensity of χ_M'' to χ_M' in both *cis*-Fe(Ph_2dhbq)(DMF)$_2$ and *trans*-Fe(Ph_2dhbq)(DMA)$_2$ suggests that most of the sample is not undergoing slow relaxation. In addition to the weak signal, the broadness and asymmetry of the observed peaks indicates a wide window of accessible relaxation times, likely due to polydispersity in coupled chain lengths.

The in-phase ac susceptibility (χ_M'), measured as a function of temperature at a fixed ac frequency (the 'zero-field DC susceptibility'), reveals the effective lengths of the chains in these solids (**Figs. 4.5, C9**) when plotted as $\ln(\chi_M'T)$ versus $1/T$.[39,44] Here, the linear region was fit (see Appendix C for details) to yield the domain wall energy (Δ_ξ). These values are considerably larger for the *cis* chain versus the *trans* chains, with 37 cm^{-1} for *cis*-$Fe(Ph_2dhbq)(DMF)_2$ and 6 cm^{-1} for *trans*-$Fe(Ph_2dhbq)(DMA)_2$. The extension of the chains with increased exchange coupling follows expectations for single-chain magnet materials.[39,44] Likewise, *trans*-$Fe(Ph_2dhbq)(DMA)_2Br_{0.55}$, exhibits a larger domain wall energy 12 cm^{-1}, relative to the undoped chain, which is expected given the increased exchange coupling.

The correlation length (n) was determined as described in Appendix C and gives the average number of contiguous metal ions coupled via the exchange interaction (J). As expected, for the *cis* chain we obtain n = 12 while *trans*-$Fe(Ph_2dhbq)(DMA)_2$ yields n = 4. Interestingly, the doped *trans*-$Fe(Ph_2dhbq)(DMA)_2Br_{0.55}$ yields the same correlation length as the undoped (n = 4), despite possessing larger exchange coupling as well as a larger domain wall energy. Overall, the magnetic characterization demonstrates clear differences between each of the three chains. While none of the chains behave as a true "single chain magnet", there is evidence of long range ordering in all samples, and a rare example of valence tautomerization in *cis*-$Fe(Ph_2dhbq)(DMF)_2$.

Conclusion

The combined synthetic and characterization efforts described above provide a new perspective on the rational design of extended materials incorporating tetraoxolene linkers. Although previous studies have shown that changes to the metal-ion and tetraoxolene ligand greatly impact electronic structure and magnetic behavior,[17,50] this work shows that dramatic changes in magnetic properties can be observed even when the metal and bridging ligand identities remain constant. Slight alterations of the chain geometry are sufficient to change the preferred distribution of oxidation states across the metal-bridge linkages, turning on properties such as valence tautomerism and strong magnetic coupling.

References

1. C. G. Pierpont and R. M. Buchanan, Coordination Chemistry Reviews, 1981, 38, 45–87.

2. W. P. Griffith, Transition Met Chem, 1993, 18, 250–256.

3. C. G. Pierpont, Coordination Chemistry Reviews, 2001, 216–217, 99–125.

4. E. Evangelio and D. Ruiz-Molina, European Journal of Inorganic Chemistry, 2005, 2005, 2957–2971.

5. T. Tezgerevska, K. G. Alley and C. Boskovic, Coordination Chemistry Reviews, 2014, 268, 23–40.

6. J. A. DeGayner, K. Wang and T. D. Harris, J. Am. Chem. Soc., 2018, 140, 6550–6553.

7. A. Dei, D. Gatteschi, L. Pardi and U. Russo, Inorg. Chem., 1991, 30, 2589–2594.

8. I.-R. Jeon, B. Negru, R. P. Van Duyne and T. D. Harris, J. Am. Chem. Soc., 2015, 137, 15699–15702.

9. J. A. DeGayner, I.-R. Jeon, L. Sun, M. Dincă and T. D. Harris, J. Am. Chem. Soc., 2017, 139, 4175–4184.

10. M. Hmadeh, Z. Lu, Z. Liu, F. Gándara, H. Furukawa, S. Wan, V. Augustyn, R. Chang, L. Liao, F. Zhou, E. Perre, V. Ozolins, K. Suenaga, X. Duan, B. Dunn, Y. Yamamto, O. Terasaki and O. M. Yaghi, Chem. Mater., 2012, 24, 3511–3513.

11. L. E. Darago, M. L. Aubrey, C. J. Yu, M. I. Gonzalez and J. R. Long, J. Am. Chem. Soc., 2015, 137, 15703–15711.

12. L. S. Xie, G. Skorupskii and M. Dincă, Chem. Rev., 2020, 120, 8536–8580.

13. E. M. Miner, L. Wang and M. Dincă, Chem. Sci., 2018, 9, 6286–6291.

14. M. E. Ziebel, C. A. Gaggioli, A. B. Turkiewicz, W. Ryu, L. Gagliardi and J. R. Long, J. Am. Chem. Soc., 2020, 142, 2653–2664.

15. J. W. Gittins, C. J. Balhatchet, Y. Chen, C. Liu, D. G. Madden, S. Britto, M. J. Golomb, A. Walsh, D. Fairen-Jimenez, S. E. Dutton and A. C. Forse, J. Mater. Chem. A, 2021, 9, 16006–16015.

16. S. Kitagawa and S. Kawata, Coordination Chemistry Reviews, 2002, 224, 11–34.

17. M. L. Mercuri, F. Congiu, G. Concas and S. A. Sahadevan, Magnetochemistry, 2017, 3, 17.

18. S. Benmansour, A. Abhervé, P. Gómez-Claramunt, C. Vallés-García and C. J. Gómez-García, ACS Appl. Mater. Interfaces, 2017, 9, 26210–26218.

19. C. J. Kingsbury, B. F. Abrahams, D. M. D'Alessandro, T. A. Hudson, R. Murase, R. Robson and K. F. White, Crystal Growth & Design, 2017, 17, 1465–1470.

20. J. Chen, Y. Sekine, Y. Komatsumaru, S. Hayami and H. Miyasaka, Angew. Chem. Int. Ed., 2018, 57, 12043–12047.

21. S. A. Sahadevan, A. Abhervé, N. Monni, C. Sáenz de Pipaón, J. R. Galán-Mascarós, J. C. Waerenborgh, B. J. C. Vieira, P. Auban-Senzier, S. Pillet, E.-E. Bendeif, P. Alemany, E. Canadell, M. L. Mercuri and N. Avarvari, J. Am. Chem. Soc., 2018, 140, 12611–12621.

22. J. Chen, Y. Sekine, A. Okazawa, H. Sato, W. Kosaka and H. Miyasaka, Chem. Sci., 2020, 11, 3610–3618.

23. R. Murase, C. J. Commons, T. A. Hudson, G. N. L. Jameson, C. D. Ling, K. S. Murray, W. Phonsri, R. Robson, Q. Xia, B. F. Abrahams and D. M. D'Alessandro, Inorg. Chem., 2020, 59, 3619–3630.

24. Y. Sekine, J. Chen, N. Eguchi and H. Miyasaka, Chem. Commun., 2020, 56, 10867–10870.

25. M. P. van Koeverden, B. F. Abrahams, D. M. D'Alessandro, P. W. Doheny, C. Hua, T. A. Hudson, G. N. L. Jameson, K. S. Murray, W. Phonsri, R. Robson and A. L. Sutton, Chem. Mater., 2020, 32, 7551–7563.

26. B. F. Abrahams, K. D. Lu, B. Moubaraki, K. S. Murray and R. Robson, J. Chem. Soc., Dalton Trans., 2000, 1793–1797.

27. P. R. Shildneck and Roger. Adams, J. Am. Chem. Soc., 1931, 53, 2373–2379.

28. R. L. Frank, G. R. Clark and J. N. Coker, J. Am. Chem. Soc., 1950, 72, 1827–1829.

29. Ch. Robl and A. Weiss, Zeitschrift für anorganische und allgemeine Chemie, 1987, 546, 152–160.

30. C. Robl and W. F. Kuhs, Journal of Solid State Chemistry, 1988, 74, 21–26.

31. K. Heinze, G. Huttner, L. Zsolnai, A. Jacobi and P. Schober, Chemistry – A European Journal, 1997, 3, 732–743.

32. A. Garci, J.-P. Mbakidi, V. Chaleix, V. Sol, E. Orhan and B. Therrien, Organometallics, 2015, 34, 4138–4146.

33. B. F. Abrahams, T. A. Hudson, L. J. McCormick and R. Robson, Crystal Growth & Design, 2011, 11, 2717–2720.

34. L. Wang, R. J. Papoular, N. E. Horwitz, J. Xie, A. Sarkar, D. Campisi, N. Zhao, B. Cheng, G. L. Grocke, T. Ma, A. S. Filatov, L. Gagliardi and J. S. Anderson, Angew Chem Int Ed, , DOI:10.1002/anie.202207834.

35. A. L. Spek, Acta Cryst C, 2015, 71, 9–18.

36. A. I. Gaudette, I.-R. Jeon, J. S. Anderson, F. Grandjean, G. J. Long and T. D. Harris, J. Am. Chem. Soc., 2015, 137, 12617–12626.

37. K. D. Demadis, C. M. Hartshorn and T. J. Meyer, Chem. Rev., 2001, 101, 2655–2686.

38. D. M. D'Alessandro and F. R. Keene, Chem. Soc. Rev., 2006, 10.1039.b514590m.

39. C. Coulon, H. Miyasaka and R. Clérac, in Single-Molecule Magnets and Related Phenomena, ed. R. Winpenny, Springer, Berlin, Heidelberg, 2006, pp. 163–206.

40. K. S. Pedersen, A. Vindigni, R. Sessoli, C. Coulon and R. Clérac, in Molecular Magnetic Materials, John Wiley & Sons, Ltd, 2017, pp. 131–159.

41. T. J. Woods, H. D. Stout, B. S. Dolinar, K. R. Vignesh, M. F. Ballesteros-Rivas, C. Achim and K. R. Dunbar, Inorg. Chem., 2017, 56, 12094–12097.

42. X. Liu, X. Feng, K. R. Meihaus, X. Meng, Y. Zhang, L. Li, J.-L. Liu, K. S. Pedersen, L. Keller, W. Shi, Y.-Q. Zhang, P. Cheng and J. R. Long, Angewandte Chemie, 2020, 132, 10697–10705.

43. C. Hua, J. A. DeGayner and T. D. Harris, Inorg. Chem., 2019, 58, 7044–7053.

44. H. Miyasaka, M. Julve, M. Yamashita and R. Clérac, Inorg. Chem., 2009, 48, 3420–3437.

45. L. S. Xie, L. Sun, R. Wan, S. S. Park, J. A. DeGayner, C. H. Hendon and M. Dincă, J. Am. Chem. Soc., 2018, 140, 7411–7414.

46. R. Murase, C. F. Leong and D. M. D'Alessandro, Inorg. Chem., 2017, 56, 14373–14382.

47. M. E. Ziebel, L. E. Darago and J. R. Long, J. Am. Chem. Soc., 2018, 140, 3040–3051.

CHAPTER FIVE – Weakly Exchange Coupled, Dinuclear Complexes of Cu(II) as Low-Frequency EPRI Probes

Overview

Developing next-generation Electron Paramagnetic Resonance Imaging (EPRI) probes is essential to the advancement of diagnostic medical imaging. In this work, we propose a novel design principle for EPRI probes incorporating weakly exchange coupled, first-row transition metals. We show that for select dinuclear systems, the spin-forbidden singlet-triplet (ST) transition is EPR visible. Modification of the secondary coordination sphere of $[Cu_2CA(tpy)_2][X]$ ($X = PF_6$, ClO_4, Cl) produces subtle changes in the metal-metal exchange coupling (*J*) and consequently in the position of the ST forbidden transition. The tunability of this transition via synthetic modification will help enable the development of EPRI probes with predictable transitions in the magnetic field range of modern MRI instruments (Fig. 5.1). [1]

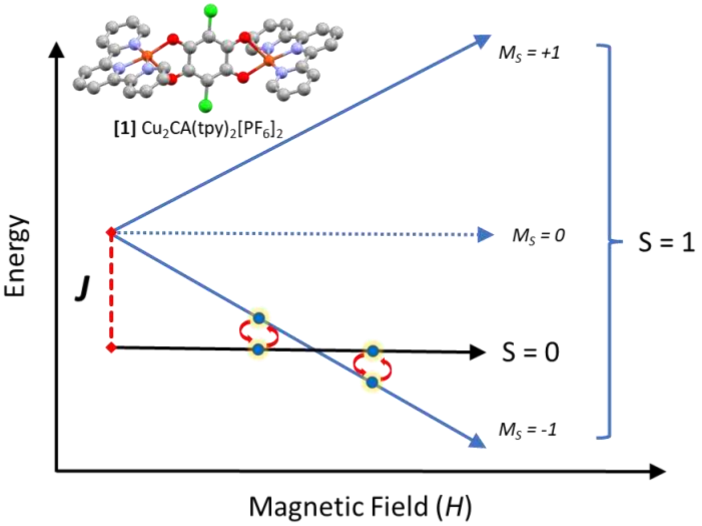

Figure 5.1. Graphical depiction of the target singlet-triplet spin forbidden transitions observed for the dinuclear complex $[Cu_2CA(tpy)_2][PF_6]_2$ (hydrogens and counterion omitted for clarity).

Introduction

Magnetic Resonance Imaging (MRI) is a powerful diagnostic technique which utilizes the relaxation of nuclear spins in an applied magnetic field to produce highly detailed images of the human body.[2] Although MRI is an indispensable tool for medical professionals, it is not able to provide detailed information about the chemical processes within the body. The ability to obtain real time, spatial resolution of chemical phenomena such as O_2 concentration, pH, and temperature within the human body could enable physicians to quickly diagnose and begin treatment rather than waiting for biopsy results or relying on invasive surgery.[3] Electron paramagnetic resonance imaging (EPRI), the electron spin analogue to MRI, may eventually enable this kind of chemically informed imaging.[4,5]

Compared to nuclear spins, electronic spins are more sensitive to their environment. This sensitivity is due in part to their larger magnetic moments, and their ability to delocalize across a molecule. As a result, subtle changes in pH, the concentration of O_2 radicals, and local temperature have measurable impacts on the relaxation behaviour of electronic spins.[1] This sensitivity can be leveraged to enable real-time imaging of biochemical and physiological processes not currently possible with MRI alone. EPRI relies on microwaves to achieve resonance between electronic spin states. Microwaves, unlike radio waves, are readily absorbed by water, and as a result, the penetration depth of the most common EPR frequency (X-Band: ~9.8 GHz) is only a few millimetres.[6] In order to increase the penetration depth of EPRI, lower frequency microwaves, on the order of 1 GHz can be employed. This lower frequency, referred to as the “L-Band” offers penetration depths up to 30mm, but at the cost of decreased signal to noise.[7] Additionally, current EPRI techniques operate exclusively at low-magnetic field strengths (~1000 G) well below the operating fields of modern MRI. Towards our goal of merging MRI and EPRI, new spin probes must be developed to produce low-frequency, high-field transitions.

Molecules with two $S = ½$ spins possess a unique yet unexplored magnetic resonance feature that could be harnessed to enable low-frequency EPR at high magnetic fields (Fig. 5.1). In a two-spin system, the spin centers can interact with each other through the superexchange coupling mechanism.[8–11] The coupling strength of this interaction, denoted by J, can vary over many orders of magnitude, and is readily tuned by synthetic modification, specifically, the coupled spins and molecular spacers separating them.[12] If the superexchange coupling is ferromagnetic, the two spins will align to produce a spin triplet state, $S = 1$. If the two spins are coupled antiferromagnetically, in contrast, they will cancel and yield a singlet, $S = 0$ state. With increasing magnetic field, the M_S levels for the triplet state will split owing to the Zeeman interaction, thus, with increasing field, an MS level of the triplet will eventually cross the $S = 0$ state. This crossing will uniquely enable very low-frequency EPR spectroscopy near that field, which is tunable by J.

Before this transition can be realized in EPRI imaging applications, we need to develop a better understanding of the chemical and electronic factors which influence it. To date, the ST transition has been observed for a small number of systems, but no investigations have attempted to develop new design principles for observing the ST transition in new compounds. The work presented in this chapter represents our initial efforts at elucidating these design principles towards the development of next generation EPRI probes.

Herein, we present the preliminary results of our investigation of the tunability of the singlet-triplet spin forbidden resonance in two families of dinuclear copper(II) ($S = 1$) complexes. Specifically, we examine the influence of the secondary coordination sphere on the EPR spectra of $[Cu_2CA(tpy)_2][X^-]_2$ (X = PF_6, ClO_4, Cl) (CA = chloranilic acid), as well as the effects of modifying the electronic structure of the auxiliary terpyridine ligand. Finally, we present preliminary findings for the series of complexes of the form $[Cu_2(tren)_2(XCN)_2][BPh_4]_2$ (X = O or S) (tren = Tris(2-aminoethyl)amine). Towards investigating the counterion dependence of the ST resonance, we reasoned that, given the close proximity of the counter ions to the Cu(II) ions in the crystal structure, introducing smaller, more coordinating ions should alter the electronic structure of the Cu(II) ions, in turn modifying the superexchange coupling (J). From our preliminary investigations, we demonstrate that changing the counter ion does impact the exchange coupling and subsequently the ST transition. However, as we will discuss, there are also additional, less well understood factors which determine the strength and "allowedness" of this transition.[13]

Experimental Section

General Considerations

All reagents were purchased from commercial sources and used as received. Synthesis followed established literature procedures as noted throughout. All techniques were performed under atmospheric conditions unless stated otherwise. Infrared spectra were recorded on a Nicolet 6700 FTIR spectrometer using a diamond window ATR. Diffuse reflectance data was collected on a Shimadzu UV 2600i UV-Vis Spectrometer using the ISR-2600 integrating sphere attachment.

Preparation of Compounds

General Notes: Reaction pH was observed to play an important role in all below synthesis. Using anything other than a calibrated pH probe resulted in various degrees of speciation and failed to produce diffraction quality crystals in all cases. Additionally, substituting KOH for either NaOH or NEt_3 produced undesirable products and little to no desired product.

Synthesis of 1,5-Bis(2'-pyridyl)pentane-1,3,5-trione: Synthesis followed literature procedure as described previously.[14] Inside a N_2 filled glovebox, a large addition funnel was charged with 25g of ethyl-2-piclanate, 3.2 g degassed anhydrous acetone, and 110mL of degassed anhydrous THF. Meanwhile, a large 3-neck flask was charged with 110mL of THF and 3.96 g NaH, and subsequently fitted with the addition funnel, a reflux condenser, and a glass stopper. The reaction was sealed and moved onto a Schlenk line and the NaH suspension was heated to reflux with stirring (90℃). Once refluxing, the addition funnel was gradually opened, and the contents were added dropwise to the NaH suspension over the course of 4 hours. The reaction was left to reflux overnight, and upon cooling the solvent was removed *in vacuo* yielding an orange/brown paste. The paste was carefully treated with ~100mL of H_2O to quench any remaining NaH and the resulting solution was filtered over celite and then adjusted to pH 7 by slow addition of ~5mL of 12N HCl resulting in precipitation of an orange/yellow solid. The hygroscopic solid (1,5-Bis(2'-pyridyl)pentane-1,3,5-trione) was dissolved in Et_2O and dried *in vacuo* before being stored over dri-rite. Purity of the trione was confirmed via ^{1}H-NMR (98.2 %)[14].

Synthesis of 4'-OH-tpy: Synthesis followed literature procedure as described previously.[15] 2.0 g of the yellow solid (1,5-Bis(2'-pyridyl)pentane-1,3,5-trione) was dissolved in 50 mL anhydrous ethanol with 4.0 g of ammonium acetate and heated to reflux for 6 hours. The solution was then reduced in volume by heating until ~25 mL remained. The resulting dark brown/black solution was cooled slowly to room temperature, and semicrystalline precipitate was collected via filtration as the solution continued to cool. The isolated solids were washed with cold Et_2O and recrystallized from anhydrous ethanol to yield the desired product as off-white needles (1.42 g 78% yield). Purity was confirmed via ^{1}H-NMR (97.4 %)[15].

Synthesis of [$Cu_2CA(tpy)_2$][ClO_4]$_2$ (**1**): **1** was synthesized as described previously with minor modifications.[16] 296 mg of $Cu(ClO_4)\cdot 6H_2O$ in 25 mL of HPLC grade H_2O was heated to 80 ℃ with stirring. To this solution was added 187 mg of 2,2';6',2''-terpyridine (tpy) dissolved in 15mL of warm acetone. In a separate flask, 84 mg of chloranilic acid (CA) was dissolved in 50 mL of HPLC grade H_2O heated to 80℃. The CA solution was then slowly added to the first solution with stirring and heating resulting in precipitation of a gray-blue precipitate which was collected on a glass frit via vacuum filtration and allowed to dry before being stored at ambient conditions (302 mg).

Synthesis of [$Cu_2CA(tpy)_2$][PF_6]$_2$ (**2**): **2** was synthesized as described previously with minor modifications.[16] 296 mg of $Cu(ClO_4)\cdot 6H_2O$ in 25 mL of HPLC grade H_2O was heated to 80 ℃ with stirring. To this solution was added 187 mg of 2,2';6',2''-terpyridine (tpy) dissolved in 15mL of warm acetone. In a separate flask, 84 mg of chloranilic acid (CA) was dissolved in 50 mL of HPLC grade H_2O heated to 80℃. The CA solution was then slowly added to the first solution with stirring and heating. To this solution was added 2 mol eq. of KPF_6 (0.8mmol) resulting in precipitation of a gray-blue precipitate which was collected on a glass frit via vacuum filtration and allowed to dry before being stored at ambient conditions (371 mg).

Synthesis of [$Cu_2CA(tpy)_2$][PF_6]$_2$ (**2'**): **2'** was obtained as described previously with minor modifications.[16] 296 mg of $Cu(ClO_4)\cdot 6H_2O$ in 25 mL of HPLC grade H_2O was heated to 80℃ with stirring. To this solution was added 187 mg of 2,2';6',2''-terpyridine (tpy) dissolved in 15 mL of warm acetone. The resulting solution was left at 90 ℃ for ~1 hour to remove acetone, and the resulting solution was adjusted to pH 8 by slow addition of ~1 mL of 1 M aqueous KOH. In a separate flask, 84 mg of chloranilic acid (CA) was dissolved in 50 mL of HPLC grade H_2O heated to 80℃. The pH of the CA solution was adjusted to pH 11 via slow addition of ~0.5 mL of 1 M aqueous KOH. The resulting CA solution was added with stirring and heating to the solution containing $Cu(ClO_4)\cdot 6H_2O$ and tpy to produce a purple-blue solution. To this solution was added 0.8 mmol KPF_6. The final solution was filtered through a glass frit and transferred into a small recrystallization dish. Single crystals suitable for diffraction were obtained over the course of 2 days of slow evaporation. Isolated crystals are small (~0.2 mm side length) and dark-purple in colour with a rectangular geometry (389 mg).

Synthesis of $[Cu_2CA(tpy)_2][Cl]_2$ (**3**): **3** was synthesized by adapting the synthesis for **1** as follows. 136 mg of $CuCl_2\cdot 2H_2O$ in 25 mL of HPLC grade H_2O was heated to 80℃ with stirring. To this solution was added 187 mg of 2,2';6',2''-terpyridine (tpy) dissolved in 15mL of warm acetone. In a separate flask, 84 mg of chloranilic acid (CA) was dissolved in 50 mL of HPLC grade H_2O heated to 80℃. The CA solution was then slowly added to the first solution with stirring and heating resulting in precipitation of a gray-blue precipitate which was collected on a glass frit via vacuum filtration and allowed to dry before being stored at ambient conditions (267 mg).

Synthesis of $[Cu_2CA(4'OH\text{-}tpy)_2]$ (**4**): **4** was obtained by adapting the synthesis for **2'** as follows. 136 mg of $CuCl_2\cdot 2H_2O$ in 25 mL of HPLC grade H_2O was heated to 80℃ with stirring. To this solution was added 199 mg of 4'-OH-tpy dissolved in 15mL of warm acetone, producing a viscous precipitate almost immediately. The resulting suspension was left at 90℃ for ~1 hour to remove acetone, and the resulting suspension was adjusted to pH 8 by slow addition of ~1mL of

1M aqueous KOH resulting in a dark green solution. In a separate flask, 84 mg of chloranilic acid (CA) was dissolved in 50 mL of HPLC grade H_2O heated to 80℃. The pH of the CA solution was adjusted to pH 11 via slow addition of ~0.5 mL of 1M aqueous KOH. The resulting CA solution was added with stirring and heating to the solution containing $CuCl_2 \cdot 2H_2O$ and tpy to produce a purple-blue solution. To this solution was added 0.8mmol KPF_6. The final solution was filtered through a glass frit and transferred into a small recrystallization dish. Single crystals suitable for diffraction were obtained over the course of 2 days of slow evaporation (296 mg). Isolated crystals are small (~0.2mm side length) and dark-purple in colour with a rectangular geometry.

X-Ray Diffraction, Structure Solving, and Refinement

All single crystal diffraction data were collected at the X-Ray diffraction facility in the Analytical Resources Core at Colorado State University using a Bruker D8 QUEST SCXRD equipped with Mo Kα source. Data were collected, integrated, and scaled using the Bruker APEX software. Absorption corrections were applied using SADABS. Space group assignments were determined by examination of systematic absences, E-statistics, and successive refinement of the structures. Crystal structures were solved using SHELXT and refined with the aid of successive difference Fourier maps by SHELXL via the OLEX2 software package.[17–19] None of the samples showed signs of decay by x-ray radiation over the course of the experiment. Hydrogen atoms were placed in ideal positions and refined using a riding model for all structures.

Powder X-Ray Diffraction

Powder X-Ray Diffraction patterns were obtained using a Bruker D8 Davinci diffractometer utilizing the LYNXEYE detector and a CuKα radiation source at 1600W (40 kV, 40mA). Samples were prepared by grinding crystalline or polycrystalline material with an agate mortar and pestle. The powdered samples were then loaded onto a zero diffraction Si wafer covered in a thin, uniform layer of vacuum grease, before being inverted to remove any excess powdered material. All patterns were collected from 2θ = 5-50˚, with a 0.02˚ increment, and a 1 sec exposure time.

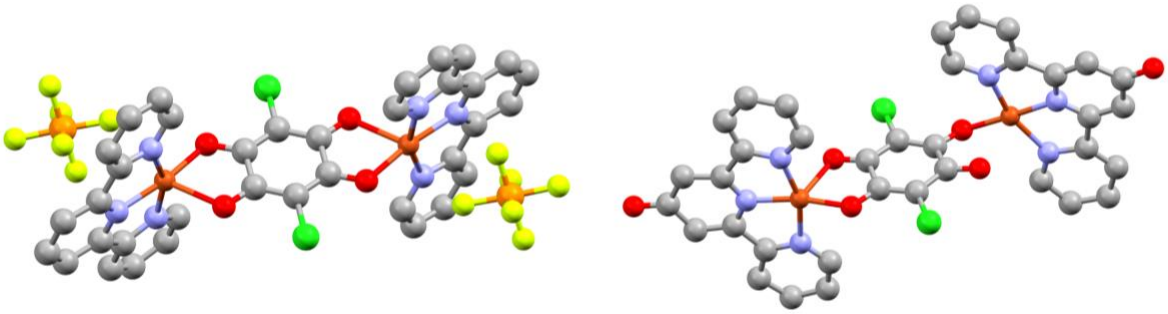

$[Cu_2CA(tpy)_2][PF_6]$ $Cu_2CA(4'\text{-}OH\text{-}tpy)_2$

Figure 5.2. SCXRD structures for **2'** and **4** collected at 100 K. Cu is orange, oxygen is red, nitrogen is blue, chlorine is light green, phosphorus is green, fluorine is yellow, carbon is grey, and hydrogen is white. The full unit cell and solvent molecules have been excluded for clarity.

Electron Paramagnetic Resonance Measurements

X-Band CW Electron paramagnetic resonance spectra were collected on a Bruker ESR-300 spectrometer equipped with a SHQE high-sensitivity resonator and a ColdEdge helium cryostat capable of reaching 5K. L-Band measurements were collected on the same spectrometer equipped with a Flexline, L-Band resonator at room temperature.

Results and Discussion

Compounds **1-4** were synthesized as described above, following literature procedures.[16] The resulting compounds were isolated in good yield as greyish blue powders and characterized by PXRD (Fig. 5.3), NIR spectroscopy (Fig. D1), and X-Band EPR (Fig. 5.4-5.10). The PXRD of compound **2** shows good agreement with the calculated pattern obtained from the SCXRD structure, although several additional small intensity peaks can be seen at lower 2θ (Fig. 5.3). Crystals of **2'** were obtained as described above and were found to be of sufficient quality and size for SCXRD (Fig. 5.2). PXRD of crushed polycrystalline **2'** shows no signs of contamination and agrees well with the calculated powder pattern. Compound **4** was crystallized following methods similar to those employed for **2'**. Single crystals of compounds **1** and **3** were not obtained despite repeated attempts; however, crystalline powders of the described materials display similar properties to **2** and suggest formation of similar dinuclear species. Attempts to crystallize **1** and **3** following the methodology used for **2'** resulted in the formation of crystals of a 2D planar network consisting of chloranilic acid bridged by Na^+ ions, and all subsequent analysis were conducted on polycrystalline samples.

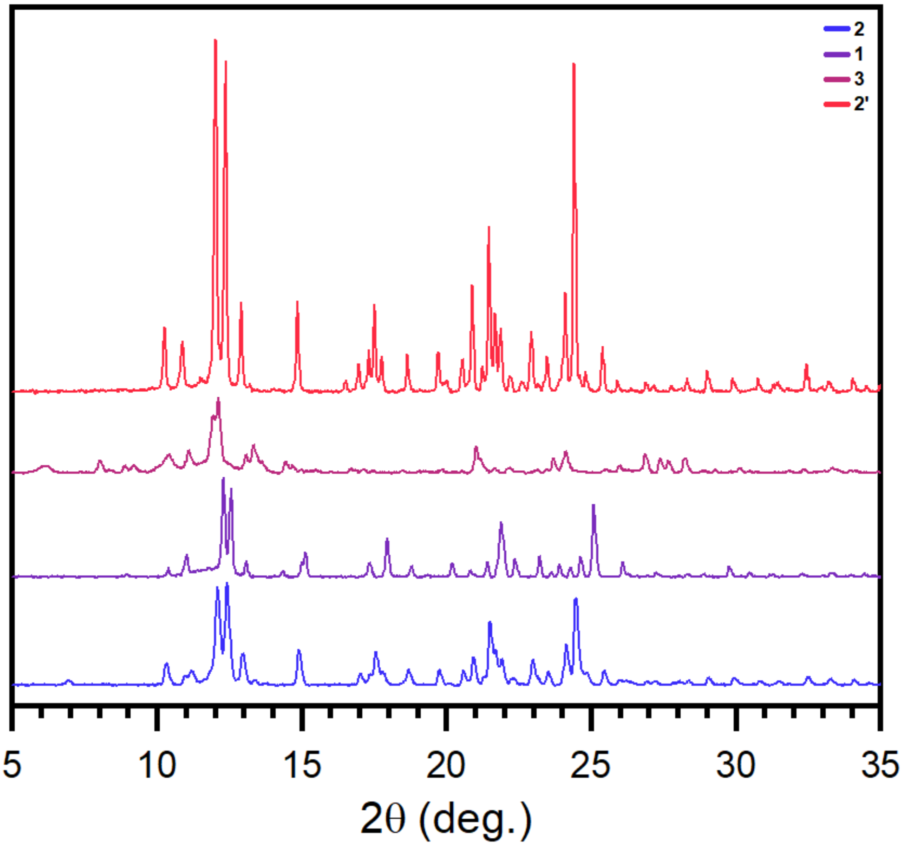

Figure 5.3. Room temperature powder diffraction patterns of **1**, **2**, **2'**, and **3** from 5°– 35° 2θ.

Investigations on the counterion dependence of [$Cu_2CA(tpy)_2$][X]

PXRD Analysis

Compounds **1, 2,** and **3**, the ClO_4, PF_6 and Cl salts of the dinuclear species were synthesized as described above and isolated as crystalline powders. PXRD analysis of the isolated products was compared to the known structure of **2'** (Fig. 5.3). Patterns for **1** and **2** indicate highly similar crystalline environment, as expected based on previous investigations. However, the Cl^- salt (**3**), appears unique among the investigated samples, with very few overlapping peak positions. In addition, the peaks of **3** also appear broader, which may indicate a lesser degree of crystallinity.

EPR Spectroscopy

Room temperature CW X-Band EPR was performed to identify the impacts of counterion on the ST forbidden transition. As expected, EPR of **2** shows good agreement with the previously reported spectra (Fig. 5.4). An asymmetric, high-intensity peak at 350 mT is attributed to the allowed transitions ($\Delta M_S = \pm 1$), which is commonly observed for Cu(II) species.[9,20,21] The asymmetry of this peak suggests anisotropy in the Cu(II) g tensor, which is expected for the non-symmetric ligand field of **2**, although the overlapping resonances at X-Band preclude accurate determination of g anisotropy. Above (450 mT) and below (220 mT) the primary resonance, we observe several lower intensity resonances which are ascribed to the ST forbidden transitions. An additional low field transition (160 mT) is observed which corresponds to the ½ field transition typically seen in S = 1 systems ($\Delta M_S = \pm 2$).[22] The presence of these weak, forbidden transitions indicates the presence of magnetic coupling (J) between adjacent Cu(II) centers, the strength of which can be determined using the following equation.

$$|J| = \frac{\Delta H g \beta}{2}$$

Here J is the exchange coupling constant expressed in wavenumbers, ΔH is the distance between the central ($\Delta M_S = \pm 1$) transition and the ST forbidden transition in G, g is the lande g factor, and β is $1/k_BT$. From this analysis, we find that $J = 0.06\ \mathrm{cm}^{-1}$ for **2** at room temperature, in good agreement with previous investigations.

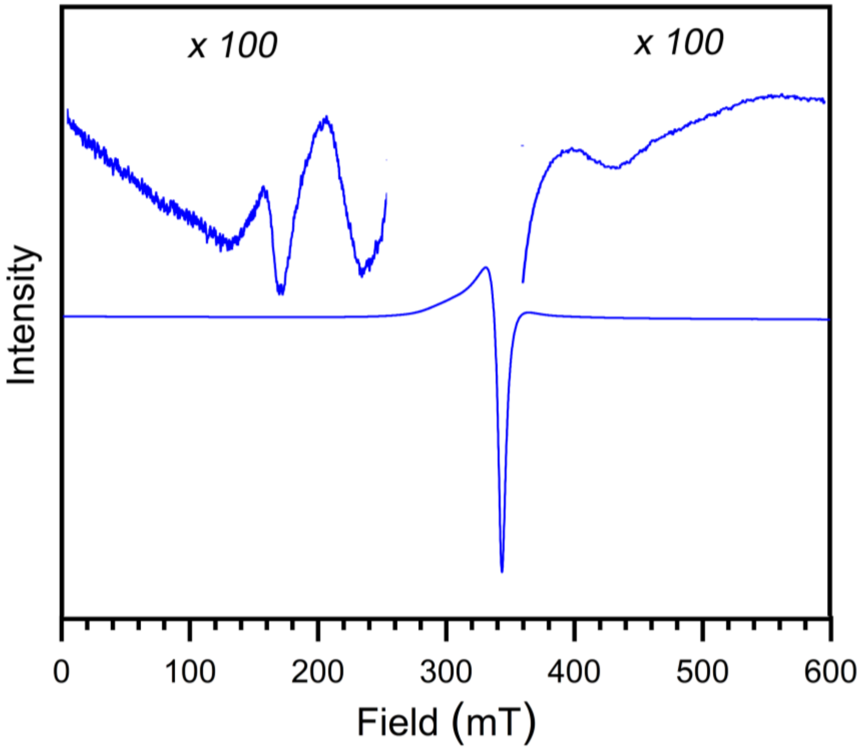

Figure 5.4. CW X-Band (9.8 GHz) EPR of **2** taken at room temperature. High and low field resonances are plotted with increased gain to improve visibility against the intensity of the main transition.

Compared to **2**, both **1** and **3** display the same primary transition (350 mT), indicating similar g anisotropy at the Cu(II) centers (Fig. 5.5). Here, the varying intensity of the peaks is due to sample volume and differences in the degree of coupling in the microwave cavity of the spectrometer. Analysis of the low field, ST transitions suggests that the counterion may have significant impact on Cu(II) coupling strength (Fig 5.5). All three species display the same, half field (ΔMS = ±2) transition (160mT); however, the ST resonance is observed to change dramatically for **3** (90 mT) as compared to **1** and **2** (220 mT). This shift indicates significantly

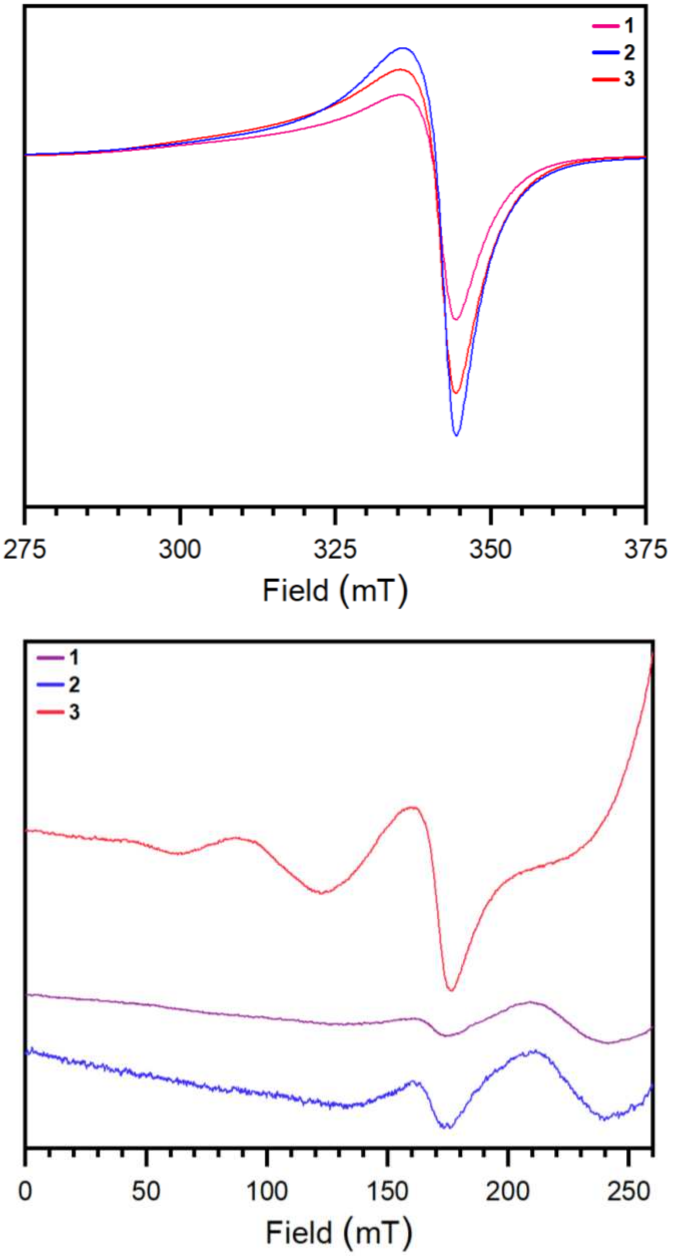

Figure 5.5. (*top*) CW X-Band (9.8 GHz) EPR of **1**, **2**, and **3** from 275 – 325 mT, and (*bottom*) from 0 – 250 mT, highlighting the ST forbidden resonances.

stronger exchange coupling value of $J = 0.11$ cm^{-1} for **3**, almost twice the observed coupling for the other species.

Without the SCXRD structure of **3**, in depth analysis of the exchange coupling variation with counterion is limited to the hypothetical; however, EPR data suggest that counterion may have a direct effect on the Cu(II) exchange coupling. Given the similarities observed for **1** and **2** which both feature larger, non-coordinating ions, it is likely that the smaller, more coordinating Cl$^-$ ion is located closer to the Cu(II) ions in the crystal structure.

Investigations of $[Cu_2CA(tpy)_2][PF_6]_2$ (2 and 2')

CW X-Band EPR analysis of **2'** presents considerable confusion to both previously published investigations as well as the analysis of **2** discussed above (Fig. 5.6). At room

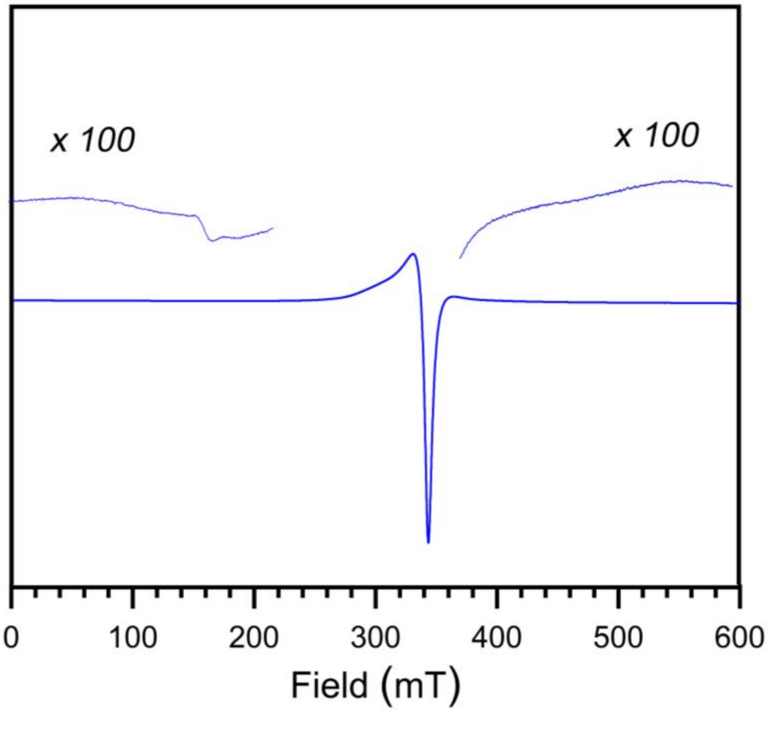

Figure 5.6. CW X-Band (9.8 GHz) EPR of **2'** taken at room temperature. High and low field resonances are plotted with increased gain to improve visibility against the intensity of the main transition.

temperature, the primary transition is the same as observed for **2**, both in field position and relative asymmetry. Surprisingly, the forbidden resonances observed for **2**, are absent for **2'**, with the exception of a very weak half-field transition (175 mT). The presence of the half-field transition suggests coupling between the Cu(II) ions; however, the lack of visible ST transitions is not well understood. One possibility, we reasoned was that the exchange coupling was even weaker for **2'** than for **2**, which could cause the ST resonances to move closer to the central resonance, precluding their observation with room temperature X-Band EPR.

Previously, it was demonstrated for [$Cu_2CA(tpy)_2$][PF_6]2, that the strength of the exchange coupling changes as a function of temperature as a result of the compression and expansion of the crystal lattice. Specifically, the exchange coupling increased (0.45 cm^{-1} – 0.51 cm^{-1}) with

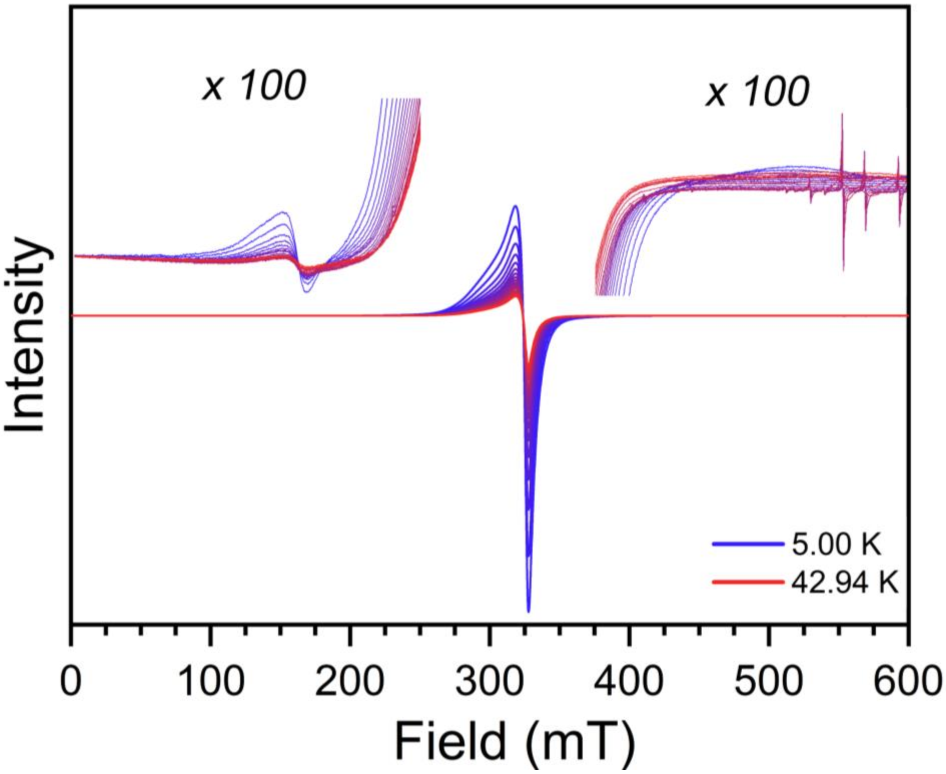

Figure 5.7. Variable temperature CW X-Band (9.8 GHz) EPR of **2'** collected from 5 K – 43 K. High and low field resonances are plotted with increased gain to improve visibility against the intensity of the main transition. Sharp, high-field resonances are indicative of oxygen contamination in the cryostat and are not a result of sample preparation.

increasing temperature (350 K - 450 K). Below 350 K, the transitions were no longer observable at X-Band, obscured by the central transition. Presently, our EPR facilities are capable of low temperature cryogenic measurements down to 5 K; however, no elevated temperature measurements are possible. Variable temperature CW X-Band EPR measurements of **2’** were collected from 5 K – 43 K to see if the missing ST transitions were temperature dependent (Fig. 5.5). In addition to the aforementioned lattice effects, low temperature measurements improve signal to noise and can resolve weaker signals not observable at room temperature. Despite this improved signal to noise, no additional signals were observed for **2’** at any of the recorded temperatures. The half-field transition (160 mT) is well resolved and does not shift with varying temperature. The absent ST transitions are presently not well understood, and merit future investigation to determine the nature of Cu(II) exchange coupling in **2’** and why it deviates from both previously recorded examples. In particular, high temperature CW X-Band EPR may expose the ST transitions if they are in fact obscured by the central transition.

Despite the unclear nature of the ST transitions in **2’**, the observation of the desired resonances for **2** prompted us to continue our investigations towards the development of L-Band EPRI probes. Room temperature CW L-Band (1.3 GHz) EPR spectroscopy of **2** was conducted in an attempt to visualize ST transitions at low frequency, which to the best of our knowledge have not been previously observed. Based on the exchange coupling value obtained from X-Band analysis, the ST Resonance should appear between 150 – 250 mT at L-Band (1.3 GHz) (Fig. 8). Room temperature CW L-Band EPR spectra of **2**, show a single, asymmetric peak (25 mT) which corresponds to the $\Delta M_S = \pm 1$ transition. No ST forbidden transition were observed, despite extended scan times and signal averaging.

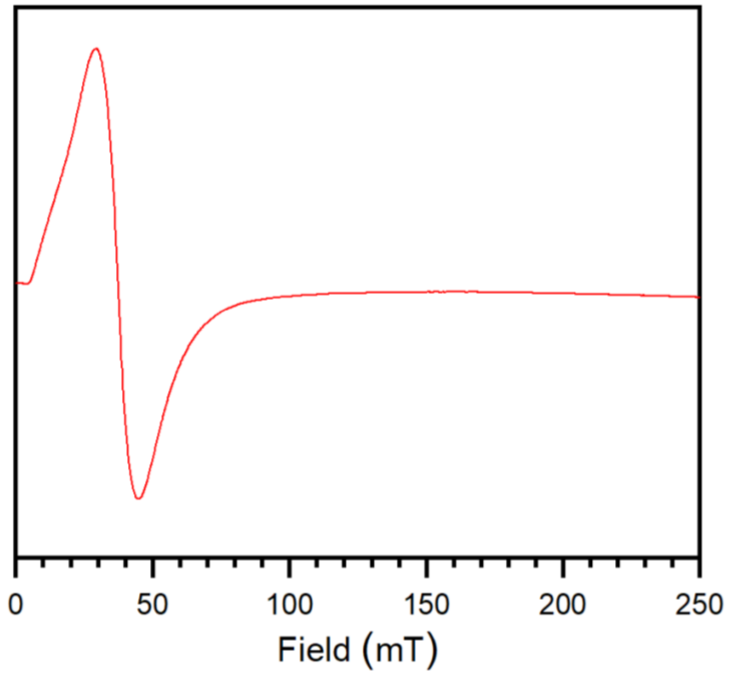

Figure 5.8. CW L-Band (1.3 GHz) EPR of **2** collected at room temperature on ground, polycrystalline sample.

Although L-Band EPR offers many advantages for EPRI applications, it also suffers from decreased signal to noise compared to higher frequencies. Given the weak intensity of the observed ST transitions at X-Band, it is possible that the decreased signal to noise prevents analysis using our current spectrometer. Future studies are under work to investigate **2** using low temperature L-Band spectroscopy, which should improve signal to noise and increase the visibility of forbidden transitions.

Investigations on ligand electronics modification [Cu_2CA(4'-OH-tpy)$_2$] (4)

Given the sensitivity of *J* to changes in the secondary coordination sphere, we reasoned that tuning the electronics of the ligands in these dinuclear systems could also give increased control over the strength of the exchange interaction. Towards this goal we attempted to synthesize the 4'-hydroxy terpyridine analogue of **2** following the synthetic procedure outlined above. Single crystals suitable for diffraction were obtained following slow evaporation of a pH 11 aqueous solution of **4** (Fig. 5.2). Structural analysis of **4** reveals that in each dinuclear species, one Cu(II) adopts a 5 coordinate geometry similar to **2'** with full coordination of the terpyridine and two bonding interactions with the chloranilic acid. In contrast, the other Cu(II) center is observed to have a 4-coordinate pseudo-planar geometry, where only a single oxygen from the choloranilic acid is bound. In addition, **4** does not crystallize with any counterions, but balances the charge of the complex with the O^- from each terpyridine ligand.

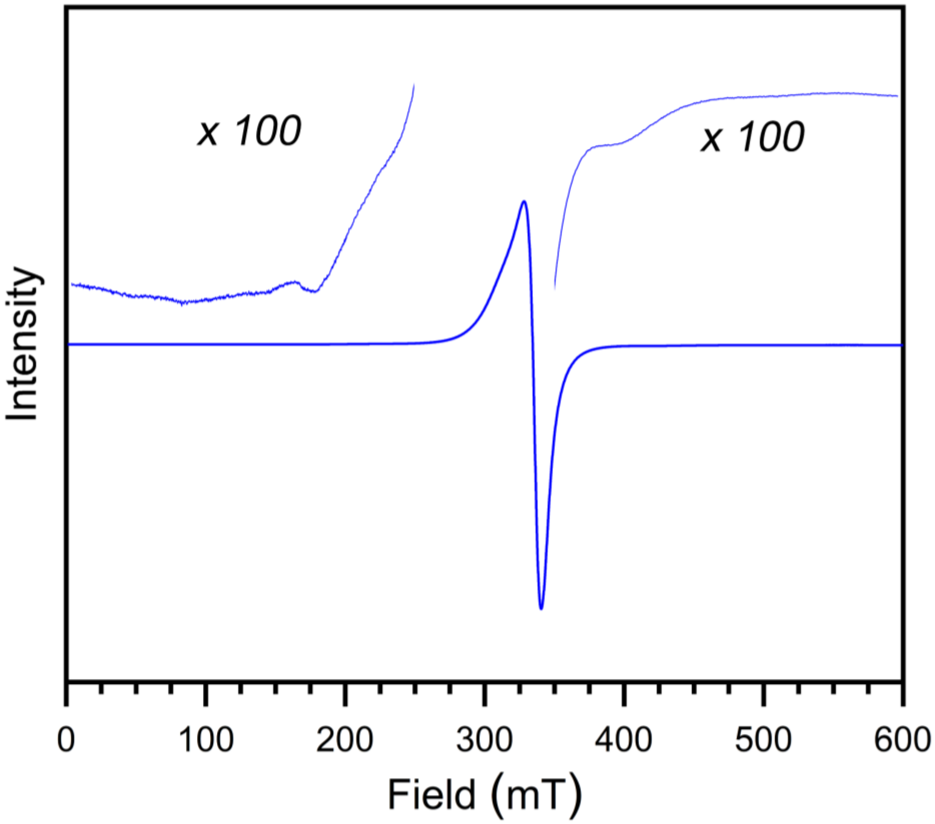

Figure 5.9. CW X-Band (9.8 GHz) EPR of **4** taken at room temperature. High and low field resonances are plotted with increased gain to improve visibility against the intensity of the main transition.

Room temperature CW X-Band EPR spectroscopy was conducted on crushed, polycrystalline samples of **4** to investigate the impacts of ligand modification on the ST transitions (Fig. 5.9). The primary transition ($\Delta M_S = \pm 1$) appears around 330 mT, and similar to **1** – **3** displays an asymmetric shoulder on the low field edge indicative of anisotropy at the Cu centers. In addition, we observe a half-field transition (ΔMs = ±2) at 170 mT indicating coupling between S = ½ Cu(II) centers. At higher field (375 mT), we observe a partially obscured resonance similar in shape to previously identified ST transitions; however, due to the broad shoulder of the central resonance, the low-field ST transition is not clearly visible. The position of the visible, high field ST transition indicates reduced strength of the exchange coupling between the Cu(II) ions ($J = 0.04\ \mathrm{cm}^{-1}$) which may be explained by the increased Cu – Cu distance (8.04 Å vs. 7.94 Å for **2'**). These preliminary results demonstrate that the ST forbidden resonance is surprisingly robust to changes in the structure of these dinuclear complexes; however, it is still not clear why the resonances vanish in **2'**. Future investigations will attempt to elucidate the origin of the ST transition in these complexes, towards the development of practical synthetic guidelines for the design of complexes with strong, tuneable ST transitions.

Conclusions

Our preliminary investigations into this family of exchange coupled Cu(II) complexes represents the first attempt at developing design principles for tuning the ST forbidden resonance via modulation of exchange coupling strength. It is shown that modifying the secondary coordination sphere for **1** – **3** can alter the degree of exchange coupling, and thus the location of the ST resonance. In addition, we have shown that the ST transition is surprisingly robust with regards to the local geometry of the Cu ions, as evidenced by the presence of the ST transition for the unique structure observed for **4**. EPR investigations at elevated temperatures, as well as high and low frequency will help to provide a more complete picture of the underlying phenomena responsible for the ST transition.

Finally, as evidenced by our preliminary L-Band investigations, increased signal intensity will likely be essential towards the development of low frequency EPRI probes. Towards this goal, we are investigating a new family of dinuclear Cu(II) complexes $[Cu_2(tren)_2(XCN)_2][BPh_4]_2$ (X = O or S), which display unusually intense ST transitions.[11] Our preliminary investigations have demonstrated that the ST transitions for this family of complexes are almost two orders of magnitude more intense as compared to **1** – **4** (Fig. 5.9). These results are promising evidence that thoughtful ligand choice may enable high-intensity ST transitions visible with low-frequency EPR.

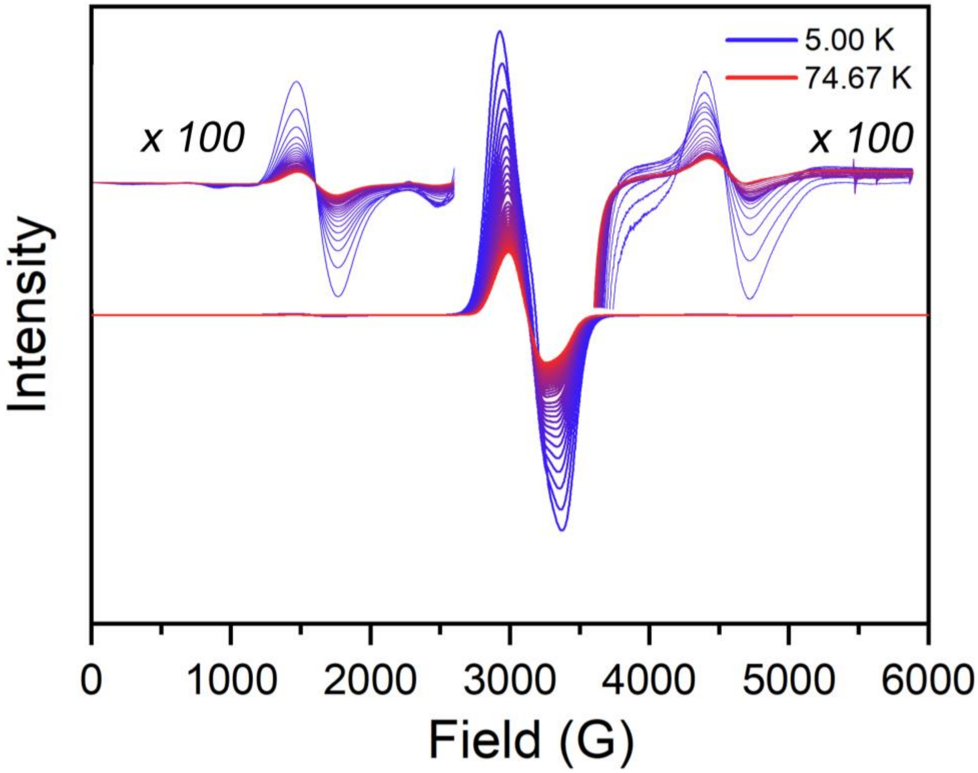

Figure 5.10. Variable temperature CW X-Band (9.8 GHz) EPR of **4** collected from 5.00 – 74.67 K. High and low field resonances are plotted with increased gain to improve visibility against the intensity of the main transition.

References

1. Campanella, A.J., Üngör, Ö., and Zadrozny, J.M. (2023). Quantum Mimicry With Inorganic Chemistry. Comments Inorg. Chem. *0*, 1–43.
2. Plewes, D.B., and Kucharczyk, W. (2012). Physics of MRI: A primer. J. Magn. Reson. Imaging *35*, 1038–1054.
3. Gertsenshteyn, I., Giurcanu, M., Vaupel, P., and Halpern, H. (2021). Biological validation of electron paramagnetic resonance (EPR) image oxygen thresholds in tissue. J. Physiol. *599*, 1759–1767.
4. Tahiliani, V.H., and Porter, J.W. (1980). Fault Current Limiters an Overview of EPRI Research. IEEE Trans. Power Appar. Syst. *PAS-99*, 1964–1969.
5. Matsumoto, K., Subramanian, S., Murugesan, R., Mitchell, J.B., and Krishna, M.C. (2007). Spatially Resolved Biologic Information from In Vivo EPRI, OMRI, and MRI. Antioxidants \& Redox Signal. *9*, 1125–1142.
6. Swartz, H.M., Williams, B.B., Zaki, B.I., Hartford, A.C., Jarvis, L.A., Chen, E.Y., Comi, R.J., Ernstoff, M.S., Hou, H., Khan, N., et al. (2014). Clinical EPR: Unique Opportunities and Some Challenges. Acad. Radiol. *21*, 197–206.
7. Jackson, S.K., Thomas, M.P., Smith, S., Madhani, M., Rogers, S.C., and James, P.E. (2004). In vivo EPR spectroscopy: biomedical and potential diagnostic applications. Faraday Discuss. *126*, 103–117.
8. Noodleman, L. (1981). Valence bond description of antiferromagnetic coupling in transition metal dimers. J. Chem. Phys. *74*, 5737–5743.
9. Larin, G.M., and Shul'Gin, V.F. (2006). Weak spin-spin exchange coupling in copper(II) dimers with long copper-copper distances. Russ. J. Inorg. Chem. *51*, 28–48.

10. Hoffmann, S.K., Hilczer, W., and Goslar, J. (1994). Weak long-distance superexchange interaction and its temperature variations in copper(II) compounds studied by single crystal EPR. Appl. Magn. Reson. *7*, 289–321.
11. Koohzad, S., Golchoubian, H., and Jagličić, Z. (2018). Two new end-on cyanato copper(II) complexes; synthesis, characterization, solvatochromism, magnetic investigation and quantum study. Polyhedron *155*, 180–188.
12. Venegas-Yazigi, D., Aravena, D., Spodine, E., Ruiz, E., and Alvarez, S. (2010). Structural and electronic effects on the exchange interactions in dinuclear bis(phenoxo)-bridged copper(II) complexes. Coord. Chem. Rev. *254*, 2086–2095.
13. Sakai, T. (2021). EPR Theories for Selection Rules to Observe the Spin Gap. Appl. Magn. Reson. *52*, 507–521.
14. Constable, E.C., and Ward, M.D. (1990). Synthesis and co-ordination behaviour of 6′,6″-bis(2-pyridyl)-2,2′ : 4,4″ : 2″,2‴-quaterpyridine; ‘back-to-back’ 2,2′ : 6′,2″-terpyridine. J. Chem. Soc., Dalt. Trans., 1405–1409.
15. Potts, K.T., and Konwar, D. (1991). Synthesis of 4’-vinyl-2,2’:6’,2’’-terpyridine. J. Org. Chem. *56*, 4815–4816.
16. Folgado, J. V., Ibáñez, R., Coronado, E., Beltrán, D., Savariault, J.M., and Galy, J. (1988). Extremely weak magnetic exchange interactions in terpy-containing copper(ii) dimers. Crystal and molecular structure of Cu(terpy) (CA)-H2O and [Cu2(terpy)2(CA)](PF6)2 complexes (terpy = 2,2′:6′,2″-terpyridine, CA = Dianion of chloranilic acid). Inorg. Chem. *27*, 19–26.
17. Sheldrick, G.M. (2015). OLEX2. Acta Crystallog. Sect. C Struct. Chem. *71*, 3–8.
18. Sheldrick, G.M. (2015). SHELLX. Acta Crystallogr. Sect. A Found. Crystallogr. *71*, 3–8.

19. Sheldrick, G.M. (2000). SADABS.

20. Paulson, J.A., Krost, D.A., McPherson, G.L., Rogers, R.D., and Atwood, J.L. (1980). Structural, spectroscopic, and theoretical studies of an exchange-coupled manganese(II)-copper(II) dimer. Inorg. Chem. *19*, 2519–2525.

21. Ghann, W., Sobhi, H., Kang, H., Chavez-Gil, T., Nesbitt, F., and Uddin, J. (2017). Synthesis and Characterization of Free and Copper (II) Complex of N,N′-Bis-(Salicylidene)Ethylenediamine for Application in Dye Sensitized Solar Cells. J. Mater. Sci. Chem. Eng. *05*, 46–66.

22. Calvo, R. (2007). EPR measurements of weak exchange interactions coupling unpaired spins in model compounds. Appl. Magn. Reson. *31*, 271–299.

CHAPTER 6 - Summary

This dissertation presents four independent investigations into the relaxation behavior of first-row transition metal complexes, and the impacts of electron – electron interactions on spin relaxation. Precise control of electronic spin relaxation is desirable for a range of applications including quantum computing, spintronics, and data storage; unfortunately, the energy barrier to spin relaxation is incredibly small, and even minor interactions can have profound effects on relaxation times. Broadly, the goal of this research is to expand our understanding of both the fundamental forces which impact spin relaxation, while developing new strategies for designing transition metal complexes which display desired spin relaxation properties. Towards this goal, we have investigated four unique areas of magnetic relaxation phenomena: *1) Extended magnetic relaxation in spin abundant environments, 2) Novel synthetic methodologies for the creation of low-coordinate extended solids, 3) Magnetostructural correlations in 1D transition metal coordination polymers, and 4) Synthetic tunability of the singlet to triplet forbidden EPR transition in exchange coupled complexes.*

Towards extending magnetic relaxation times in spin abundant environments, we have shown, for the first time, that relaxation times may be extended by diluting in paramagnetic species. This counterintuitive behavior is shown to be the result of the anisotropic dipolar interactions present between adjacent spin centers within the crystal lattice. Although the intentional design/directing of crystal packing is not currently achievable, the results of this research may still enable dilution and extended relaxation in systems for which traditional diluents are not synthetically accessible.

The work presented in chapter three represents the early stages of what we envision to be a new class of materials with novel magnetic, optical, and electronic properties. Specifically, we have shown that the simple transamination reaction is a viable pathway to transform mononuclear low-coordinate transition metal complexes into higher nuclearity species. Through careful synthetic tuning of steric bulk and reaction conditions we believe this idea can be extended towards the development of extended solids incorporating the same low-coordinate metal centers. This, as of yet, unexplored area of chemistry offers potentially revolutionary new transition metal-based materials capable of imitating rare earth metal properties. Continued efforts to realize these materials will focus on the role of ligand sterics, reaction conditions, and judicious choice of starting materials.

In a similar fashion, the investigations discussed in chapter four represent the early stages of investigations into the relationship between chemical structure and material properties for tetraoxolene bridged coordination polymers. This work shows that dramatic changes in magnetic properties can be observed even when the metal and bridging ligand identities remain constant. Slight alterations of the chain geometry are sufficient to change the preferred distribution of oxidation states across the metal-bridge linkages, turning on properties such as valence tautomerism and strong magnetic coupling. Future studies are needed to help increase our ability to predict and rationally design future materials with desirable properties.

Finally, the work discussed in chapter five represents the early stages of investigations towards the development of high-field, low-frequency EPRI probes. These molecules are currently not well understood and future research will continue to develop our understanding of the relationship between chemical structure and the singlet triplet, spin forbidden resonance.

APPENDIX A

Experimental Details

General considerations

All synthetic methods were carried out under an inert N_2 atmosphere inside of a VigorTech brand glovebox. Anhydrous metal(II) chloride salts were prepared following literature procedure.[1] Acetonitrile (CH_3CN) was dried using a commercial solvent system and stored in the glovebox over dried 4 Å molecular sieves for 48 h prior to use. Molecular sieves were activated by heating to 285 ˚C under reduced pressure overnight before being stored in the glovebox. Tetraphenylphosphonium bromide was recrystallized from acetone and dried under reduced pressure at 70 ˚C overnight before being pumped into the glovebox for storage. Benzene thiophenol (HSPh) and potassium tert-butoxide (KO-tBu) were purchased from Sigma Aldrich and used as received.

Synthetic Methods.

Preparation of $(Ph_4P)_2[M(SPh)_4]$ (where M = **Co, Ni, Fe, Mn,** and **Zn)** was performed according to previous literature methods for the synthesis of **Co** by substituting the appropriate MCl_2 salt.[2] Subsequent dilutions were prepared similarly, starting with the desired mixed stoichiometry of MCl_2 and $CoCl_2$ salts. Successful co-crystallization of the dilution samples was confirmed via Inductively Coupled Plasma Optical Emission Spectroscopy (ICP-OES) and comparison of powder x-ray diffraction patterns to the pure **1** (see Fig A22). Of note, it was found that initial stoichiometry of MCl_2 salt frequently did not directly correlate to final stoichiometry of the crystalline samples. For example, the 2:1 Ni:Co dilution was prepared beginning with a 1:1 Ni:Co solution, while the 9:1 Ni:Co dilution was prepared beginning with a 10:1 Ni:Co stoichiometry. Throughout the course of dilution synthesis, it was observed that more accurate final dilution concentrations were obtained when the $CoCl_2$ to be added was taken from a stock solution of $CoCl_2$ in acetonitrile, and the solutions were kept at an elevated temperature (48 ˚C) for the first hour after adding $(PPh_4)[SPh]$ to the MCl_2 solution. Although some of the inaccuracy may be the result of small fluctuations in recorded mass caused by static build up in the glove box, the inconsistency of incorporation for all diluents suggests that to some extent co-crystallization does not occur at the same rate between different species of the metal thiophenol complexes, and thus ICP-OES must be used to determine the actual extent of incorporation prior to analysis.

$(Ph_4P)_2[Co_{1.0}Ni_{2.1}(SPh_4)]$ (1:2 Co:Ni): To 1 mL of a 0.06 mM solution of anhydrous $CoCl_2$ in acetonitrile was added 7.78 mg (0.06 mmol) of anhydrous $NiCl_2$ and then diluted with acetonitrile to a final volume of 2 mL. This solution was stirred and heated at 45 °C to increase solubility of $NiCl_2$. KSPh (0.88 mmol) was generated through the stoichiometric reaction of 98.7 mg KO-tBu and 90.36 µL of HSPh in 2 ml of MeCN to yield a white slurry. 371.0 mg (0.87 mmol) of $(Ph_4P)Br$ was heated with stirring in 2 mL acetonitrile to give a colorless solution. The solution of $(Ph_4P)Br$ was added to the KSPh slurry and an immediate color change to yellow was observed and a fine white precipitate formed. The solution was filtered over Celite to remove the white solid and the resulting yellow solution of $(Ph_4P)[SPh]$ was then added to the hot solution of metal chloride salts with stirring. The reaction immediately turned a deep green and slowly became a dark reddish-brown over the course of several minutes. Once all remaining $NiCl_2$ was seen to have been dissolved into solution (~1 hr) the vial was removed from heat and allowed to sit undisturbed overnight in the glovebox. Upon decanting, a single gigantic crystal (2 cm x 1 cm) formed in the bottom of the vial. The single crystal was rinsed with Et_2O (2 x 2 mL) and dried under vacuum. ICP-OES: Ni: 67.4% Co: 32.6%. Powder X-ray diffraction data indicate the same crystal structure as for pure $(Ph_4P)_2[Co(SPh)_4]$ (Fig. A3).

$(Ph_4P)[Co_{1.0}Ni_{9.1}(SPh_4)]$ (1:9 Co:Ni): Same procedure as for above except the starting stoichiometry for $NiCl_2$ and $CoCl_2$ was 14.1 mg (0.109 mmol) to 1.41 mg (0.0109 mmol) respectively. Block-like, red/brown crystals grew overnight. ICP-OES: Ni: 90.1%, Co: 9.9%. Powder X-ray diffraction data indicate the same crystal structure as for pure $(Ph_4P)_2[Co(SPh)_4]$ (Fig A3).

$(Ph_4P)[Co_{1.0}Ni_{33.8}(SPh_4)]$ (1:34 Co:Ni): Same procedure as above except $CoCl_2$ was massed out as a solid before being dissolved in acetonitrile with $NiCl_2$. The starting stoichiometry for $NiCl_2$ and $CoCl_2$ was 14.1 mg (0.109 mmol) and 3.04 mg (0.023 mmol) respectively. Small, block-like red/brown crystals grew overnight. ICP-OES: Ni: 97.1% Co: 2.9%. Powder X-ray diffraction data indicate the same crystal structure as for pure $(Ph_4P)_2[Co(SPh)_4]$ (Fig A3).

$(Ph_4P)[Co_{1.0}Fe_{15.3}(SPh_4)]$ (1:15 Co:Fe): Same procedure as for above except the starting stoichiometry for $FeCl_2$ and $CoCl_2$ was 12.67 mg (0.10 mmol) and 2.59 mg (0.02 mmol) respectively. Solid precipitated as an orange-green microcrystalline powder which was isolated on a filter frit before being washed with Et_2O (2 x 5 ml). ICP-OES: Fe: 93.9% Co: 6.1%. Powder X-ray diffraction data indicate the same crystal structure as for pure $(Ph_4P)_2[Co(SPh)_4]$ (Fig A3).

$(Ph_4P)[Co_{1.0}Mn_{14.5}(SPh_4)]$ (1:15 Co:Mn): Same procedure as for above except the starting stoichiometry for $MnCl_2$ and $CoCl_2$ was 12.60 mg (0.10 mmol) and 2.59 mg (0.02 mmol) respectively. Block-like, green/yellow crystals grew overnight. ICP-OES: Mn: 95.6% Co: 4.3%.

Powder X-ray diffraction data indicate the same crystal structure as for pure $(Ph_4P)_2[Co(SPh)_4]$ (Fig A3).

$(Ph_4P)[Co_{1.0}Mn_{1.27}(SPh_4)]$ (1:1.27 Co:Mn): Same procedure as for above except the starting stoichiometry for $MnCl_2$ and $CoCl_2$ was 7.6 mg (0.06 mmol) and 7.8 mg (0.06 mmol) respectively. Block-like, green/yellow crystals grew overnight. ICP-OES: Mn: 66.9% Co: 44.1%. Powder X-ray diffraction data indicate the same crystal structure as for pure $(Ph_4P)_2[Co(SPh)_4]$ (Fig A3).

$(Ph_4P)[Co_{1.0}Zn_{33.3}(SPh_4)]$ (1:33.3 Co:Zn): Same procedure as for above except the starting stoichiometry for $ZnCl_2$ and $CoCl_2$ was 0.49 mg (0.003 mmol) and 15.83 mg (0.116 mmol) respectively. Block-like, green/yellow crystals grew overnight. ICP-OES: Zn: 97.55% Co: 2.45%. Powder X-ray diffraction data indicate the same crystal structure as for pure $(Ph_4P)_2[Co(SPh)_4]$ (Fig A3).

$(Ph_4P)[Co_{1.0}Zn_{3.33}(SPh_4)]$ (1:3.33 Co:Zn): Same procedure as for above except the starting stoichiometry for $ZnCl_2$ and $CoCl_2$ was 5.2 mg (0.04 mmol) and 10.2 mg (0.08 mmol) respectively. Block-like, green/yellow crystals grew overnight. ICP-OES: Zn: 71.0% Co: 29.0 %. Powder X-ray diffraction data indicate the same crystal structure as for pure $(Ph_4P)_2[Co(SPh)_4]$ (Fig A3).

*Magnetic Measurements***.** Magnetic data were collected on a Quantum Design MPMS SQUID magnetometer. Samples were prepared by placing finely ground, microcrystalline samples into a gelatin capsule, restraining the powder with molten eicosane and finally wrapping the capsule in Teflon tape. Direct-current (dc) measurements were obtained with a 1000 G applied field and temperatures ranging from 1.8 K to 300 K. All DC measurements were corrected for the diamagnetic contribution of the sample holder, as well as the restraining material and ligand framework (calculated using Pascal's constants).[3] Alternating-current (ac) susceptibility measurements were collected at the parameters described in the main paper as well as the figures presented below. For AC susceptibility measurements of dilutions, all values of $\chi_M{}'$ and $\chi_M{}''$ are given per moles Co^{2+}, as determined by ICP analyses. $\chi_M{}'$ values calculated utilizing this dilution factor appear artificially high because of the unaccounted contribution of the diluents, but $\chi_M{}''$ values were, generally, in agreement with previously published magnetic data for pure **Co** and $Zn(SPh)_4^{2-}$ dilutions.[2] In Figs. A14-A17, values of $\chi_M{}'$ and $\chi_M{}''$ are normalized to those of **Co** for best comparison. For DC susceptibility of pure compounds this strategy was not necessary, and good fits were found considering the total number of moles present in each sample. $\chi_M T$ fits were calculated using the PHI software suite and associated spin Hamiltonian by parameterizing the anisotropic gyromagnetic ratios (g_x, g_y, and g_z), the zero field splitting (D) and the transverse anisotropy (E).[4] Fits for $\chi_M{}''$ were generated through the Origin software suite fitting package by using the following Cole-Cole equation (1.1) and parameterizing τ, α, χ_T and χ_S. Initial guess values were estimated from the $\chi_M{}'$ graphs.

$$\chi''(\omega) = (\chi_T - \chi_S)\frac{(\omega\tau)^{1-\alpha}\cos\left(\frac{\pi\alpha}{2}\right)}{1 + 2(\omega\tau)^{1-\alpha}\sin\left(\frac{\pi\alpha}{2}\right) + (\omega\tau)^{2-2\alpha}} \qquad (1.1)$$

Details of Magnetic Susceptibility Fitting.

$\chi_M T$ fits were performed using the PHI software suite and the following spin Hamiltonian:

$$\hat{\mathbf{H}} = \mu_B \mathbf{B}\{\mathbf{g}\}\hat{\mathbf{S}} + D\left\{\hat{\mathbf{S}}_z^2 - \frac{1}{3}S(S+1)\right\} + E\left(\hat{\mathbf{S}}_x^2 - \hat{\mathbf{S}}_y^2\right)$$

In the process of fitting, we tried numerous models as we balanced the desire to obtain new fits with not overparameterizing the models. Hence, we tested isotropic and anisotropic gyromagnetic ratios (g_x, g_y, and g_z), positive/negative values of zero field splitting (D) and positive/negative values of the transverse anisotropy (E).[4] In the case of **Ni**, it was found that fitting with an isotropic g gave a reasonable quality fit without having to invoke anisotropy in g. For **Co**, **Fe**, and **Mn**, attempts to fit with an isotropic g were attempted, but anisotropic g values gave much better fits.

Details of Temperature-Dependent Magnetic Relaxation Time Fitting.

Relaxation time data (τ) were fit with equation (1.2) in Origin:

$$1/\tau = AT^{\mathrm{n}} + 1/\tau_{\mathrm{QTM}} \tag{1.2}$$

Here, A is a weighting factor for the contribution of the Raman process in magnetic relaxation at a given temperature, n is the Raman exponent, and τ_{QTM} is the time of the quantum tunneling of the magnetization. Selection of these two relaxation processes for fitting followed the elimination of the other alternatives. The direct process, for which $1/\tau \propto B^{-4}$, was omitted because the complexes are being analyzed at 0 G DC magnetic field, and the rate of the process would hence be too slow to contribute.[5] The Orbach process[6] was omitted because there is no clear linear region in the Arrhenius plots (see Fig. 2.3). Importantly, previous attempts to fit the variable-temperature τ data for **1** using the Orbach process extracted "U_{eff}" » 20 cm^{-1}, though that value fall s far lower than $2D$ for the complex (the minimum value of U possible and > 100 cm^{-1}), indicating that the process is likely not actually dominant at these temperatures.[7] Other relaxation mechanisms, e.g. from local vibrational modes,[8] or other thermally activated processes[9] were omitted because these mechanisms are typically active only at T > 100 K. The best fit parameters are summarized in Table A2. Fitting the equation to the data produced better fits when $\ln(\tau)$ was used for computing residuals as opposed to τ.

For all dilutions of **1** in **2**, the best fits to the variable temperature data produced non-integral values of the Raman exponent – possibly indicating that the relaxation might be attributable to multiple processes with differing exponents, since n should be an integer for any individual Raman process.[10] Further evidence of this fact could be the Raman exponent variation from 6 to 8 for these dilutions, when Kramer's ions are expected to have n = 9. Ultimately, future studies will be required to resolve this discrepancy. We note that restraining the exponent to the nearest whole-number value did not substantially vary the other terms, A or τ_{QTM}, sufficiently to disrupt the observed trends.

Electron Paramagnetic Resonance Measurements and Fitting Details.

High-frequency EPR spectra on $(Ph_4P)_2[Fe(SPh)_4]$ and $(Ph_4P)_2[Ni(SPh)_4]$ were recorded with a home-built spectrometer at the EMR facility of NHMFL. The instrument is a transmission-type device in which waves are propagated in cylindrical light-pipes. The microwaves were generated by a phase-locked oscillator (Virginia Diodes) operating at a frequency of 8-20 GHz and generating its harmonics, of which the 4th, 8th, 12th, 16th, 24th and 32nd were available. A superconducting magnet (Oxford Instruments) capable of reaching a field of 17 T was employed.[11] Samples of $(Ph_4P)_2[Fe(SPh)_4]$ were ground to a fine powder in a glovebox prior to use for sample prep. This grinding was imperfect as evidenced by the "grass pattern" of peaks observed in some of the HF-EPR spectra (Fig. A3).

Samples of $(Ph_4P)_2[Mn(SPh)_4]$ used for EPR analyses were ground into a fine powder inside of an inert atmosphere glovebox and loaded into a quartz EPR tube (Wilmad 707-SQ-250M) and sealed with a septum. The EPR tubes were then quickly transported to a high vacuum schlenk line and sealed under dynamic vacuum (~100 mTorr). Room temperature EPR spectra were recorded on a Bruker ESR-300 spectrometer (Bruker Biospin, Rheinstetten, Germany) at 9.838 GHz with fields ranging from 0-600 mT.

HF-EPR spectra for Fe were fit using the program SPIN locally developed at the National High Magnetic Field Laboratory. A standard spin Hamiltonian for $S = 2$ was used:

$$\hat{\mathbf{H}} = \mu_B \mathbf{B}\{\mathbf{g}\}\hat{\mathbf{S}} + D\left\{\hat{\mathbf{S}}_z^2 - \frac{1}{3}S(S+1)\right\} + E\left(\hat{\mathbf{S}}_x^2 - \hat{\mathbf{S}}_y^2\right) + B_4^0 O_4^0 + B_4^4 O_4^4$$

To determine the parameters, multiple spectra were recorded at various microwave frequencies and the positions of the canonical resonances were fitted (Fig. S3). Powder spectra were subsequently simulated showing very good agreement with the experiment. The fitting procedures resulted in g_x = 2.051(1), g_y = 2.095(1), g_z = 2.010(1), D = +5.848(1) cm^{-1}, E = +1.428(1) cm^{-1}, B_4^0 = –7.8(4)×10^{-4} cm^{-1}. Inclusion of the quartic term with B_4^0 significantly improved the fit, while no improvement resulted from taking B_4^4 into account. It was thus assumed to be zero.

Fitting of the 381 GHz and X-Band spectra for **Mn** was performed with the EasySpin[12] program in MatLab with the *pepper* function for solid-state EPR. The following spin Hamiltonian was used:

$$\hat{\mathbf{H}} = \mu_B \mathbf{B}\{\mathbf{g}\}\hat{\mathbf{S}} + D\left\{\hat{\mathbf{S}}_z^2 - \frac{1}{3}S(S+1)\right\} + E\left(\hat{\mathbf{S}}_x^2 - \hat{\mathbf{S}}_y^2\right) + \boldsymbol{IAS}$$

The following parameters were used to fit the experimental data $g_{x,\,y,\,z}$, D, E, and isotropic line broadening. HF-EPR spectra of Mn were simulated holding the A value isotropic (A_{iso} = 252 MHz) and approximately the same magnitude as is generally observed for Mn^{2+} ions. The simulated spectra for **Fe** were calculated by full diagonalization of the electronic Hamiltonian using the 'matrix' method in *pepper*. In contrast, the **Mn** spectra were computed by full diagonalization of the electronic Hamiltonian and first-order perturbation of the nuclear spins. This method offers significant reduction in computational time and generated identical spectra to the full diagonalization for this complex.

Powder X-Ray Diffraction.

Powder X-Ray Diffraction patterns were obtained using a Bruker D8 Discover Series II diffractometer utilizing the LYNXEYE detector and a CuKα radiation source at 1600W (40 kV, 40mA). Samples were prepared in an inert atmosphere glovebox by loading 0.6mm diameter quartz capillaries with uniformly powdered sample and sealed using capillary wax before being centered on the goniometer. All patterns were collected from $2\theta = 5\text{-}50^\circ$, with a 0.02° increment, and a 1 sec exposure time.

Other Physical Methods.

ICP-OES was carried out using a PerkinElmer Optima 7300 DV and the TOPM standards program in the Plant and Soil Science Laboratory at Colorado State University. All samples and reference standards were prepared by digesting in HNO_3 and diluting to 10% HNO_3 by volume with HPLC grade H_2O (filtered through 0.2 μm filter) and subsequent filtering of the digested sample through a glass fiber filter. Scanning electron microscopy (SEM) analysis was performed on a JEOL JSM-6500F field emission electron microscope at a working voltage of 15.5 kV and with an Oxford X-Max 80 mm^2 EDS detector. Samples were prepared on aluminum pucks inside of an inert atmosphere glovebox by placing finely ground polycrystalline samples on a small piece of carbon tape and subsequently removing any non-adhered crystallites. Once prepared, samples were transported to the SEM stage under a blanket of N_2 before being quickly loaded into the reduced pressure sample chamber. Minimal degradation has been observed on this timescale (based on PXRD patterns). Due to the polycrystalline nature of the samples, care was taken to only analyze crystallites which presented flat surfaces. EDS mapping of imperfectly aligned crystallites produced unreliable measurements.

Additional Discussion of Sample Homogeneity.

Sample homogeneity in the analyzed materials was arrived at from the aggregate of multiple structural techniques. First, PXRD data demonstrate that the cocrystallizations do not produce new crystalline phases of materials. However, the overlap of the diffraction patterns means that the technique can not differentiate between mixtures of pure crystals versus crystals that contain mixtures of metals within their habits. The former possibility is likely not the case on the basis of sample color. Dilutions of **Co** (green crystals) in **Zn** (white/colorless crystals) do not produce separate green and white crystals, but rather a homogeneous (by eye) collection of lighter-green crystals than the starting **Co**. Similarly, the other dilutions produce crystals that are colored as a mix of the two pure materials. Furthermore, our preliminary EDS analyses show that there is distribution of **Co** in the diluent crystals. Although EDS analysis of polycrystalline samples cannot provide excellent accuracy due to sample orientation, our initial analysis suggests reasonable homogeneity on μm length scales from crystallite to crystallite. Finally, the magnetic analyses suggest effective dilution: In the fitting of the individual variable-frequency scans, the α parameter from the Cole-Cole equation describes the distribution in relaxation times for the sample, but practically correlates to the width of the χ_M'' peak (in frequency space). For pure Co, α increases from 0.025 at 6.5 K to 0.276 at 2 K, indicating that upon transition to the tunneling regime, there are more potential relaxation times available to $[Co(SPh)_4]^{2-}$. Upon dilution in **Ni**, α increases with increasing concentration of $[Ni(SPh)_4]^{2-}$: 0.384, 0.56, and 0.58 for 1:2, 1:9 and 1:34 dilutions of **Co** in **Ni**, respectively. This increase in α mirrors what typically happens when Co is dissolved in Mn, Fe, and Zn (Table S4)[7]. This increase is likely due to a measure of inhomogeneity at the nanometer scale in the solid solution phases of the dilutions, as varying local concentrations of open-shell bath molecules in the immediate environment would then impart varying impacts on τ_{QTM}, and hence, a spread in the relaxation times.

Additional NMR Analyses.

As an alternative hypothesis to the $S_{\mathrm{eff}} = 0$ interpretation in the text, we tested whether the true operative effect of the bath could be less dependent on spin magnitude than the timescale of the fluctuations of the $[M(SPh)_4]^{2-}$ bath spins. Ample literature evidence demonstrates that half-filled shell ions like Mn^{2+} and Gd^{3+} tend to have orders of magnitude longer magnetic relaxation times than integer spin systems.[13] Hence, the **Mn** bath spins may exhibit slow enough relaxation to enable interaction with **Co** and facilitate tunneling. In contrast, the integer-spin **Fe** and **Ni** bath spins, which could have significantly faster relaxation, are decoupled from **Co** and ineffective at modulating the tunneling process. Preliminary solid-state magic angle spinning ^1H nuclear magnetic resonance spectra on **Mn**, **Fe**, **Ni**, and **Zn** (see below, Figs. A19 and A20) suggest that this is not the case, but further investigations at low temperature are warranted.

Solid-State Nuclear Magnetic Resonance Measurements and Fitting Details. Solid-state ^1H NMR spectra were obtained using a CMX-Infinity (Chemagnetics, Fort Collins, CO USA) spectrometer operating at 8.5 T (360 MHz for ^1H) employing a single-resonance probe, using a 4.0 mm (rotor diameter) MAS module with a spinning speed of 15 kHz and using a rotating-frame RF intensity of 62.5 kHz (4.0 μs π/2 pulse). As the probe exhibits a significant ^1H

background (relative to the signal obtained from the samples studied here), it was necessary to experimentally suppress the background. This was accomplished with the so-called DEPTH method[14] that utilizes a number of π pulses with systematically varied rotating-frame phases to preserve the sample's legitimate signal (which arises in the more intense rotating-frame RF field in the center of the sample coil) and suppresses the background signal (which arises in the less intense rotating-frame RF field surrounding the sample coil). Saturation recovery data were collected by first saturating all ^1H magnetization using ten π/2 pulses of constant phase, each spaced out at roughly ¼ of the MAS rotation period (16.6 μs), followed by a systematically varied interval to permit re-establishment of the Boltzmann magnetization, and lastly followed by a DEPTH-3 sequence (one π/2 and two π pulses) to observe the then-recovered magnetization with background suppression.[14]

Magnetization recovery time plots were fit by employing the single exponential rise equation [1.3]

$$m(t) = m(\infty) \times (1 - \eta e^{\frac{-t}{T_1}}) \tag{1.3}$$

Here $m(t)$ is the magnetization intensity at time t, $m(\infty)$ is the predicted magnetization intensity at infinity, η is the efficiency of magnetization saturation, and T_1 is the spin lattice relaxation. The magnetization $m(t)$ was taken from recorded spectra and both $m(\infty)$ and T_1 were parametrized and extracted from the best fit line to the recorded data. In the case of **Co** and **Ni** the magnetization recovery appears to have two relaxation regimes which were fit independently using equation [1.3]. Reported T_1 values for these complexes are the average of the two extracted T_1s. The relaxation of **Fe** does not appear to follow an easily interpretable monoexponential behavior, highlighted in Fig. A15. Hence, it is difficult to directly quantitate T_1 for comparison between the molecules in this study, and deeper analyses will ultimately be pursued to enable understanding.

Our initial rationale was that a faster ^{1}H relaxation rate would evidence a more dynamic electron spin bath and potentially correlate to impact on relaxation in **Co**.[15] Each species shows a single, broad peak (Fig. A19) in the ^{1}H spectrum centered around 6.5 ppm (^{1}H chemical shift relative to TMS). Preliminary saturation recovery experiments performed on this peak (see Appendix A and Fig. A20) reveal a range of ^{1}H relaxation rates. Here, 90% of the ^{1}H magnetization is recovered by 0.5, 2.5, 6.0, and 9.0 s for **Ni**, **Mn**, **Co**, and **Fe**, respectively. The ^{1}H nuclei in **Zn** did not recover fully in our measurement, and 90% recovery can be extrapolated to occur by ca. 20 s. These preliminary data suggest that differing rates of electron spin dynamics in **Ni**, **Mn**, and **Fe** are not the principal factor in controlling the relaxation times of Co. If they were, the ^{1}H relaxation rates of **Ni** and **Fe** would be expected to be nearly the same timescale to reflect similar bath electron spin relaxation times. Furthermore, the rate for **Mn** would be expected to be distinct from **Ni**, **Fe**, **Co**, and **Zn**, since dilution in **Mn** exclusively hastens the relaxation time of $[Co(SPh)_4]^{2-}$ faster than the bath of pure **Co**. Yet, the ^{1}H relaxation rate in **Mn** lands squarely in the middle of the studied complexes. Previous literature shows that temperature and field can have a profound impact on the nuclear relaxation spectra for magnetic molecules.[16] In addition to the difference in field strength between the NMR and magnetometric analyses, the recorded NMR spectra are taken at near room temperature (~298 K), far different than the 2 K of the magnetometer. The active relaxation pathways are likely different from those active in the low-*T* regime observed for our magnetic susceptibility data. As discussed in the main body of the paper, we propose another explanation, not directly related to relaxation times, to rationalize the observed behavior of the paramagnetic diluents.

In addition to T_1, another potential probe for reporting the electron spin bath dynamics would be the T_2^* of the protons. In principle, if one can assign the peaks and the peak shape is simple and symmetric, the peak linewidth can yield this parameter. However, peak assignment cannot made with the data, due to the paramagnetism of the samples and peak width from the detailed experimental conditions. We do note that the similarity in peak shifts is surprising considering the paramagnetic nature of the compounds (Fig. A14), which is metal dependent. In general, we would expect to see less influence from the paramagnetic ion for resonant frequencies of the counterion (Ph_4P^+), so the identified peak might stem primarily from counterion protons, but further studies would be necessary to conclusively assign them. Together, this inability to clearly assign the peak and the non-symmetric peak shapes preclude the extraction of any useful T_2^* data for our analysis.

Dipolar Field Model and Calculation Details

The below details are partitioned into four subsections. In the first two subsections, we briefly define the out of phase magnetic susceptibility and its relationship to a relaxation rate, then we discuss relaxation rate in the context of an $S = {}^1/_2$ ion induced by a dipolar magnetic field. In the last two sections, we justify treatment of the embedded Co(II) ions of $[Co(SPh)_4]^{2-}$ as effective $S = {}^1/_2$ species, then describe how we calculated the expectation values of the dipolar field components $c_h^n = \langle h_n h_n \rangle$ ($n = x, y, z$) depicted and analyzed in the main manuscript. A visual depiction of the easy-axis vectors and transformed axis is given below (See Fig. A24).

Out-of-phase magnetic susceptibility description used for model:

First, we describe the relationship between the out-of-phase susceptibility and spin relaxation rate, which yielded the c_M'' versus frequency plots depicted in the main manuscript and here in Appendix A (Figs. 2.3, A8-A18). The AC magnetic field (H) used to measure the relaxation behavior has a simple sinusoidal, linearly polarized form, where ω is the frequency of the applied field:

$$\boldsymbol{H}(t) = \boldsymbol{H}\, sin(\omega t) \tag{1}$$

the power absorbed by the spin system at a given frequency, $P(\omega)$, is:

$$P(\omega) = -\frac{1}{T}\int_0^T M^i\,(t) dH^i(t) = \frac{\omega}{2} H^i H^j \chi_{ij}''(\omega) \tag{2}$$

where M^i is the *i*-th component of the magnetization, *T* is the period, and χ'' is the imaginary part of the magnetic susceptibility tensor:

$$\chi(\omega) \equiv \chi'(\omega) + i\chi''(\omega). \tag{3}$$

Below we take the independent spin approximation and consider the χ due to a single spin for simplicity. It is useful to relate χ to the time-correlation function or relaxation function defined as

$$\Phi^{ij}(t) \equiv \frac{1}{2}\langle S^i(t)S^j + S^j(t)S^i\rangle - \langle S^i\rangle\langle S^j\rangle \tag{4}$$

where S^i is the *i*-th component of the spin operator. The symmetrization is to ensure that $\Phi^{ij}(t)$ is real. Below we assume $\langle S\rangle = 0$ in the absence of external magnetic fields. The fluctuation-dissipation theorem dictates that

$$\gamma^2 \Phi^{ij}(\omega) = \frac{2\hbar}{1 - e^{-\beta\hbar\omega}} (\chi'')^{ij}(\omega) \tag{5}$$

where $\gamma = g\mu_B/\hbar$ is the gyromagnetic ratio and g is the Landé g-factor for the electronic spin. Since our interest is in χ''_{ij}, it is sufficient to consider only the time correlation function, Φ. In the case that Φ(t) is described by a simple exponential decay, $\Phi(t) = \Phi_0 e^{-\Gamma|t|}$, where Γ is the decay rate ($\Gamma > 0$), we have:

$$\Phi(\omega) = \frac{2\Gamma}{\omega^2 + \Gamma^2} \Phi_0 \tag{6}$$

In the present experiments the frequency ω (< 1000 Hz) is much smaller than $k_B T/\hbar \sim 10^{11}$ Hz. So $e^{-\beta\hbar\omega} \approx 1 - \beta\hbar\omega$, and we can obtain χ'':

$$\chi''(\omega) \approx \frac{\gamma^2}{k_B\, T} \frac{\omega\Gamma}{\omega^2 + \Gamma^2} \Phi_0 \tag{7}$$

which is non-monotonic with ω and takes its maximum at $\omega = \Gamma$. Thus, the position of the low-frequency peak of $\chi''(\omega)$ corresponds to the decay rate. If more complex fitting functions (e.g., the Cole-Cole function)[17] of the experimental $\chi''(\omega)$ are needed, the decay behavior is likely to be more complicated than the simple exponential form.

Relaxation of an S = ½ spin:

In this subsection we give a general discussion on the relaxation of an $S = 1/2$ spin in the presence of a DC magnetic field and explain the difficulty in modeling it when the DC field vanishes. The consideration of $S = 1/2$ is also motivated by the fact that the low-frequency behavior of the $\chi''(\omega)$ for Co spins is governed by the low-energy Kramers doublet behaving as a spin-$1/2$.

We assume that the DC magnetic field is along z, and the spin is also subject to a fluctuating magnetic field ($\boldsymbol{h}$) which is assumed to be much weaker than the DC field ($\boldsymbol{h}_0$). The Hamiltonian is:

$$H = -h_0\sigma_z - \boldsymbol{h}(t) \cdot \boldsymbol{\sigma} \tag{8}$$

where $\boldsymbol{\sigma}$ is the Pauli matrix vector and all numerical factors are absorbed into h_0 and $\boldsymbol{h}(t)$. We also assume that $\boldsymbol{h}(t)$ has a zero time-average. For simplicity we consider the time correlation function Φ^{ii} only, i.e.

$$\Phi^{ii}(t) = \langle \sigma^i(t)\sigma^i \rangle - \langle \sigma^i \rangle^2 \tag{9}$$

When $|\boldsymbol{h}| \ll h_0$, Φ^{ii} can be calculated from time-dependent perturbation theory. Denoting $H_0 = -h_0\sigma_z$ and $H(t) = -\boldsymbol{h}(t) \cdot \boldsymbol{\sigma}$, up to 2nd order of h one can find:

$$\sigma^i(t) \approx \sigma_0^i(t) - \frac{1}{\hbar^2}\int_0^t dt_1 \int_0^{t_1} dt_2\, U_0^\dagger(t) \left[\left[\sigma^i, \sigma_0^j(-t_2)\right], \sigma_0^k(-t_1)\right] U_0(t) \langle h^j(t_2) h^k(t_1) \rangle_h \tag{10}$$

where $\langle h^j(t_2)h^k(t_1)\rangle_h$ is the stochastic average over $\boldsymbol{h}(t)$, and $U_0(t) \equiv \exp(-itH_0/\hbar)$. We assume $\boldsymbol{h}(t)$ to be described by a Gauss-Markov process with the autocorrelation

$$\langle h^j(t_2)h^k(t_1)\rangle_h = c_h\delta^{jk}e^{-\Gamma_h|t_1-t_2|} \tag{11}$$

Here, c_h is the variance of the dipolar fields at $\Delta t = 0$, δ^{ij} is the Kronecker delta, and Γ_h is the phenomenological decay rate. The integrals in Eq. 10 can be done explicitly, leading to:

$$\begin{aligned}
\sigma^+(t) &= \sigma_0^+(t)\left[1-\frac{c_h}{\hbar^2}\left(\frac{|t|}{\Gamma_h}+\frac{e^{-\Gamma_h|t|}-1}{\Gamma_h^2}-\frac{|t|}{2i\omega_0-\Gamma_h}+\frac{e^{2i\omega_0 t-\Gamma_h|t|}-1}{(2i\omega_0-\Gamma_h)^2}\right)\right]\\
\sigma^-(t) &= \sigma_0^-(t)\left[1-\frac{c_h}{\hbar^2}\left(\frac{|t|}{\Gamma_h}+\frac{e^{-\Gamma_h|t|}-1}{\Gamma_h^2}+\frac{|t|}{2i\omega_0+\Gamma_h}+\frac{e^{-2i\omega_0 t-\Gamma_h|t|}-1}{(2i\omega_0+\Gamma_h)^2}\right)\right]\\
\sigma^z(t) &= \sigma^z\left[1-\frac{c_h}{\hbar^2}\left(\frac{2|t|\Gamma_h}{4\omega_0^2+\Gamma_h^2}+\frac{e^{2i\omega_0 t-\Gamma_h|t|}-1}{(2i\omega_0-\Gamma_h)^2}+\frac{e^{-2i\omega_0 t-\Gamma_h|t|}-1}{(2i\omega_0+\Gamma_h)^2}\right)\right]
\end{aligned} \tag{12}$$

where $\omega_0 \equiv h_0/\hbar$. Therefore, all components have a common form:

$$\sigma^i(t) = \sigma_0^i(t)[1-f(t)] \approx \sigma_0^i(t)e^{-f(t)} \tag{13}$$

A more complete discussion on the approximation involved in the last step can be found in Ref.[18] The decay behavior of $\sigma^i(t)$ is thus due to the linear in t terms in Eq. 12. These can also be obtained by taking the long-time limit ($|t| \to \infty$), which gives:

$$\sigma^{+}(t) \approx \sigma_0^{+}(t)\exp\left[-\frac{c_h}{\hbar^2}\left(\frac{|t|}{\Gamma_h}-\frac{|t|}{2i\omega_0-\Gamma_h}\right)\right]$$
$$\sigma^{-}(t) \approx \sigma_0^{-}(t)\exp\left[-\frac{c_h}{\hbar^2}\left(\frac{|t|}{\Gamma_h}+\frac{|t|}{2i\omega_0+\Gamma_h}\right)\right] \quad (14)$$
$$\sigma^{z}(t) \approx \sigma^{z}\exp\left[-\frac{c_h}{\hbar^2}\left(\frac{2|t|\Gamma_h}{4\omega_0^2+\Gamma_h^2}\right)\right]$$

In the $\omega_0 \to 0$ limit relevant to the AC susceptibility measurements, one cannot truncate the perturbation series at 2nd order (to be discussed further below). However, in the following regime:

$$\sqrt{c_h}/\hbar \ll \omega_0 \ll \Gamma_h \quad (15)$$

the 2nd order perturbation result should still be valid, which gives:

$$\Gamma^{\pm} = \Gamma^{z} = \frac{2c_h}{\hbar^2\Gamma_h} \quad (16)$$

Where Γ^z is the axial component of the relaxation rate. Although Eq. 15 may not be satisfied in the present experiments, the relaxation rate in Eq. 16 is still a useful reference for making qualitative estimates. For example, when $[Co(SPh)_4]^{2-}$ is diluted by **Ni** or **Zn** which does not contribute to the fluctuating dipolar fields at low temperatures, the dipolar field felt by each $[Co(SPh)_4]^{2-}$ is only due to the other Co ions, felt at long range. Then it is natural to expect that Γ_h ~ Γ, and Eq. 16 suggests that:

$$\Gamma \sim \Gamma_h \sim \frac{\sqrt{2c_h}}{\hbar} \tag{17}$$

We will see below that in the other limit $\Gamma_h \ll \frac{\sqrt{c_h}}{\hbar}$, Γ is of the same order as Γ_h and is independent of c_h. Therefore Eq. 17 is expected to hold approximately when Γ_h is not too small compared to $\sqrt{c_h}/\hbar$.

A nonperturbative treatment of zero-field spin relaxation was first developed by Kubo and Toyabe,[19] by treating $\boldsymbol{h}(t)$ as a random vector that can be described as a Gauss-Markov process. Analytic results can be obtained using this approach in the static limit ($\Gamma_h = 0$) and isotropic $c_h^n = c_h$. The result is the Kubo-Toyabe relaxation function:

$$\Phi^{zz}(t) = \frac{1}{3} + \frac{2}{3}\left(1 - \frac{c_h t^2}{\hbar^2}\right) e^{-\frac{c_h t^2}{2\hbar^2}}, \tag{18}$$

which approaches a constant as $t \to \infty$. When Γ_h is finite the $\frac{1}{3}$ will be replaced by a complex time-dependent function and only numerical results can be obtained in general. Therefore, the long-time decay behavior necessarily comes from finite Γ_h. In the present case, since Γ_h itself is implicitly dependent on c_h (as the bath spins are coupled together through the dipolar interaction), such a calculation is not necessarily useful. Instead, we may consider the other limit $\Gamma_h \ll \frac{\sqrt{c_h}}{\hbar}$ that was not able to be addressed using the perturbation method. For isotropic c_h, Ref. [6] showed analytically that in this limit the long-time behavior of Φ^{zz} is described by an infinite sum of exponentially decaying functions with different decay rates:

$$\Gamma_n = \left(\frac{-1+\sqrt{17}}{2} + 2n\right)\Gamma_h, n = 0,1,2, \ldots \tag{19}$$

The long-time decay is then governed by $\Gamma_0 \approx 1.56\Gamma_h$. Therefore, qualitatively we expect that the decay rate is of the same order of magnitude as Γ_h in the limit of $\Gamma_h \ll \frac{\sqrt{c_h}}{\hbar}$ as well, and $\frac{\sqrt{c_h}}{\hbar}$ serves as an upper bound of Γ. The main problem with this approach is, however, that Γ_h depends on the microscopic details of the bath, some of which are experimentally unknown here and therefore its value cannot be given by this theory.

Relaxation of an effective *S* = ½ pseudospin of a single Co ion

The cobalt complex of the report is an $S = 3/2$ molecule with large zero-field splitting. The local Hamiltonian of an isolated Co ion is governed by the crystal electric field (CEF) contribution. By keeping terms up to 2nd order in spin operators we have the following simplified CEF Hamiltonian:

$$H_{CEF} = DS_z^2 + E\left(S_x^2 - S_y^2\right), \tag{20}$$

here *D* and *E* are input from fits of experimental data. For $S = \frac{3}{2}$, the spin operators take the following form in the S_z eigenstate basis $\{|m = -\frac{3}{2}\rangle, |m = -\frac{1}{2}\rangle, |m = \frac{1}{2}\rangle, |m = \frac{3}{2}\rangle\}$:

$$S_x = \begin{pmatrix} 0 & \frac{\sqrt{3}}{2} & 0 & 0 \\ \frac{\sqrt{3}}{2} & 0 & 1 & 0 \\ 0 & 1 & 0 & \frac{\sqrt{3}}{2} \\ 0 & 0 & \frac{\sqrt{3}}{2} & 0 \end{pmatrix}, S_y = \begin{pmatrix} 0 & \frac{\sqrt{3}}{2}i & 0 & 0 \\ -\frac{\sqrt{3}}{2}i & 0 & i & 0 \\ 0 & -i & 0 & \frac{\sqrt{3}}{2}i \\ 0 & 0 & -\frac{\sqrt{3}}{2}i & 0 \end{pmatrix}, S_z = \begin{pmatrix} -\frac{3}{2} & 0 & 0 & 0 \\ 0 & -\frac{1}{2} & 0 & 0 \\ 0 & 0 & \frac{1}{2} & 0 \\ 0 & 0 & 0 & \frac{3}{2} \end{pmatrix} \tag{21}$$

where we have set $\hbar = 1$. For the case of (Ph$_4$P)$_2$[Co(SPh)$_4$], $D < 0$ and $|D| \gg |E|$, the two low-energy eigenstates mainly consist of the states with $m = \pm\frac{3}{2}$. At the lowest temperatures (below 10 K, where the χ'' measurements were performed) the size of the *D* ensures near complete population of these levels and negligible population of the higher lying $m = \pm\frac{1}{2}$ levels. Thus, we define them as up and down eigenstates of a pseudospin $S = \frac{1}{2}$, as follows (assuming $E > 0$):

$$|\uparrow\rangle = u|m = 3/2\rangle - \sqrt{1-u^2}|m = -1/2\rangle \tag{22}$$

$$|\downarrow\rangle = v|m = -3/2\rangle - \sqrt{1-v^2}|m = 1/2\rangle$$

where

$$u = \left[1 + \left(\frac{\sqrt{D^2+3E^2}+D}{\sqrt{3}E}\right)^2\right]^{-\frac{1}{2}}, v = \frac{\sqrt{D^2+3E^2}-D}{\sqrt{3E^2+\left(\sqrt{D^2+3E^2}-D\right)^2}} \tag{23}$$

u, v approach 1 as $|E/D| \to 0$. One can then define the pseudospin operators $\tilde{\boldsymbol{\sigma}}$ as the usual Pauli matrices but in the $|\uparrow\rangle$, $|\downarrow\rangle$ basis. Moreover, the original $S = \frac{3}{2}$ operators projected to the pseudospin space and rotated to the $|\uparrow\rangle$, $|\downarrow\rangle$ basis have the following form

$$(S_x, S_y, S_z)_{ps} = (g_x\tilde{\sigma}^x, g_y\tilde{\sigma}^y, g_z\tilde{\sigma}^z), \tag{24}$$

$$(g_x, g_y, g_z) = \left(\frac{D-3E}{2\sqrt{D^2+3E^2}} + \frac{1}{2}, -\frac{D+3E}{2\sqrt{D^2+3E^2}} - \frac{1}{2}, -\frac{D}{2\sqrt{D^2+3E^2}} + \frac{1}{2}\right) \approx \frac{3}{2}\left(\frac{E}{D}, \frac{E}{D}, 1\right)$$

Since $|E/D| \ll 1$, magnetic fields predominantly couple to the z component of the pseudospin only. Thus, if one calculates χ'' and Φ using the $S = \frac{1}{2}$ results in the previous subsections, the power absorption is dominated by χ''_{zz} since the other contributions will be suppressed by E^2/D^2. On the other hand, in the expression of $\sigma_z(t)$ (or rather $\tilde{\sigma}^z(t)$) one would just need to do the following replacement:

$$c_h \to \frac{9E^2\gamma_{Co}^2\hbar^2}{8D^2}(c_h^x + c_h^y) \tag{25}$$

if different components of the fluctuating magnetic fields are allowed to have different variances. We have also recovered the gyromagnetic ratio of Co ($\gamma_{\mathrm{Co}} = g_{\mathrm{Co}}\mu_B/\hbar$) and $\hbar$. A crude estimate of the relaxation rate based on Eq. 16 is then

$$\Gamma^z = \frac{9E^2\gamma_{Co}^2}{4D^2\Gamma_h}(c_h^x + c_h^y) \tag{26}$$

or, if $\Gamma^z \sim \Gamma_h$

$$\Gamma_z \sim \frac{3|E\gamma_{Co}|}{2|D|}\sqrt{c_h^x + c_h^y} \tag{27}$$

From this result, we see that the relaxation rate is directly driven by magnetic dipolar field components in the xy plane relative to the embedded spin. We also see that the rate is dependent on the E of the embedded ion. As E is extremely small[20] and likely consistent in the different environments owing to the strong structural similarities of the MS_4 coordination shells,[21] the rate changes as a function of bath are more likely to be impacted by changes in c_h^x and c_h^y, which are diluent dependent.

Estimation of c_h

In this subsection we provide estimates of the c_h in the present experimental system. The dipolar magnetic field generated at the position of a Co ion in $[\mathrm{Co(SPh)_4}]^{2-}$ (assumed to be the origin) by another spin ($\boldsymbol{S}_i''$) is:

$$h_i = \frac{\mu_0 \gamma_b}{4\pi r_i^3}[3\hat{\boldsymbol{r}}(\boldsymbol{S}_i'' \cdot \hat{\boldsymbol{r}}_i) - \boldsymbol{S}_i''], \tag{28}$$

where γ_b is the gyromagnetic ratio of bath spins, $\hat{\boldsymbol{r}}_i$ is the distance separating the two spins, and μ_0 is the vacuum permeability. The total dipolar field at origin is:

$$\boldsymbol{h}_d = \sum_i \boldsymbol{h}_i \tag{29}$$

For the convenience of studying the temperature dependence of the bath spins, we introduce a basis $\{\hat{\boldsymbol{e}}_j''\} = \{\hat{\boldsymbol{x}}'', \hat{\boldsymbol{y}}'', \hat{\boldsymbol{z}}''\}$ consistent with the local coordinates of a bath spin S_j (according to which its D and E are defined). Similarly, the local basis for the Co ion at the origin is defined as $\{\hat{\boldsymbol{e}}_j'\} = \{\hat{\boldsymbol{x}}', \hat{\boldsymbol{y}}', \hat{\boldsymbol{z}}'\}$. As a first approximation, we assume the bath spins do not have correlation with each other. Then, taking $\langle h^{z'}\, h^{z'} \rangle$ as an example,

$$\langle h^{z'}\, h^{z'} \rangle = \sum_{ij} \langle h_i^{z'} h_j^{z'} \rangle = \sum_i \langle h_i^{z'} h_i^{z'} \rangle \tag{30}$$

$$= \sum_i \left(\frac{\mu_0 \gamma_b}{4\pi r_i^3}\right)^2 \left[9(\hat{\boldsymbol{r}}_i \cdot \hat{\boldsymbol{z}}')^2 \langle (\boldsymbol{S}_i'' \cdot \hat{\boldsymbol{r}}_i)^2 \rangle - 3(\hat{\boldsymbol{r}}_i \cdot \hat{\boldsymbol{z}}')\Big(\langle (\boldsymbol{S}_i'' \cdot \hat{\boldsymbol{r}}_i)(S_i'')^{z'} \rangle + \langle (S_i'')^{z'} (\boldsymbol{S}_i'' \cdot \hat{\boldsymbol{r}}_i) \rangle\Big)\right.$$

$$\left. + \langle (S_i'')^{z'} (S_i'')^{z'} \rangle \right]$$

$\langle S^\alpha S^\beta \rangle$ for independent spins in thermal equilibrium should be:

$$\langle S^\alpha S^\beta \rangle = \frac{1}{Z} Tr\left[e^{-\beta H} S^\alpha S^\beta\right] = \frac{1}{Z} \sum_i e^{-\beta \varepsilon_i} (U^\dagger S^\alpha S^\beta U)_{ii} \tag{31}$$

Where U is the unitary transformation that diagonalizes H. Due to the independent spin assumption, samples of different dopant concentrations can be considered simply by making:

$$\langle h_i^\alpha h_i^\alpha \rangle = f_{\mathrm{Ni}} \langle h_i^\alpha h_i^\alpha \rangle_{\mathrm{Ni}} + f_{\mathrm{Co}} \langle h_i^\alpha h_i^\alpha \rangle_{\mathrm{Co}} \tag{32}$$

where f_s is the concentration of species s, and $\langle h_i^\alpha h_i^\alpha \rangle_s$ is the correlation calculated with all bath spins being species s. It is important to note that in calculating $\langle h_i^\alpha h_i^\alpha \rangle_s$ one must use the correct spin Hamiltonians, i.e. $S = \frac{3}{2}$ for Co, and $S = 1$ for Ni. Also, for Ni, since its ground state is a singlet (i.e. $D > 0$), the dipolar field due to Ni is not active unless the temperature is comparable to $|D|$. Fundamentally this is because the effect of the "dipolar field" in Co spin relaxation comes from intra-band transitions among the low-energy modes in the bath. Therefore, we accounted for this effect in our calculation by replacing $\boldsymbol{S}$ with $P\boldsymbol{S}P$, where P is a projection operator that projects out matrix elements across nondegenerate levels.

In calculating $c_h^\alpha \sim \langle h^\alpha h^\alpha \rangle$ we use $\gamma_s = g_s \mu_B / \hbar$ where s = {**Ni** or **Co**}, together with the parameter values listed in Tables A5 and A6. c_h therefore has units of T^2 (T = Tesla), and the spin operators are dimensionless.

The much smaller c_h in the case of **Ni** when one uses the projection operator is due to the inactive $m = \pm 1$ levels of its spin at low temperatures. Thus, the typical size of the fluctuating dipolar magnetic field, when the bath spins have dipole moments, is $\sim 10^{-3}$ T. This can be converted to a frequency by doing the substitution in Eq. 25. Since $\frac{g_{Co}\mu_B E}{D} \times 1T \sim 10^{-9}$ eV, the fluctuating dipolar field corresponds to an energy scale of $\sim 10^{-11} - 10^{-12}$ eV, or $10^3 - 10^4$ Hz. This is much larger than the $\Gamma = \frac{1}{\tau} < 10^2$ Hz measured experimentally. The experimental system is therefore in the limit of $\Gamma_h \ll \frac{\sqrt{c_h}}{\hbar}$, when $[Co(SPh)_4]^{2-}$ is diluted by nonmagnetic ions such as Zn(II). Thus, the slowing down of **Co** relaxation as the concentration of **Ni** increases is due to the decreasing Γ_h. Although qualitatively it is reasonable to expect that Γ_h should decrease with decreasing c_h, their precise relationship can only be established by understanding the dynamics of the correlated bath spins, which is beyond the theories presented here and will be left for future study. Nonetheless, the qualitative trend is in agreement with the zero-field splitting and spin relaxation processes that are well-documented for mononuclear single molecule magnets like $[Co(SPh)_4]$.[22] On the other hand, when the bath spins are **Mn**, the relaxation rate seems to approach the $\frac{\sqrt{c_h}}{\hbar}$. Thus Eq. 17 may be used to estimate the dependence of Γ on the concentration of **Mn**.

Table A1: Summary of spin Hamiltonian parameters obtained from susceptibility and EPR analyses of **Co, Ni, Fe,** and **Mn**.

	Co		**Ni**		**Fe**		**Mn**	
	$\chi_\mathrm{M}T$	EPR[a]	$\chi_\mathrm{M}T$	EPR[a]	$\chi_\mathrm{M}T$	HF-EPR[g]	$\chi_\mathrm{M}T$	HF-EPR
g_x	2.076	-	-	-	2.02	2.051(1)	1.895	2.000
g_y	2.075	-	-	-	2.08	2.095(1)	2.001	2.000
g_z	2.576	-	-	-	1.95	2.010(1)	2.124	2.004
g_iso[b]	2.24	-	5.105[c]	-	2.02	2.052	2.007	-
D (cm^{-1})	–61.40	-	67.59	-	5.89	5.848(1)	0.354	–0.12
E (cm^{-1})[d]	0.011	-	–0.25	-	1.45	1.428(1)	0.00	–0.04
A_iso (MHz)[f]								252

[a]EPR silent on the instruments for this study. [b]Generally computed. [c]Extracted from fitting, as an isotropic g enabled the best simulation of the $\chi_\mathrm{M}T$ data. [d]For $\chi_\mathrm{M}T$, these values are at best interpreted as $|E|$. [f]Computed – but for HF-EPR, A_iso set to that from the X-band analyses. [g]Values (and uncertainties) extracted from the Florida map (Fig. S3).

Table A2: Summary of extracted relaxation parameters from fitting variable-temperature ac magnetic susceptibility data on **1** and dilutions in **2**.

	Pure Co		**1:2 Co:Ni**		**1:9 Co:Ni**		**1:34 Co:Ni**	
n[a]	5.6(1)	6	6.2(2)	6	6.09(8)	6	7.96(9)	8
A (K^{-n}s^{-1})	0.029(7)	0.014(1)	0.09(2)	0.112(4)	0.07(1)	0.08(2)	0.0026(3)	0.0026(1)
τ_QTM (s)	0.0066(4)	0.0060(3)	0.039(3)	0.041(3)	-[b]		-[b]	

[a]Values of n with uncertainties were obtained from fits, values without uncertainties were restrained to that value. [b]No QTM was extracted from the fitting process for these samples.

Table A3: Relaxation rates determined from fits of the zero-field ac susceptibility measurements for dilutions of **Co** in **Ni**, **Fe**, **Mn**, and **Zn** (All data were recorded at 2.0 K)

Ni Dilution	**Pure Co**	**73% Co**	**58% Co**	**25% Co**	**9% Co**	**3% Co**
1/τ (s^{-1})	177.3	96.2	62.7	32.9	5.9	0.7

Fe Dilution	**84% Co**	**57% Co**	**24% Co**	**16% Co**	**6% Co**
1/τ (s^{-1})	147.9	101.2	53.7	42.0	16.9

Mn Dilution	**81% Co**	**43% Co**
1/τ (s^{-1})	632.9	8222.6

Zn Dilution	**29% Co**	**2.5% Co**
1/τ (s^{-1})	22.2	1.6

Table A4: Extracted α parameters from AC susceptibility fitting for various dilutions of **Co** in **Ni**. All parameters are taken from zero-field data.

Pure Co		**1:2 Co:Ni**		**1:9 Co:Ni**		**1:34 Co:Ni**	
T (K)	**α**	*T* (K)	**α**	*T* (K)	**α**	*T* (K)	**α**
2.0	0.276	2.0	0.384	1.8	0.562	1.8	-[b]
2.3	0.267	2.5	0.296	2.0	0.522	2.0	0.579
2.6	0.245	3.0	0.208	2.3	0.433	2.3	0.496
3.0	0.193	3.5	0.159	2.6	0.351	2.6	0.370
3.5	0.130	4.5	0.116	3.0	0.275	3.0	0.340
4.0	0.090	5.5	0.081	3.5	0.229	3.5	0.315
4.5	0.067			4.0	0.198	4.0	0.362
5.0	0.049			4.5	0.182	4.5	0.293
5.5	0.032			5.0	0.180	5.0	0.378
6.0	0.027			5.5	0.182	5.5	0.395
6.5	0.025			6.0	0.154	6.0	0.276
				6.5	0.183	6.5	0.319

Table A5: Extracted α parameters from AC susceptibility fitting for various dilutions of **Co** into **Ni, Fe,** and **Mn** at 2 K. All values are taken from zero-field data.

Sample	Temperature (K)	α
Co	2	0.276
1:2 Co:Ni	2	0.384
1:9 Co:Ni	2	0.522
1:34 Co:Ni	2	0.579
1:17 Co:Fe	2	0.389
1:14.5 Co:Mn	2.3	0.276
1:1.27 Co:Mn	2	0.352

Table A6: Parameter values used in the calculations of c_h for **Ni**, **Co** and **Mn** bath spins.

Parameter	Unit	Value
$\hbar$	$[\mathrm{eV}][\mathrm{sec}]$	6.582×10^{-16}
$\hbar$	$[\mathrm{Joule}][\mathrm{sec}]$	1.05×10^{-34}
μ_B	$\frac{[\mathrm{Joule}]}{[\mathrm{Tesla}]}$	9.27×10^{-24}
μ_0	$\frac{[\mathrm{Henry}]}{[\mathrm{Meter}]}$	$4\pi \times 10^{-7}$
c	$\frac{[\mathrm{cm}]}{[\mathrm{sec}]}$	2.998×10^{10}
g_{Ni}	-	5.105
g_{Co}	-	2.24
g_{Mn}	-	2.126
$\gamma = \frac{g\mu_B}{\hbar}$	$\frac{[\mathrm{eV}]}{[\mathrm{Tesla}]}\frac{1}{[\mathrm{eV}][\mathrm{sec}]}$	$g \times 5.788 \times 10^{-5} \times \frac{1}{6.582 \times 10^{-16}}$
D_{Ni}	$[\mathrm{eV}]$	$+67.54\ \mathrm{cm}^{-1} \times \hbar[\mathrm{eV\ sec}] \times c[\mathrm{cm/sec}]$
E_{Ni}	$[\mathrm{eV}]$	$-0.25\ \mathrm{cm}^{-1} \times \hbar[\mathrm{eV\ sec}] \times c[\mathrm{cm/sec}]$
D_{Co}	$[\mathrm{eV}]$	$-61.4\ \mathrm{cm}^{-1} \times \hbar[\mathrm{eV\ sec}] \times c[\mathrm{cm/sec}]$
E_{Co}	$[\mathrm{eV}]$	$+0.0011\ \mathrm{cm}^{-1} \times \hbar[\mathrm{eV\ sec}] \times c[\mathrm{cm/sec}]$
D_{Mn}	$[\mathrm{eV}]$	$-0.097\ \mathrm{cm}^{-1} \times \hbar[\mathrm{eV\ sec}] \times c[\mathrm{cm/sec}]$
E_{Mn}	$[\mathrm{eV}]$	$+0.008\ \mathrm{cm}^{-1} \times \hbar[\mathrm{eV\ sec}] \times c[\mathrm{cm/sec}]$

Table A7: Calculated values of c_h for **Ni**, **Co** and **Mn** as bath spins in units of T^2 at 2 K.

	Ni (no projection)	Ni (projection)	Co	Mn
c_h^x	5.1×10^{-5}	2.7×10^{-7}	6.7×10^{-5}	9.66×10^{-5}
c_h^y	1.1×10^{-4}	4.8×10^{-8}	2.8×10^{-5}	7.14×10^{-5}
c_h^z	1.6×10^{-4}	8.0×10^{-8}	4.1×10^{-5}	1.02×10^{-4}

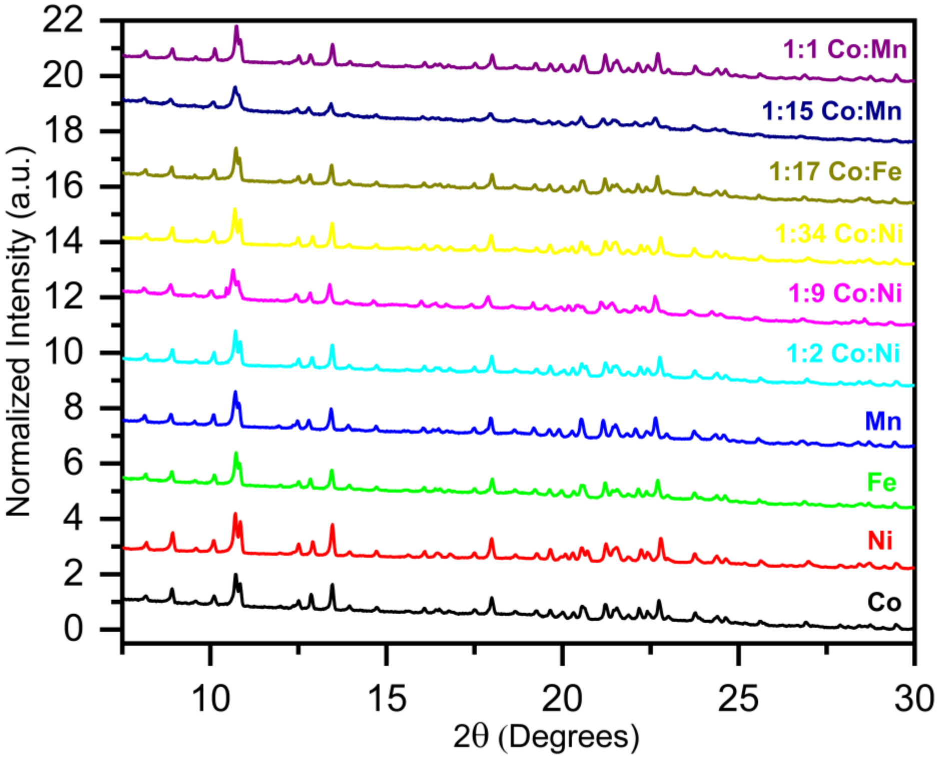

Figure A1: PXRD patterns for pure $(Ph_4P)_2[\mathbf{M}(SPh)_4]$ samples and paramagnetic dilutions – dilution stoichiometries are indicated on the graph.

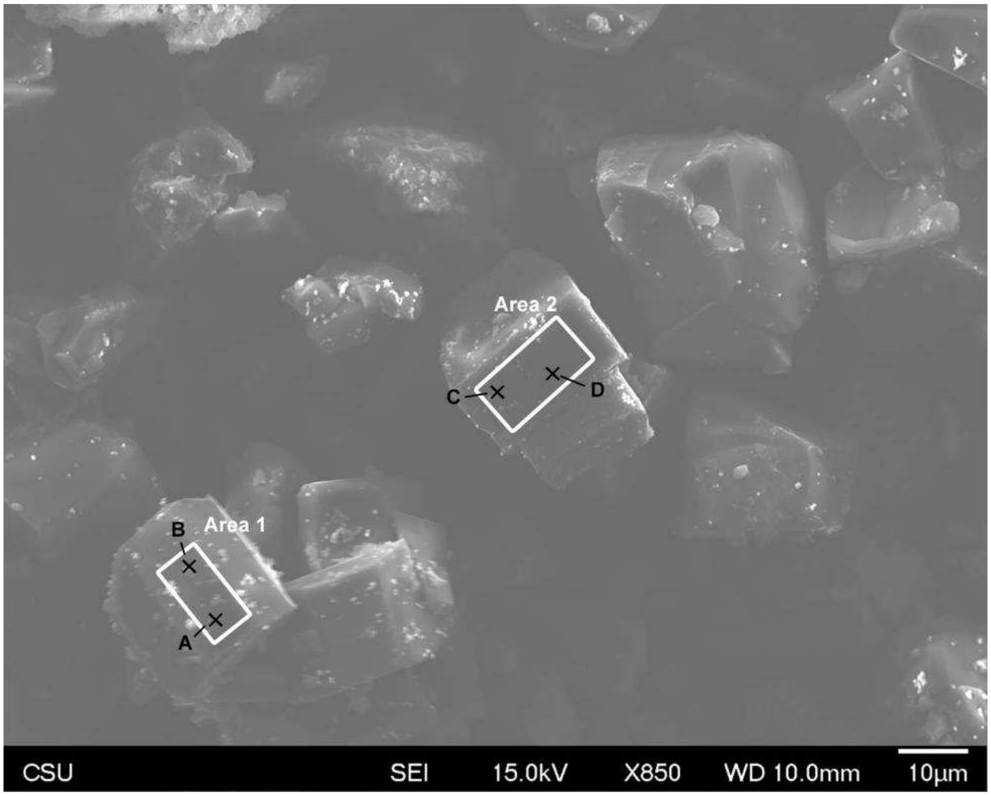

Figure A2: SEM EDS mapping of polycrystalline **Co** in **Fe** (16% **Co** by ICP-OES). Fe and Co atomic percentages for EDS points and areas are given in **Table S5**.

Table A7: EDS elemental mapping analysis for **Fig. A2**. Apparent concentrations have been normalized to Co

Sample Point	Fe Apparent Conc.	Co Apparent Conc.	% Co
Area 1	5.48	1	15.4
Point A	5.12	1	16.3
Point B	5.5	1	15.4
Area 2	6.04	1	14.2
Point C	5.76	1	14.8
Point D	6.19	1	13.9

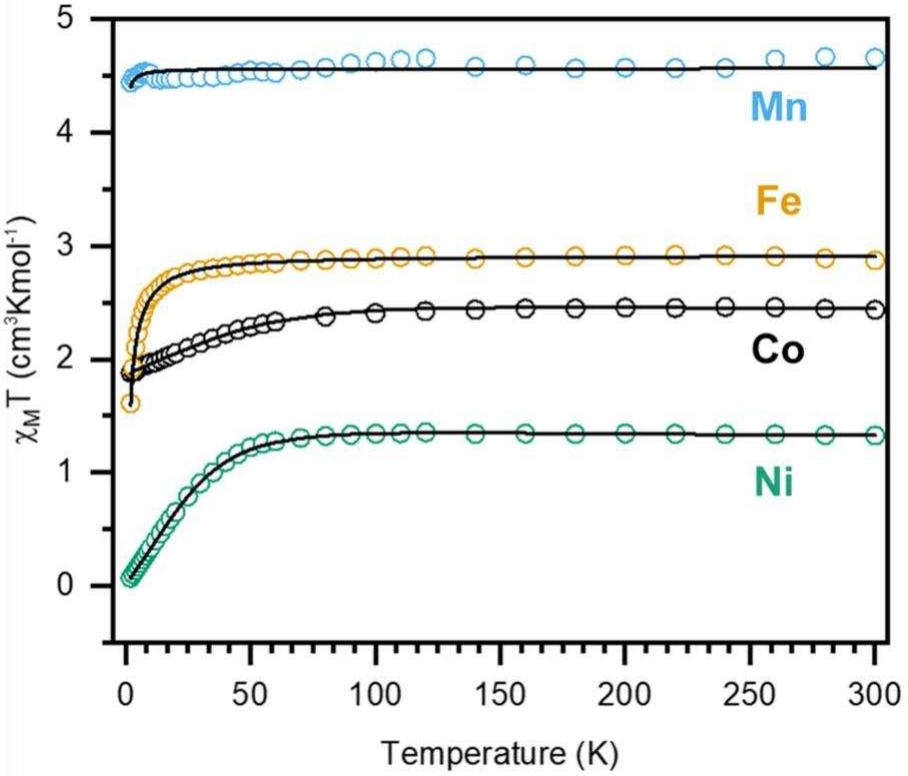

Figure A3: Variable temperature dc susceptibility ($\chi_M T$) data under an applied dc magnetic field of 1000 G for pure, polycrystalline samples of **Co, Ni, Fe,** and **Mn**. Fit lines were generated using PHI and the spin Hamiltonian parameters g_z, D, and E as outlined in the main paper.

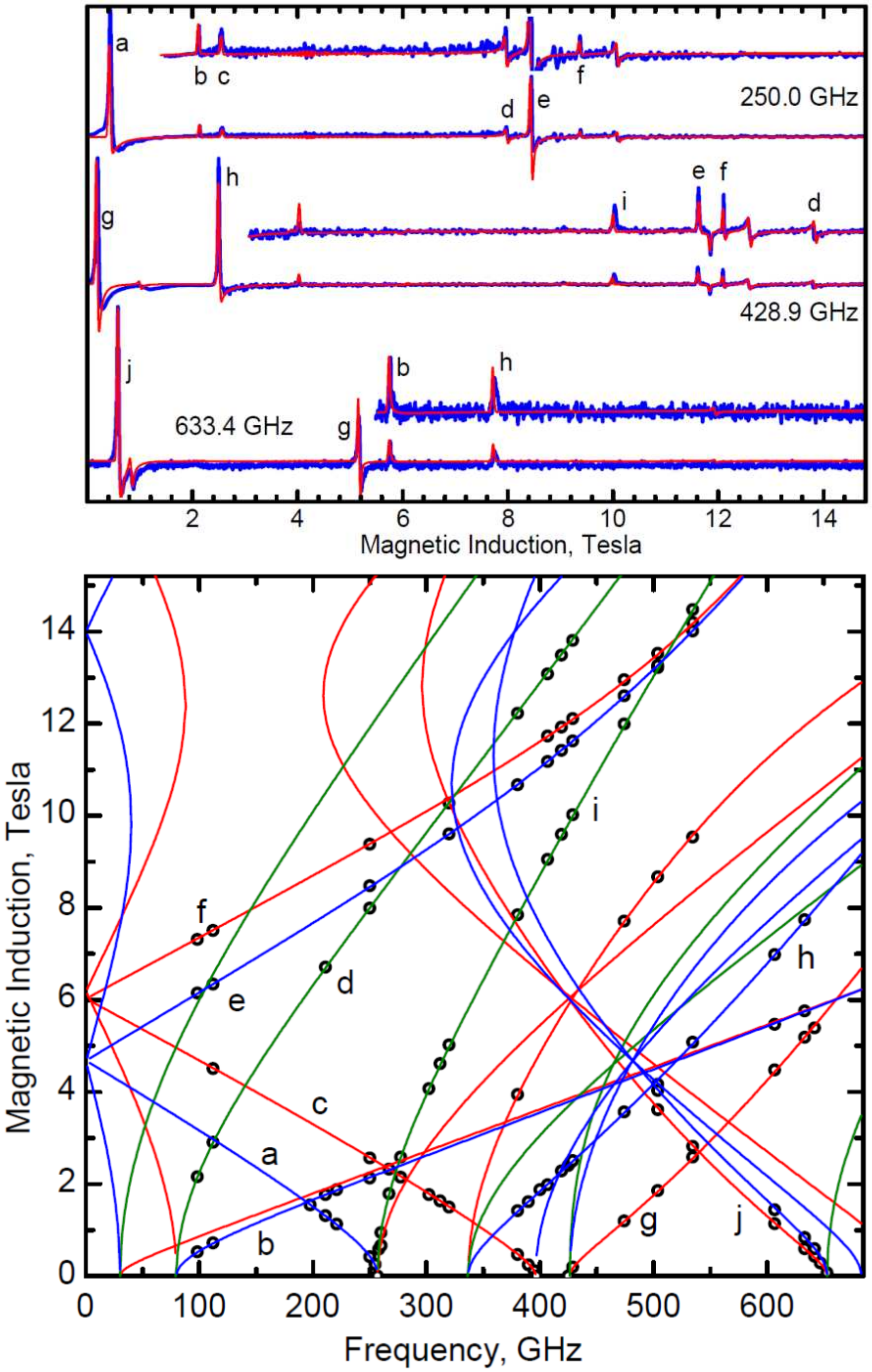

Figure A4: ***Top:*** HF EPR spectra of **Fe** recorded at 20 K with microwave frequencies indicated. Blue: experimental; red: simulated. Labels “a” through “j” refer to branches in map below. ***Bottom:*** Frequency dependencies of the resonance fields observed for Fe(SPh)$_4$. Circles: experimental points. The green, blue and red lines were calculated for the X, Y and Z directions, respectively.

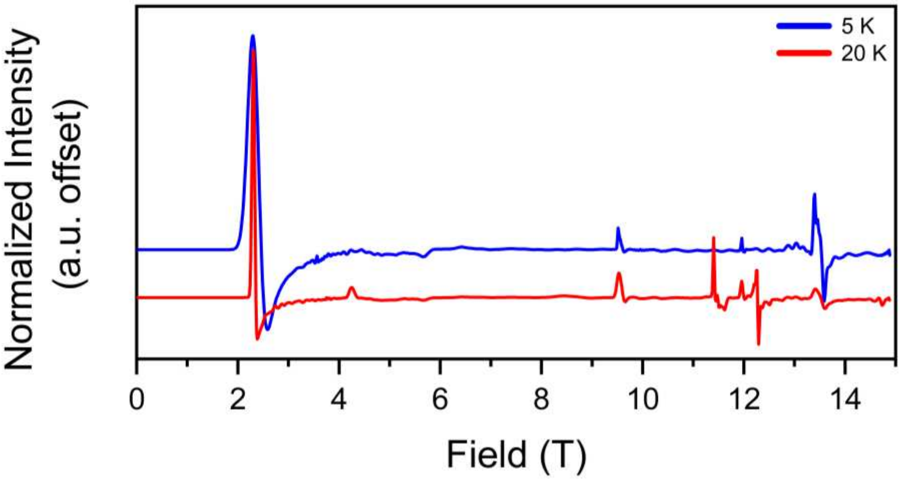

Figure A5: Variable-temperature high field, high frequency EPR spectra for **Fe**, collected at 20 and 5 K, and 419 GHz. Spectra are normalized to the highest intensity peak to clearly illustrate the identity of the ground state transitions.

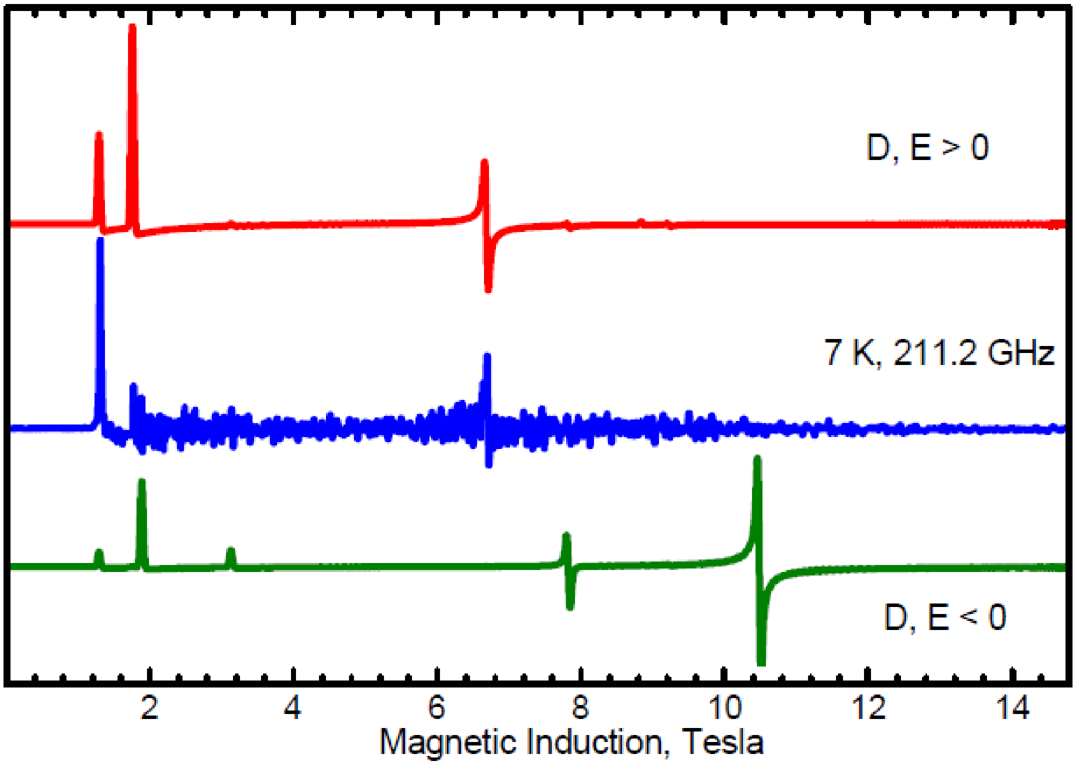

Figure A6: High-field, high-frequency EPR simulation comparison for positive (top) and negative (bottom) signs for *D* and *E* parameters for **Fe** at 7 K and 211.2 GHz.

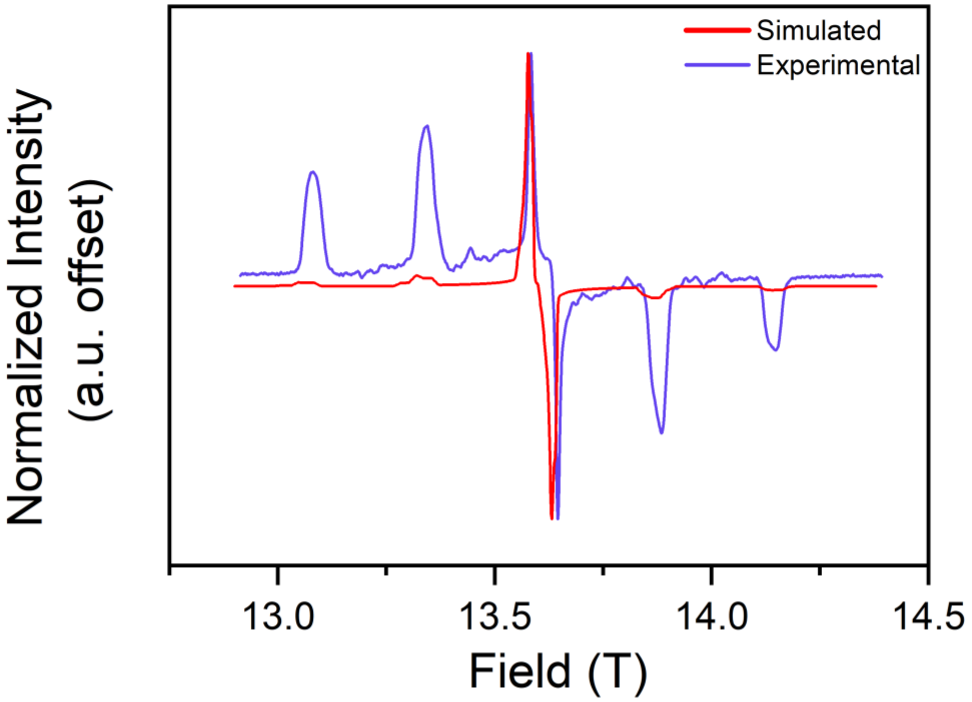

Figure A7: 381 GHz, 50 K EPR spectra for a crushed, crystalline sample of **Mn**. The simulated spectra were generated using the *Easyspin* package in MATLAB as outlined in the SI experimental section. Parameters for these best simulations can be found in Table S1**.**

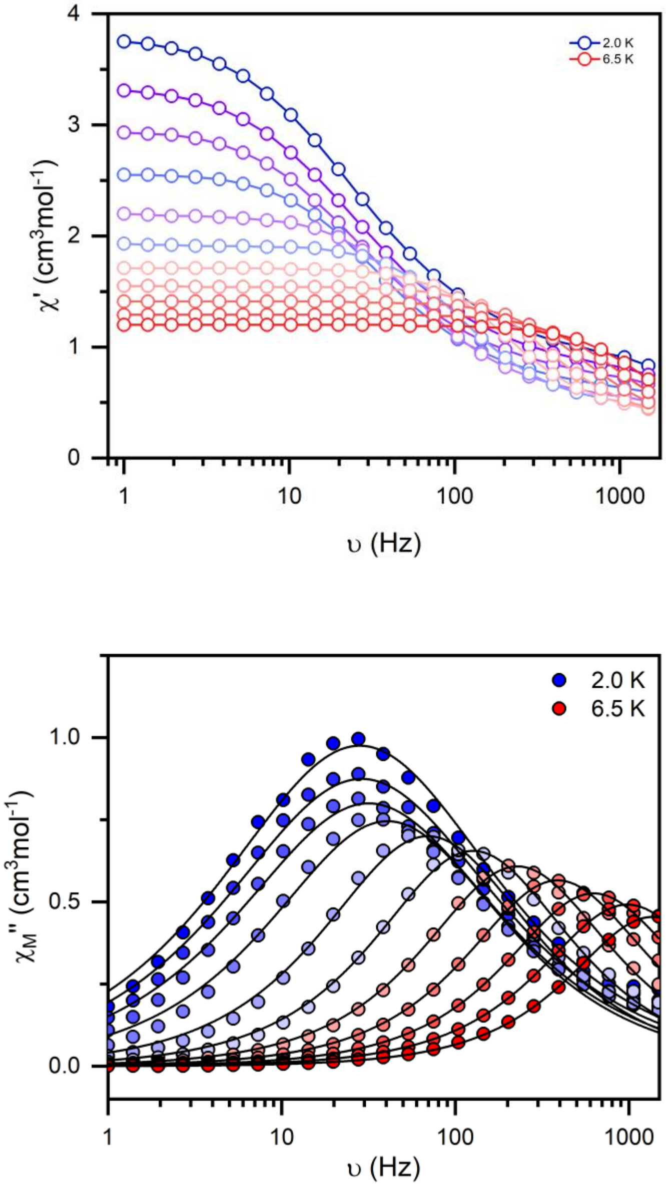

Figure A8: Variable temperature ac susceptibility data under zero applied field from (2.0 – 6.5 K) for a pure, polycrystalline sample of **Co**.

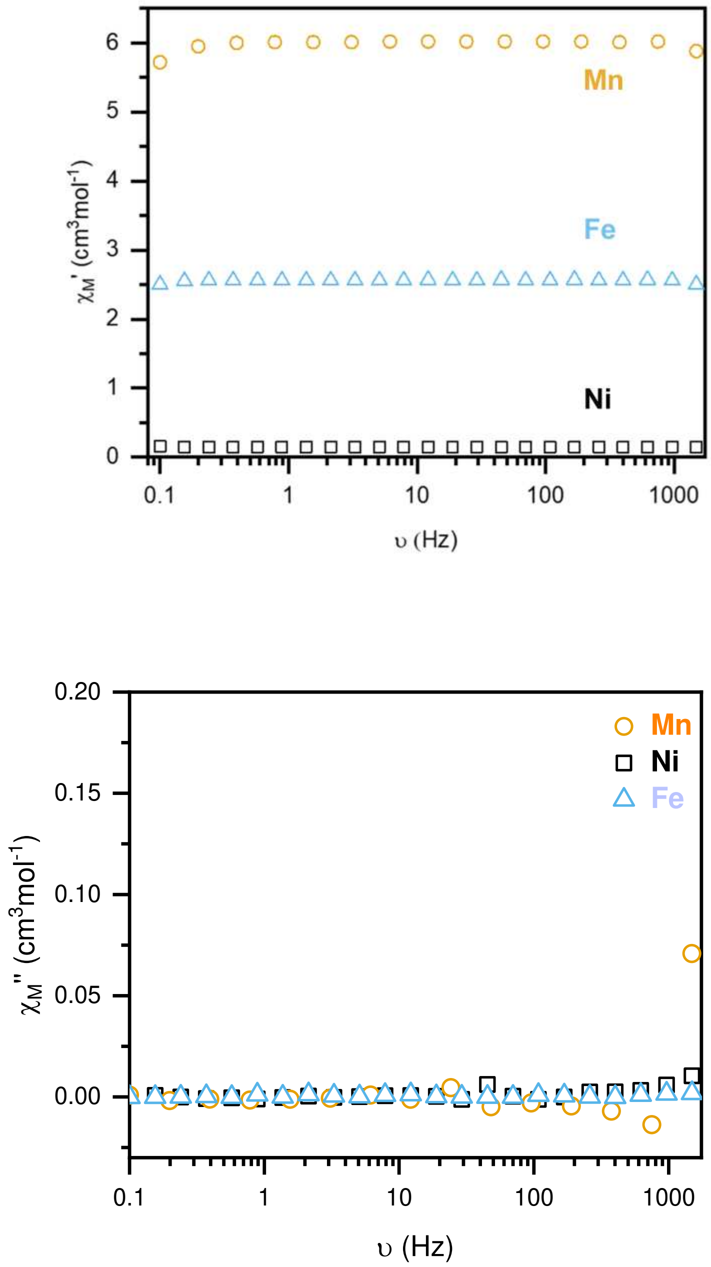

Figure A9: Variable-frequency ac susceptibility data under zero applied field at 3.0 K for pure, polycrystalline samples of **Ni, Fe,** and **Mn**.

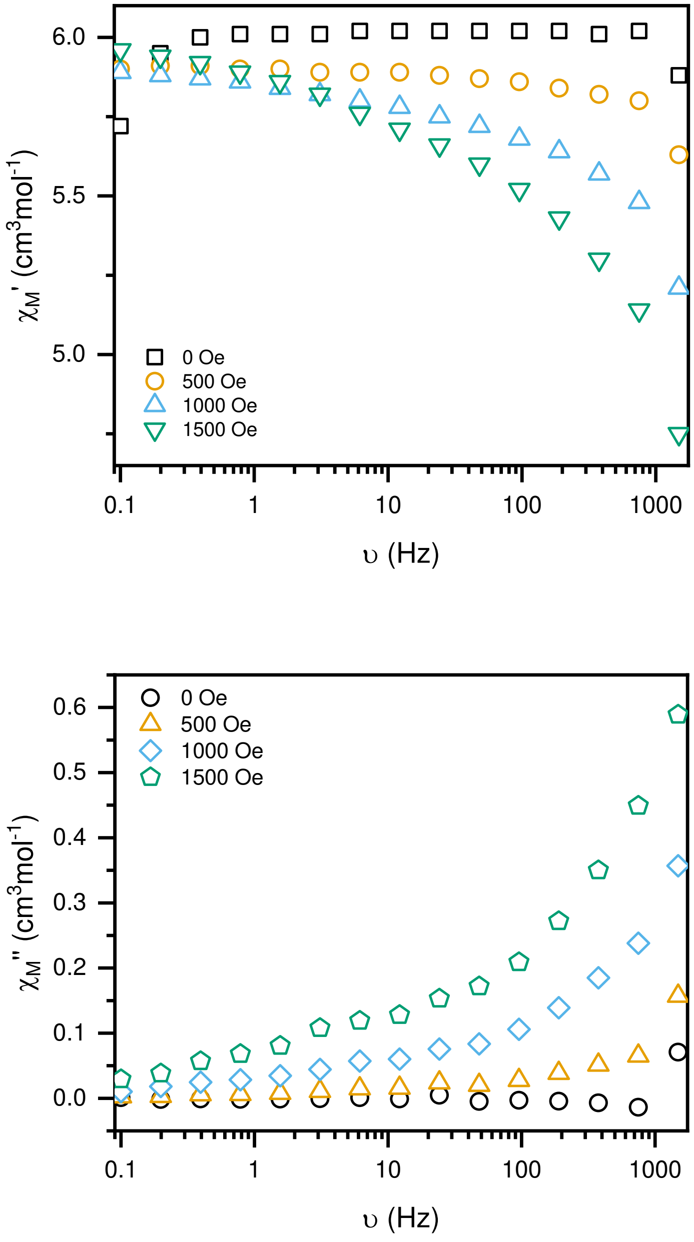

Figure A10: Variable-field, variable-frequency ac susceptibility data collected at 3.0 K on a polycrystalline sample of **Mn** restrained in eicosane**.**

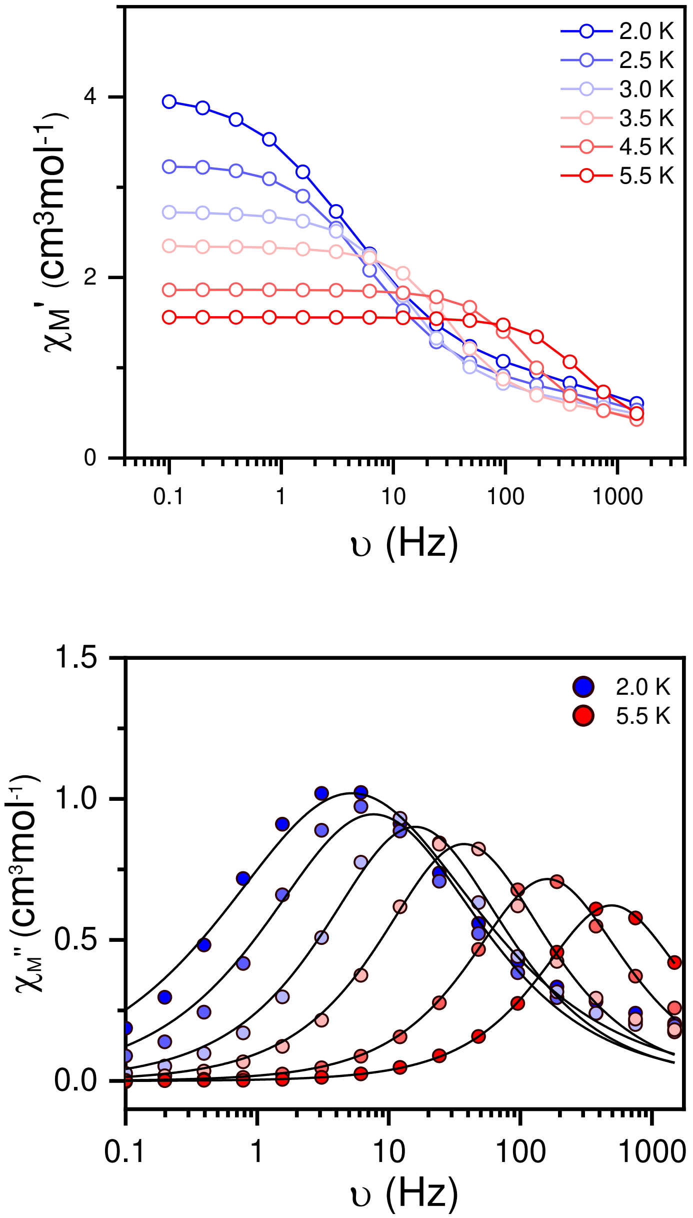

Figure A11: Variable temperature ac susceptibility data under zero applied field for a pure, polycrystalline sample of **1:2 Co:Ni**. Top: In-phase susceptibility, and Bottom: Out-of-phase susceptibility. Fit lines for bottom were generated using equation (1.1) as described in the SI. All ac susceptibility measurements were adjusted for moles of **Co** in the sample, as determined by ICP-OES.

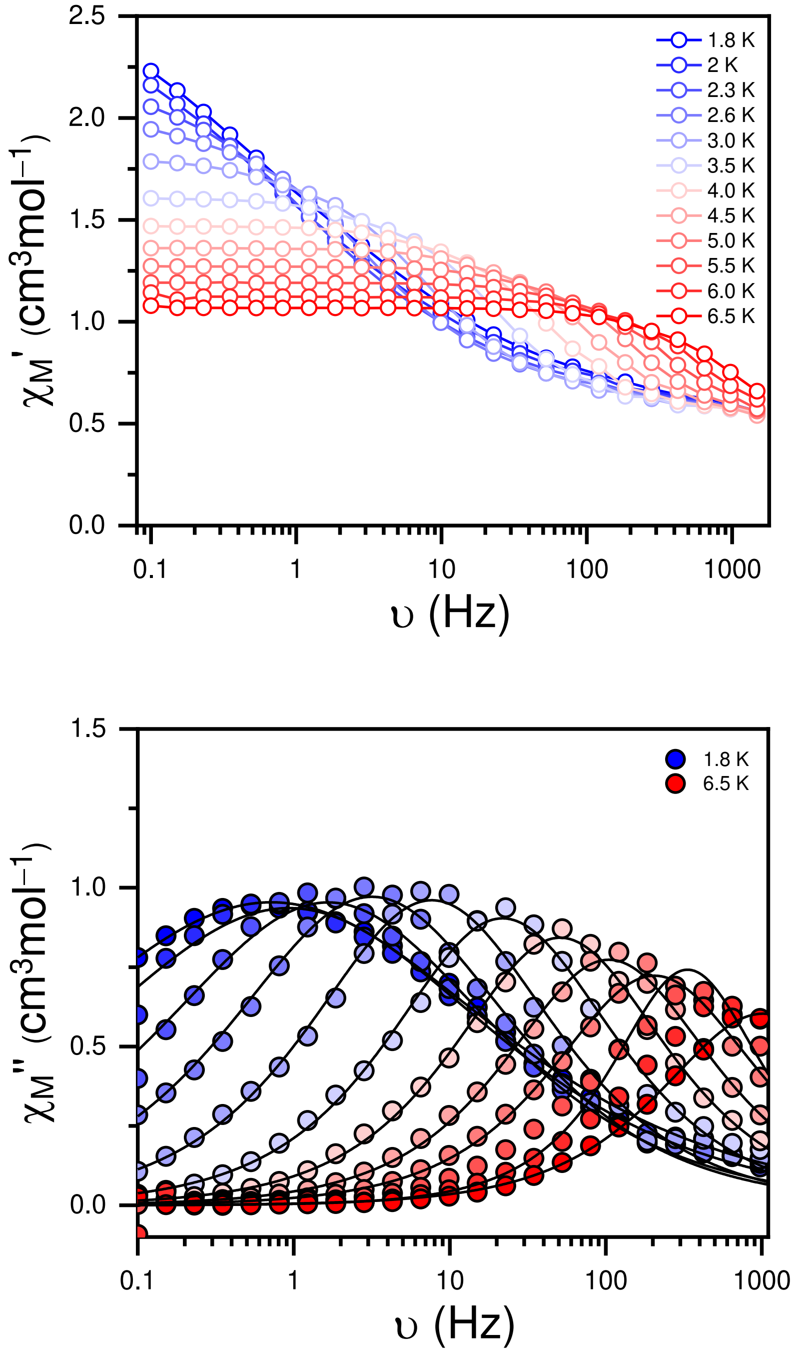

Figure A12: Variable temperature ac susceptibility data under zero applied field for a pure, polycrystalline sample of **1:9 Co:Ni**. Top: In-phase susceptibility, and Bottom: Out-of-phase susceptibility. Fit lines for bottom were generated using equation (1.1) as described in the SI. All ac susceptibility measurements were adjusted for moles of **Co** in the sample, as determined by ICP-OES.

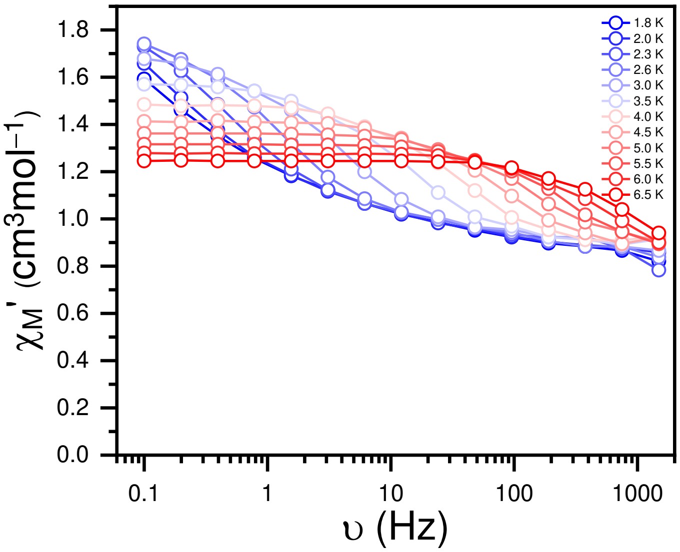

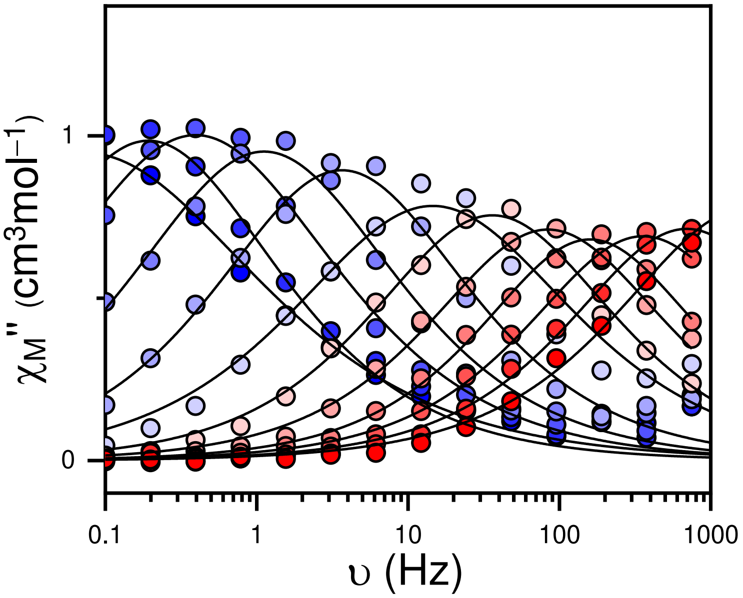

Figure A13: Variable temperature ac susceptibility data under zero applied field for a pure, polycrystalline sample of **1:34 Co:Ni**. Top: In-phase susceptibility, and Bottom: Out-of-phase susceptibility. Fit lines for bottom were generated using equation (1.1) as described in the SI. All ac susceptibility measurements were adjusted for moles of **Co** in the sample, as determined by ICP-OES.

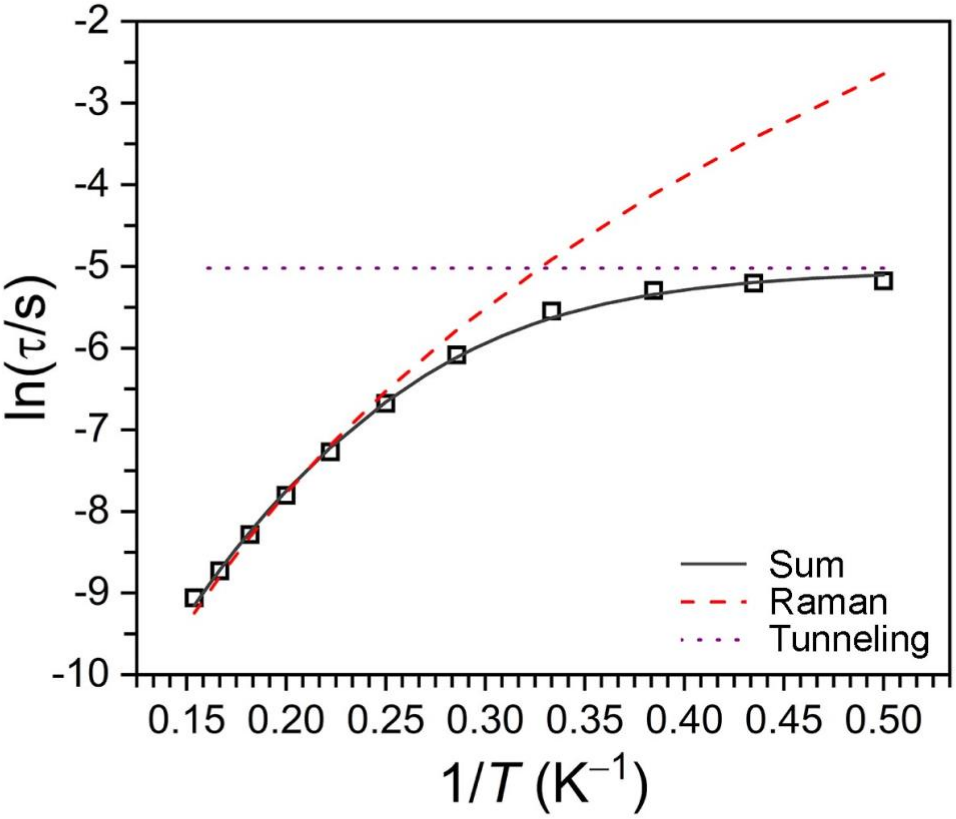

Figure A14: Variable temperature relaxation time for pure **Co** (black squares) and deconvoluted fit. See experimental section and Table S2 for fitting details. The parameters yielding these simulations are A = 0.029(7) $K^{-n}s^{-1}$, n = 5.6(1), and τ_{QTM} = 0.0066(4) s.

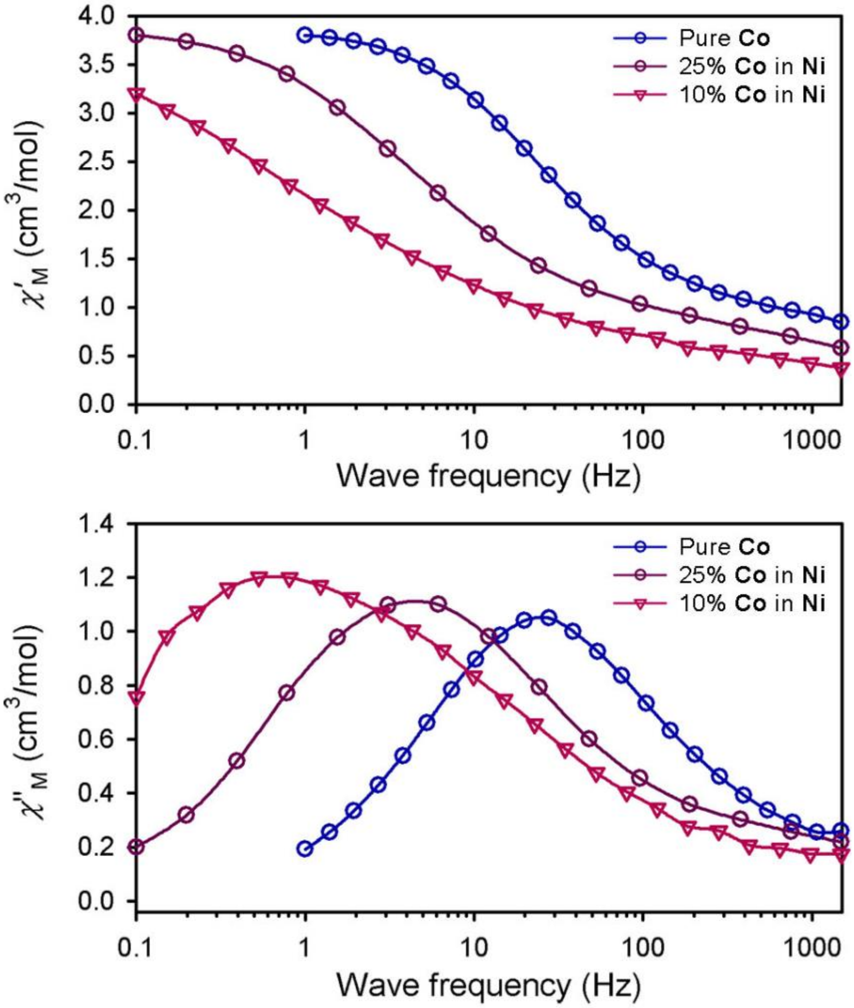

Figure A15: Select in- and out-of-phase ac susceptibility data (χ_M' and χ_M'', respectively) for **Co:Ni** dilutions at 2 K. Magnitudes of χ_M' and χ_M'' are normalized to the values for pure **Co** at 2 K. Solid lines are guides for the eye.

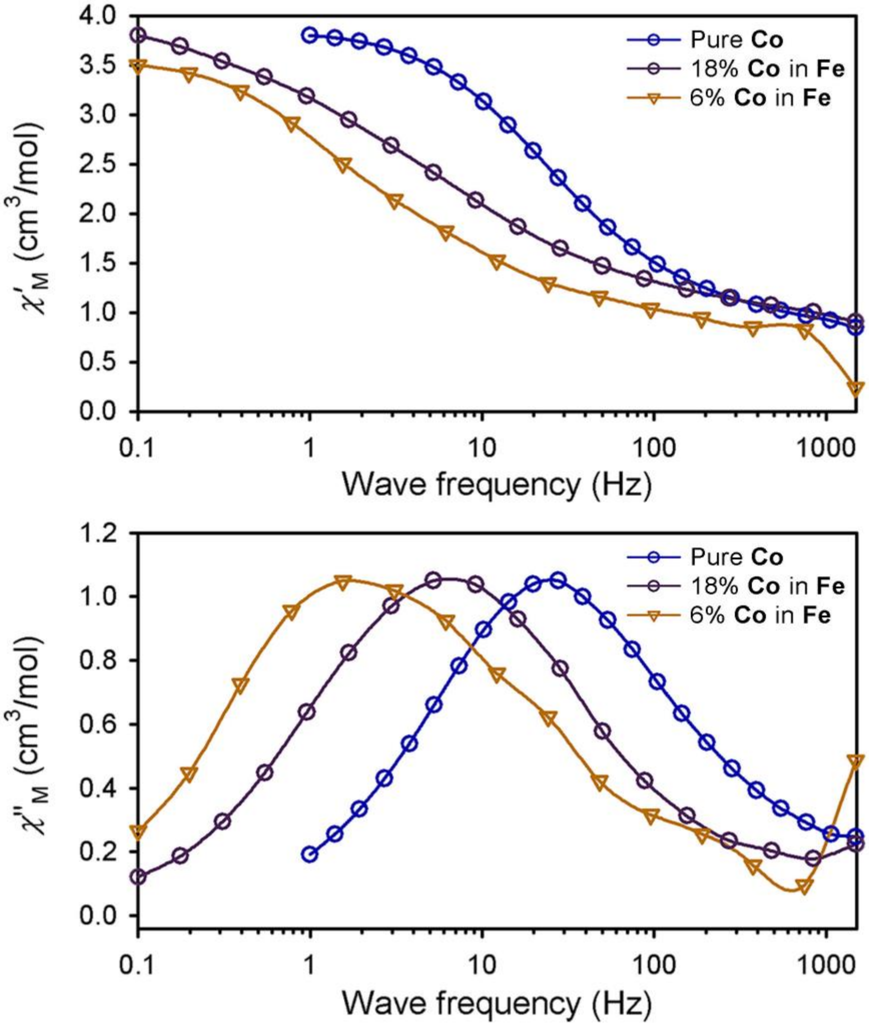

Figure A16: Select in- and out-of-phase ac susceptibility data (χ_M' and χ_M'', respectively) for **Co:Fe** dilutions at 2 K. Magnitudes of χ_M' and χ_M'' are normalized to the values for pure **Co** at 2 K. Solid lines are guides for the eye.

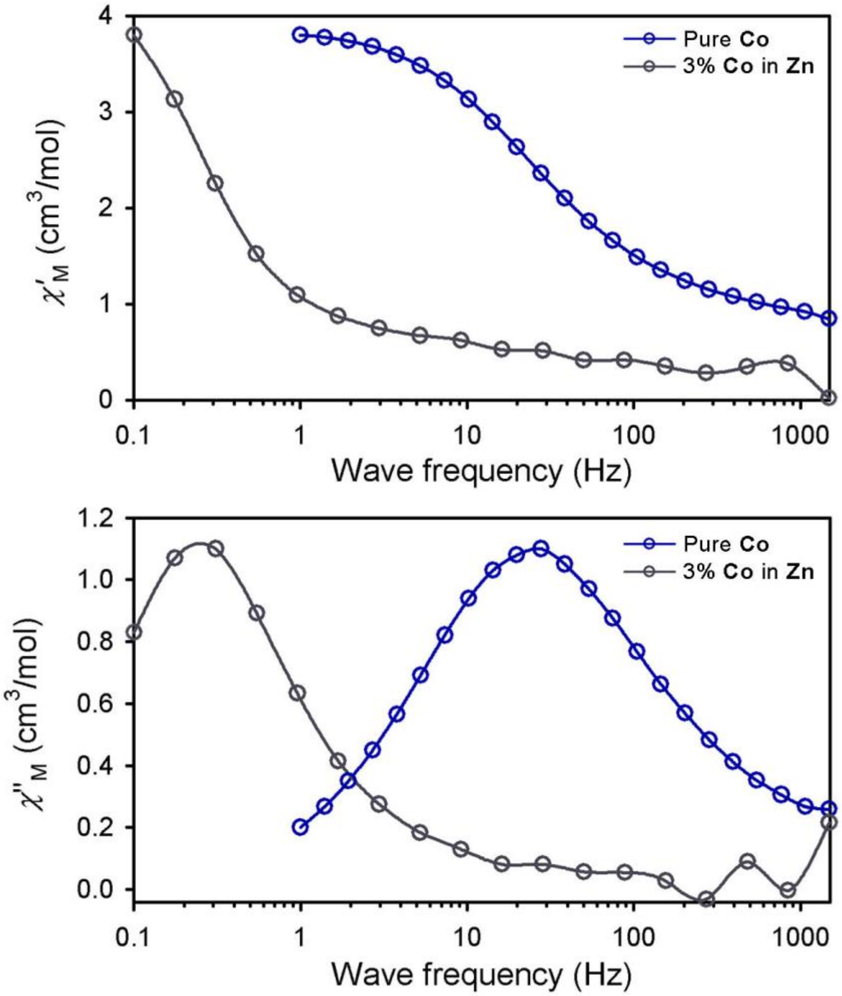

Figure A17: Select in- and out-of-phase ac susceptibility data (χ_M' and χ_M'', respectively) for **Co:Zn** dilutions at 2 K. Magnitudes of χ_M' and χ_M'' are normalized to the values for pure **Co** at 2 K. Solid lines are guides for the eye.

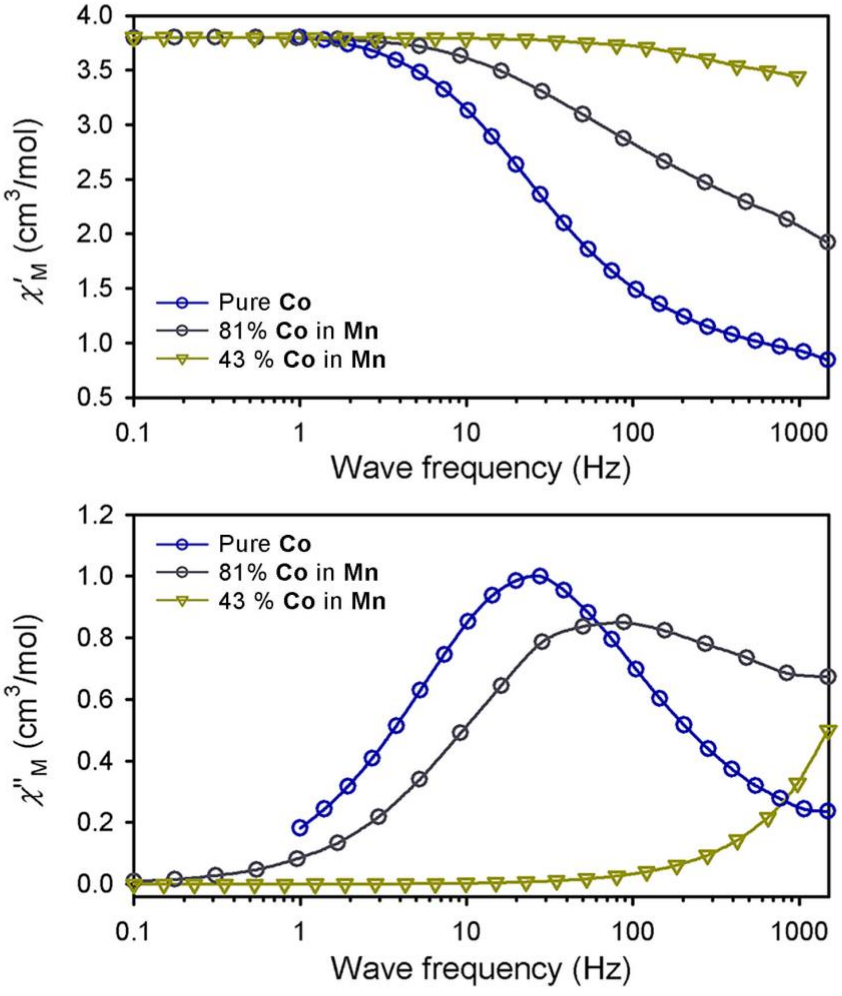

Figure A18: Select in- and out-of-phase ac susceptibility data (χ_M' and χ_M'', respectively) for **Co:Mn** dilutions at 2 K. Magnitudes of χ_M' and χ_M'' are normalized to the values for pure **Co** at 2 K. Solid lines are guides for the eye.

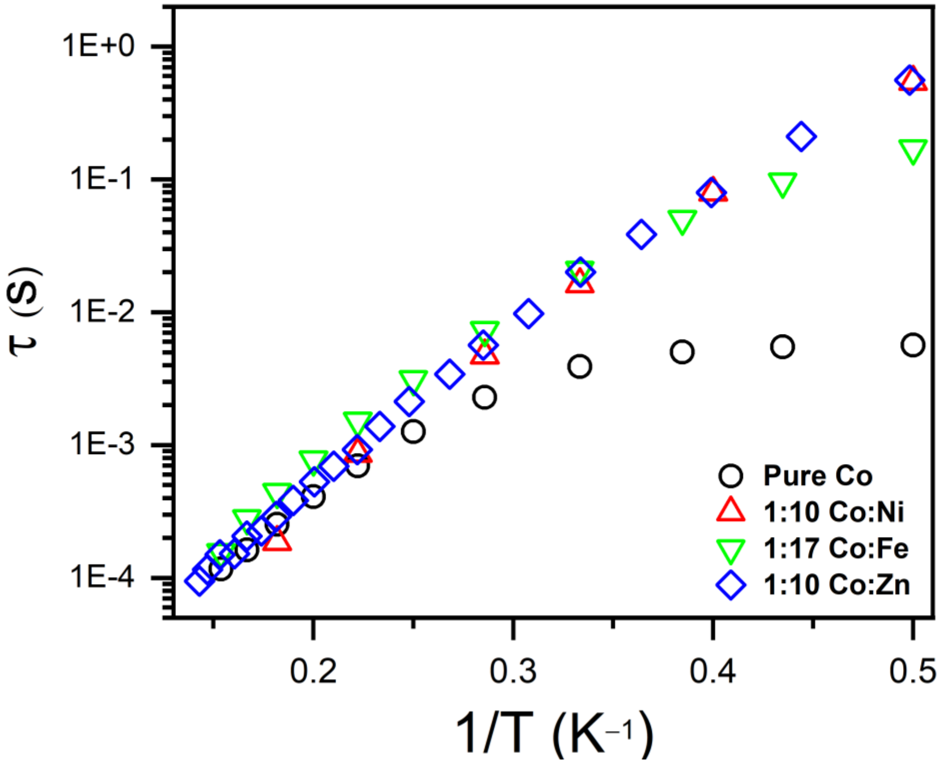

Figure A19: Arrhenius plot comparison of dilutions of **Co** in **Fe**, **Ni**, and **Zn**[7] to the Arrhenius plot of pure **Co**. All relaxation rates were extracted from variable frequency ac susceptibility with zero applied magnetic field.

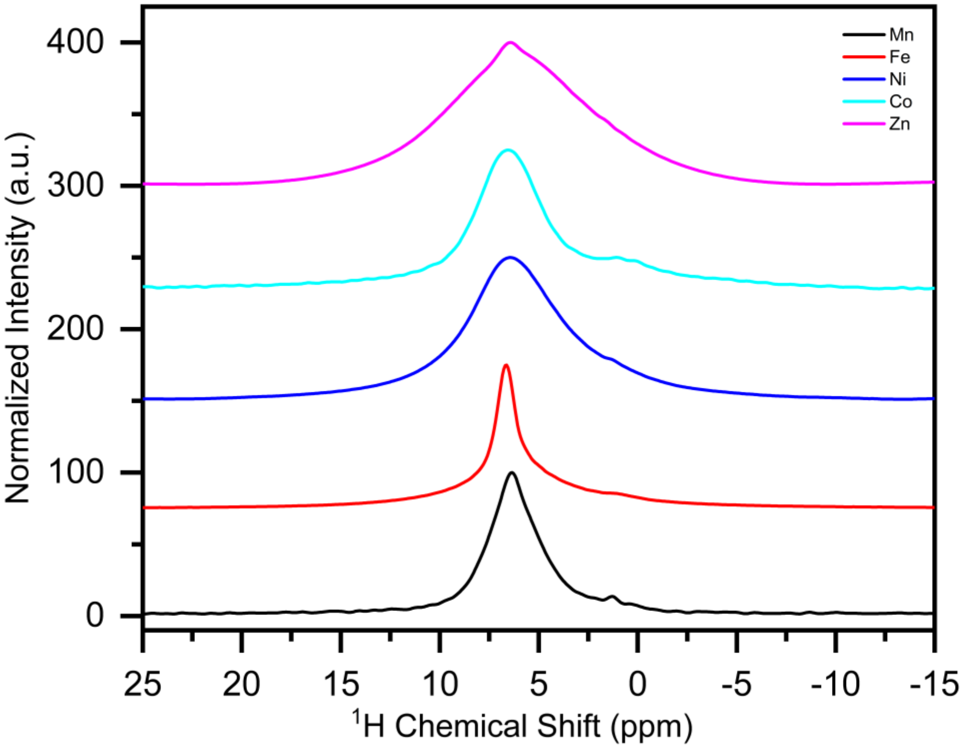

Figure A20: Solid-state NMR spectra for pure compounds (**Co, Ni, Fe, Mn,** and **Zn**) collected at room temperature at 15 kHz MAS. Spectra shown are from the longest recorded τ scan (see SI experimental) for each compound.

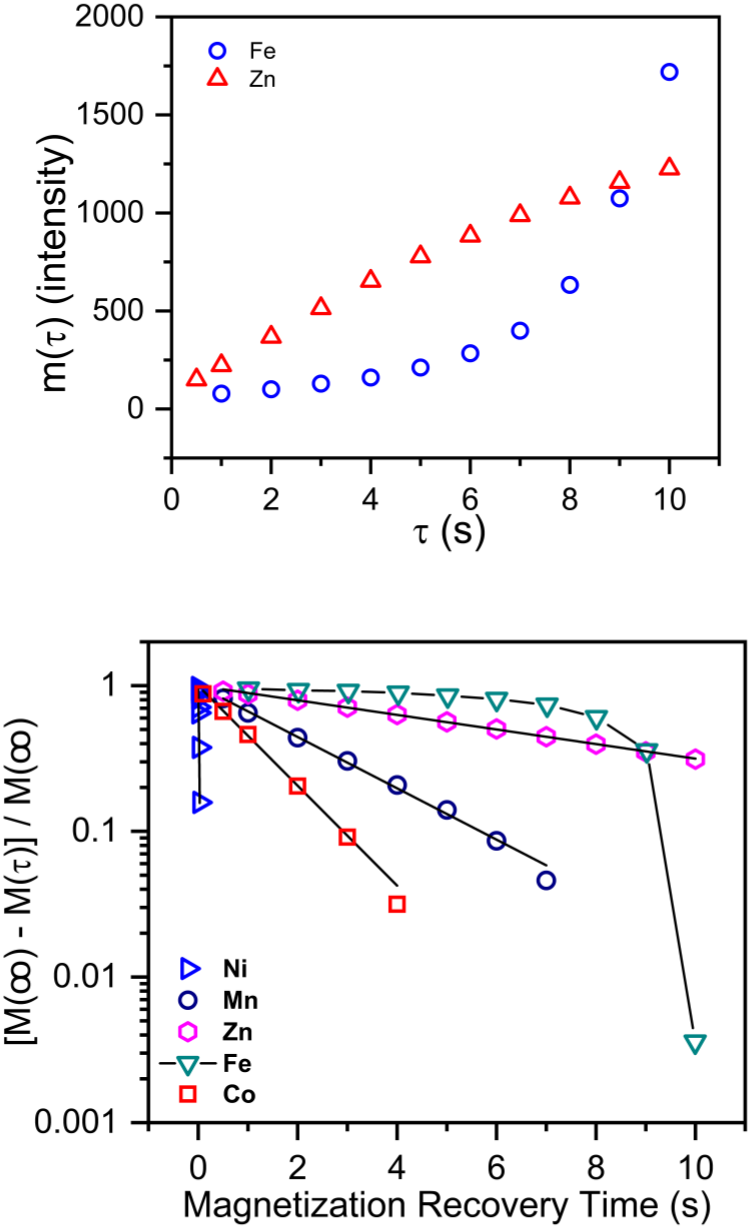

Figure A21: Magnetization recovery data obtained from the room temperature, solid state NMR spectra of the pure compounds. M(∞) and T_1 were extracted from exponential fits to the data (See SI). ***Top***: Comparison of anomalous **Fe** recovery to the recovery of **Zn** (τ represents time after saturating pulses). ***Bottom***: Magnetization recovery data plotted on a log scale. Black lines are fits to extract T_1 (The black line for **Fe** data is simply a guide for the eye, as no simple relaxation behavior is observed).

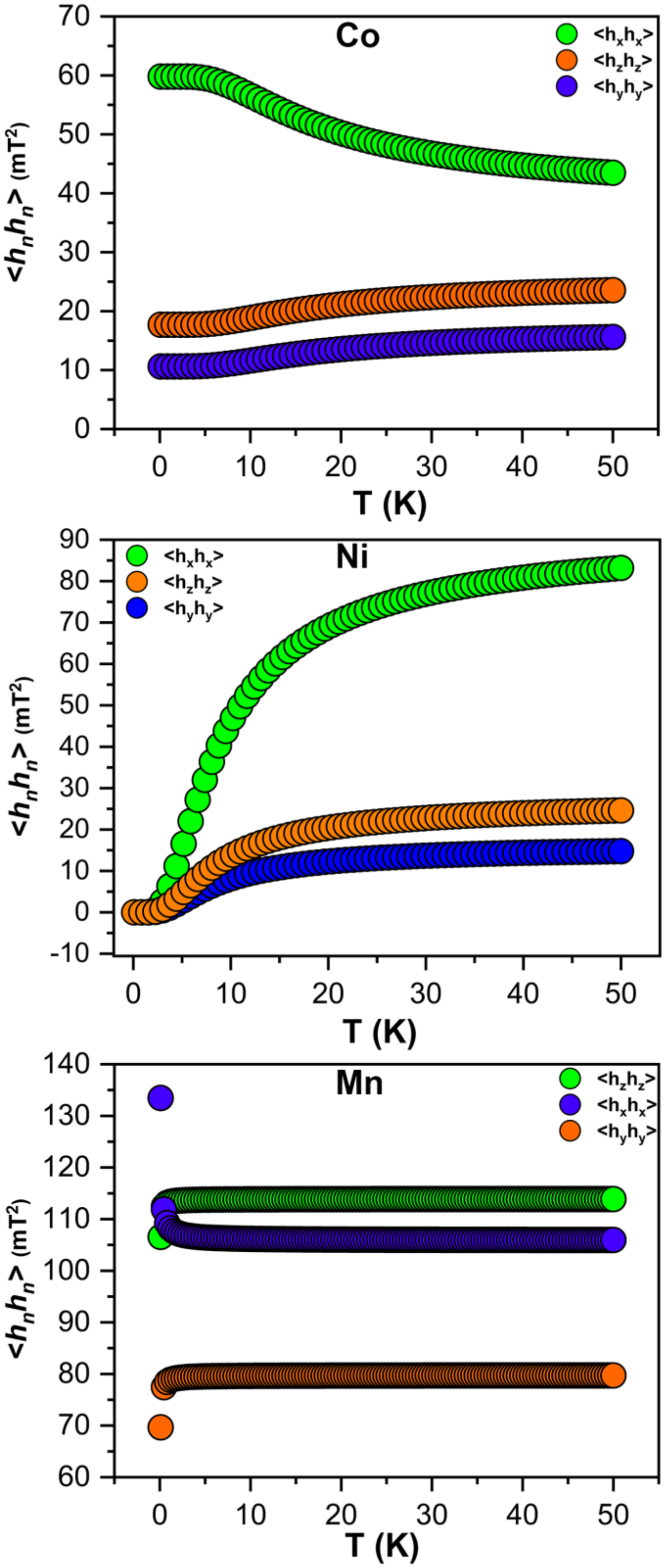

Figure A22: Variable temperature, orientation dependence of the dipolar fields calculated for crystalline matrices of **Co** (top), **Ni** (middle), and **Mn** (bottom) in mT^2. (*note*: <$h_n h_n$> is synonymous

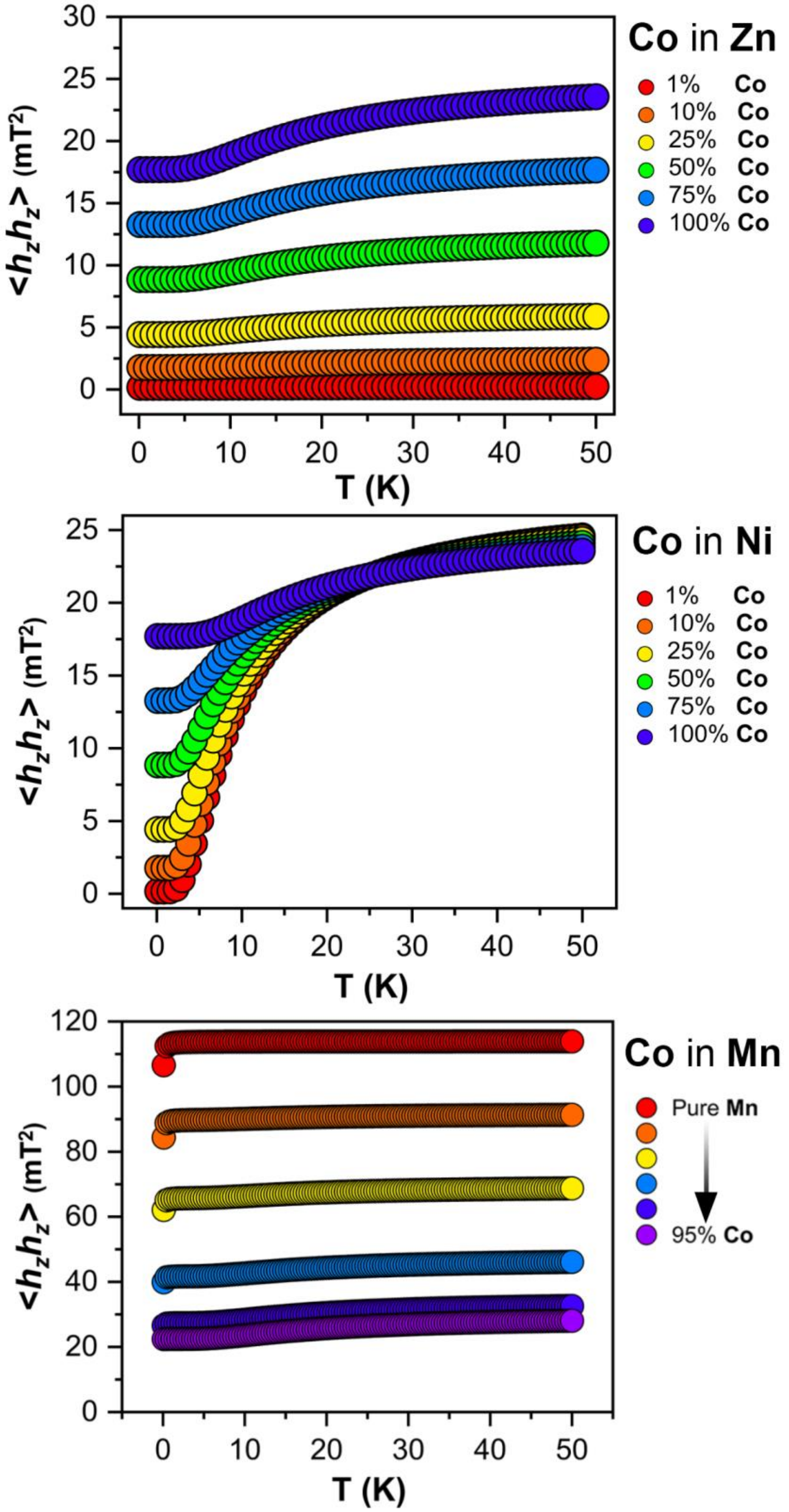

Figure A23: Variable temperature, concentration dependence of the dipolar fields calculated for crystalline matrices of **Co** in **Zn**, **Ni**, and **Mn** in mT^2. (*note*: $<h_n h_n>$ is synonymous with c_h^n)

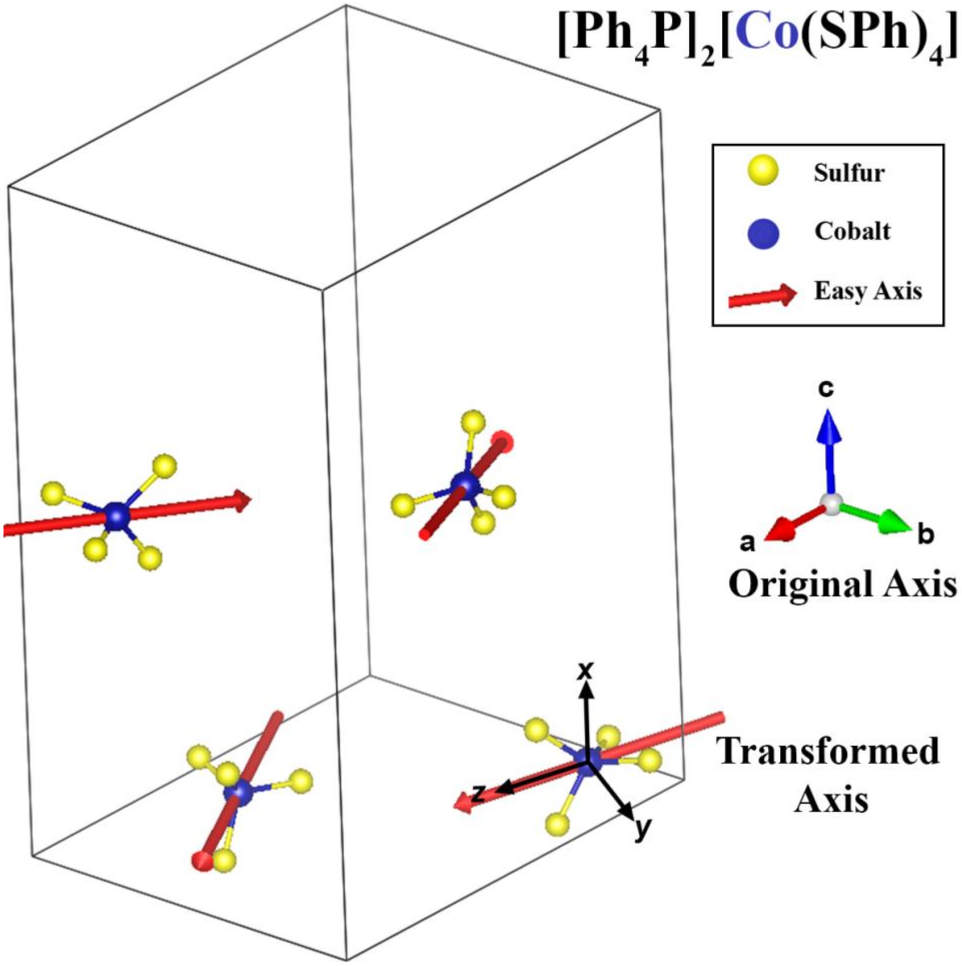

Figure A24: Visual depiction of the easy-axis vector orientation and axis transformation used to calculate dipolar fields.

References

1. R. Möseler, E. G. Horvath and B. Horvath, *Z. anorg. allg. Chem.*, 1979, **177**, 165–177.
2. J. M. Zadrozny, J. Telser and J. R. Long, *Polyhedron*, 2013, **64**, 209–217.
3. G. A. Bain and J. F. Berry, *J. Chem. Educ.*, 2009, **85**, 532.
4. N. F. Chilton, R. P. Anderson, L. D. Turner, A. Soncini and K. S. Murray, *J. Comput. Chem.*, 2013, **34**, 1164–1175.
5. A. Schweiger and G. Jeschke, *Principles of Pulse Electron Paramagnetic Resonance*, Oxford University Press, Oxford, 2001.
6. R. Orbach, *Proc. Phys. Soc.*, 1961, **77**, 821–826.
7. J. M. Zadrozny and J. R. Long, *J. Am. Chem. Soc.*, 2011, **133**, 20732–20734.
8. J. G. Castle and D. W. Feldman, *Phys. Rev.*, 1965, **137**, 671–673.
9. V. A. Atsarkin, V. V Demidov and G. A. Vasneva, *Phys. Rev. B*, 1997, **56**, 9448–9453.
10. R. Orbach, *Proc. R. Soc. London. Ser. A. Math. Phys. Sci.*, 1961, **264**, 458–484.
11. A. K. Hassan, L. A. Pardi, J. Krzystek, A. Sienkiewicz, P. Goy, M. Rohrer and L. C. Brunel, *J. Magn. Reson.*, 2000, **142**, 300–312.
12. S. Stoll and A. Schweiger, *J. Magn. Reson.*, 2006, **178**, 42–55.
13. L. J. Berliner, G. R. Eaton and S. S. Eaton, *Distance Measurements in Biological Systems by EPR*, Springer US, Boston, MA, 2002, vol. 19.
14. R. A. Faulkner, J. A. DiVerdi, Y. Yang, T. Kobayashi and G. E. Maciel, *Materials (Basel).*, 2013, **6**, 18–46.

15. M. Mariani, F. Borsa, M. J. Graf, S. Sanna, M. Filibian, T. Orlando, K. P. V. Sabareesh, S. Cardona-Serra, E. Coronado and A. Lascialfari, *Phys. Rev. B*, 2018, **97**, 1–10.

16. P. Santini, S. Carretta, E. Liviotti, G. Amoretti, P. Carretta, M. Filibian, A. Lascialfari and E. Micotti, *Phys. Rev. Lett.*, 2005, **94**, 1–4.

17. K. S. Cole and R. H. Cole, *J. Chem. Phys.*, 1941, **9**, 341–351.

18. R. Kubo and K. Tomita, *J. Phys. Soc. Japan*, 1954, **9**, 888–919.

19. R. Kubo, T. Endo, S. Kamohara, M. Shimizu, M. Fujii and H. Takano, *J. Phys. Soc. Japan*, 1987, **56**, 1172–1177.

20. E. A. Suturina, J. Nehrkorn, J. M. Zadrozny, J. Liu, M. Atanasov, T. Weyhermüller, D. Maganas, S. Hill, A. Schnegg, E. Bill, J. R. Long and F. Neese, *Inorg. Chem.*, 2017, **56**, 3102–3118.

21. D. E. Fenton, R. R. Schroeder and R. L. Lintvedt, *J. Am. Chem. Soc.*, 1978, **100**, 1934.

22. D. Gatteschi, R. Sessoli and J. Villain, *Molecular Nanomagnets*, Oxford University Press, New York, NY, 2006.

APPENDIX B

Supplementary Figures

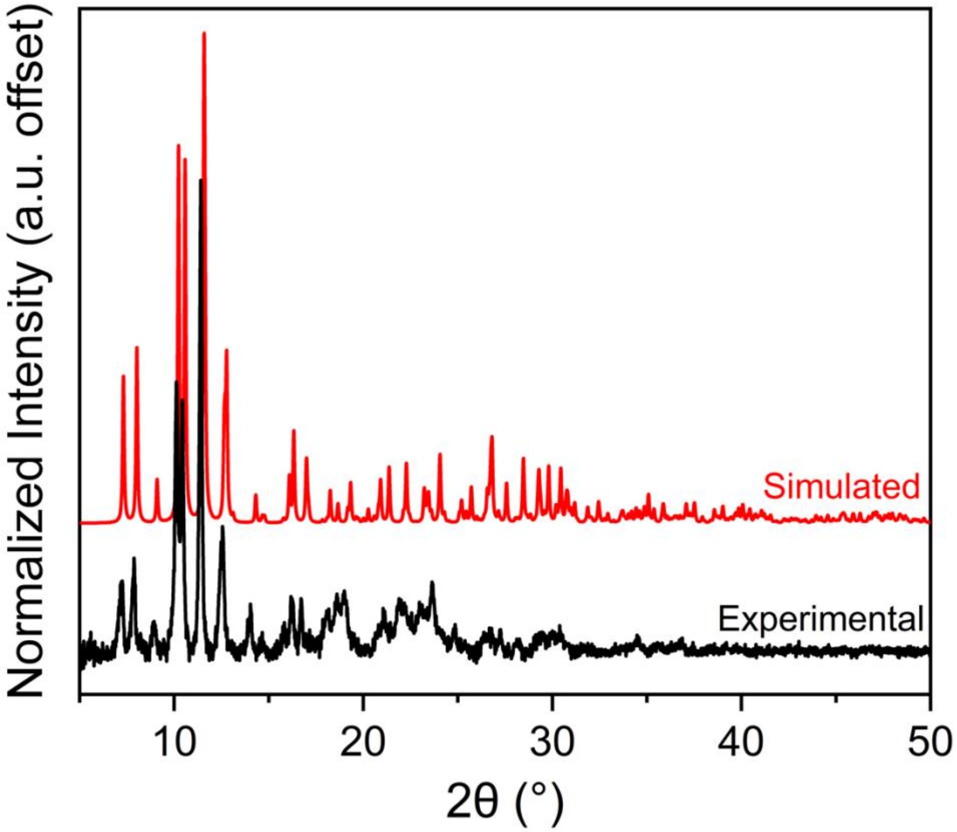

Figure B1: PXRD pattern for [{(Me_3Si_2)$_2$N}Fe{μ-p-{HN($SiMe_3$)}(C_6Me_4){N($SiMe_3$)}}$_2$Fe{N($SiMe_3$)$_2$}] (1). The simulated pattern was generated using Mercury software. Due to improper beam alignment, the recorded pattern, is offset by ~0.14 ˚.

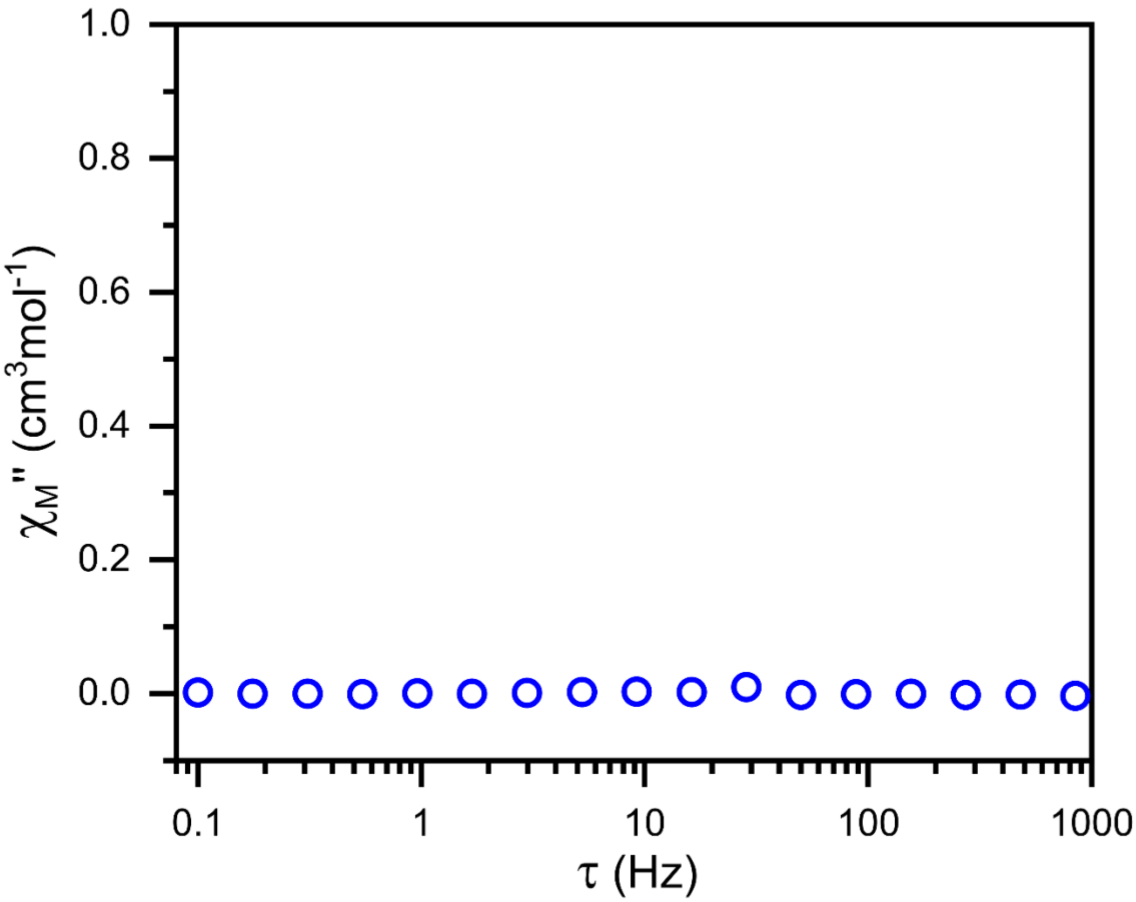

Fig B2: Variable-field ac susceptibility data under zero applied field at 2.0 K for a pure, polycrystalline sample of **1.**

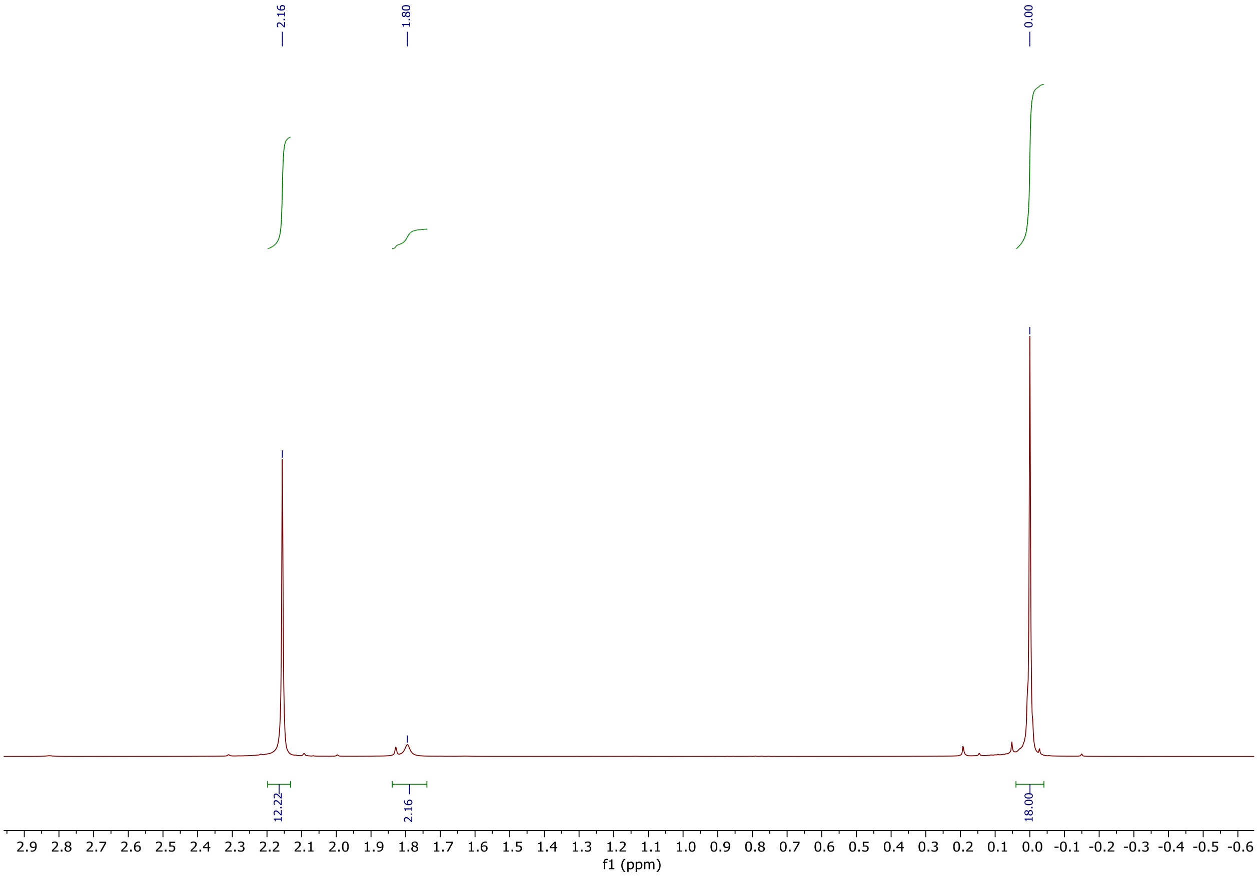

Fig B3: ^{1}H-NMR Spectra of **L** taken in C_6D_6 at 25 °C on a 400 MHz spectrometer. Peaks are referenced to solvent residual peaks, and assignments are given in the experimental.[26]

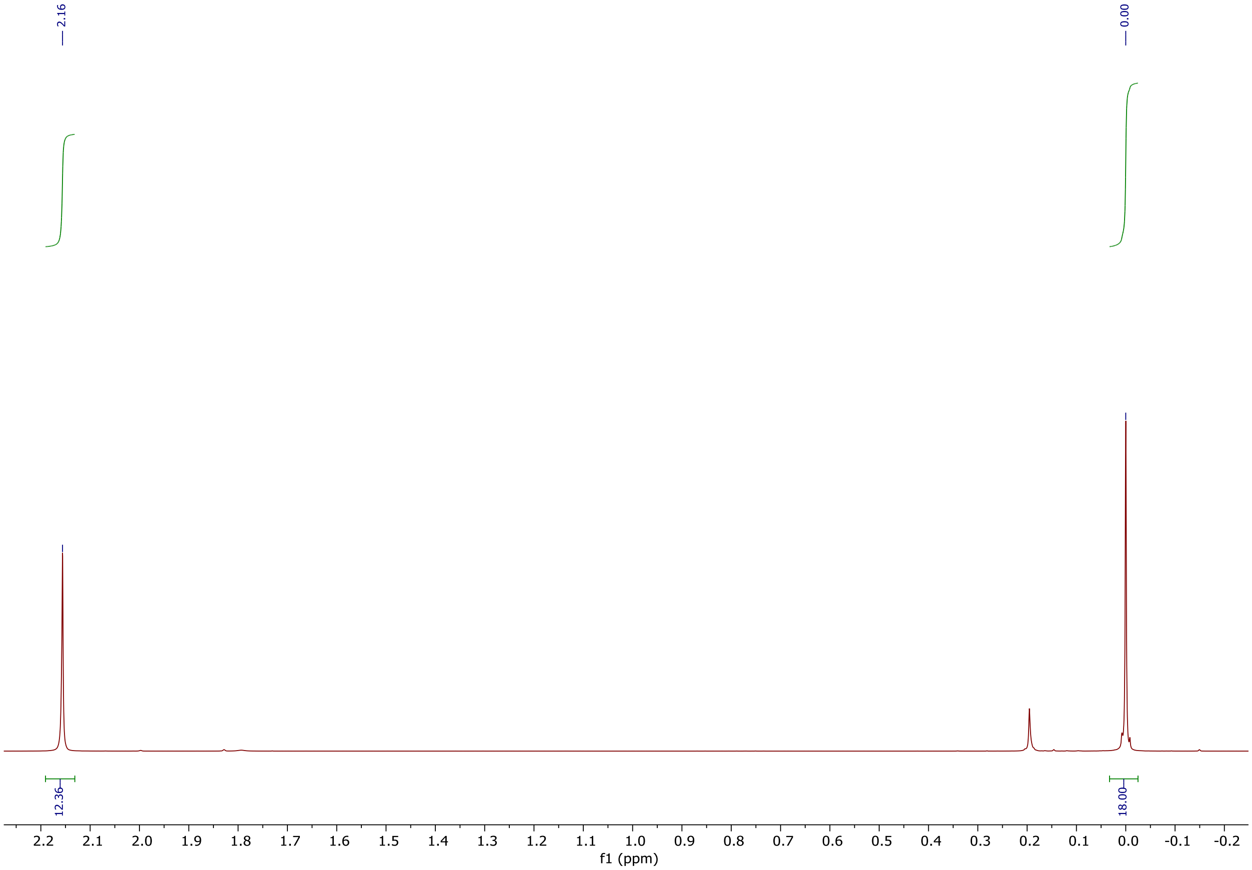

Fig B4: ^{1}H-NMR Spectra of **L-D** taken in C_6D_6 at 25 °C on a 400 MHz spectrometer. Peaks are referenced to solvent residual peaks, and assignments are given in the experimental.

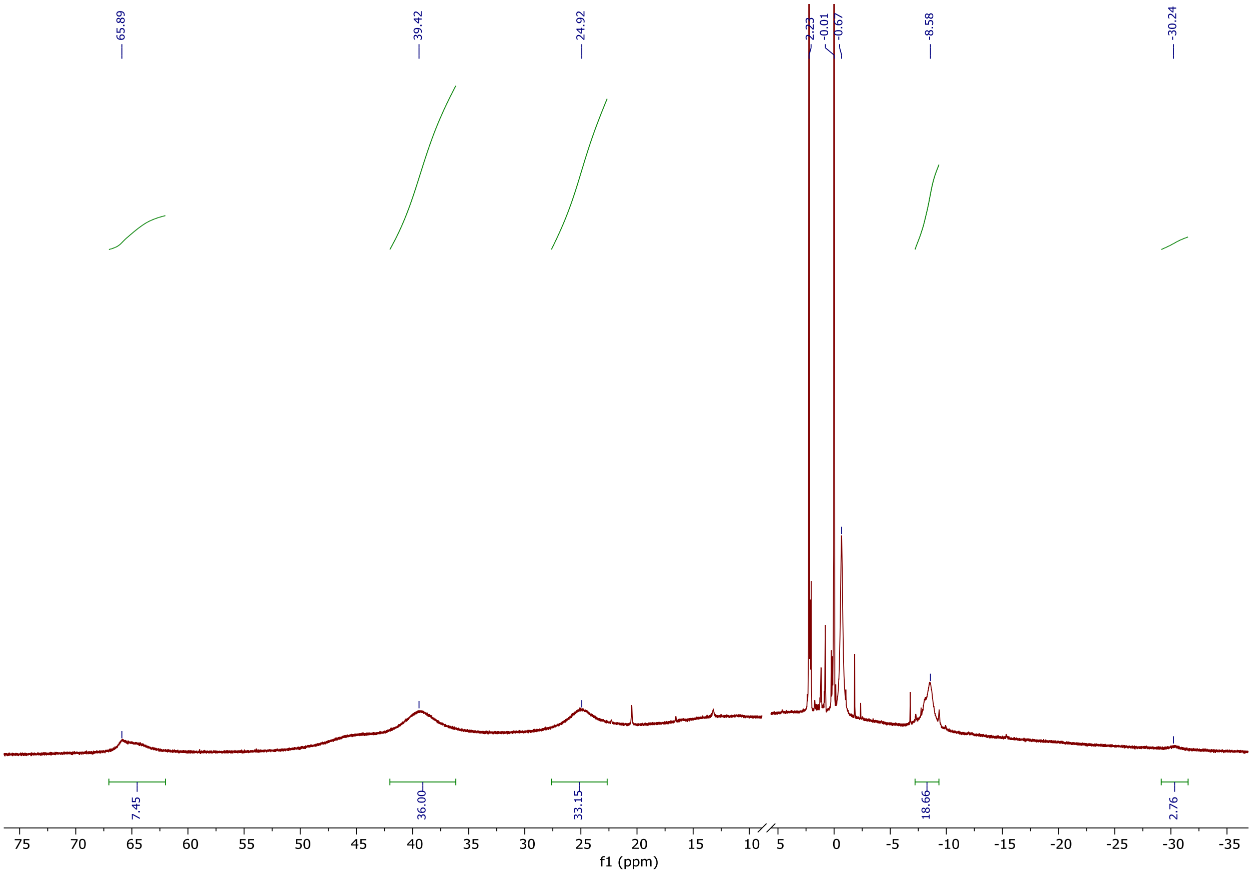

Fig B5: ^{1}H-NMR Spectra of **1** taken in C_6D_6 at 25 °C on a 400 MHz spectrometer. Peaks are referenced to solvent residual peaks. Peaks in diamagnetic region correspond to free ligand in solution (Fig S3).

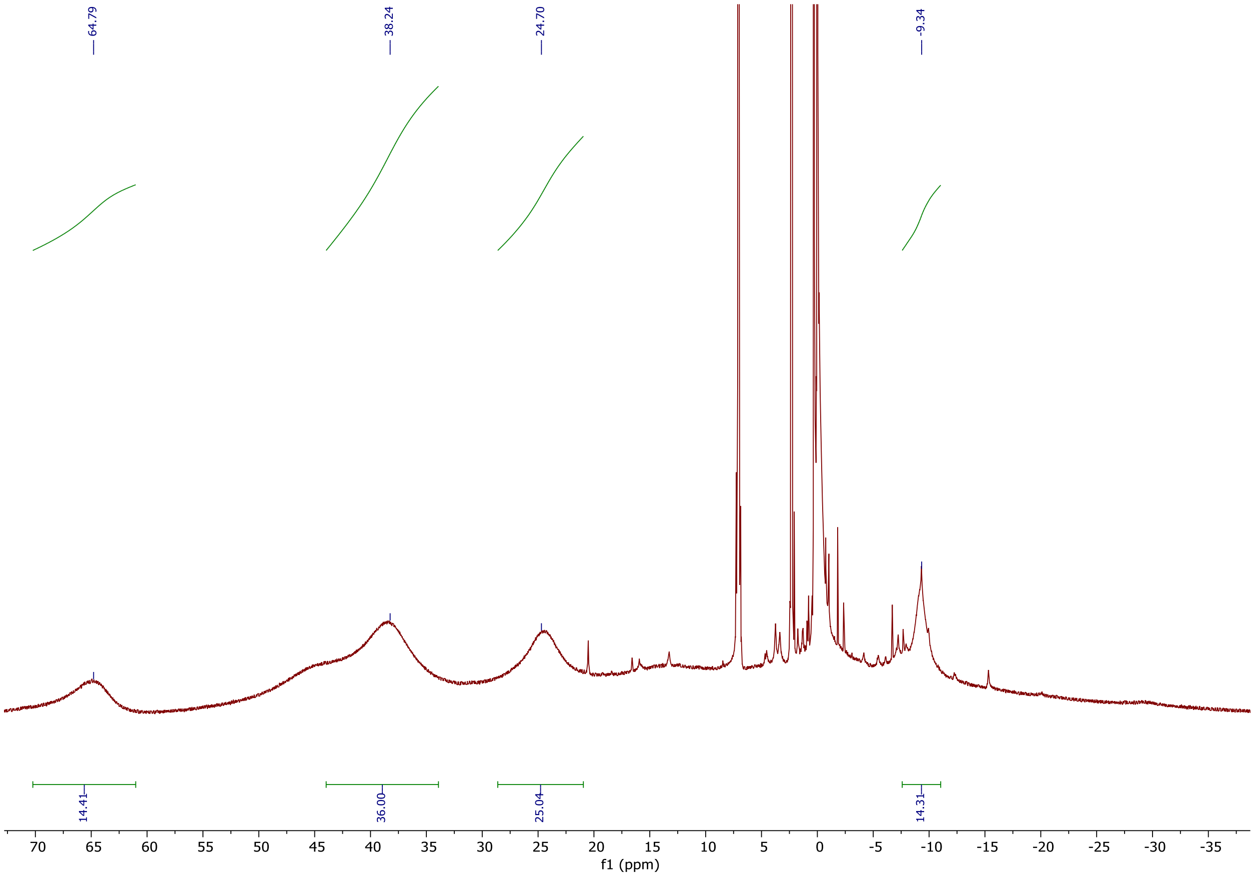

Fig. B6. ^{1}H-NMR Spectrum of **1-D** taken in C_6D_6 at 25 °C on a 400 MHz spectrometer. Peaks are referenced to solvent residual peaks. Peaks in diamagnetic region correspond to free ligand in solution (Fig. S3).

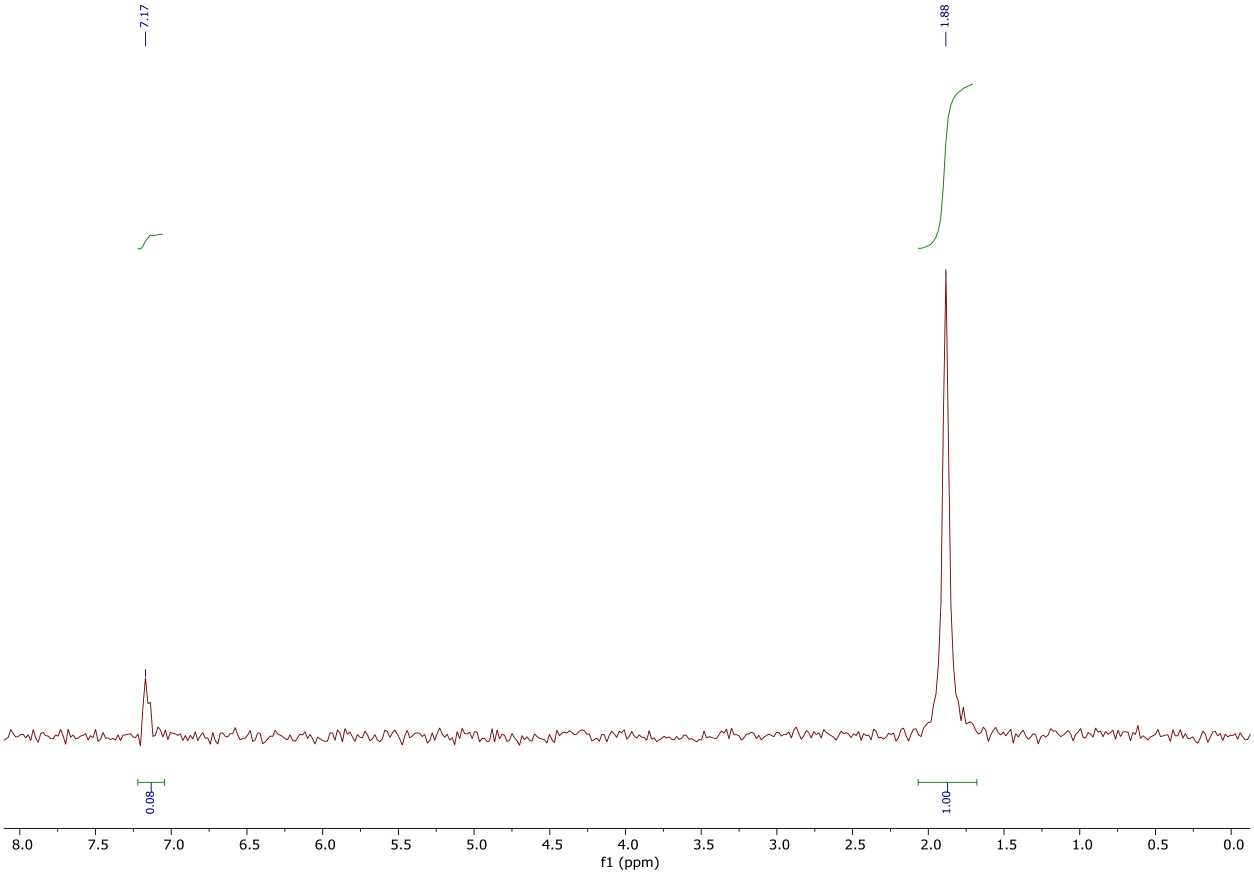

Fig. B7. ^{2}H-NMR Spectrum of **L-D** taken in C_6H_6 (spiked with C_6D_6 as a reference) at 25 °C on a 400 MHz spectrometer.

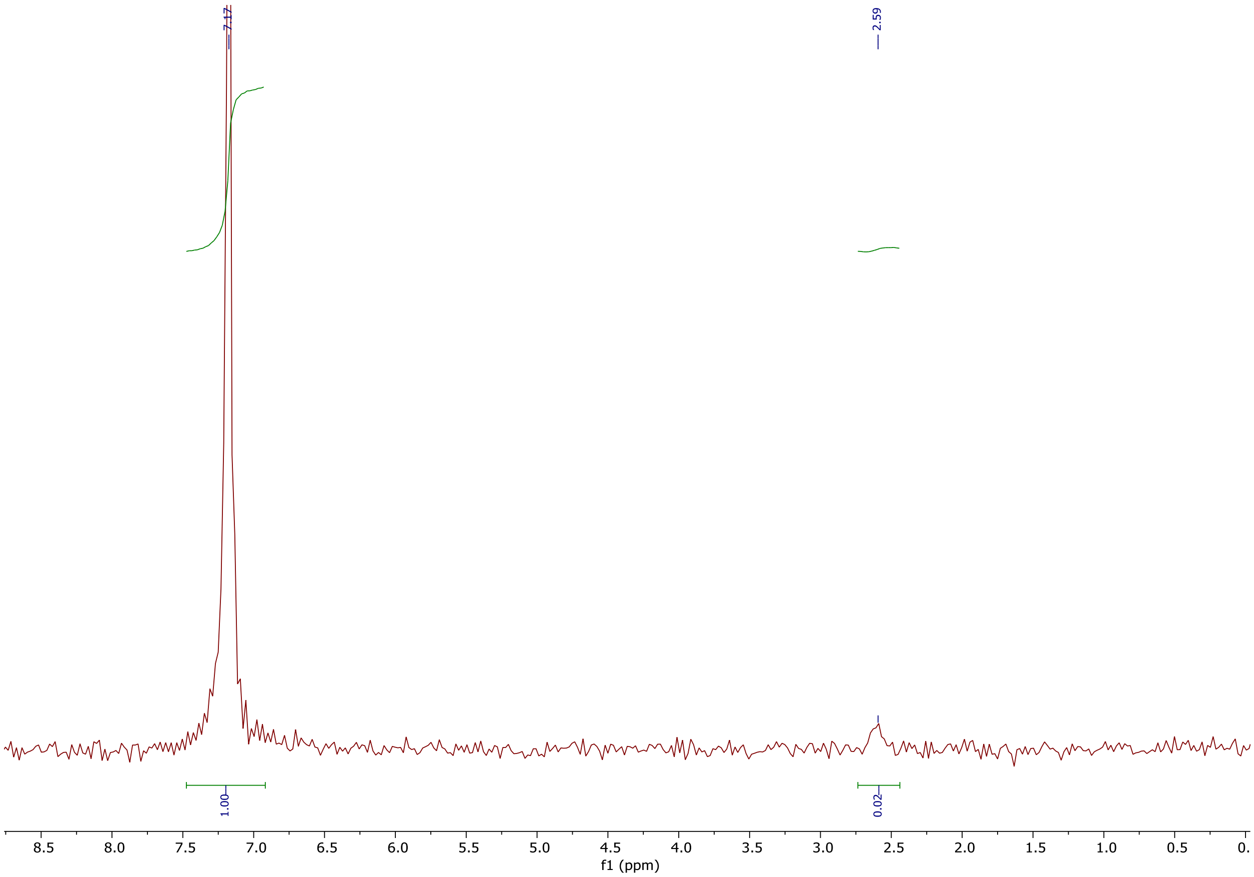

Fig. B8. ^{2}H-NMR Spectrum of **1-D** taken in C_6H_6 (spiked with C_6D_6 as a reference) at 25 °C on a 400 MHz spectrometer.

APPENDIX C

Experimental Details

Reactions were performed using standard Schlenk or glovebox techniques under a nitrogen atmosphere unless otherwise specified. Reactions involving hydrated metal salts were performed in a water-containing glovebox, and products were transferred to a water-free glovebox for washing. Reagents and solvents were purchased from commercial vendors (Millipore Sigma, TCI America, Alfa Aesar, Fisher Scientific, Oakwood Chemical, Combi-Blocks) and used without further purification. Deuterated solvents ($CDCl_3$, DMSO-d_6, MeOD) were purchased from Cambridge Isotope Laboratories.

NMR spectra were acquired using Bruker AV300, AV301, DRX499, or AV500 spectrometers. All ^1H and ^{13}C NMR spectra were referenced to residual deuterated solvent peaks. ESI-MS data was collected on a Bruker Esquire Ion Trap in positive ion mode. High-resolution C, H, N, Br combustion analysis was conducted by Atlantic Microlabs Inc. Attenuated total reflectance infrared (ATR-IR) spectra were collected on a Perkin Elmer Frontier FT-IR/FIR instrument equipped with a diamond ATR accessory. Diffuse reflectance UV-vis-NIR spectra were collected on a Shimadzu UV-3600i Plus spectrophotometer equipped with a Harrick Scientific Praying Mantis diffuse reflectance attachment. Samples were diluted with $BaSO_4$, ground with a spatula, and analyzed in air immediately following removal from the glovebox. The Kubelka-Munk transformation was performed to convert the spectra from raw reflectance data using the formula $F(R) = (1 - R)^2/2R$, where R is the reflectance and F(R) is the transformed data.

Powder X-ray diffraction (PXRD) data were collected on a Bruker D2 PHASER benchtop diffractometer equipped with a LINXEYE XE-T detector. Dry samples were ground with a spatula and analyzed as powders on a monocrystalline Si substrate.

Zero-field ^{57}Fe Mössbauer spectra were measured with a constant acceleration spectrometer (SEE Co, Minneapolis, MN). Samples were prepared by suspending 60-100 mg of ground analyte in Paratone oil and immobilized by rapid freezing in liquid nitrogen. Isomer shifts are given relative to Fe foil at room temperature. Data were analyzed and simulated with Igor Pro 6 software (WaveMetrics, Portland, OR) using Lorentzian fitting functions.

Magnetic data were collected on a Quantum Design MPMS3 SQUID magnetometer. Samples were prepared by placing finely ground, microcrystalline powder into a polyethylene sample holder and restraining the powder with molten eicosane. Samples were transported to the instrument under an inert atmosphere and immediately loaded into the sample chamber to minimize atmospheric exposure.

Electrical conductivity measurements were obtained using a BioLogic SP-200 Potentiostat.

Synthetic Procedures

Ligand Synthesis

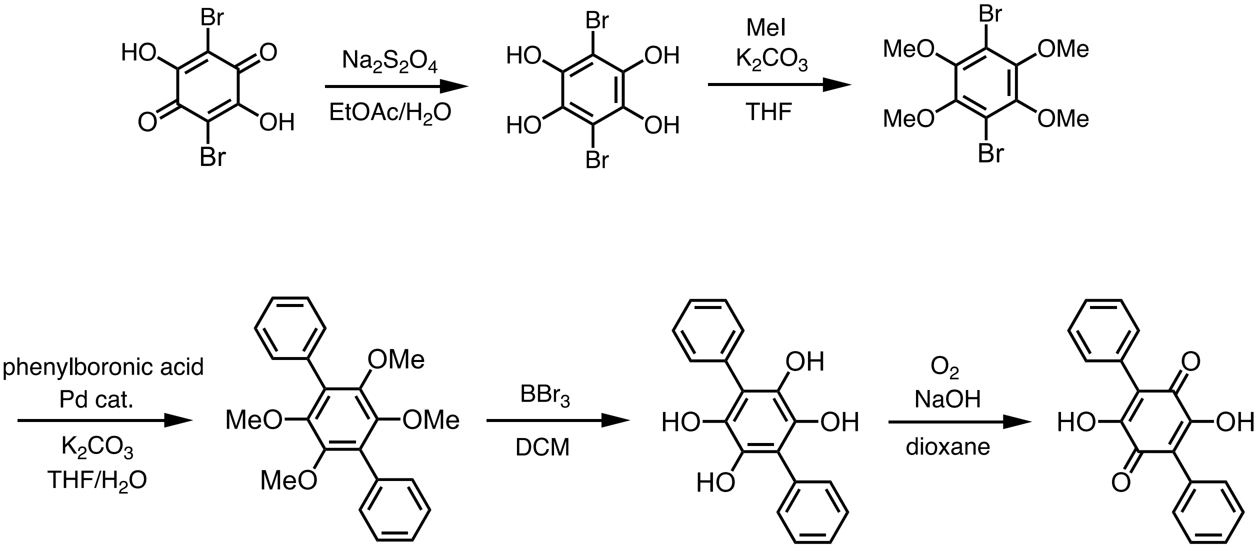

Scheme C1: General synthetic route towards Ph$_2$dhbq^{n-} ligands in both the reduced (H$_4$Ph$_2$dhbq) and oxidized (H$_2$Ph$_2$dhbq) forms.

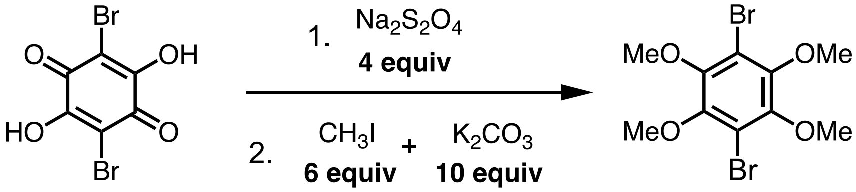

Synthesis of 1,4-dibromo-2,3,5,6-tetramethoxybenzene: This compound was prepared using modified procedures from the literature.[1,2] A Schlenk flask was charged with bromanilic acid (2.00

g, 6.71 mmol) and EtOAc (100 mL), and the mixture was sparged with N_2 for 30 min. While under nitrogen, a 1M aqueous sodium dithionite solution (not degassed; 26.8 mL, 26.8 mmol, 4 eq.) was added dropwise. The reaction was stirred at room temperature overnight. The EtOAc layer was isolated, and the aqueous layer was extracted with additional EtOAc (2 × 50 mL). The combined organic layers were dried over $MgSO_4$ and reduced to a solid *in vacuo*. The solid was suspended in DCM and filtered, washing through with additional DCM, to give 3,6-dibromobenzene-1,2,4,5-tetraol as a white solid (1.95 g, 97%). This compound was carried forward without additional characterization. A flame-dried Schlenk flask under a nitrogen atmosphere was charged with 3,6-dibromobenzene-1,2,4,5-tetraol (3.53 g, 11.8 mmol), K_2CO_3 (16.3 g, 118 mmol, 10 eq.), and DMF (degassed/anhydrous; 70 mL). Methyl iodide (4.4 mL, 70.8 mmol, 6 eq.) was added via syringe and the mixture was stirred at room temperature overnight. The reaction was quenched with H_2O (150 mL) and stirred for 10 min. Additional H_2O (250 mL) was added to precipitate out a white solid. The precipitate was collected by vacuum filtration and washed with H_2O (200 mL) followed by MeOH (20 mL) to yield 1,4-dibromo-2,3,5,6-tetramethoxybenzene as a white powder (3.65 g, 87%). ^{1}H NMR matches the previously reported spectrum for this compound.[2]

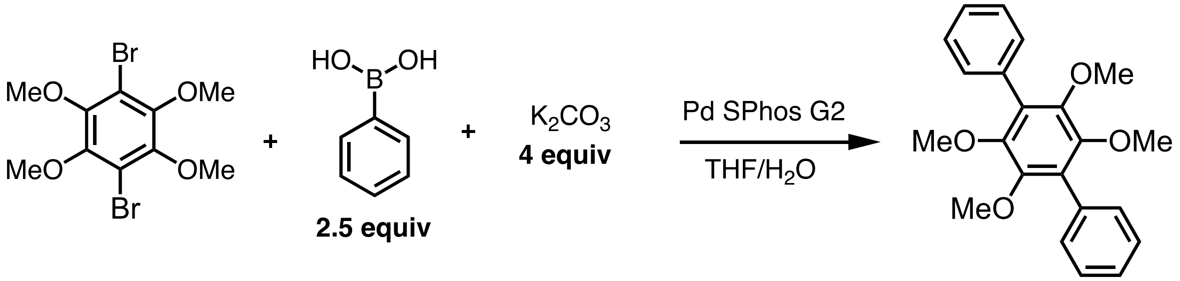

Synthesis of 2',3',5',6'-tetramethoxy-1,1':4',1''-terphenyl: This compound was prepared using a modified procedure from the literature.[3] In a Schlenk flask, 1,4-dibromo-2,3,5,6-

tetramethoxybenzene (3.51 g, 9.86 mmol), K_2CO_3 (5.45 g, 39.4 mmol, 4 eq.), and phenylboronic acid (3.00 g, 24.6 mmol, 2.5 eq.) were suspended in a mixture of THF (150 mL) and H_2O (50 mL). The mixture was sparged with N_2 for 45 min and Pd SPhos G2 (0.142 g, 0.197 mmol, 2 mol%) was added. The reaction was refluxed under N_2 at 70 °C for 24 hr. The THF was removed *in vacuo*, H_2O (150 mL) was added, and the solution was extracted with $CHCl_3$ (3 × 100 mL). The combined organic layers were washed with H_2O (100 mL), dried over $MgSO_4$, and the solvent was removed *in vacuo*. The resulting solid was suspended in MeOH (100 mL) and recovered via vacuum filtration before washing with additional MeOH to yield 2',3',5',6'-tetramethoxy-1,1':4',1''-terphenyl as a white, crystalline solid (3.21 g, 93%). ^{1}H NMR matches the previously reported spectrum for this compound.[4]

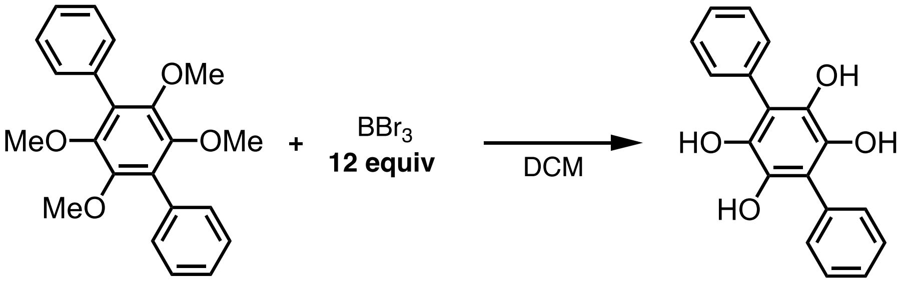

Synthesis of [1,1':4',1''-terphenyl]-2',3',5',6'-tetraol (H_4Ph_2dhbq): In an oven-dried Schlenk flask under a nitrogen atmosphere, 2',3',5',6'-tetramethoxy-1,1':4',1''-terphenyl (3.24 g, 9.25 mmol) was dissolved in DCM (degassed/anhydrous; 200 mL). The solution was cooled to –78 °C. Neat BBr_3 (10.5 mL, 111 mmol, 12 eq.) was added via cannula transfer. The cold bath was allowed to expire over the course of ~3 hr and the reaction was stirred at room temperature overnight. The reaction was cooled to 0 ˚C. While still under N_2, H_2O (not degassed; 200 mL) was added very slowly and carefully to quench the reaction. The reaction was allowed to stir for 2 hr under N_2. The cold bath was removed, and the DCM was removed *in vacuo*. The resulting precipitate was recovered by vacuum filtration. The precipitate was washed with H_2O (3 × 50 mL) followed by cold MeOH (10 mL), and allowed to dry under flowing nitrogen to yield H_4Ph_2dhbq as a white solid (2.58 g, 95%). ^{1}H NMR (500 MHz, MeOD): δ 6.13 (t, 6.9 Hz, 2H), 6.23 (t, 7.7 Hz, 4H), 6.29 (d, 7.2 Hz, 4H). ^{13}C{^{1}H} NMR (75 MHz, DMSO-d_6 + MeOD): δ 124.27, 128.12, 129.22, 132.54, 136.27, 137.56. MS (ESI) *m/z*: 317.1 ([M+Na]$^+$, calc'd for $C_{18}H_{14}O_4Na$: 317.1).

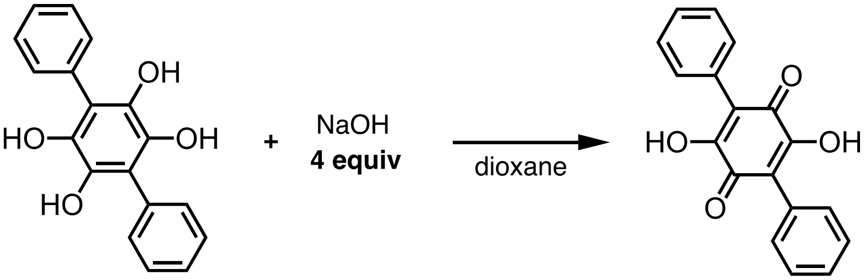

Synthesis of polyporic acid (H_2Ph_2dhbq): A reaction vessel was charged with H_4Ph_2dhbq (505 mg, 1.73 mmol) and *p*-dioxane (45 mL). 1M aqueous NaOH (7.0 mL, 7 mmol, 4 eq.) was added dropwise and the resulting solution was stirred open to air overnight. The reaction was acidified with 2M aqueous HCl (10 mL), diluted with H_2O (200 mL), and extracted into DCM (3 × 80 mL). The combined organic layers were washed with H_2O (80 mL) and the solvent was removed *in vacuo*. The resulting precipitate was dried under flowing N_2 to give H_2Ph_2dhbq as a brown solid (482 mg, 95%). ^{1}H NMR matches the previously reported spectrum for this compound.[4]

Fe(Ph_2dhbq) Chain Syntheses from Fe^{III}

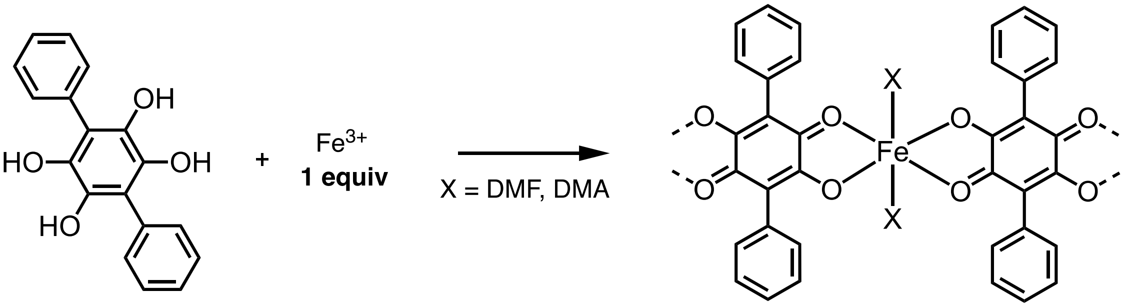

Scheme C2: Generalized synthesis of *cis*-Fe(Ph_2dhbq)$(DMF)_2$ and *trans*-Fe(Ph_2dhbq)$(DMA)_2Br_{0.55}$ from H_4Ph_2dhbq and Fe^{III}.

General synthesis of cis-Fe(Ph_2dhbq)$(DMF)_2$ from Fe^{III}: In a glovebox with a nitrogen atmosphere, a 20 mL scintillation vial was charged with a solution of H_4Ph_2dhbq (25.2 mg, 85.5 µmol) in 5 mL DMF. To the vial was added a solution of $FeCl_3 \cdot 6H_2O$ (23.0 mg, 85.1 µmol, 1.0 eq.) in 5 mL DMF. The vial was sealed and heated at 120 ˚C for 5 days to give small, dark, intergrown crystals. The mother liquor was removed, the crystals were washed with DMA (5 × 2.5 mL), and then recovered by vacuum filtration to give *cis*-Fe(Ph_2dhbq)$(DMF)_2$ as a dark solid (34.0 mg, 81%). Anal. Found: C, 57.57; H, 4.74; N, 5.53 ($FeC_{24}H_{24}N_2O_6(H_2O)_{0.35}$, calc'd: C, 57.81; H, 4.99; N, 5.62).

Synthesis of cis-Fe(Ph_2dhbq)($DMF)_2$ from Fe^{III} for SCXRD: In a glovebox with a nitrogen atmosphere, a 4 mL scintillation vial was charged with a solution of H_4Ph_2dhbq (2.5 mg, 8.5 µmol) in 0.5 mL DMF. A solution of $FeCl_3 \cdot 6H_2O$ (2.0 mg, 7.4 µmol, 0.9 eq.) in 0.5 mL DMF was layered on top. The vial was sealed and heated at 120 ˚C for 1 week to give very small, dark, crystals of *cis*-Fe(Ph_2dhbq)($DMF)_2$ suitable for X-ray diffraction.

General synthesis of trans-Fe(Ph_2dhbq)($DMA)_2Br_{0.55}$ from Fe^{III}: In a glovebox with a nitrogen atmosphere, a 20 mL scintillation vial was charged with a solution of H_4Ph_2dhbq (24.3 mg, 82.6 µmol) in 5 mL DMA. To the vial was added a solution of $FeBr_3$ (25.6 mg, 86.6 µmol, 1.0 eq.) in 5 mL DMA. The vial was sealed and heated at 120 ˚C for 5 days to give small, dark crystals. The mother liquor was removed, the crystals were washed with DMA (5 × 2.5 mL), and then recovered by vacuum filtration to give *trans*-Fe(Ph_2dhbq)($DMA)_2Br_{0.55}$ as a dark solid (15.9 mg, 37%). Anal. Found: C, 53.54; H, 5.33; N, 5.55; Br, 6.98 ($FeC_{26}H_{28}N_2O_6(C_4H_9NO)_{0.40}(H_2O)_{1.05}Br_{0.55}$, calc'd: C, 53.63; H, 5.49; N, 5.44; Br, 7.11).

Synthesis of trans-Fe(Ph_2dhbq)($DMA)_2Br_{0.55}$ from Fe^{III} for SCXRD: In a glovebox with a nitrogen atmosphere, a 4 mL scintillation vial was charged with a solution of H_4Ph_2dhbq (2.5 mg, 8.5 µmol) in 0.5 mL DMA. A solution of $FeBr_3$ (2.5 mg, 8.5 µmol, 1.0 eq.) in 0.5 mL DMA was layered on top. The vial was sealed and heated at 120 ˚C overnight to give small, dark crystals of *trans*-Fe(Ph_2dhbq)($DMA)_2Br_{0.55}$ suitable for X-ray diffraction.

Fe(Ph$_2$dhbq) Chain Syntheses from Fe^{II}

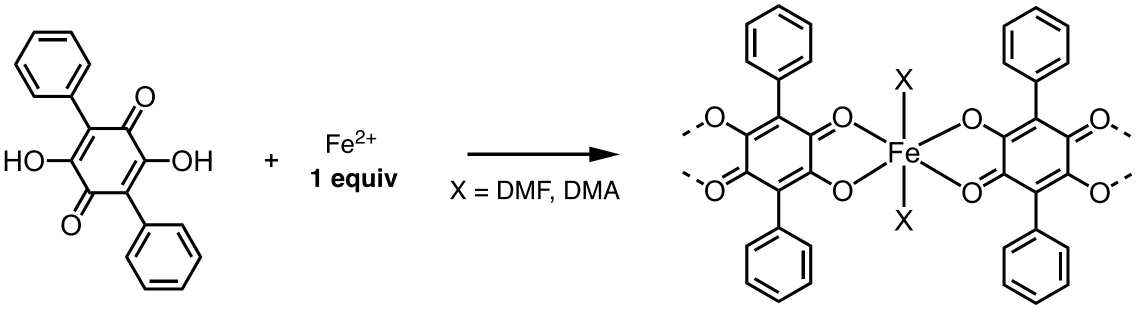

Scheme C3: Generalized synthesis of *cis*-Fe(Ph$_2$dhbq)(DMF)$_2$ and *trans*-Fe(Ph$_2$dhbq)(DMA)$_2$ from H$_2$Ph$_2$dhbq and Fe^{II}.

General synthesis of cis-Fe(Ph$_2$dhbq)(DMF)$_2$ from Fe^{II}: In a glovebox with a nitrogen atmosphere, a 20 mL scintillation vial was charged with a solution of H$_2$Ph$_2$dhbq (26.2 mg, 89.6 μmol) in 5 mL DMF. To the vial was added a solution of FeCl$_2$·4H$_2$O (16.9 mg, 84.8 μmol, 0.9 eq.) in 5 mL DMF. The vial was sealed and heated at 120 ˚C for 5 days to give a dark, polycrystalline powder. The solvent was removed, the powder was washed with DMF (5 × 2.5 mL), and then recovered by vacuum filtration to give *cis*-Fe(Ph$_2$dhbq)(DMF)$_2$ as a dark solid (30.3 mg, 72%). Anal. Found: C, 57.56; H, 4.88; N, 5.67 ($FeC_{24}H_{24}N_2O_6(H_2O)_{0.45}$, calc'd: C, 57.60; H, 5.02; N, 5.60).

General synthesis of trans-Fe(Ph$_2$dhbq)(DMA)$_2$ from Fe^{II}: In a glovebox with a nitrogen atmosphere, a 20 mL scintillation vial was charged with a solution of H$_2$Ph$_2$dhbq (24.9 mg, 85.1

μmol) in 5 mL DMA. To the vial was added a solution of $FeCl_2 \cdot 4H_2O$ (16.9 mg, 85.1 μmol, 1.0 eq.) in 5 mL DMA. The vial was sealed and heated at 120 ˚C for 5 days to give small, dark crystals. The mother liquor was removed, the crystals were washed with DMA (5 × 2.5 mL), and then recovered by vacuum filtration to give *trans*-Fe(Ph_2dhbq)$(DMA)_2$ as a dark solid (23.0 mg, 52%). Anal. Found: C, 59.85; H, 5.43; N, 5.49 ($FeC_{26}H_{28}N_2O_6$, calc'd: C, 60.01; H, 5.42; N, 5.38).

Synthesis of trans-Fe(Ph_2dhbq)$(DMA)_2$ from Fe^{II} for SCXRD: In a glovebox with a nitrogen atmosphere, a 4 mL scintillation vial was charged with a solution of H_2Ph_2dhbq (2.4 mg, 8.3 μmol) in 0.5 mL DMA. A solution of $FeCl_2 \cdot 4H_2O$ (1.7 mg, 8.6 μmol, 1.0 eq.) in 0.5 mL DMF was layered on top. The vial was sealed and heated at 120 ˚C for 4 days to give small, dark crystals of *trans*-Fe(Ph_2dhbq)$(DMA)_2$ suitable for X-ray diffraction.

Dc Magnetic Measurements and Analyses

Direct-current (dc) measurements were obtained with a 1000 G applied field and temperatures ranging from 1.8 K to 300 K. All dc measurements were corrected for the diamagnetic contribution of the sample holder, as well as the restraining material and ligand framework (calculated using Pascal's constants).[5] Fits to the dc susceptibility were modeled using analytical solutions to the appropriate spin Hamiltonian (described below) within the Origin software package.[6] C_{eff} was determined experimentally via linear regression of plots of $1/\chi_M$ and T (See Fig. C6-C8). The dc susceptibility data of *cis*-Fe(Ph_2dhbq)$(DMF)_2$ were modeled using an analytical solution to the Seiden Model,[7] derived from the following spin Hamiltonian:

$$\mathcal{H} = \sum_{i=1}^{N-1} \mathcal{H}_i \ , \mathcal{H}_i = J[S_i + S_{i+1}]s_i \qquad \mathbf{(S1)}$$

Here, **Si** is the vector representation of the spin quantum number of the transition metal ions with a length of S, **si** is the spin quantum number of the radical (S = ½), and ***J*** is the metal–radical exchange coupling constant. In the low temperature limit, where J is large relative to k_BT, the molar susceptibility (χ_M) of the chain is described by the following expression:

$$\chi_M \cong \frac{\beta\mu_B^2}{3}\frac{\beta JS}{2}\left(g_S S - \frac{J}{|J|}g_s s\right)^2 \qquad \mathbf{(S2)}$$

Where β is $1/k_BT$, ***g*S** and ***S*** are respectively the g factor and spin of the metal ion, and likewise ***g*s** and ***s*** are the *g* factor and spin of the radical. It should be noted that this model does not account for finite chain sizes, and as such the data below the observed χT_{max} was not included in the fit. Additionally, because this model considers only metal–radical coupling, temperatures above the valence tautomerization transition temperature ($T_{1/2}$) were excluded from the fitting. The dc susceptibility data of *trans*-Fe(Ph_2dhbq)(DMA)$_2$ and *trans*-Fe(Ph_2dhbq)(DMA)$_2$Br$_{0.55}$ were modeled using an analytical solution derived from the classical-spin Heisenberg model for a chain of like spins derived from the following spin Hamiltonian:[8,9]

$$\mathcal{H} = -2J\sum_{-\infty}^{+\infty} \vec{S_\imath}\vec{S}_{i+1} \qquad \mathbf{(S3)}$$

From **S3**, it has been shown that the following analytical expression can be used to describe the average susceptibility (<χ>):[10,11]

$$\frac{<\chi>T}{C_{eff}} \approx \frac{2}{c+2e^{(-4\beta JS^2)}} \quad \mathbf{(S4)}$$

Here, C_{eff} is the effective Curie constant, defined as the Curie constant for a single isolated spin center in the chain, and c is the average chain length In order attempt to account for the presence of Robin-Day Class II/III delocalization in *trans*-Fe(Ph_2dhbq)($DMA)_2Br_{0.55}$, best fits were determined by evenly weighting contributions from an $S = 2$ and an $S = 5/2$ system. While we acknowledge this method does not truly account for the electron delocalization we observe in the Mossbauer spectra, the exchange coupling values did not change significantly from treating the system as entirely $S = 2$ to treating is as entirely $S = 5/2$.

Ac Magnetic Measurements and Analyses

Alternating current (ac) magnetic susceptibility measurements were performed at zero applied magnetic field on samples made from Fe^{III} and Fe^{II}. Ac frequencies were scanned between 1 and 1500 Hz, with an oscillating field amplitude of 4 G.

The in-phase ac magnetic susceptibility (χ_M') under zero-field was modeled using an Arrhenius-like equation, which captures the temperature-dependent growth of the chain-like magnetic units from Ising spins in response to an activation energy to spin reversal:

$$\chi_M' T = C_{eff} e^{\Delta_\xi/(k_B T)} \quad \mathbf{(S5)}$$

Here, C_{eff} is the effective Curie constant, Δ_ξ/k_B is the domain wall energy, and T is the temperature. Plots of $\ln(\chi_M' T)$ versus $1/T$, ignoring the data above $T_{1/2}$ when applicable, produces a linear regime at the lowest temperatures for all samples. This enables the extraction of Δ_ξ/k_B via linear regression.

The maximum in $\chi_M'T$ also correlates to the average number of units (n) coupled via exchange (the correlation length):

$$n = (\chi_M' T_{\max})/C_{eff} \quad \textbf{(S6)}$$

Quantitative analysis of the out-of-phase (χ_M'') susceptibility was not undertaken for several reasons. First, although out-of-phase susceptibility had non-zero signal for both the *trans*-Fe and *cis*-Fe samples, the relative intensity of χ_M'' to χ_M' suggests that much of the sample is not undergoing slow relaxation. In addition to the weak signal, the broadness of the observed peaks suggests that the observed relaxation phenomena are the product of more than a single relaxing species/ relaxation pathway. As a result, we believe that any fitting/ analysis of this data would be tenuous at best and is unlikely to provide any useful information outside of what was just discussed.

Table C1. Extracted domain wall energy (ξ/k_B), correlation length, Exchange coupling, g-factor and C_{eff} for *cis*-Fe(Ph_2dhbq)($DMF)_2$, *trans*-Fe(Ph_2dhbq)(DMA$)_2$, and *trans*-Fe(Ph_2dhbq)(DMA$)_2$Br$_{0.55}$ obtained as described above.

Compound	$\Delta\xi/k_B$ (cm^{-1})	**Correlation Length**	C_{eff}	**Exchange Coupling** J (cm^{-1})	g_S
cis-Fe(Ph_2dhbq)(DMF$)_2$	37.03	14	3.21	-230 (±4)	2.38
trans-Fe(Ph_2dhbq)(DMA$)_2$	6.02	6	3.70	+0.30 (±0.00 5)	2.3
trans-Fe(Ph_2dhbq)(DMA$)_2$Br$_{0.55}$	12.19	4	4.12	+0.64 (±0.01)	-

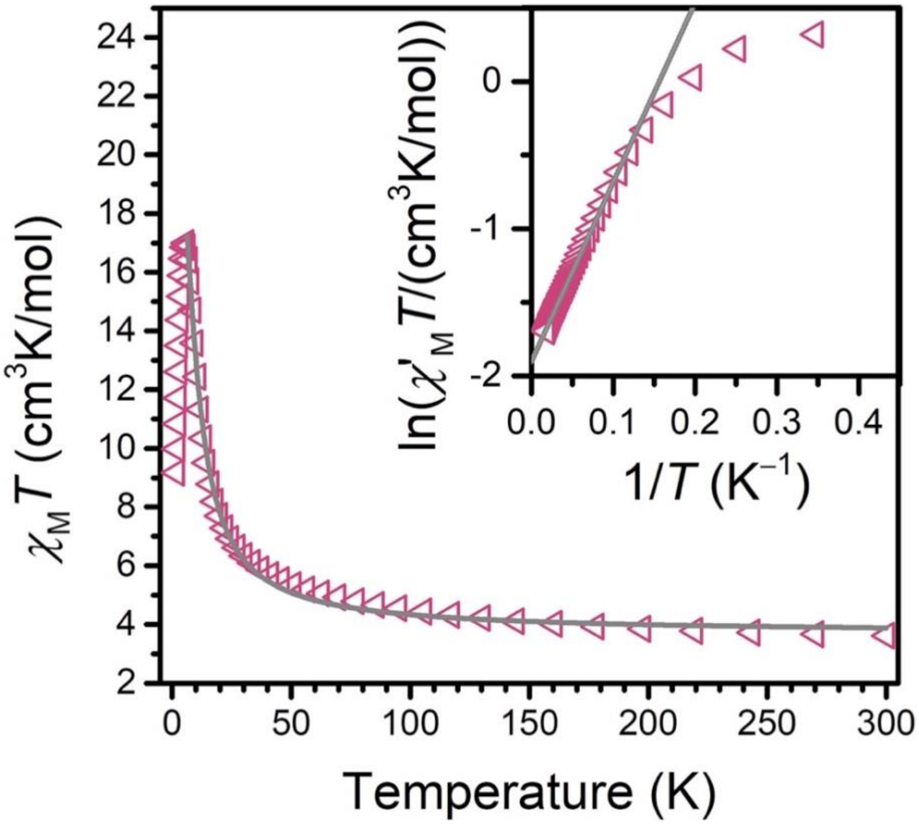

Figure C1. Dc magnetic susceptibility ($\chi_M T$) measurements for *trans*-Fe(Ph_2dhbq)(DMA)$_2$$Br_{0.55}$ under an applied field of 1000 G. The solid line is a best fit with $J = +0.82$ cm^{-1}. Inset: variable-temperature in-phase ac magnetic susceptibility (χ_M') of *trans*-Fe(Ph_2dhbq)(DMA)$_2$$Br_{0.55}$. The gray line is a linear fit that yields a correlation length of 4. Data were collected at zero dc field with an applied ac field frequency of 1 Hz.

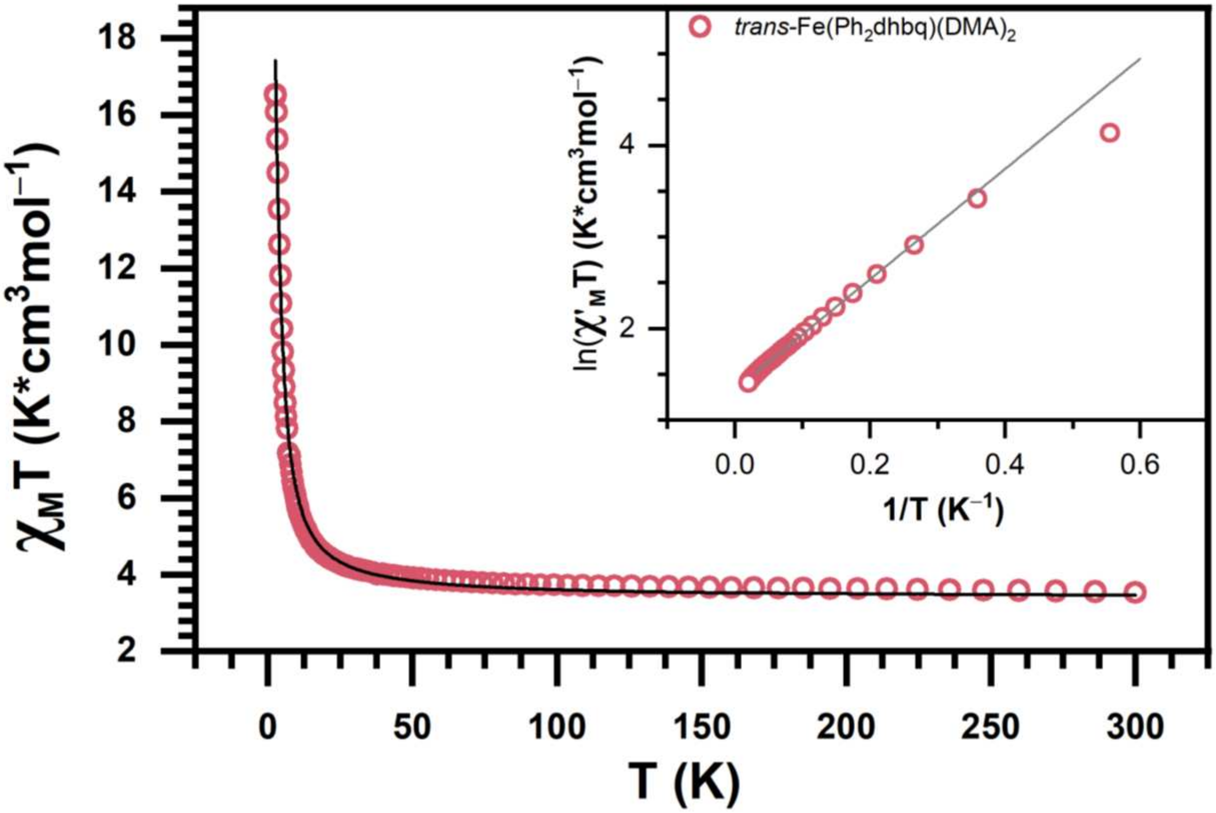

Figure C2. Dc magnetic susceptibility ($\chi_M T$) measurements for *trans*-Fe(Ph_2dhbq)(DMA)$_2$ under an applied field of 1000 G. The solid line is a best fit with $J = +0.82$ cm^{-1}. Inset: variable-temperature in-phase ac magnetic susceptibility (χ_M') of *trans*-Fe(Ph_2dhbq)(DMA)$_2$. The solid line is a linear fit that yields a correlation length of 4. Data were collected at zero dc field with an applied ac field frequency of 1 Hz.

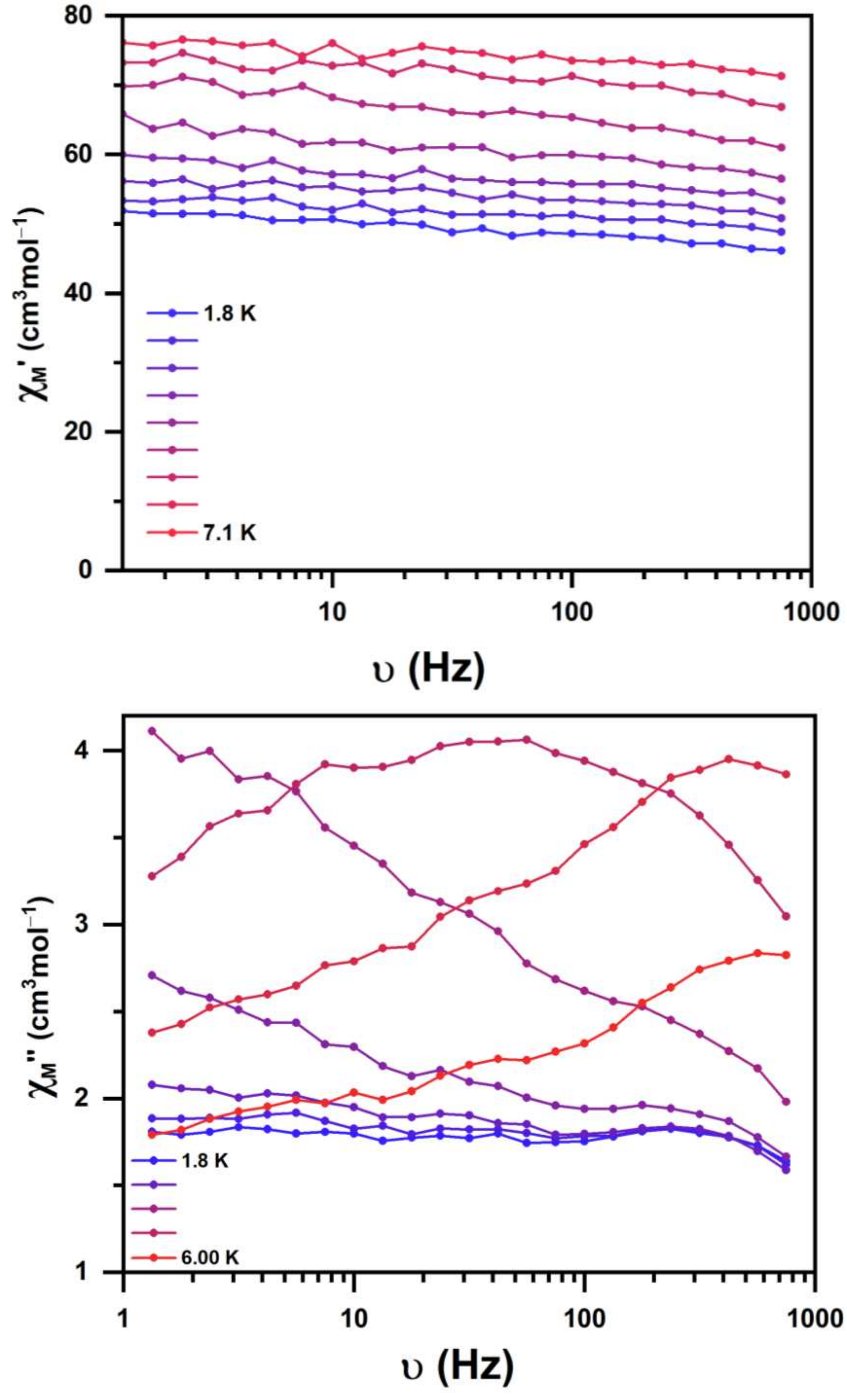

Figure C3. Frequency dependence of the in-phase (χM') and out-of-phase (χM") ac magnetic susceptibility of ground samples of *cis*-Fe(Ph_2dhbq)$(DMF)_2$ synthesized from Fe^{III} at temperatures between 1.8 and 7.1 K.

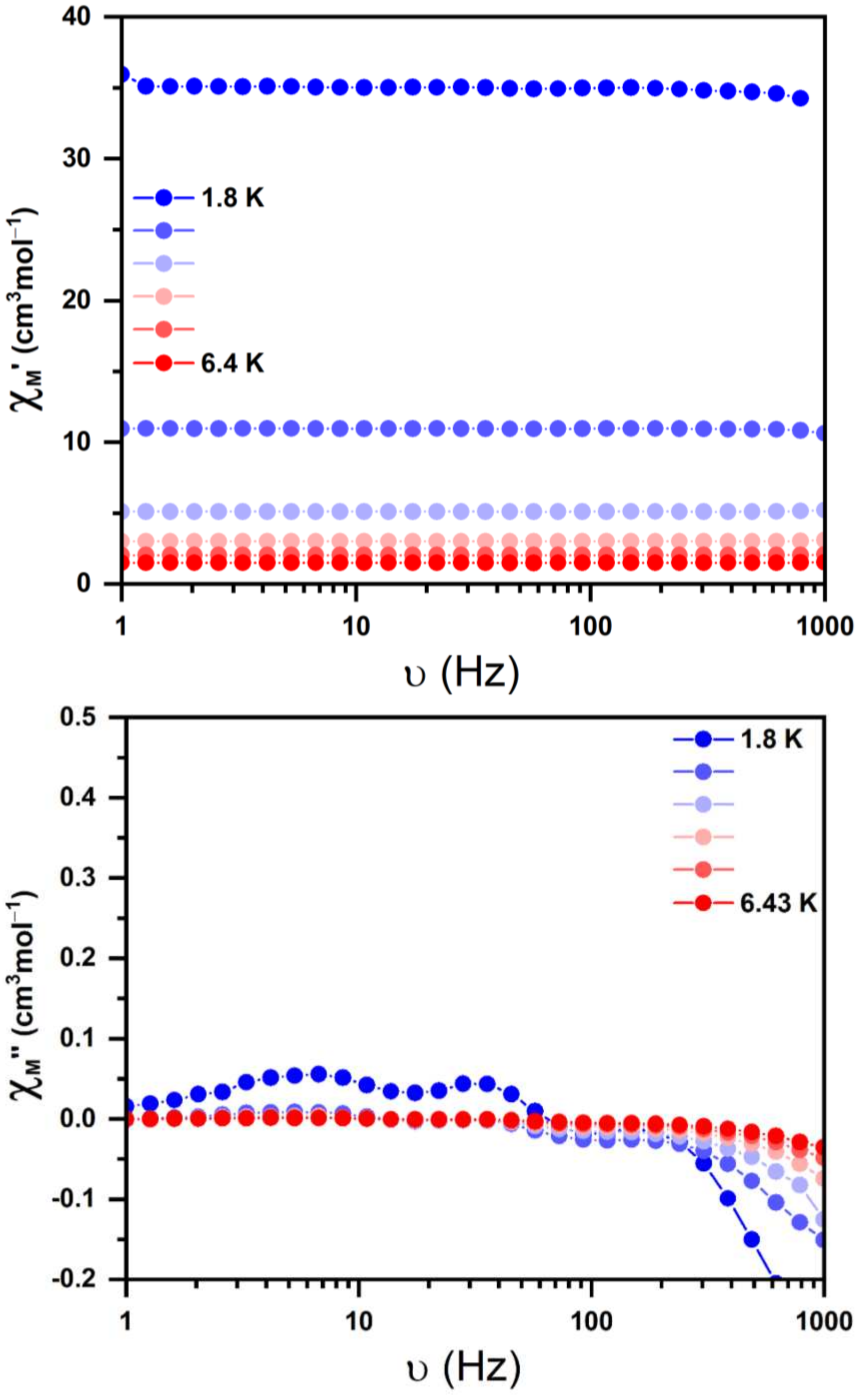

Figure C4. Frequency dependence of the in-phase (χ_M') and out-of-phase (χ_M'') ac magnetic susceptibility of ground samples of *trans*-Fe(Ph_2dhbq)($DMA)_2$ at temperature between 1.8 and 6.4 K.

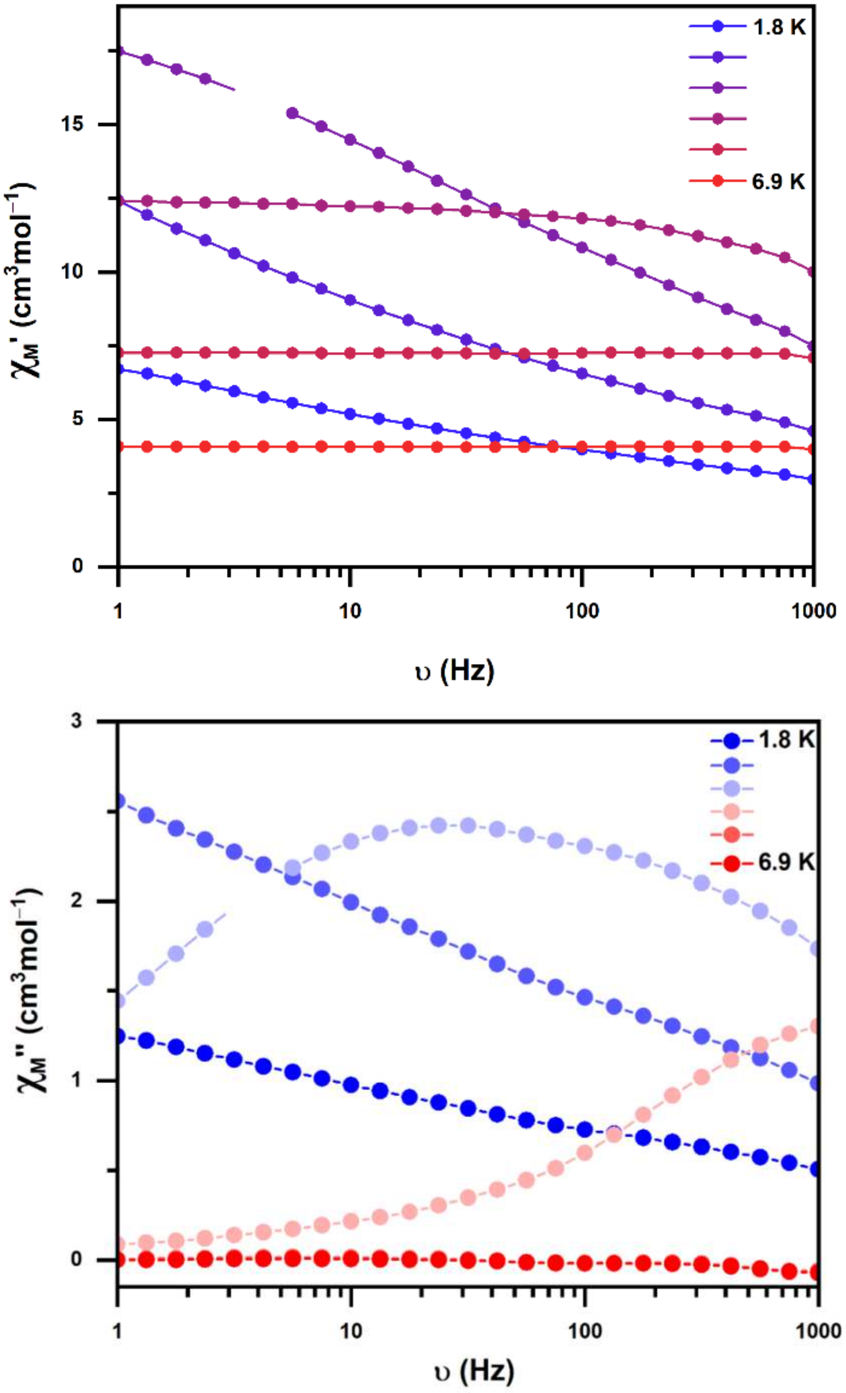

Figure C5. In-phase (χ_M') and out-of-phase (χ_M'') ac magnetic susceptibility as a function of frequency for ground samples of *trans*-Fe(Ph$_2$dhbq)(DMA)$_2$Br$_{0.55}$ at temperatures between 1.8 and 6.9 K.

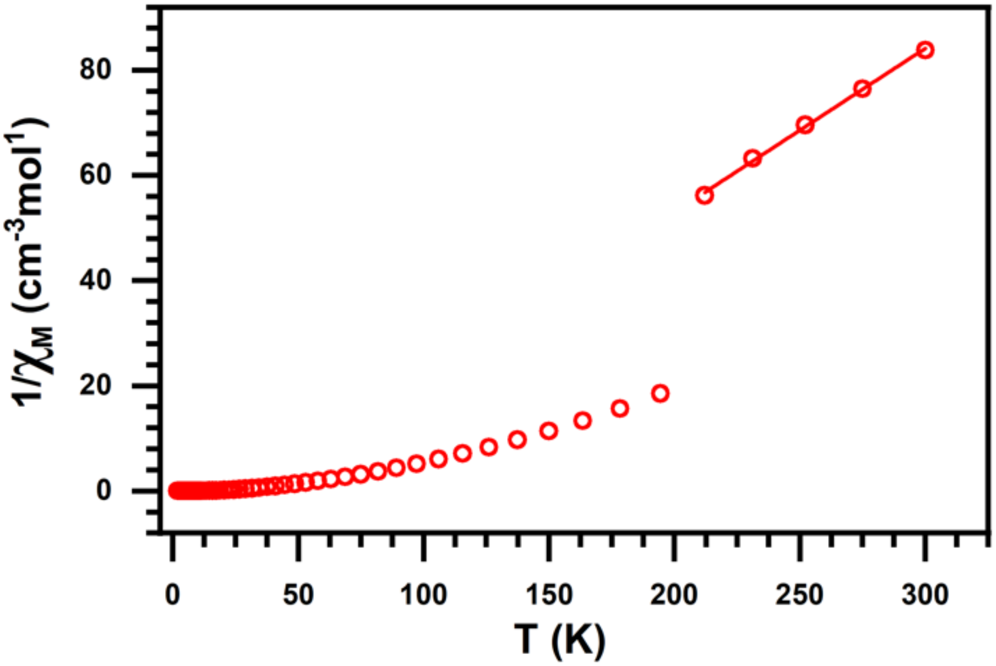

Figure C6. Inverse susceptibility as a function of temperature for *cis*-Fe(Ph_2dhbq)($DMF)_2$ synthesized from Fe^{III} obtained at 1000 G. The solid line represents the linear fit used to obtain the value for C_{eff}.

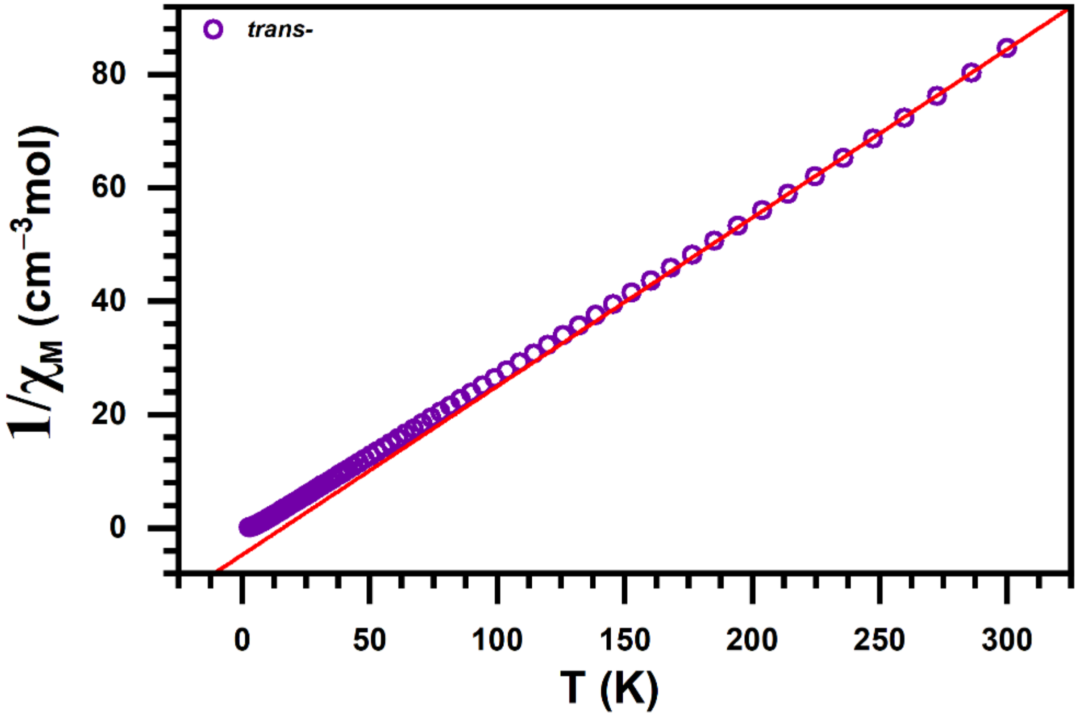

Figure C7. Inverse susceptibility as a function of temperature for *trans*-Fe(Ph_2dhbq)($DMA)_2$ obtained at 1000 G. The solid line represents the linear fit used to obtain the value for C_{eff}.

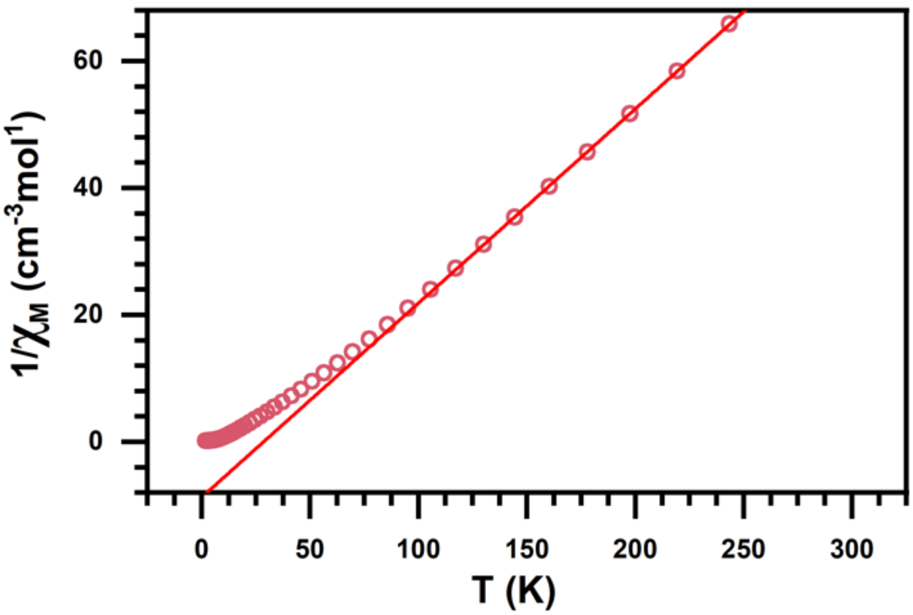

Figure C8. Inverse susceptibility as a function of temperature for *trans*-Fe(Ph_2dhbq)$(DMA)_2Br_{0.55}$ obtained at 1000 G. The solid line represents the linear fit used to obtain the value for C_{eff}.

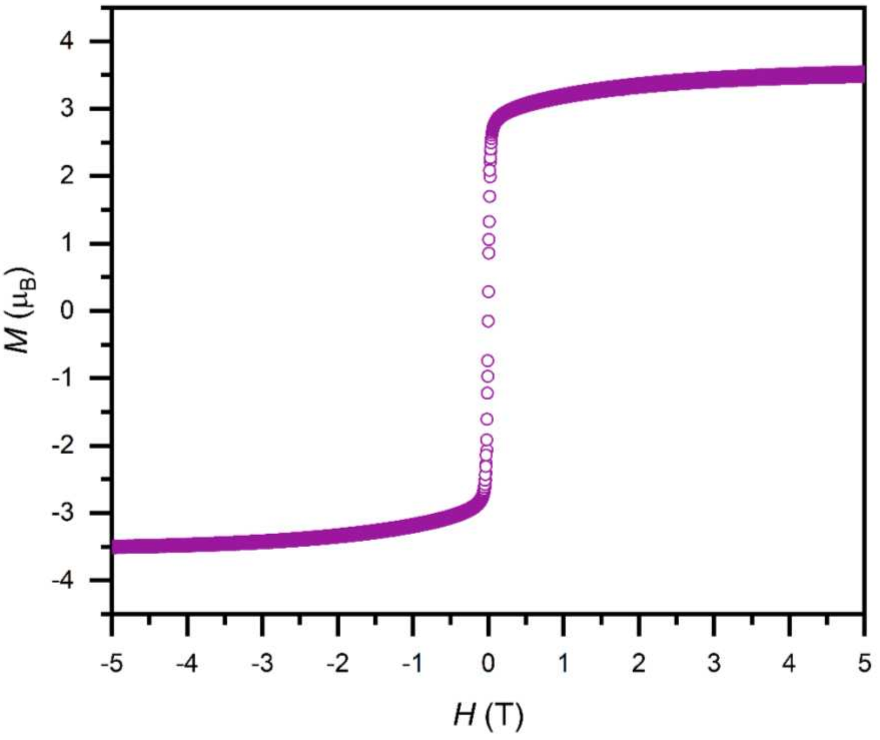

Figure C9. Variable field magnetization data for *cis*-Fe(Ph_2dhbq)$(DMF)_2$ collected at 2.25 K.

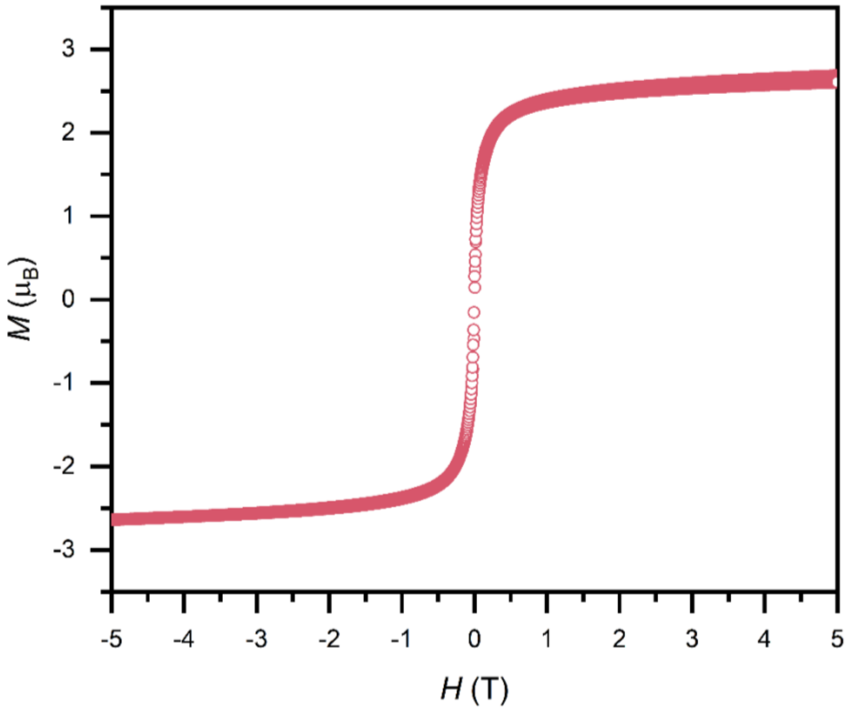

Figure C10. Variable field magnetization data for *trans*-Fe(Ph_2dhbq)(DMA)$_2$ collected at 2.25 K.

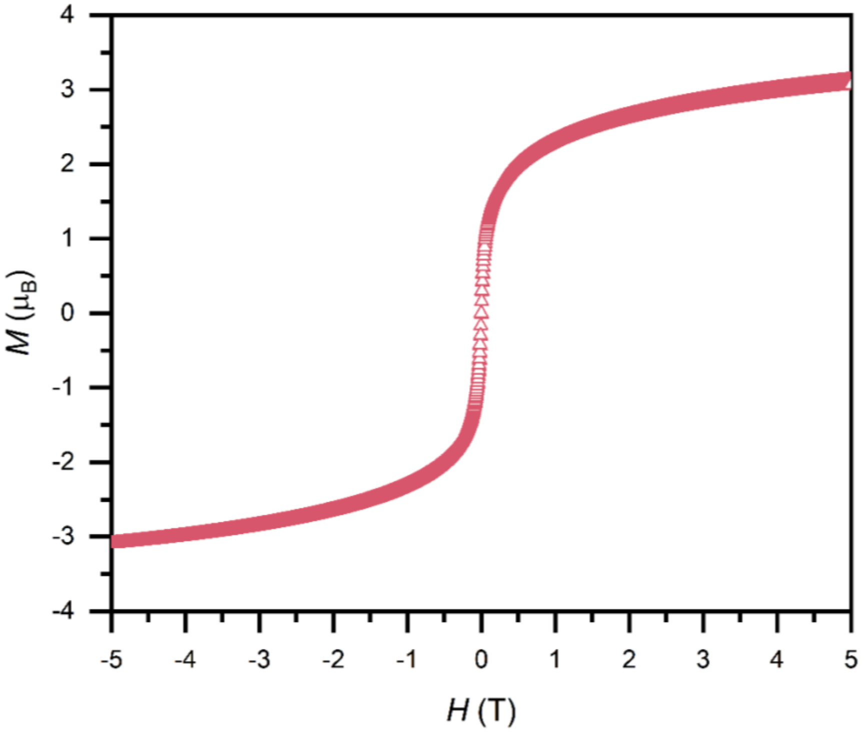

Figure C11. Variable field magnetization data for *trans*-Fe(Ph_2dhbq)(DMA)$_2$Br$_{0.55}$ collected at 2.25 K.

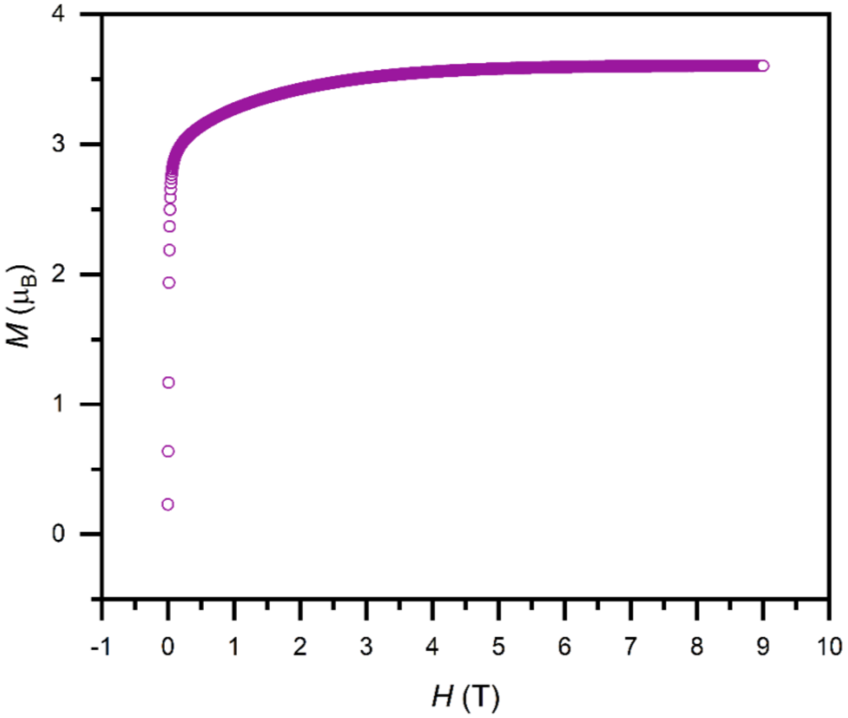

Figure C12. Variable field magnetization data for *cis*-Fe(Ph_2dhbq)(DMF)$_2$ collected at 2.25 K.

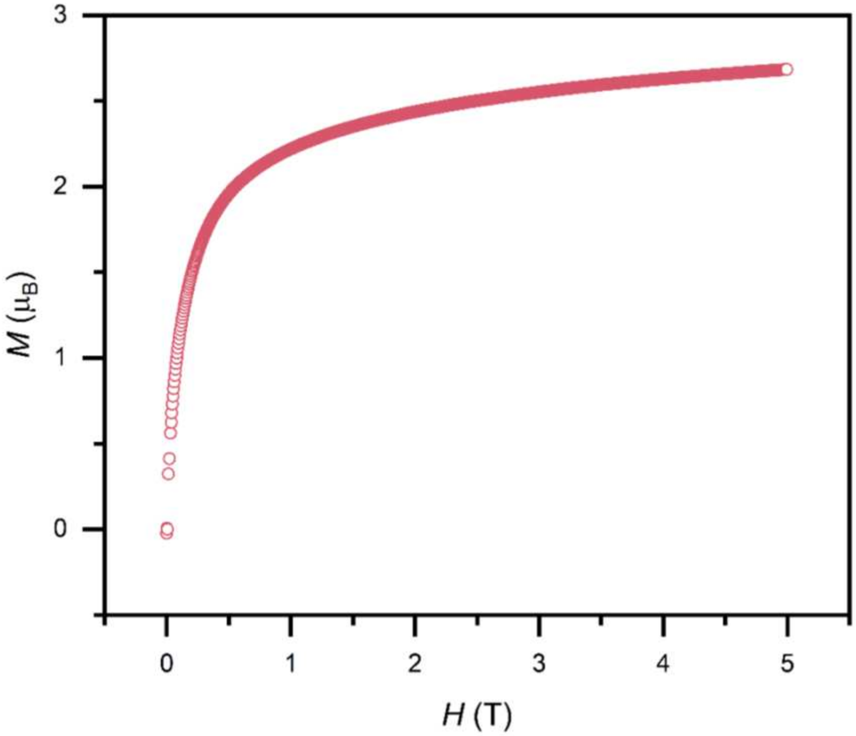

Figure C13. Variable field magnetization data for *trans*-Fe(Ph_2dhbq)(DMA)$_2$ collected at 2.25 K.

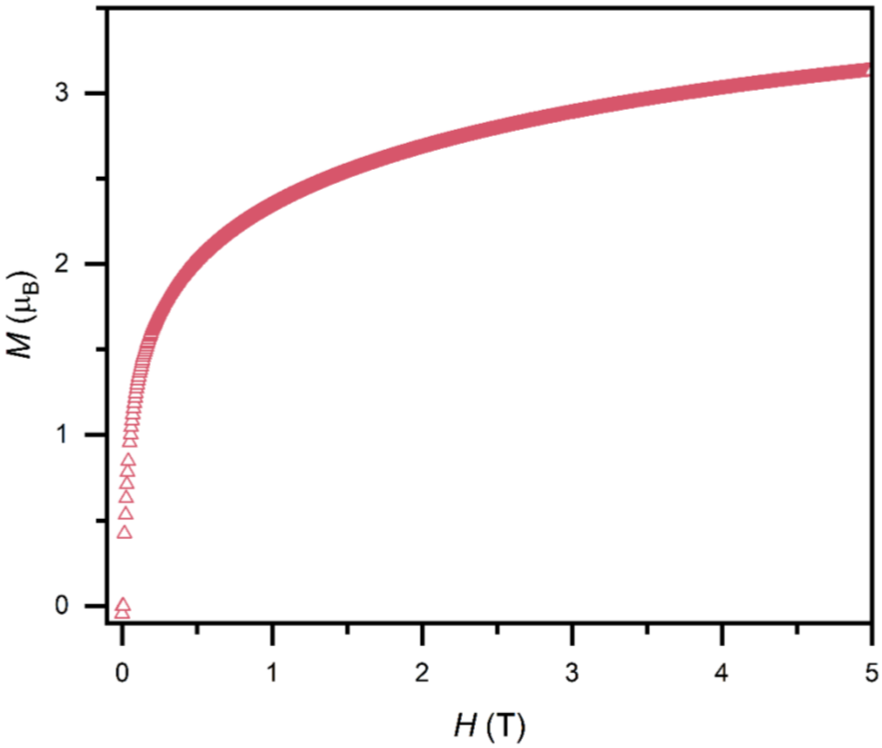

Figure C14. Variable field magnetization data for *trans*-Fe(Ph$_2$dhbq)(DMA)$_2$Br$_{0.55}$ collected at 2.25 K.

APPENDIX D

Supplementary Figures

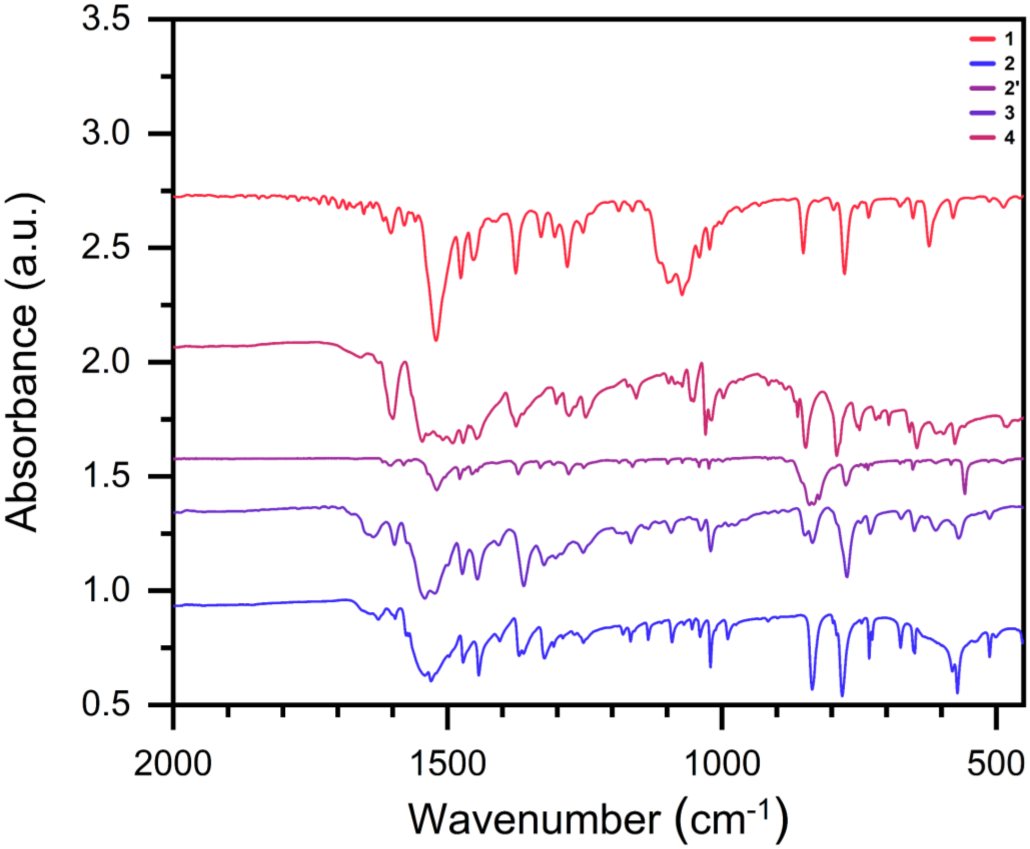

Figure D1. Room temperature IR/NIR spectra for **1** – **4** from 450 – 2000 cm^{-1}.